

The Spatial and Temporal Variability of Nearshore Currents

David Johnson, B.Sc.(Hons), MPhil

School of Water Research

Faculty of Engineering, Computing and Mathematics

This thesis is submitted in fulfilment of the requirements for the degree of
Doctor of Philosophy of the University of Western Australia

· March, 2004 ·

Abstract

The nearshore current field, defined here as the residual horizontal flow after averaging over the incident wave period, exhibits variability at a range of time and space scales. Some of the variable currents are low frequency gravity wave motions. However, variable, rotational (in the sense of possessing vertical vorticity) flow can also exist as part of the overall nearshore current field. A field and numerical modelling investigation of these variable rotational currents has been carried out.

Drifters, which were developed for surf zone use, enabled measurement of the nearshore current structure; the design and testing of these new instruments is described. Two sets of field measurements, using the new drifters and Eulerian instruments were carried out for conditions with swell perpendicular to a plane beach and in strong longshore currents. In the perpendicular swell conditions, an interesting and well-defined feature of the measured trajectories was the development of transient rip currents. Discrete vortices were also observed. In the longshore current case, trajectories with the longshore current displacement removed had complex meandering paths. Lagrangian data were used to make estimates of length scales and dispersion, both of which provide strong evidence that the current field cannot be due to low frequency gravity waves alone. Under the assumption of equi-partition of kinetic and potential energy for low frequency gravity waves, Eulerian measurements of velocities and pressure show significant energy due to non-divergent, rotational flow in both the perpendicular swell and longshore current case.

A numerical model that can simulate horizontal flow with a directionally spread, random wave field incident on a plane beach was implemented. The model developed transient rip currents that are qualitatively very similar to those seen in the drifter trajectories from the field. The number and intensity of rip currents in the model depended on the beach slope and incident wave spectra. The energy content and cross-shore flux (and hence transport of material) of the rotational current flow component in the simulated flow fields is comparable to that due to low frequency gravity waves. The modelling also provided some evidence that there may be universal characteristics of the rotational currents.

The field results and modelling show that variable rotational currents are ubiquitous in the field even when longshore currents and hence shear waves are not present. The term "infragravity turbulence" is suggested to describe the general class of nearshore hydrodynamics not directly associated with shear waves, which is largely disorganised, but contains well defined features such as transient rip currents and large scale horizontal vortices. The results have important implications in the understanding of the transport of material, including sediment, biological material, pollution, and sometimes bathers, in the nearshore zone.

Contents

Preface	vii
Acknowledgements	viii
Notation	x
1 Introduction	1
1.1 Overview	1
1.2 Significance	3
2 Background	5
2.1 Introduction	5
2.2 Nearshore current systems	6
2.2.1 Longshore currents	6
2.2.2 Topographic rip currents	6
2.2.3 Undertow	7
2.3 Variable nearshore currents	8
2.3.1 Infragravity waves	8
2.3.2 Shear waves	9
2.3.3 Topographic rip current instability	9
2.3.4 Transient rip currents	10
2.3.5 Large scale horizontal vortices	10
2.3.6 Undertow variability	11
2.4 Field measurement techniques	11
2.4.1 Eulerian arrays	12
2.4.2 Lagrangian techniques	12
2.5 Summary	13
3 Theoretical framework	15
3.1 Introduction	15
3.2 Nearshore currents	15
3.2.1 Governing equations for nearshore currents	16
3.2.2 Incident wave forcing	16

3.2.3	Lateral mixing	18
3.2.4	Bottom friction	18
3.3	Quasi-steady currents	18
3.4	Variable currents	19
3.4.1	Rotational and divergent currents	20
3.4.2	Energetics	26
3.4.3	Forced variable rotational currents	28
3.5	Summary	29
4	Surf zone drifters	31
4.1	Introduction	31
4.2	Drifter Design	32
4.2.1	Design of the receiver unit	34
4.2.2	Drogue design	36
4.3	Modelling surfzone drifter dynamic response	37
4.3.1	Approximating the hydrodynamics of the surfzone	38
4.3.2	A rigid body model for the drifter assembly	39
4.3.3	Simulation results	43
4.4	Measurement errors	46
4.4.1	Analysis of Position errors	48
4.4.2	Errors in velocity and acceleration calculations	50
4.5	Field validation	54
4.6	Summary and conclusions	58
5	Field measurements of transient rip currents	59
5.1	Introduction	59
5.2	Field site and methodology	62
5.2.1	Field site	62
5.2.2	Field methodology	63
5.3	Eulerian measurements	65
5.3.1	Wave recorder	65
5.3.2	ADCP	65
5.4	Descriptive analysis of the rip currents	70
5.4.1	Rip event 3a (Figure 5.7)	70
5.4.2	Rip event 3b (Figure 5.8)	73
5.4.3	Rip event 2a (Figure 5.10)	73
5.4.4	Rip event 2b (Figure 5.11)	76
5.5	Analysis of drifter clusters	78
5.5.1	Dynamics of the clusters in the rip neck	82

5.5.2	Cluster dispersion	84
5.6	Spatial variability of the current field	88
5.7	Discussion	90
5.8	Summary and conclusions	92
6	Field measurements of longshore currents	95
6.1	Introduction	95
6.2	Field site and methodology	95
6.2.1	Field site	95
6.2.2	Field methodology and incident wave conditions	96
6.3	ADCP data	98
6.4	Drifter trajectories	99
6.5	Cluster dispersion	105
6.6	Discussion	107
6.7	Summary and conclusions	108
7	Numerical modelling	111
7.1	Introduction	111
7.2	Model implementation	114
7.2.1	Discretization of wave spectra	116
7.3	Experiments	119
7.3.1	Model domain	119
7.3.2	Wave spectra	119
7.3.3	Simulation runs	121
7.4	Results	123
7.4.1	Longshore timeseries	130
7.5	Comparison of transient rip occurrence	132
7.6	Transient rip generation	135
7.6.1	Vorticity balance	139
7.6.2	Feedback	140
7.7	The rotational flow field	145
7.7.1	Partitioning the flow field	145
7.7.2	Cross-shore flux	147
7.7.3	Energy partition	147
7.7.4	Longshore wavenumber spectra	150
7.8	Effect of bottom friction and subgrid mixing	151
7.9	Discussion	154
7.10	Summary and conclusions	157

8	Discussion and Conclusions	159
8.1	Introduction	159
8.2	Original contribution	159
8.3	Questions and ideas	160
8.3.1	Incident wave field feedback	160
8.3.2	Three-dimensional effects	162
8.3.3	Infragravity turbulence	163
8.3.4	Nearshore mixing	166
8.4	Further work	169
8.4.1	Idealised infragravity turbulence	169
8.4.2	Field work	170
8.5	Conclusions	170
	References	180
A	Models and scales for the forcing terms	181
A.1	Incident wave forcing, S	181
A.2	Lateral mixing, L	182
A.3	Bottom friction, B	183
A.4	Reynolds type stress, T	184

Preface

All of the work contained herein was carried out by the author under the supervision of C. Pattiaratchi between April 2001 and February 2004. This work is original, and the usual references are made to existing literature. The main part of the thesis consists of four journal papers which have been submitted for publication. Two of these have been reviewed, revised and accepted, so the final material incorporates some of the suggestions of the reviewers.

Acknowledgments

First, thankyou to Chari Pattiaratchi for all the help, encouragement and advice. He also gave the intellectual freedom to follow my own ideas, and for that I am grateful. I am grateful to Aafke, Antwanet, Alexis, Ashley, Drew, Glenn, Jeff, Joe, Kate, Kathryn, Kristen, Selma for getting wet and sunburnt helping out with fieldwork.

All of the numerical modelling was carried out using a modified version of *Fun-wave2D* from *Center for Applied Coastal Research, University of Delaware*. The high quality source code and documentation that is freely available to the scientific community is gratefully acknowledged. Simulations were run on a high performance computer at the Western Australian Interactive Virtual Environments Centre (IVEC).

I would like to acknowledge the helpful comments and questions from the anonymous reviewers of manuscripts which form part of Chapter 4 and all of Chapter 5. Stephen Henderson made numerous helpful comments and suggestions in preparing the manuscript which is Chapter 5.

Finally, but most importantly, family and friends, both at home and work, who have supported me and made it all fun; thankyou all very much. Malene, thankyou for being you, for encouraging me and putting up with me, and for the very practical help of proof reading.

This work was carried out while I was in receipt of a University Postgraduate Award (International) from the University of Western Australia; I am grateful for the financial support during my study. This is contribution ED1526 from the Centre for Water Research, University of Western Australia.

Notation

In general bold face vector notation will be used. As this work is mainly concerned with horizontal currents, vectors and vector operators are two dimensional unless stated otherwise,

$$\begin{aligned}\mathbf{U} &= [U, V] \\ \mathbf{U} \times \mathbf{X} &= UX - VY \\ \nabla b &= \left[\frac{\partial b}{\partial x}, \frac{\partial b}{\partial y} \right] \\ \nabla \cdot \mathbf{U} &= \frac{\partial U}{\partial x} + \frac{\partial V}{\partial y} \\ \nabla \times \mathbf{U} &= \frac{\partial V}{\partial x} - \frac{\partial U}{\partial y} \\ \nabla^\perp b &= \left[-\frac{\partial b}{\partial y}, \frac{\partial b}{\partial x} \right]\end{aligned}$$

Note that the cross product and curl operators produce a “pseudo” scalar. Individual components of the three dimensional position and velocity vector are denoted by x, y, z and u, v, w respectively and may involve a change of case or other embellishment such as \bar{u}, u', \tilde{u} . There is occasional use of index notation such that,

$$U_i = [U_1, U_2] = [U, V]$$

and where a repeated index implies summation over all possible index values.

A list of symbols is given on the next page. This only includes quantities that occur throughout the thesis. Some of are temporarily redefined in Chapter 4, but this is made clear with a footnote. Symbols that only occur locally in one section are not included in the list.

List of symbols

$\bar{\zeta}, \zeta_o, \zeta$	Total/Quasi-steady/Variable current vorticity
$\bar{\eta}, \eta_o, \eta$	Total/Quasi-steady/Variable wave-average surface elevation
$\tilde{\eta}$	Instantaneous surface elevation
ν_t	Turbulent eddy viscosity
ν_u	Pseudo eddy viscosity of mixing due to variable currents
Σ	Incident wave directional spreading parameter
ϕ	Variable current flux potential
ψ	Variable current flux stream function
ω	Incident wave angular frequency
a	Incident wave amplitude
$\bar{\mathbf{B}}, \mathbf{B}_o, \mathbf{B}$	Total/Quasi-steady/Variable incident wave forcing
C, C_g	Incident wave phase/group speed
E	Incident wave energy
f	Oscillation frequency
f_w	Wave friction factor
g	Gravitational acceleration
h, h^*	Static/Quasi-steady water depth
\bar{h}	Total wave-averaged water depth
H, H_s	Monochromatic/Significant wave height
\mathbf{k}	Incident wave number vector
\mathbf{K}	Dispersion coefficient
$\bar{\mathbf{L}}, \mathbf{L}_o, \mathbf{L}$	Total/Quasi-steady/Variable incident wave forcing
\mathbf{Q}^w	Incident wave mass flux
$\bar{\mathbf{S}}, \mathbf{S}_o, \mathbf{S}$	Total/Quasi-steady/Variable incident wave forcing
T	Wave period
$\tilde{\mathbf{u}}$	Instantaneous (depth dependent) velocity
$\tilde{\mathbf{u}}^w$	Incident wave component of instantaneous velocity
$\bar{\mathbf{U}}, \mathbf{U}_o, \mathbf{u}$	Total/Quasi-steady/Variable current
$\bar{\mathbf{U}}^1$	Wave-averaged current variation

Chapter 1

Introduction

1.1 Overview

The nearshore zone is the region at the coastline including the surfzone where waves break and the region immediately seaward. It is a highly energetic region in which the incident waves, swell and locally generated sea, dissipate their energy. Hydrodynamic processes occur at a range of space and time scales as shown in Figure 1.1. Nearshore currents are a general term for horizontal flows which have lower frequencies than, and are driven by, the incident waves.

This work is concerned with nearshore currents which vary both spatially over length scales of $10 - 100\text{ m}$ and temporally over timescales of $100 - 1000\text{ s}$, but are *not* due to infragravity waves. The variable currents considered are not related to topography and can exist on a longshore uniform beach. This mode of nearshore current motion, which co-exists and interacts with the array of other hydrodynamic process, can be generically understood as variable (transient) rotational currents. Variable rotational currents include transient rip currents, shear waves, and large scale horizontal vortices (Figure 1.1).

This thesis presents work undertaken by both field measurements and numerical modelling. The field work has obtained Lagrangian measurements of the nearshore current structure. An important part of the field aspect of the work has been the development of a surfzone drifter capable of making Lagrangian measurements of nearshore currents. The numerical modelling approach has used a Boussinesq model to investigate the dynamics of the nearshore currents by simulating the instantaneous flow, and then recovering the wave-averaged currents. The first part of the field work and the modelling investigated transient rotational currents in the absence of quasi-steady mean flows. A second set of Lagrangian field measurements were carried out in a longshore current.

The outline of the thesis structure is as follows. The next two chapters outline the

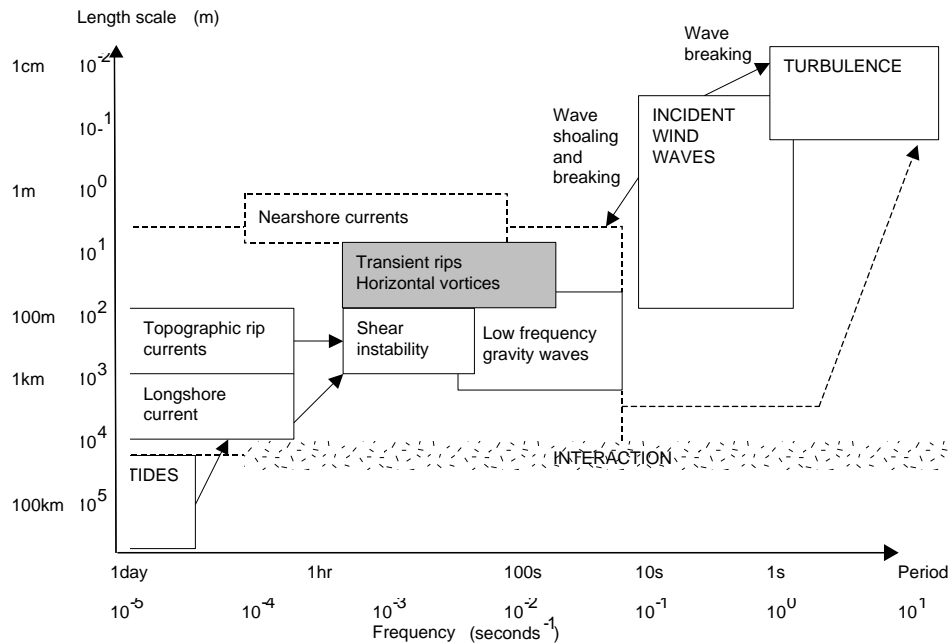


Figure 1.1: Hydrodynamic processes in the nearshore zone.

context for the original work which has been carried out. Chapter 2 is an overview of the state of knowledge about nearshore currents. Chapter 3 outlines the mathematical framework for a quantitative description and provides a formal definition of the transient rotational currents and their relationship to other types of nearshore currents. The main part of the original work has already been published/submitted as four papers and a conference proceedings:

1. Johnson, D., Stocker, R., Head, R., Imberger, J. and Pattiaratchi, C.B. A compact, low-cost GPS drifter for use in the oceanic nearshore zone, lakes and estuaries. *Journal of Atmospheric and Oceanic Technology* **20** 1880-1884
2. Johnson, D. and Pattiaratchi, C. Application and modelling of surf zone drifters. In press, *Coastal Engineering*
3. Johnson, D. and Pattiaratchi, C. (2004) Transient rip currents and nearshore circulation on a swell dominated beach. *Journal of Geophysical Research* **109**, (C02026), doi:10.1029/2003JC001798
4. Johnson, D. and Pattiaratchi, C.B. A small, low-cost GPS drifter for use in coastal studies. COPEDEC VI proceedings, Engineering the Coastal Environment , September 15-19 2003, Colombo, Sri Lanka.

5. Johnson, D. and Pattiaratchi, C.B. Boussinesq modelling of transient rip currents. Submitted to *Continental Shelf Research*

The first two papers have been combined and form Chapters 4, which describes the design and testing of the surf zone drifter. Chapter 5 is essentially paper 3, concerning field measurements of transient rip currents and associated circulation. Chapter 6 describes a series of longshore current experiments; it is an extension of material published in the conference proceedings. The final paper, which describes the numerical modelling of transient nearshore currents forms Chapter 7. Finally, Chapter 8 is an overall discussion of the work, including a synthesis of conclusions and suggestions for future research. The exact text in chapters 4, 5 and 7 differs slightly from the papers; cross references have been changed to chapter numbers, equation notation has been standardised, and the paper abstracts and summary/conclusions have been combined into a single summary at the end of each chapter. As Chapters 4, 5 and 7 are self contained papers, there is some repetition of introductory material and to a lesser extent discussion.

1.2 Significance

A better understanding of nearshore currents is important, as they are the primary transport mechanism for material in the nearshore zone. Although the instantaneous velocities are usually dominated by the incident wave field, the relatively short time scale of these motions means that they act primarily as a mobilising and stirring mechanism. The wave-averaged currents are of interest in determining the net displacement of material. Specific areas of application include:

- Movement of sediment and associated morphological change.
- Transport and dispersion of biogeochemical material, potentially including pollution, in the nearshore zone.
- Public safety in locations with strong offshore directed currents.

The effect of variations in nearshore currents on sediment transport is of particular practical interest in coastal engineering. As sediment transport rates usually show a non-linear relationship with current velocities, long time mean values of undertow or longshore current may not give accurate results. Periodic events such as transient rip currents may also have profound effects on cross-shore sediment exchange. The investigation of variable currents described in this work should help to further the understanding of these transport processes.

Observing the structure of time-varying currents is difficult as it requires high sensor density over a wide area. While the longshore spatial characteristics of low

frequency waves are estimated from analysis of the cross spectra between pairs of eulerian instruments (Huntley et al., 1981; Oltman-Shay and Guza, 1987), nonlinear features associated with shear instabilities of longshore currents or topographic rip currents are not easily identifiable. Measurement of transient phenomena, which is the focus of this work, is also difficult with fixed instruments. Coherent flow structures such as eddies are potentially far easier to observe directly with a Lagrangian technique. While Lagrangian techniques have been used previously to examine rip currents (Sasaki et al., 1981; Brander and Short, 2000), these have relied on visual fixing techniques and have low temporal resolution. The only example in the literature (to the author's knowledge) of high frequency Lagrangian measurements of the spatial flow structure in the surf zone are those of Schmidt et al. (2003) using GPS drifters developed concurrently with those described here. The development of accurate Lagrangian measurement techniques is clearly important as an alternative viewpoint in field investigations of nearshore hydrodynamics; the development, modelling, and validation of a surf zone drifter, presented in this work, is an important contribution towards that goal.

Chapter 2

Background

2.1 Introduction

This chapter presents an overview of the current knowledge of nearshore currents. A conceptual distinction is made between “quasi-steady” and “variable” currents (this distinction is made more precise in Chapter 3). Quasi-steady currents are steady in the sense that they are the long time average flow velocities which change slowly as the incident wave climate or bottom topography changes. In this sense they are also semi-permanent nearshore current systems with a fixed spatial structure. Variable currents, by contrast, are transient in nature, varying spatially and temporally, and, by definition, possessing a zero long-time mean flow. Whether or not these variable nearshore flows are termed “currents” themselves is a really a matter of definition, but they are referred to as such in this work. As quasi-steady and variable currents co-exist and interact, their distinction is a separation of timescales rather than fundamental physical processes.

In the field there is a complex mixture of variable horizontal currents. Various modes of motion have been identified and defined based on their physical nature. A general classification of surf zone currents in terms of rotational and divergent motions has been discussed by Peregrine (1998). Divergent gravity wave motions may be free or forced and are collectively termed infragravity waves. Shear waves, transient rip currents, and large scale horizontal vortices by contrast are rotational rather than wave-like and can also be free or forced.

The reason for presenting a general overview of nearshore currents is partly to make a careful definition of the distinct types of nearshore motion, and partly because a particular mode of motion does not exist in isolation and is inevitably influenced by the others. Section 2.2 gives an overview of quasi-steady nearshore current systems and Section 2.3, variable currents. Section 2.4 briefly reviews field measurement techniques to place the development of the surf zone drifter described

in Chapter 4 in context.

2.2 Nearshore current systems

The two main types of nearshore current systems which have a quasi-steady horizontal flow are longshore currents and topographic rip currents. As they have a dominant influence on the transport of material in the nearshore zone, in particular sediment, investigations into both of these current systems have occupied a large amount of the research effort to date.

2.2.1 Longshore currents

The longshore current is driven by obliquely incident waves. Analyses of the longshore current structure are normally based on a depth-averaged description (Longuet-Higgins, 1970a,b) in which the driving mechanism is the transfer of alongshore momentum (radiation stress gradients) from the incident wave field to the mean longshore current. This is balanced by frictional forces at the bed and lateral exchange of momentum. The model has been very successful in predicting longshore currents on monotonic beach profiles (Thornton and Guza, 1986). However when applied to a barred beach profile, the same formulation predicts strong jets over the bar rather than the wider currents in the trough which are observed in the field. The problem with the standard model has been that the horizontal eddy mixing coefficient required to produce observed longshore current profiles in this case is far greater than can be realistically explained by small scale turbulent mixing alone.

2.2.2 Topographic rip currents

Rip currents are a generic name given to offshore directed flows and often resemble jets with a strong constrained flow which broadens once it passes beyond the surf zone. The primary driving mechanism for the rip current circulation are longshore variations in the radiation stress. The resulting local imbalance of the setup and radiation stress forces a narrow region of offshore directed flow. Conservation of mass must be satisfied, so that around the rip neck, there is also an onshore flow which can be due to the wave induced flux (both from breaking and Stokes drift) or a diffuse onshore mean flow (or both). The longshore variation of the radiation stress has been attributed to several mechanisms. These mechanisms are summarised in Table 2.1.

A specific distinction can be made between "topographic" rip currents, the last group in Table 2.1, which occur due to alongshore spatial variability in bottom

Table 2.1: Generation mechanisms for the formation of rip currents [adapted from Dalrymple (1978)]

Mechanism		Author(s)
Wave - wave	Incident/synchronous edge wave interaction	Bowen (1969b)
	Incident/infragravity edge wave interaction	Sasaki and Horikawa (1978)
	Intersecting wave trains	Dalrymple (1975)
	Incident wave group/edge wave interaction	Symonds and Ranasinghe (2001)
Wave - current	Refractive wave/current interaction	Dalrymple and Lozano (1978)
	Dissipative wave/current interaction	Murray and Reydellet (2002)
Wave - topography	Bottom topography	Bowen (1969b)
	Coastal boundary - breakwater	Liu and Mei (1976)
	Coastal boundary - islands	Mei and Angelides (1977)
	Barred coastline	Dalrymple (1978)
	Coupled sediment/water interaction	Hino (1975)

topography causing spatially variable transformation of the incident wave field, and the first two groups, which can in theory occur on a longshore uniform beach.

Topographic rip currents are usually associated with a channel in an offshore bar. The morphology of the rip current system can change slowly in time; a topographic rip current system is described by Brander (1999), in which the rip is constrained to a channel that migrates or changes due to erosion and deposition. Such systems can be extremely large (Brander and Short, 2000) and are often the type which cause danger to bathers (Short and Hogan, 1994). In the absence of topographic control, the wave-wave or wave-current interaction mechanisms are unlikely to remain spatially fixed or constant in time and are therefore "transient". A tendency in previous investigations to not distinguish between topographic or transient rip currents (in part because this is difficult to do in the field) may partially explain the lack of success in predicting rip current spacing (Huntley and Short, 1992).

2.2.3 Undertow

Nearshore currents exhibit a three dimensional structure due to the undertow, the wave-averaged (in the same sense as for horizontal currents) offshore directed current which exists below trough level in the nearshore zone. While a vertical average of the three dimensional flow allows the horizontal current, which is the focus of this work, to be properly defined, there are physical effects of the vertical non-uniformity. The most important effect is described by (Svendsen and Putrevu, 1994) and can be understood physically as a shear dispersion of momentum, analogous to that described by Taylor (1954) for solutes, in which the vertical non-uniformity serves to mix momentum horizontally. This dispersive effect can be an order of magnitude larger than the turbulent mixing and is believed to play an important role in determining the shape of longshore current profiles. The shear dispersion effect on the (depth-averaged) horizontal current can be modelled as an enhanced horizontal

eddy viscosity (Ozkan-Haller and Kirby, 1999). Additional three dimensional effects, while relatively smaller in magnitude, have been shown to modify the nature of a three-dimensional flow from the depth uniform case Putrevu and Svendsen (1999).

2.3 Variable nearshore currents

While longshore or rip currents are the long time mean flow, there is a variable flow with frequencies below that the incident waves, but still fluctuating faster than significant changes in incident wave climate or topography. Two well understood classes of variable horizontal flow are low frequency gravity waves, also termed "infragravity" waves, and shear waves, sometimes termed "far infragravity" waves. Another kind of variable horizontal current which have been observed, and proposed theoretically are "transient" rip currents, temporary offshore directed flows that occur in variable locations.

2.3.1 Infragravity waves

The nearshore zone has a spectrum of energetic infragravity waves, with periods in the range 20 s to 200 s . The total horizontal velocity current variance associated with infragravity waves is often large and may even exceed the incident wave signal (Guza and Thornton, 1985). Numerous field studies have shown infragravity waves to be ubiquitous in the nearshore.

Infragravity waves fall into two general classes, depending on whether they are directly forced. Free waves consist of edge waves, trapped to the shoreline by refraction (Eckart, 1951; Ursell, 1952) and leaky waves, which escape back into deep water. Edge waves can only have discrete dispersion curves dependent on the beach slope and therefore are clearly identifiable in cross-spectral analysis (Huntley et al., 1981; Oltman-Shay and Guza, 1987). The generation of edge waves in the surf zone is believed to be due to a non-linear interaction of the incident wave field and the edge wave waveform (Lippmann et al., 1997). The forced waves are variations in wave-averaged surface elevation and velocity directly induced by the variability of the incident wave field. In deep water these "group bound long waves" propagate with the wave group packets (Longuet-Higgins and Stewart, 1962). The variation of wave breaking associated with wavegroups then forces low frequency motion in the surf zone (Symonds et al., 1982; Schäffer and Svendsen, 1988). A real wave field potentially gives rise to a complex pattern of bound infragravity waves.

2.3.2 Shear waves

Shear waves, with typical periods of 100 *s* to 1000 *s* exist in the “far” infragravity band, and were initially identified by Oltman-Shay et al. (1989) in longshore current measurements. These waves have been described theoretically by Bowen and Holman (1989) as originating from a shear instability in the longshore current. Unlike infragravity waves described above, the restoring mechanism is the conservation of potential vorticity rather than gravity. These waves can be described as “free” in the sense that they are oscillations of the background vorticity gradient of the quasi-steady longshore current.

Numerical simulations of longshore currents (Allen et al., 1996; Ozkan-Haller and Kirby, 1999) have shown that as the shear instabilities become finite, meanders increase in size and eventually pinch off from the main flow and form discrete vortices and narrow jets. The total velocity variance associated with shear waves can be similar and may exceed that due to infragravity waves (Howd et al., 1991). Kirby et al. (1998b) have shown that resonant interactions can exist between shear waves and infragravity waves. Whether and how these interactions occur in the general case in the field is not presently well understood.

2.3.3 Topographic rip current instability

A common observation of topographic rip currents is that Eulerian measurements of wave-averaged velocity fluctuates or pulses. One explanation previously proposed is that the rip current forcing is modulated due to wave groups (Cook, 1969; Aagaard et al., 1997) and the rip current pulses at the frequency of the wave group envelope. This mechanism however has not been confirmed in many cases, and Bowman et al. (1988a,b) find to the contrary. An alternative mechanism that would cause pulsing is non-linear instability, similar to shear waves but associated with the shear of the mean rip current flow. Haller and Dalrymple (2001) have shown that fluctuations predicted by a linear stability analysis are consistent with laboratory measurements of pulsing in topographic rip currents. There is visual evidence from the field consistent with instability of the mean flow (Cook, 1969). Pictures in Shepard et al. (1941) clearly show the rip head separating with an associated vortex pair, whilst shorewards a new vortex pair appears to be forming, consistent with an unstable jet type flow. Doppler sonar images of Smith and Largier (1995) and numerical experiments (Chen et al., 1999; Haas et al., 1999, 2003) also show the repeated formation of counter rotating vortex pairs which are advected offshore.

2.3.4 Transient rip currents

Transient rip currents, also called "mini rips" or "flash rips" are short-lived features that are caused by the first three groups of mechanisms in Table 2.1. They are caused by spatial variability of the hydrodynamics rather than strong bathymetric control; in this sense, they are "forced" motions. This type of rip current has been generated in the laboratory with intersecting wave trains (Dalrymple, 1975; Fowler and Dalrymple, 1991) and synchronous incident/edge waves (Bowen, 1969a). Rip currents, which migrate in response to the variation of the incident wave field, are proposed as an alternative explanation for low frequency oscillations attributed to shear waves (Fowler and Dalrymple, 1991). As well as the mechanisms in Table 2.1, transient rip currents have been observed to form in numerical simulations of longshore currents as mentioned in Section 2.3.2, where offshore directed jets are ejected from the main longshore flow.

Field measurements and observations of what were known to be transient rip currents are scarce. There have been attempts to fit observed rip spacing to proposed generation mechanisms (Dalrymple and Lozano, 1978; Murray et al., 2003). Qualitative observation of the dynamics of transient rip generation were presented by Vos (1976). These observations were of transient rip current generation at the highest part of a wave crest and subsequent positive feedback with the emerging rip current. This is at odds with the usual radiation stress based theories where rip currents form at locations of *low* waves. Tang and Dalrymple (1989) made measurements of nearshore currents where rip currents were observed to be migrating and pulsating. While the rip currents could not be unambiguously identified in frequency space, circumstantial evidence strongly suggested that flow associated with the rip currents produced a peak in the low frequency band $< 0.002Hz$ and was correlated to incident wave grouping.

2.3.5 Large scale horizontal vortices

As described in the previous section, the formation of vortex pairs and subsequent shedding offshore is observed in the region of rip currents. Lagrangian velocity data of Schmidt et al. (2003) show the presence of a persistent eddy within the surf zone at the shoreward end of offshore flow in the rip neck. Nonlinear numerical models of longshore currents consistently show vortices shed from longshore current instabilities (Allen et al., 1996; Ozkan-Haller and Kirby, 1999). Another mechanism for generation of vortical structures in the horizontal flow was proposed by Peregrine (1998) and further investigated theoretically by Bühler and Jacobson (2001). This is due to discontinuous wave breaking, as is ubiquitous in random wave field with finite crest lengths, inducing vorticity in the wave-averaged flow.

Very densely spaced Eulerian instruments would be required to identify vortices in the nearshore zone. As this presents a significant logistic challenge, actual velocity measurements (rather than visual observation or photographs) of coherent vortices in the field are limited to those of Schmidt et al. (2003).

2.3.6 Undertow variability

A theoretical analysis of the time variation of undertow in infragravity waves has been carried out by Putrevu and Svendsen (1995). Other than results of laboratory experiment by Okayasu and Katayama (1992) there does not appear to be any published data which considers this time variation. However, the variability of the undertow structure implies variations in the shear dispersion mechanism and other three dimensional effects.

Recently, there have been numerical investigations using quasi-3D (Q3D) models which implicitly model interactions between time varying undertow and horizontal currents. For leaky mode infragravity waves, Van Dongeren and Svendsen (2000) find significant temporal variations in the three dimensional effects which act to modify the infragravity wave envelope. Instabilities of topographic rip currents (Haas et al., 2003) and longshore currents (Zhao et al., 2003) are significantly damped with the inclusion of the Q3D terms, presumably mainly due to the lateral dispersion mechanism. In addition, Zhao et al. (2003) showed that the vertical structure of the horizontal velocity introduces vortex tilting into the vorticity dynamics, otherwise absent from a purely 2D horizontal description. However, in terms of the cross-shore mixing of longshore momentum, which determines the mean shape of the longshore current, the 2D fluctuations of the shear waves were equally or more important than the Q3D terms. It is worth noting that the inclusion of three dimensional effects into Q3D models does not show directly whether the *time variation* of the Q3D effects is itself important; qualitatively similar effects to including Q3D terms was found by Ozkan-Haller and Kirby (1999) in the 2D case by simply increasing the (time invariant) lateral mixing coefficient.

2.4 Field measurement techniques

A variety of techniques have been used to obtain spatial information about the current structure. The majority of field investigations have used Eulerian sensors of varying numbers and arrangements. A few have used Lagrangian techniques such as drifters or dye to map the spatial structure of current systems. Novel instruments such as sector scanning sonar (Smith and Largier, 1995) and video (Holland et al., 1997; Symonds et al., 1997) have also provided new ways to observe the spatial

structure of nearshore current systems.

2.4.1 Eulerian arrays

Arrays of Eulerian instruments have been the key investigation tool for the measurement of infragravity and shear waves in the field. By combining cross-spectra from pairs of instruments in the longshore direction, longshore wavenumber/frequency spectra can be estimated (Huntley et al., 1981; Oltman-Shay and Guza, 1987; Oltman-Shay et al., 1989). The resulting dispersion curves are compelling evidence for the existence of edge waves (Huntley et al., 1981) and shear waves (Oltman-Shay et al., 1989).

Cross-shore arrays of instruments have been used to estimate the cross-shore distribution energy (Guza and Thornton, 1985) and reflection coefficients for infragravity waves (Elgar et al., 1994). The use of two dimensional arrays, consisting of a rectangular grid of sensors, is also being developed and offers the potential for observing more detailed spatial structure (Sheremet et al., 2001).

Transient rip currents were measured with an cross-shore/longshore array by Tang and Dalrymple (1989), as mentioned in Section 2.3.4. This provided observations of longshore migration of an individual rip. Longshore wavenumber-frequency spectra in this case showed peaks at very low frequencies consistent with transient rip currents, however there is no theoretical spectral form with which to compare.

2.4.2 Lagrangian techniques

A few Lagrangian measurements in the surf and nearshore zone have been obtained, mainly to measure topographic rip currents. The methods employed have included:

1. Surface floats and drogued drifters fixed using a compass from a boat or the shore (Shepard et al., 1941; Shepard and Inman, 1950; Sonu, 1972).
2. "Live" floats, where swimmers floating in rip currents were tracked by theodolite fixes (Short and Hogan, 1994; Brander and Short, 2000).
3. Floats and balloons tracked using sequential aerial photographs taken from a balloon (Sasaki and Horikawa, 1975, 1978).
4. Dye releases and sequential observation/photographs (e.g. Sonu, 1972; Bowen and Inman, 1974; Rodriguez et al., 1995; Brander, 1999; Takewaka et al., 2003)

The dye release experiments of Bowen and Inman (1974); Rodriguez et al. (1995) and Takewaka et al. (2003) provide the only known measurements of dispersion in real surf zones.

Very recently, and concurrent with the work described here, a surf zone drifter using GPS position fixing was designed and successfully deployed by Schmidt et al. (2003). This work presented the first published Lagrangian current data with high temporal and spatial resolution.

2.5 Summary

The nearshore current field consists of a complex mix of motions. The horizontal currents can be classified as:

- Quasi-steady current systems - longshore currents, topographic rip currents
- Variable divergent currents - free and forced infragravity waves
- Variable rotational currents - shear waves, transient rips, large scale vortices.

These currents co-exist and interact. The quasi-steady current systems can generate variable rotational currents through a shear instability mechanism. Spatially variable incident wave forcing is also known, in theory and the laboratory, to generate transient rip currents, another type of variable rotational current. Numerical simulations have shown the generation and shedding of other discrete features like vortices by nonlinear shear waves. While the interaction of shear and edge wave modes have been shown to be possible, the extent of interaction between infragravity waves and other variable rotational motions in the field is unknown.

Nearshore currents are three dimensional because of undertow. The primary effect on the horizontal depth-averaged currents is an enhancement of lateral momentum transfer. Like the horizontal current, the undertow is temporally variable. While this is implicitly included in Quasi-3D models, a general theoretical understanding of the importance of the actual variation of undertow is not known.

Field data has primarily been obtained using Eulerian methods, and an assumption of a wave-like structure for the variable currents allows the longshore spatial variability to be resolved. Variable currents such as transient rip currents have been measured as they migrate through an array of sensors. Lagrangian techniques have received relatively little use, but provide an alternative viewpoint, and allow the spatial structure of arbitrary variable currents to be measured.

Chapter 3

Theoretical framework

3.1 Introduction

The purpose of this chapter is to provide a mathematical framework for the description and analysis of the nearshore currents discussed in a qualitative way in the remainder of this work. The basic equations for the horizontal depth and wave-averaged nearshore current are well established in the literature. These are first defined, and terms which arise from the incident wave forcing, lateral mixing of momentum and bottom friction are reviewed. From this starting point, the nearshore current field is then partitioned into quasi-steady, variable rotational and variable divergent parts, and equations are derived for each. The reason for this is to clearly identify the quasi-steady flow associated with nearshore current systems, variable flow due to low frequency gravity waves, and variable flow due to rotational flow. The initial part of the chapter, Section 3.2 is review of previous work. Most of what follows is original in terms of the decomposition of the current field; references to similar work and ideas are presented where relevant.

3.2 Nearshore currents

The horizontal nearshore current is defined here as:

$$\bar{\mathbf{U}} = \frac{1}{h + \bar{\eta}} \overline{\int_{-h}^{\tilde{\eta}} \tilde{\mathbf{u}} dz} \quad (3.1)$$

where $\tilde{\mathbf{u}}$ and $\tilde{\eta}$ are the instantaneous horizontal velocity vector and surface elevation. The undisturbed water depth is h and the overline operator, \bar{b} , acting on an arbitrary scalar or vector component b , indicates averaging over the incident wave motion. For what follows, the nearshore current therefore refers to the depth and wave-averaged horizontal velocities. For the idealised case of monochromatic waves, the wave-

averaging operator is defined as a boxcar filter (Svendsen and Putrevu, 1997)

$$\bar{b} = \frac{1}{T} \int_{t-T/2}^{t+T/2} b dt', \quad (3.2)$$

where T is the wave period, which exactly removes the incident wave motion. For the case of a real random wave field, without a single well defined period, the wave-averaging operator is better thought of as a lowpass filter with cutoff below the incident wave frequencies. In practice, an optimally designed filter kernel is preferable to a boxcar shape.

3.2.1 Governing equations for nearshore currents

As outlined by Svendsen and Putrevu (1997), a set of equations for the nearshore current can be derived by integrating the Navier-Stokes equations in the vertical and then wave-averaging. The derivation of the equations is well established in the literature and will not be repeated here. The detailed treatment of individual terms for the case with depth-uniform currents is presented in Mei (1989). The end result is a set of forced shallow water equations for the nearshore current vector, $\bar{\mathbf{U}}$

$$\frac{\partial \bar{\eta}}{\partial t} + \nabla \cdot [(\bar{\eta} + h)\bar{\mathbf{U}}] = 0 \quad (3.3)$$

$$\frac{\partial \bar{\mathbf{U}}}{\partial t} + (\bar{\mathbf{U}} \cdot \nabla) \bar{\mathbf{U}} = -g\nabla \bar{\eta} + \bar{\mathbf{S}} + \bar{\mathbf{L}} + \bar{\mathbf{B}} \quad (3.4)$$

where $\bar{\mathbf{S}}$, $\bar{\mathbf{L}}$ and $\bar{\mathbf{B}}$ are terms for the forcing per unit volume due to the incident waves, lateral momentum mixing, and bottom friction, respectively. The three forcing terms are complicated quantities which are partially due to terms involving the horizontal velocities, which appear from the depth and wave-averaging. A rigorous derivation of the forcing terms is presented Putrevu and Svendsen (1999). Equation 3.4 is the same as their eq. (45) with the additional terms including the effects of depth variation of the wave-averaged current assigned to either $\bar{\mathbf{S}}$ or $\bar{\mathbf{L}}$. In practice, evaluation of the forcing terms requires various closure schemes. Each forcing term and common parameterisations are discussed in more detail in Section 3.2.2 to 3.2.4. Additional details of the exact form of some of these models is also given in the Appendix.

3.2.2 Incident wave forcing

The term $\bar{\mathbf{S}}$ represents the transfer of momentum from the incident wave motion to the lower frequency motion of the nearshore currents. After depth and wave

averaging, the nonlinear term generates three terms in addition to $(\bar{\mathbf{U}} \cdot \nabla) \bar{\mathbf{U}}$:

$$\frac{\partial}{\partial x_j} \overline{\int_{-h}^{\tilde{\eta}} (\tilde{u}_i - \bar{U}_i) (\tilde{u}_j - \bar{U}_j) dz} + \frac{\partial}{\partial x_j} \overline{\int_{-h}^{\tilde{\eta}} \bar{U}_i (\tilde{u}_j - \bar{U}_j) + (\tilde{u}_i - \bar{U}_i) \bar{U}_j dz} \quad (3.5)$$

If $\bar{\mathbf{U}}$ varies sufficiently slowly compared to the averaging interval or for the case of monochromatic waves with a single well defined period, the second and third terms disappear, leaving the classic radiation stress gradient of Longuet-Higgins and Stewart (1962, 1963, 1964). This has formed the theoretical basis for most of the present understanding of wave driven nearshore currents. In random waves, where the averaging process defined in Equation 3.2 is over short timescales (say 20 seconds) so as to retain temporal resolution in the "current" part of the signal, the second term may have significant magnitude. In the more general case of depth varying wave-averaged currents, there are also additional terms (usually neglected) which arise due to interaction of the wave and depth-varying current components (Putrevu and Svendsen, 1999).

The forcing for the classical radiation stress for a steady monochromatic wave-train of linear waves is,

$$S_i = \frac{1}{\rho(\bar{\eta} + h)} \frac{\partial}{\partial x_j} \left[\frac{EC_g}{C} \left(\delta_{ij} + \frac{k_i k_j}{|k^2|} \right) - \frac{E}{2} \delta_{ij} \right] \quad (3.6)$$

where E, C_g, C are the energy, group speed and phase speed of the wave field. k_i is the the wavenumber vector, ρ is the water density and δ_{ij} is the Kronecker delta.

Time variation of the radiation stress due to wave groups has been modelled by allowing a linear wave field to modulate slightly (Schäffer, 1994). However this approach still assumes $\overline{\mathbf{U}(\tilde{\mathbf{u}} - \bar{\mathbf{U}})} = \mathbf{0}$, which in a truly random wave field is not strictly valid except over quite long times. Dalrymple (1975) shows how intersecting wave trains can in theory generate spatially varying wave forcing which drive rip currents. Kennedy and Kirby (2003) have developed a closure for $\bar{\mathbf{S}}$ for narrow banded wave fields, which is progress towards a parameterisation of temporally and spatially varying forcing due to fully random wave fields.

All of the existing radiation stress type closures rely critically on the the parameterisation of wave breaking to determine gradients of \mathbf{u}^w within the surf zone, which in the absence of a general theory for breaking waves, is usually quite crude. A common (and physically sensible) approach is a depth dependent breaking criteria which leads to spatially varying wave forcing depending on the topography.

3.2.3 Lateral mixing

The mixing term, $\bar{\mathbf{L}}$ represents the lateral spreading of the nearshore current momentum by small scale turbulence. In addition, Svendsen and Putrevu (1994) showed how the vertical variation of the wave-averaged current acts to spread momentum laterally in a manner analogous to shear dispersion. They showed this effect to be larger than lateral turbulent mixing in typical surf zone conditions. The shear dispersion mechanism appears in the equations of Putrevu and Svendsen (1999) as if it was an eddy viscosity term. The combined lateral mixing can be modelled with an eddy viscosity type closure using an enhanced viscosity coefficient which depends on the incident wave properties. An approximate form, assuming the shear dispersion coefficients are proportional to the incident wave flux, is given by,

$$L_i \sim \frac{1}{(h + \bar{\eta})} \frac{\partial}{\partial x_j} \left\{ (h^* + \bar{\eta}) \left[\left(\nu_t + \frac{Q_j^w Q_k^w}{\nu_t} \right) \frac{\partial \bar{U}_i}{\partial x_k} + \left(\nu_t + \frac{Q_i^w Q_k^w}{\nu_t} \right) \frac{\partial \bar{U}_j}{\partial x_k} \right] \right\} \quad (3.7)$$

where ν_t is a turbulent eddy viscosity (similar value for vertical and horizontal) due mainly to wave breaking and Q_i^w is the mass flux associated with the incident waves. Because the incident wave fluxes are not isotropic, the dispersion coefficients are directionally dependent and some can often be neglected (Ozkan-Haller and Kirby, 1999). In particular, for the common case of a straight beach, the cross shore mixing term involving $Q_x^w Q_x^w$ is dominant.

3.2.4 Bottom friction

The effect of bottom friction on the nearshore current is expressed by $\bar{\mathbf{B}}$. To model this term requires assumptions about the bottom shear stresses themselves which is commonly assumed to be a quadratic friction law dependent on the instantaneous velocity near the bed. After wave-averaging this approximately gives a linear dependence on the nearshore current with the friction coefficient, f_b , dependent on the typical local incident wave orbital speed, \hat{u}^w , and a wave friction factor (Allen et al., 1996; Lippmann et al., 1997; Ozkan-Haller and Kirby, 1999),

$$\bar{\mathbf{B}} \sim -\frac{f_w \hat{u}^w \bar{\mathbf{U}}}{h + \bar{\eta}} \quad (3.8)$$

3.3 Quasi-steady currents

The time dependent nearshore current and surface elevation and forcing terms can be divided into quasi-steady and variable components,

$$\bar{\mathbf{U}} = \mathbf{U}_o + \mathbf{u}; \quad \bar{\eta} = \eta_o + \eta; \quad \bar{\mathbf{S}} = \mathbf{S}_o + \mathbf{S}; \quad \bar{\mathbf{L}} = \mathbf{L}_o + \mathbf{L}; \quad \bar{\mathbf{B}} = \mathbf{B}_o + \mathbf{B} \quad (3.9)$$

The quasi-steady part, \mathbf{U}_o is the part of the current which is steady in the sense that it is constant for a given incident wave field and bottom topography. This could be the mean longshore current or the mean flow of a topographic rip current. The variable part then consists of flow due to motions like infragravity or shear waves. Substituting the decompositions 3.9 into 3.3 and 3.4 and carrying out a long time average, denoted $\overline{\cdot}$ such that $\overline{\mathbf{u}} = 0$ and $\overline{\mathbf{u}\mathbf{U}_o} = 0$ gives an equation for the quasi-steady current,

$$\nabla \cdot (\mathbf{U}_o h^*) = -\overline{\nabla \cdot (\mathbf{u}\eta)} \quad (3.10)$$

$$(\mathbf{U}_o \cdot \nabla) \mathbf{U}_o = -g\nabla\eta_o + \mathbf{S}_o + \mathbf{L}_o + \mathbf{B}_o - \mathbf{T} \quad (3.11)$$

where $h^* = h + \eta_o$ and $\mathbf{T} = \overline{(\mathbf{u} \cdot \nabla) \mathbf{u}}$. Equation 3.11 in the absence of a variable current with obliquely incident waves on an alongshore uniform beach is the classic model for the longshore current (Bowen, 1969a; Longuet-Higgins, 1970a). Equations 3.10 and 3.11 are not necessarily limited to a longshore current and equally describe a topographic rip current or other spatially variable quasi-steady current. The term on the RHS of Equation 3.10 is a net mass flux (a ‘‘Stokes drift’’ for the variable current component) and in general will be small so that $\overline{\nabla \cdot (\mathbf{u}\eta)} = -\nabla \cdot (\mathbf{U}_o h^*) \approx 0$.

The splitting of the current is analogous to a Reynolds type decomposition; the nonlinear terms involving the variable part of the current field produce a stress like term, \mathbf{T} , in the long time average equations (Slinn et al., 1998; Ozkan-Haller and Kirby, 1999). The variable current mixing is partially responsible for the cross-shore distribution of longshore momentum in longshore currents as originally suggested by Bowen and Holman (1989).

3.4 Variable currents

By subtracting Equations 3.10 and 3.11 from 3.3 and 3.4 respectively, equations for the variable part of the nearshore current field are obtained,

$$\frac{\partial \eta}{\partial t} + \nabla \cdot (h^* \mathbf{u}) + \nabla \cdot (\eta \mathbf{U}_o) + \nabla \cdot (\eta \mathbf{u}) = 0 \quad (3.12)$$

$$\frac{\partial \mathbf{u}}{\partial t} + (\mathbf{u} \cdot \nabla) \mathbf{u} + (\mathbf{U}_o \cdot \nabla) \mathbf{u} + (\mathbf{u} \cdot \nabla) \mathbf{U}_o = -g\nabla\eta + \mathbf{S} + \mathbf{L} + \mathbf{B} + \mathbf{T} \quad (3.13)$$

This shows that the evolution of the variable current is influenced the quasi-steady current field through the nonlinear terms involving \mathbf{U}_o .

Taking the curl of Equation 3.12 yields an equation for the vertical vorticity of

the variable current,

$$\begin{aligned} & \frac{\partial \zeta}{\partial t} + (\mathbf{U}_o \cdot \nabla) \zeta + (\mathbf{u} \cdot \nabla) \zeta_o + (\mathbf{u} \cdot \nabla) \zeta = \\ & -\zeta(\nabla \cdot \mathbf{U}_o) - \zeta(\nabla \cdot \mathbf{u}) - \zeta_o(\nabla \cdot \mathbf{u}) + \nabla \times [\mathbf{S} + \mathbf{L} + \mathbf{B} + \mathbf{T}] \end{aligned} \quad (3.14)$$

where $\zeta = \nabla \times \mathbf{u}$ and $\zeta_o = \nabla \times \mathbf{U}_o$. This can also be written as an equation for the potential vorticity:

$$\frac{D}{Dt} \left(\frac{\zeta + \zeta_o}{\eta + h^*} \right) = \nabla \cdot \mathbf{U}_o \zeta_o + \frac{1}{\eta + h^*} \nabla \times [\mathbf{S} + \mathbf{L} + \mathbf{B} + \mathbf{T}] \quad (3.15)$$

where $\frac{DA}{Dt} = \frac{\partial A}{\partial t} + ([\mathbf{u} + \mathbf{U}_o] \cdot \nabla) A$. Equation 3.15 is also (necessarily) equivalent to $\nabla \times (3.4) - \nabla \times (3.11)$.

3.4.1 Rotational and divergent currents

The general solutions of Equations 3.12 and 3.13 can be either irrotational, divergent gravity wave motions or rotational motions. The variable current vector can be formally partitioned into divergent and rotational parts,

$$\mathbf{u} = \mathbf{u}^D + \mathbf{u}^R \quad (3.16a)$$

$$\nabla \times (h^* \mathbf{u}^D) = 0 \quad (3.16b)$$

$$\nabla \cdot (h^* \mathbf{u}^R) = 0 \quad (3.16c)$$

by applying a Helmholtz decomposition to $h^* \mathbf{u}$. Imposing suitable boundary conditions leads to a unique decomposition (Majda and Bertozzi, 2002). While the basic idea is straightforward, the exact definition of the partition is more arbitrary as the decomposition could also be applied to \mathbf{u} or $(\eta + h^*) \mathbf{u}$. Thus the terms “rotational” and “divergent” are not absolute in nature and in this case apply to a flux rather than the actual velocity. By using $h^* \mathbf{u}$, the two modes separate very naturally in the linearised equations for flow over varying topography. The surface elevation is associated with the divergent component in the linearised continuity equation as,

$$\frac{\partial \eta}{\partial t} = -\nabla \cdot h^* \mathbf{u}^D \quad (3.17)$$

and the velocity in the rotational component is equivalent to the velocity under a “rigid-lid” approximation. Defining a transport stream function, ψ so that,

$$h^* \mathbf{u}^R = \left[-\frac{\partial \psi}{\partial y}, \frac{\partial \psi}{\partial x} \right] = \nabla^\perp \psi \quad (3.18)$$

means that:

$$\nabla \times h^* \mathbf{u} = \nabla \times h^* \mathbf{u}^R = \nabla \times \nabla^\perp \psi = \nabla^2 \psi \quad (3.19)$$

Similarly, a potential, ϕ , exists for the divergent part as $h^* \mathbf{u}^D = \nabla \phi$ and $\nabla \cdot h^* \mathbf{u} = \nabla^2 \phi$. This particular choice of decomposition leads to some complications in dealing with the nonlinear terms in the momentum equation, however it fits well with the separation of infragravity and shear wave modes. In addition, it has advantages when considering the energetics of the velocity components (Section 3.4.2).

Expressions for the divergence and vorticity and divergence of \mathbf{u}^D and \mathbf{u}^R follow directly from the definition of the partition,

$$\nabla \times \mathbf{u}^D = -\frac{\nabla h^*}{h^*} \times \mathbf{u}^D \quad (3.20a)$$

$$\nabla \cdot \mathbf{u}^R = -\frac{\nabla h^*}{h^*} \cdot \mathbf{u}^R \quad (3.20b)$$

Note that $\nabla \times \mathbf{u}^R \neq \zeta$, but rather is related by:

$$\nabla \times \mathbf{u}^R = \zeta + \frac{\nabla h^*}{h^*} \times \mathbf{u}^D \quad (3.21)$$

Momentum equations for the rotational and divergent flow fields can be formally separated by projecting the vector fields onto non-divergent and irrotational subspaces. This is similar to the projection of the Navier-Stokes equations onto a non-divergent vector subspace (Majda and Bertozzi, 2002). The projection operators are defined by:

$$\Pi^R[\mathbf{A}] = \frac{1}{h^*} \nabla^\perp \nabla^{-2} \nabla \times h^* \mathbf{A} \quad (3.22a)$$

$$\Pi^D[\mathbf{A}] = \frac{1}{h^*} \nabla \nabla^{-2} \nabla \cdot h^* \mathbf{A} \quad (3.22b)$$

where ∇^{-2} is the inverse of the Laplacian operator and \mathbf{A} is an arbitrary horizontal vector. When applied to the vector \mathbf{u} the operators give:

$$\Pi^R[\mathbf{u}] = \frac{1}{h^*} \nabla^\perp \nabla^{-2} \nabla \times (h^* \mathbf{u}) = \frac{1}{h} \nabla^\perp \nabla^{-2} \nabla^2 \psi = \frac{\nabla^\perp \psi}{h} = \mathbf{u}^R \quad (3.23a)$$

$$\Pi^D[\mathbf{u}] = \frac{1}{h^*} \nabla \nabla^{-2} \nabla \cdot (h^* \mathbf{u}) = \frac{1}{h} \nabla \nabla^{-2} \nabla^2 \phi = \frac{\nabla \phi}{h^*} = \mathbf{u}^D \quad (3.23b)$$

as expected. Note also that $\Pi^R = \mathbf{I} - \Pi^D$, where \mathbf{I} is the identity operator, as the projections are orthogonal. Also, because $\nabla \times h^* \Pi^D[\mathbf{A}] = 0$, $\nabla \times h^* \mathbf{A} = \nabla \times h^* \Pi^R[\mathbf{A}]$. Similarly $\nabla \cdot h^* \mathbf{A} = \nabla \cdot h^* \Pi^D[\mathbf{A}]$, so multiplying by h^* and taking the curl or divergence leaves only terms from the rotational or divergent partition respectively.

Applying the projection to Equation 3.13 separates the time evolution of each

partition:

$$\begin{aligned} \frac{\partial \mathbf{u}^R}{\partial t} + \Pi^R [(\mathbf{u} \cdot \nabla) \mathbf{u} + (\mathbf{U}_o \cdot \nabla) \mathbf{u} + (\mathbf{u} \cdot \nabla) \mathbf{U}_o] \\ = -g \nabla \eta^R + \mathbf{S}^R + \mathbf{L}^R + \mathbf{B}^R + \mathbf{T}^R \end{aligned} \quad (3.24a)$$

$$\begin{aligned} \frac{\partial \mathbf{u}^D}{\partial t} + \Pi^D [(\mathbf{u} \cdot \nabla) \mathbf{u} + (\mathbf{U}_o \cdot \nabla) \mathbf{u} + (\mathbf{u} \cdot \nabla) \mathbf{U}_o] \\ = -g \nabla \eta^D + \mathbf{S}^D + \mathbf{L}^D + \mathbf{B}^D + \mathbf{T}^D \end{aligned} \quad (3.24b)$$

where $\nabla \eta^R = \Pi^R[\nabla \eta]$, $\nabla \eta^D = \Pi^D[\nabla \eta]$ and $\mathbf{S}^R = \Pi^R[\mathbf{S}]$, $\mathbf{S}^D = \Pi^D[\mathbf{S}]$ and similarly for \mathbf{L} , \mathbf{B} and \mathbf{T} . In most cases, it is not straightforward to express the projected terms explicitly and these are left in symbolic form. Equations in terms of ψ and ϕ can be derived from Equations 3.24a and 3.24b by multiplying by h^* and then taking the curl or divergence; these then describe (respectively) the evolution of the rotational or divergent part of the complete flow. This is not done here, as the resulting equations do not provide any particular advantage over Equations 3.24a and 3.24b for the analysis and discussion that follows.

Of interest here is to gain some qualitative understanding by examining the relative sizes of terms in Equations 3.24a and 3.24b. To non-dimensionalise terms in Equations 3.24a and 3.24b, the following scales are introduced:

$$\mathbf{U}_o \sim \mathcal{U}^o, \quad \mathbf{u}^R \sim \mathcal{U}^R, \quad \mathbf{u}^D \sim \mathcal{U}^D, \quad \nabla h^* \sim s, \quad \mathbf{x} \sim \mathcal{L}$$

The length scales of spatial variability, \mathcal{L} , of the three current components are assumed similar but timescales are specific to each type of motion. Based on the expectation that the rotational flow will have vortical type structures and that the divergent flows will be wave-like, these are defined as $\tau^R \sim \mathcal{L}/\mathcal{U}^R$, $\tau^D \sim \mathcal{L}/\sqrt{gh^*}$. The scaling is carried out locally for a specific depth h^* and bottom slope s . The following parameters are introduced to characterise the relative sizes of the various scales of the flow:

- $\epsilon = \mathcal{A}/h^*$ Ratio of surface elevation to water depth.
- $\alpha = \mathcal{U}^D/\mathcal{U}^R$ Ratio of variable divergent and rotational velocity.
- $\beta = \mathcal{U}^o/\mathcal{U}^R$ Ratio of quasi-steady velocity to variable rotation velocity.
- $\varsigma = \beta/\alpha = \mathcal{U}^o/\mathcal{U}^D$ Ratio of quasi-steady velocity to variable divergent velocity.
- $Fr^D = \mathcal{U}^D/\sqrt{gh^*}$ Ratio of divergent velocity to shallow water wave celerity.
- $Fr^R = \mathcal{U}^R/\sqrt{gh^*}$ Ratio of rotational velocity to shallow water wave celerity.
- $\kappa = s\mathcal{L}/h^*$ Ratio of flow length scale to relative variation of water depth.

For typical nearshore conditions away from the immediate vicinity of the shoreline, $\epsilon \ll 1$ and $Fr^R \sim Fr^D \ll 1$. In addition, the linearised momentum equation for \mathbf{u}^D implies that $\mathcal{U}^D \sim \mathcal{A}\sqrt{gh^*}/h^*$ so $Fr^D \sim \epsilon$. Other parameters can be directly related but are defined separately to make the magnitude of each term as transparent as possible. The κ parameter characterises the effect that the beach slope has on the dynamics.

The appropriate scaling for the *projected* terms is not necessarily a direct application of appropriate scales to the individual terms. Immediate application of the scaling terms implies $\Pi^R [(\mathbf{u}^D \cdot \nabla) \mathbf{u}^D] \sim (\mathcal{U}^D)^2/\mathcal{L}$. However, by using various vector identities and the fact that $\nabla \times (h^* \mathbf{u}^D) = 0$, it turns out that,

$$\Pi^R [(\mathbf{u}^D \cdot \nabla) \mathbf{u}^D] = \Pi^R \left[\mathbf{u}^D \left(\frac{\nabla h^*}{h^*} \cdot \mathbf{u}^D \right) + \frac{1}{2} (\mathbf{u}^D \cdot \mathbf{u}^D) \frac{\nabla h^*}{h^*} \right] \quad (3.25)$$

which implies that $\Pi^R [(\mathbf{u}^D \cdot \nabla) \mathbf{u}^D] \sim (\mathcal{U}^D)^2 s$. Similarly, the $\Pi^R [\nabla \eta]$ term is $\mathcal{O}(\mathcal{A}s/h^*)$ because $\Pi^R [\nabla \eta] = \Pi^R [-\eta \nabla h^*/h^*]$ and $\Pi^D [(\mathbf{u}^R \cdot \nabla) \mathbf{u}^R] \sim (\mathcal{U}^R)^2 s$.

The forcing terms are non-dimensionalised based on the models in Section 3.2 (details are in the Appendix) to give:

$$\begin{aligned} \mathbf{S}^R &\sim 0.1g\gamma^2 s \vartheta^R, & \mathbf{L}^R &\sim \gamma^2 g^{1/2} h^{*3/2} \mathcal{U}^R / \mathcal{L}^2, & \mathbf{B}^R &\sim f_w \gamma \omega \mathcal{U}^R & \mathbf{T}^R &\sim \mathcal{U}^R \mathcal{U}^o / \mathcal{L}^2 \\ \mathbf{S}^D &\sim 0.1g\gamma^2 s \vartheta^D, & \mathbf{L}^D &\sim \gamma^2 g^{1/2} h^{*3/2} \mathcal{U}^D / \mathcal{L}^2, & \mathbf{B}^D &\sim f_w \gamma \omega \mathcal{U}^D & \mathbf{T}^D &\sim 0 \end{aligned}$$

where ϑ^R and ϑ^D are non-dimensional numbers characterising the variability of forcing, γ is a depth dependent breaking coefficient, and ℓ is a mixing length for the lateral spread of quasi-steady momentum by the variable currents.

The full non-dimensional momentum equations for \mathbf{u}'^R , \mathbf{u}'^D and η' are:

$$\begin{aligned} &\frac{\partial \mathbf{u}'^R}{\partial t'} + \Pi^R \left[(\mathbf{u}'^R \cdot \nabla) \mathbf{u}'^R + \beta (\mathbf{U}'_o \cdot \nabla) \mathbf{u}'^R + \beta (\mathbf{u}'^R \cdot \nabla) \mathbf{U}'_o \right. \\ &\quad \left. + \alpha (\mathbf{u}'^D \cdot \nabla) \mathbf{u}'^R + \alpha (\mathbf{u}'^R \cdot \nabla) \mathbf{u}'^D + \kappa \alpha^2 (\mathbf{u}'^D \cdot \nabla) \mathbf{u}'^D \right. \\ &\quad \left. + \alpha \beta (\mathbf{U}'_o \cdot \nabla) \mathbf{u}'^D + \alpha \beta (\mathbf{u}'^D \cdot \nabla) \mathbf{U}'_o \right] \\ &= -\frac{\alpha \kappa}{Fr^R} \nabla \eta'^R + \frac{0.1 \gamma^2 \kappa \vartheta^R}{(Fr^R)^2} \mathbf{S}'^R + \frac{\gamma^2 h^*}{Fr^R \mathcal{L}} \mathbf{L}'^R + f_w \gamma \omega \tau^R \mathbf{B}'^R + \frac{\beta \ell}{\mathcal{L}} \mathbf{T}^R \end{aligned} \quad (3.26a)$$

$$\begin{aligned} &\frac{\partial \mathbf{u}'^D}{\partial t'} + Fr^D \Pi^D \left[(\mathbf{u}'^D \cdot \nabla) \mathbf{u}'^D + \varsigma (\mathbf{U}'_o \cdot \nabla) \mathbf{u}'^D + \varsigma (\mathbf{u}'^D \cdot \nabla) \mathbf{U}'_o \right. \\ &\quad \left. + \frac{1}{\alpha} (\mathbf{u}'^D \cdot \nabla) \mathbf{u}'^R + \frac{1}{\alpha} (\mathbf{u}'^R \cdot \nabla) \mathbf{u}'^D + \frac{\kappa}{\alpha^2} (\mathbf{u}'^R \cdot \nabla) \mathbf{u}'^R \right. \\ &\quad \left. + \frac{\varsigma}{\alpha} (\mathbf{U}'_o \cdot \nabla) \mathbf{u}'^R + \frac{\varsigma}{\alpha} (\mathbf{u}'^R \cdot \nabla) \mathbf{U}'_o \right] \\ &= -\nabla \eta'^D + \frac{0.1 \gamma^2 \kappa \vartheta^D}{Fr^D} \mathbf{S}'^D + \frac{\gamma^2 h^*}{\mathcal{L}} \mathbf{L}'^D + f_w \gamma \omega \tau^D \mathbf{B}'^D \end{aligned} \quad (3.26b)$$

The nonlinear terms depending on relative magnitudes of \mathbf{u}^R , \mathbf{u}^D and \mathbf{U}_o . As the beach slope decreases and/or overall depth increases further offshore, $\kappa \rightarrow 0$ and the equations tend to those for constant h^* . The projection operators for constant h^* produce the same result as (for example), $\nabla \times \mathbf{u}^D = \nabla \times \Pi^D[\mathbf{u}] = 0$ and

$$\Pi^R \left[(\mathbf{u}^D \cdot \nabla) \mathbf{u}^D \right] = \Pi^R \left[\nabla (|\mathbf{u}^D|^2/2) \right] = \nabla^\perp \nabla^{-2} \nabla \times \nabla (|\mathbf{u}^D|^2/2) = \mathbf{0} \quad (3.27)$$

Note that $\Pi^R[\nabla\eta] = 0$ for constant h^* , emphasising the fact that variations in η are not inherent to the dynamics of \mathbf{u}^R . Even in the general case of variable h^* , there can be a purely rotational motion with $\eta = 0$ everywhere¹. However, this is not to say that in the general case, that \mathbf{u}^R (as defined by Equation 3.16a) cannot be influenced by $\nabla\eta$, or in fact will tend to generate changes in η through mechanisms analogous to Lighthill radiation.

All of the nonlinear terms in the equation for \mathbf{u}^D are $\mathcal{O}(Fr^D)$, implying that the dynamics of the divergent motion will be close to linear, providing $Fr \ll 1$; this is a reasonable assumption for divergent current motion away from the shoreline. Both the wave forcing and lateral mixing are $\mathcal{O}(1/Fr)$ times larger for \mathbf{u}^R than for \mathbf{u}^D (assuming $\alpha \sim 1$). This simply falls out of the scaling as the result of the relative dominance of $\nabla\eta^D$ rather than preferential mixing or forcing of rotational flow.

Two non-dimensional versions of the continuity equation exists depending on whether τ^R or τ^D is the dominant timescale for $\partial\eta/\partial t$.

$$\frac{\partial\eta'}{\partial t'} + \alpha \left[\nabla \cdot \mathbf{u}'^D + \kappa \nabla h^{*'} \cdot \mathbf{u}'^D \right] + \beta \nabla \cdot (\eta \mathbf{U}'_o) + \nabla \cdot (\eta \mathbf{u}'^R) + \alpha \nabla \cdot (\eta \mathbf{u}'^D) = 0 \quad (3.28a)$$

$$\frac{\partial\eta'}{\partial t'} + \nabla \cdot \mathbf{u}'^D + \kappa \nabla h^{*'} \cdot \mathbf{u}'^D + Fr^D \left[\gamma \nabla \cdot (\eta \mathbf{U}'_o) + \frac{1}{\alpha} \nabla \cdot (\eta \mathbf{u}'^R) + \nabla \cdot (\eta \mathbf{u}'^D) \right] = 0 \quad (3.28b)$$

For typical nearshore conditions with $\alpha \leq 1$, where divergent flow is of the same magnitude or greater than the rotational flow (this is shown to be the case later in Chapter 5, but may be violated in the presence of longshore currents, Chapter 6 and Lippmann et al. (1999)), the timescale τ^D is the appropriate one, giving Equation 3.28b.

Within the general set of equations, models for the well known modes of nearshore currents can be identified.

¹A general proof is not available, however, analytical solutions are known for the weakly nonlinear case (Feddersen, 1998), and numerical solutions to the fully nonlinear case (e.g. Allen et al., 1996)

Shear waves: \mathbf{u}^R $\alpha \ll 1$ $\beta \sim 1$, $\frac{0.1\gamma^2\kappa\vartheta^R}{(Fr^R)^2} \ll 1$

$$\begin{aligned} \nabla \cdot (h^* \mathbf{u}^R) &= 0 & (3.29) \\ \frac{\partial \mathbf{u}^R}{\partial t} + \Pi^R \left[(\mathbf{u}^R \cdot \nabla) \mathbf{u}^R + (\mathbf{U}_o \cdot \nabla) \mathbf{u}^R + (\mathbf{u}^R \cdot \nabla) \mathbf{U}_o \right] &= \mathbf{L}^R + \mathbf{B}^R + \mathbf{T} \end{aligned}$$

For a longshore current, $\mathbf{U}_o = V_o(x)$, these are essentially the same as the governing equations of Feddersen (1998) for nonlinear shear waves (he did not include lateral mixing). The curl of Equation 3.30, which is the same as Equation 3.14 where $\mathbf{u} = \mathbf{u}^R$, can be written in terms of the stream function as (Note that $\nabla h^* \times \nabla^\perp \psi = \nabla \psi \cdot \nabla h^*$ and $\nabla^\perp \psi \cdot \nabla b = \nabla \psi \times \nabla b$):

$$\begin{aligned} \frac{D}{Dt} \left(\nabla^2 \psi - \nabla \psi \cdot \frac{\nabla h^*}{h^*} \right) + \frac{\nabla \psi}{h^*} \times \left(\nabla^2 \psi - \nabla \psi \cdot \frac{\nabla h^*}{h^*} + h^* \nabla \times \mathbf{U}_o \right) \\ = h^* \nabla \times \left[\mathbf{L}^R + \mathbf{B}^R + \mathbf{T} \right] \end{aligned} \quad (3.30)$$

If the nonlinear terms involving ψ with itself are neglected, this leaves equation of the classic linear stability analysis of (Bowen and Holman, 1989). If $\mathbf{U}_o = U_o(y)$, an equation governing topographic rip current instabilities is obtained (Haller and Dalrymple, 2001).

Free infragravity waves: \mathbf{u}^D $Fr^D \ll 1$ $Fr^D \zeta \sim 1$, $\alpha \gg 1$, $\frac{0.1\gamma^2\kappa\vartheta^D}{Fr^D} \ll 1$

$$\frac{\partial \eta}{\partial t} + \nabla \cdot (h^* \mathbf{u}^D) + \nabla \cdot (\eta \mathbf{U}_o) = 0 \quad (3.31)$$

$$\frac{\partial \mathbf{u}^D}{\partial t} + \Pi^D \left[(\mathbf{U}_o \cdot \nabla) \mathbf{u}^D + (\mathbf{u}^D \cdot \nabla) \mathbf{U}_o \right] = -g \nabla \eta^D + \mathbf{B}^D \quad (3.32)$$

This set of equations describes free infragravity waves in the presence of a quasi-steady current. For a longshore current, $\mathbf{U}_o = V_o(x)$, these are the equations of Howd et al. (1992) (although they neglect bottom friction).

Forced infragravity waves: \mathbf{u}^D $Fr^D \ll 1$ $Fr^D \zeta \sim 1$, $\alpha \gg 1$, $\frac{0.1\gamma^2\kappa\vartheta^D}{Fr^D} \sim 1$

$$\frac{\partial \eta}{\partial t} + \nabla \cdot (h^* \mathbf{u}^D) + \nabla \cdot (\eta \mathbf{U}_o) = 0 \quad (3.33)$$

$$\frac{\partial \mathbf{u}^D}{\partial t} + \Pi^D \left[(\mathbf{U}_o \cdot \nabla) \mathbf{u}^D + (\mathbf{u}^D \cdot \nabla) \mathbf{U}_o \right] = -g \nabla \eta^D + \mathbf{S}^D + \mathbf{B}^D \quad (3.34)$$

If there is no quasi-steady current and neglecting bottom friction, these two

equations can be combined to give:

$$\frac{\partial^2 \eta}{\partial t^2} = \nabla \cdot (gh^* \nabla \eta) + \nabla \cdot h^* \mathbf{S} \quad (3.35)$$

This is the linearised equation for *forced* infragravity waves (Schäffer, 1993).

Combining the unforced linearised equations for \mathbf{u}^R and \mathbf{u}^D yields a single equation governing all free wave motions as shown by Kirby et al. (1998b). With a longshore current where $\mathbf{U}_o = [0, V]$, and by assuming solution of the form $\{\eta, u, v\}(x, y, t) = \{\check{\eta}, \check{u}, \check{v}\}(k, \omega) e^{i(kx - \omega t)}$, an eigenvalue problem is formed where solutions are all of the possible (linear) wave modes (both gravity waves and shear waves). In this model, nonlinear interaction terms due to resonance are shown to transfer energy between resonant modes belonging to \mathbf{u}^R and \mathbf{u}^D . In the more general case, while the rotational and divergent partitions will interact locally and instantaneously, there is not necessarily a net transfer of energy between rotational and divergent flow.

3.4.2 Energetics

The flux form of the density normalised kinetic energy (KE) equation for the total variable flow can be derived from the dot product of $(h^* + \eta)\mathbf{u}$ and Equation 3.13 added to Equation 3.3 multiplied by $|u|^2/2$,

$$\begin{aligned} & \frac{\partial}{\partial t} \left(\frac{\bar{h}|u|^2}{2} \right) + \nabla \cdot \left([\mathbf{u} + \mathbf{U}_o] \frac{\bar{h}|u|^2}{2} \right) + \bar{h}\mathbf{u} \cdot (\mathbf{u} \cdot \nabla) \mathbf{U}_o \\ & = -\bar{h}\mathbf{u} \cdot \nabla g\eta + \bar{h}\mathbf{u} \cdot [\mathbf{S} + \mathbf{L} + \mathbf{B} + \mathbf{T}] \end{aligned} \quad (3.36)$$

where $|u|^2 = \mathbf{u} \cdot \mathbf{u}$ and $\bar{h} = h^* + \eta$. The second term is the local flux divergence of kinetic energy, the third term is the extraction of energy from the quasi-steady flow and the fourth term the conversion of potential energy associated with the variable surface elevation to kinetic energy. The set of terms involving forcing represents the work done on the flow by the incident wave forcing and dissipation and spreading of energy by lateral mixing and dissipation by bottom friction.

The equation for the potential energy (PE) of the total variable current field is obtained by multiplying Equation 3.3 by $g\eta$,

$$\frac{\partial}{\partial t} \left(\frac{g\eta^2}{2} \right) + \nabla \cdot \left([\mathbf{u} + \mathbf{U}_o] \bar{h}g\eta \right) = \bar{h}\mathbf{U}_o \cdot \nabla g\eta + \bar{h}\mathbf{u} \cdot \nabla g\eta \quad (3.37)$$

Here, the second term is the local net flux divergence of potential energy. The third and fourth terms are the transfer between potential and kinetic energy of the quasi-steady and variable flow. The fourth term (necessarily) has the opposite sign to the

equivalent term in Equation 3.36. Note that the divergence terms in Equations 3.36 and 3.37 vanish when integrated over a domain with periodic or closed boundaries, so do not contribute to the total (area integrated) change of either KE or PE. The addition of Equations 3.36 and 3.37 is an equation for the total energy,

$$\begin{aligned} & \frac{\partial}{\partial t} \left(\frac{\bar{h}|u|^2 + g\eta^2}{2} \right) + \nabla \cdot \left(\bar{h}[\mathbf{u} + \mathbf{U}_o] \left[\frac{|u|^2}{2} + g\eta \right] \right) \\ & = -\bar{h}\mathbf{u} \cdot (\mathbf{u} \cdot \nabla) \mathbf{U}_o + \bar{h}\mathbf{U}_o \cdot \nabla g\eta + \bar{h}\mathbf{u} \cdot [\mathbf{S} + \mathbf{L} + \mathbf{B} + \mathbf{T}] \end{aligned} \quad (3.38)$$

The area integral of Equation 3.38 for a domain Ω where the boundaries are periodic or \mathbf{u}^R and \mathbf{u}^D vanish at the boundary is,

$$\begin{aligned} & \frac{\partial}{\partial t} \int_{\Omega} \left(\frac{\bar{h}|u|^2 + g\eta^2}{2} \right) d\Omega = \\ & \int_{\Omega} \left\{ -\bar{h}\mathbf{u} \cdot (\mathbf{u} \cdot \nabla) \mathbf{U}_o + \bar{h}\mathbf{U}_o \cdot \nabla g\eta + \bar{h}\mathbf{u} \cdot [\mathbf{S} + \mathbf{L} + \mathbf{B} + \mathbf{T}] \right\} d\Omega \end{aligned} \quad (3.39)$$

which shows that the energy increases as it is extracted from the quasi-steady flow and input through work done by the incident wave forcing. Dissipation due to bottom friction and lateral mixing reduces the total energy. For a nearshore current system in state of quasi-steady balance, the integral of the series of terms in the curly bracket is zero.

The total kinetic energy of the variable currents can be expanded in terms of \mathbf{u}^R and \mathbf{u}^D as,

$$KE = \frac{1}{2}\bar{h}|u|^2 = \frac{1}{2}\bar{h}\mathbf{u} \cdot \mathbf{u} = \frac{1}{2}\bar{h}|u^R|^2 + \frac{1}{2}\bar{h}|u^D|^2 + \bar{h}\mathbf{u}^R \cdot \mathbf{u}^D \quad (3.40)$$

As \mathbf{u}^R and \mathbf{u}^D are an orthogonal decomposition, this means that (with suitable assumptions concerning the boundaries) $\int_{\Omega} \bar{h}\mathbf{u}^R \cdot \mathbf{u}^D d\Omega = 0$. Therefore the area integral of total kinetic energy associated with the variable currents in the nearshore zone of an open beach is cleanly separated into a rotational and a divergent contribution.

At a local point, the kinetic energy is not cleanly partitioned between the rotational and divergent contributions. However, a simple approximation regarding the energy balance of the divergent part of the flow is an approximate equipartition of KE and PE so that,

$$h \overbrace{|u^D|^2} \approx g \overbrace{|\eta|^2} \quad (3.41)$$

This was shown to be valid by Lippmann et al. (1999) where the divergent current field consists of a superposition of linear edge and leaky mode waves, and where there is no variation of surface elevation associated with \mathbf{u}^R . The ratio, R , of potential

and kinetic energy is,

$$R = \frac{KE}{PE} = \frac{\overbrace{h|u|^2}}{\underbrace{g|\eta|^2}} = \frac{\overbrace{h|u^D|^2} + \overbrace{h|u^R|^2}}{\underbrace{h|u^D|^2}} \quad (3.42)$$

assuming $\overbrace{\mathbf{u}^R \mathbf{u}^D} = 0$. The fraction of total energy associated with the rotational flow is $1 - 1/R$. A point measurement of \mathbf{u} and η is sufficient to calculate R , and Equation 3.41 can be used to estimate the relative quantity of rotational and divergent current energy.

3.4.3 Forced variable rotational currents

A general class of motions which are not infragravity or shear waves are *forced* rotational currents. These are described by the same equations as for shear waves but with:

$$\frac{0.1\gamma^2\kappa\vartheta^R}{(Fr^R)^2} \sim 1 \quad (3.43)$$

so that variations in the incident wave forcing are important:

$$\nabla \cdot (h^* \mathbf{u}^R) = 0 \quad (3.44)$$

$$\begin{aligned} \frac{\partial \mathbf{u}^R}{\partial t} + (\mathbf{u}^R \cdot \nabla) \mathbf{u}^R + (\mathbf{U}_o \cdot \nabla) \mathbf{u}^R + (\mathbf{u}^R \cdot \nabla) \mathbf{U}_o \\ = -g\nabla\eta^R + \mathbf{L}^R + \mathbf{B}^R + \mathbf{S}^R \end{aligned} \quad (3.45)$$

This flow is also governed by an equation like Equation 3.30 but with the addition of the term $\nabla \times \mathbf{S}^R$. Physically, such a flow may derive its vorticity from both the interaction with the quasi-steady current *and* from incident wave forcing. The quasi-steady current terms do not necessarily produce new vorticity, but may simply serve to advect existing vorticity.

While infragravity waves have been clearly classified as free or forced and include all of the divergent motions in the surf zone, consideration of variable rotational currents has been largely confined to (free) shear waves. However, there is a mathematically well defined forced rotational flow which includes transient rip currents. The rotational flow is generated by the spatially variable incident wave forcing contained within \mathbf{S}^R , which in essence is the same as the intersecting wave train mechanism proposed by Dalrymple (1975).

3.5 Summary

The equations used to describe depth and incident wave-averaged horizontal nearshore currents are a set of forced shallow water equations. The forcing terms arise as a result of averaging over small scale turbulence and incident wave motions. The current can be partitioned into a part that is quasi-steady and a variable part. The variable part can be decomposed into a divergent and rotational part; the partition separates a flux which is the product of the depth-averaged velocity and the quasi-steady depth. The formal separation involves a projection operator that splits the momentum equation into evolution equations. While the resulting equations are complex, non-dimensionalising with typical surf zone scales allows an analysis of the relative sizes of the terms, and indicate that some of the nonlinear terms can be neglected.

The well known classes of nearshore current motion are identified; free and forced infragravity waves belong to the divergent current, while shear waves belong to the rotational part. Forced rotational currents are also identified as currents partially of wholly generated by variations in the incident wave forcing rather than a pure shear instability. These currents can therefore exist on a beach with perpendicular incident waves and no longshore current.

Chapter 4

Surf zone drifters

4.1 Introduction

Lagrangian data of a current system are valuable for understanding the detailed structure and making estimates of dispersion. These types of measurements in the surf zone are extremely rare, but are useful for confirming model and theoretical predictions of the spatial structure and transient features of the surfzone current system.

The few existing Lagrangian measurements in the surf and nearshore zone were obtained with a variety of techniques. Surface floats and drogued drifters were used by Shepard et al. (1941), Shepard and Inman (1950) and Sonu (1972) to investigate rip currents. Positions were obtained by compass fixes from boats and the shore. Floats and balloons were tracked using sequential aerial photographs taken from a balloon in the experiments of Sasaki and Horikawa (1975, 1978). The method of Short and Hogan (1994) used "live" floats, where swimmers floating in rip currents were tracked by theodolite fixes. This technique was used by Brander and Short (2000) to investigate the dynamics of a large rip system. Dye has also been used for flow visualisation and measurement of current speeds (e.g. Sonu, 1972; Brander, 1999).

Since the removal of Selective Availability (SA), position fixing using the Global Positioning System (GPS) is now the best option for surf zone work. Standard GPS receivers are very small, cheap and can fix positions within a few metres anywhere in the world. Differential correction which requires an additional base station can improve accuracy even further. Modern GPS technology means that the technical challenge associated with the actual position fixing itself is now minimal.

The real challenge is that the surfzone is far from an ideal environment in which to deploy drifters. The first problem to overcome when designing drifters for the surf zone is that any floating object tends to surf when caught in a breaking wave;

its velocity is then the phase speed rather than water particle motions. The less the instrument penetrates into the water below the breaking region of the wave, the worse the effect. The second problem in the surf zone is that the depth obviously varies greatly from deep water offshore to the swash where there is water only part of the time. Any floating instrument therefore has to have the apparently incompatible requirements of significant drag in the deeper section of a wave, and the ability to move into shallow water. Finally, the only way to deploy and recover drifters within the surf zone is to carry them; they need to be small and light enough to do this easily and safely. The solution is to use a series of "soft" drogues attached to a small, compact receiver units.

Concurrent with this work on developing a surf zone drifter, a GPS surf zone drifter has also been developed by Schmidt et al. (2003). This is the first and only other published work (that the author is aware of) describing drifters specifically designed for the surf zone. Their drifter uses differential GPS for data acquisition, and a different approach to minimise surfing and receiver oscillation.

The first section of this chapter presents the drifter and drogue design. Next there is a modelling analysis of how well surf zone drifters measure depth and wave-averaged currents. The third section addresses position fixing errors and their effect on the calculation of velocity and acceleration from the drifter position data. Finally the results of field validations using the devices are presented.

4.2 Drifter Design

The drifter arrangement, shown in Figure 4.1, is a cylindrical receiver unit connected to soft parachute drogue elements. The receiver units are 32 *cm* long and 10 *cm* in diameter and obtain and record a GPS position fix at 1 *Hz*. They consist of an integrated GPS antenna/reciever wired to a datalogger and a power source in a highly robust waterproof housing. They are deployed and recovered by hand and can easily be used for repeated runs over a short period of time. Due to their small and compact nature they are easy to deploy in any location and are therefore very effective for measuring transient features.

To minimise windage and inertial effects, the drifter units are nearly neutrally buoyant so that only the upper surface covering the internal GPS antenna is above the water. In calm water, only 2 *cm* of the instrument projects above the surface, so it is reasonable to assume windage is negligible. A wire with a small ribbon is extended above the main unit to enhance visibility; tests between units with and without this visual aid show no observable wind slip due to this. The very low surface profile does mean that the unit is sometimes completely submerged in

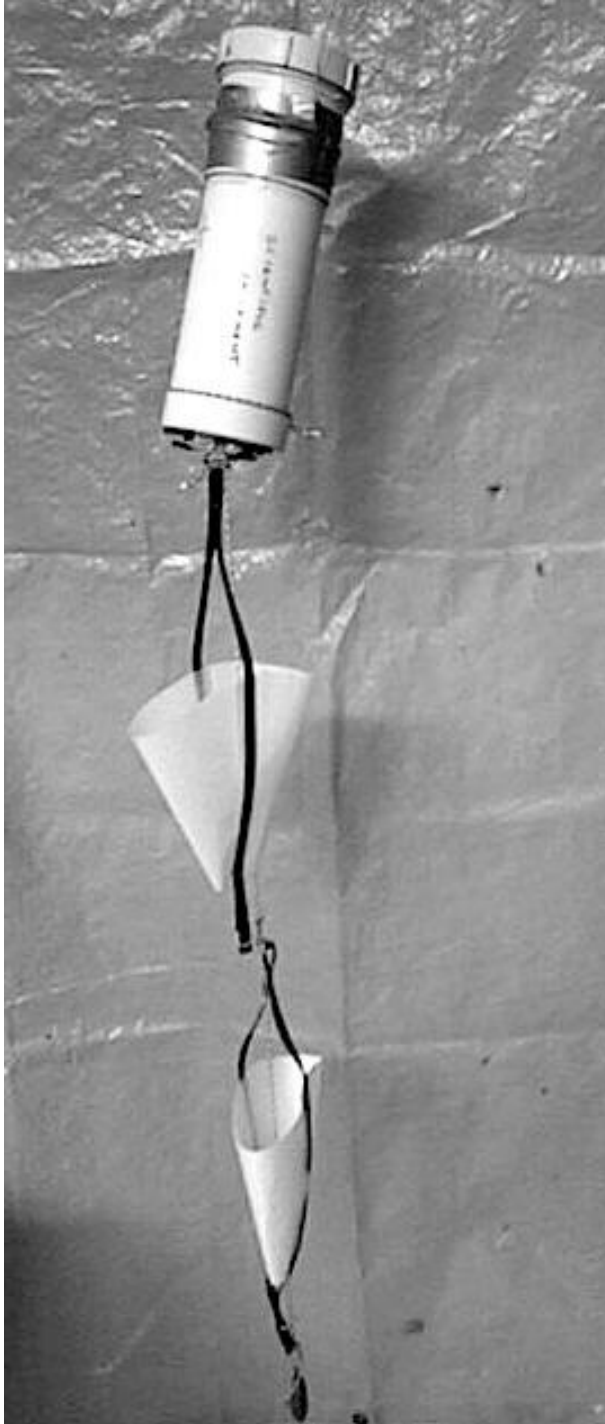


Figure 4.1: Drifter assembly of receiver unit with drogue attached.

breaking waves. When this occurs there is a gap in the data record, however data recovery even in strongly breaking waves is over 99% and data gaps are rarely more than 10 s. Any gaps in the data can be filled by interpolation; as will be seen in Section 4.4.2, the required length of the filtering interval is usually 20 s or more, so errors due to the interpolation are expected to be minimal.

4.2.1 Design of the receiver unit

The GPS receiver units, shown in Figure 4.2, have four primary components. These are an instrument casing, a receiver/antenna system, a datalogger, and a power source. The design aims were simplicity, ease of construction and low cost. No specialist skills other than the machining of the internal instrument frame are required in the construction. While specific hardware is detailed, there are other options, and it is not the intention of the author to promote a particular product.

The main casing is a 100 mm PVC sewerage pipe with standard end fittings from a hardware store, for a total length of 320 mm. This construction withstands pressure testing up to at least 40 m of seawater. The GPS receiver and the datalogger are mounted on an internal instrument frame, while a battery pack at the bottom of the casing powers the electronic components and acts as ballast, providing the unit with upright stability.

The GPS receiver is a *GARMIN GPS36* integrated receiver/antenna, which is a standard marine unit. The default device setting outputs NMEA 0183 *\$GPRMC* data sentences at a frequency of 1 Hz. All initialisation and satellite acquisition is carried out automatically by the receiver. However, this unit also provides a full configuration interface that can be used if required.

The datalogger is a *DGPS-XM Data Logger* from R. I. Keskull, Sydney. This can be wired directly to the GPS36 output through a RS232 connector. Once a good fix is obtained by the GPS36, the logger starts reading the NMEA 0183 sentences and stores position, time and date at 1 Hz. The logger can store 95200 points, equivalent to 26 hours of continuous operation. An optional operating mode can change the data recording frequency to 0.1 Hz, extending memory life to 260 hours. An LED on the logger indicates the status of the device, indicating power on/off, whether good data are being received, low memory, full memory, and low battery power. Data are downloaded from the logger via the RS232 connection to the COM port of a PC using software provided with the logger. Output data also include a status code, marking the start of each data sequence, so the logger can be used for multiple deployments without downloading operations.

Seven standard alkaline D-cells provide sufficient power for 40 hours of continuous use at 1 Hz, or at least 260 hours at 0.1 Hz. The power on/off is a reed switch latch

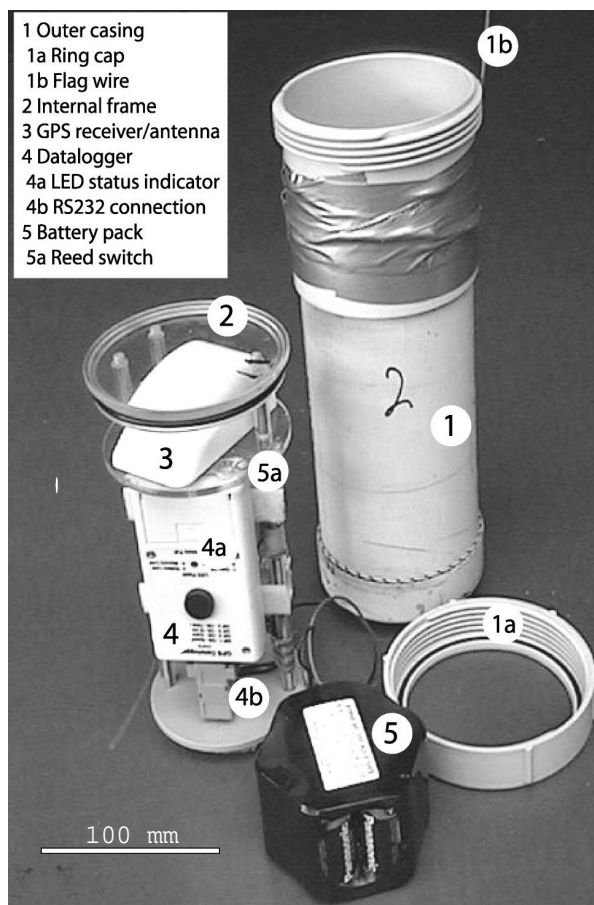


Figure 4.2: Receiver units showing the casing, battery pack and internal frame with GPS receiver/antenna and datalogger attached. Note that the duct tape around the casing is simply to attach the flag wire which carries a small ribbon to aid visibility; it has no other structural purpose.

relay that is activated with a small magnet, avoiding any penetration of the casing by a switch and enhancing the water-tight integrity of the device. The entire unit can simply be turned on and off for each individual deployment.

The total cost of components and materials is approximately US\$350 per unit (at the time of writing). For a single unit, an estimated eight hours of labour at US\$50 per hour puts the overall cost at around US\$750. When constructing multiple units, the labour time per unit is very significantly reduced, and the total cost for ten units is US\$500 each. This is about a factor of ten cheaper than commercially available GPS drifters. Most commercial units have data transmission capability, the lack of which is a limitation of the design described here and makes it unsuitable for deployments over long periods and distances. While implementation of a transmission interface for the existing design is possible with minimal modifications, this introduces an additional level of complexity and cost that is contrary to the fundamental idea of the device described herein, namely low cost and ease of construction.

4.2.2 Drogue design

The drogue is a series of parachute shaped elements which hang below the GPS drifter casing. The parachutes are made of a cone of Dacron sailcloth with webbing attachments and are almost neutrally buoyant; a small weight is attached at the end of the parachutes to keep them hanging below the receiver unit (Figure 4.3). When the receiver unit is pulled shoreward by the breaking section, the parachutes open and anchor the drifter to the orbital velocities below the breaking region. In non-breaking waves, the parachutes are closed and hang almost vertical and therefore only present their cross-sectional area. The drogue is also very effective in stabilising the receiver unit by strongly damping the oscillatory motions, both vertical and horizontal, that an un-drogued receiver experiences. In water depths less than the length of the complete drifter arrangement, the drogue may touch the bed. Drag tests in a tow tank indicate that this bottom drag is small compared to water resistance on the parachutes, however some measurement error will inevitably occur when the drogue is in contact with the bed. This means that the minimum operating depth is the length of the receiver unit (32 *cm*) while the drogue still provides sufficient resistance to surfing in large waves.

Visual observations of the drifter in breaking waves suggest that the parachutes are extremely effective in resisting surfing. When in the the overturning section of a plunging breaker, the parachutes appear to prevent the receiver from accelerating up the face and forward with the plunging lip. In spilling breakers or broken plunging waves, the receiver unit ducks underneath the foaming roller section and reappears at the surface a couple of seconds later as the wave passes over. The only situation

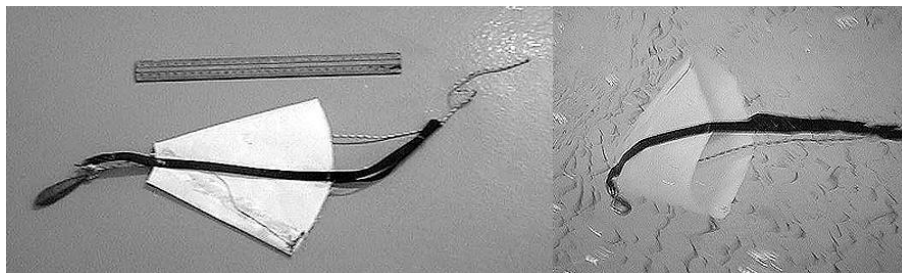


Figure 4.3: Parachute drogue made from a cone shaped piece of sailcloth with a webbing attachment. The small lead weight attached to the end of the parachute is to keep it oriented downwards in the water. The ruler shown for scale is 30cm long. The picture on the right shows a parachute drogues opening as it is pulled through the water.

in which the drifters do not perform well is when caught at the plunge point of a strongly plunging wave. Due to the strong downwards velocities, the whole assembly may be completely disrupted and rolled by the wave, the parachutes no longer correctly oriented, and the drifter then tends to surf in the developing roller section. Even if the assembly is not overturned, in strongly plunging breakers the penetration of strong breaking induced turbulence and bubbles occurs all the way to the bed. The turbulent bubble mass propagates at close to the phase speed; this was described by Ting and Kirby (1994) in their laboratory experiments on plunging waves and is experienced in the field when diving under these large waves. When caught in such strong breaking events the drogue is ineffective at anchoring the drifter to the wave orbital motion and the whole unit travels at the wave phase speed. Surfing events are very easy to identify in the data as the phase speed is much greater than orbital velocities and typical wave-averaged current speeds. Data contaminated by surfing can then easily be excluded from any analysis.

Schmidt et al. (2003) addressed the problem of surfing by attaching a disk to the base of their 50 cm long main casing. This strongly damped vertical motions, and was found to be effective in resisting surfing. Their longer receiver casing also penetrates deeper into the water below breaking wave rollers and precludes some of the need for an additional drogue.

4.3 Modelling surfzone drifter dynamic response

Exactly what a drifter is actually measuring in the surf zone is an important question. The drifter assembly experiences the pressure gradients and velocities due to the instantaneous hydrodynamics. This includes the turbulent roller section of a breaking wave which is moving with the phase speed. The fact that the assembly is made up of elements of differing shapes which are connected to each other means

that the response is fairly complex. To investigate the dynamics of the drifter motion, the drifter assembly was modelled as a series of connected rigid bodies under the influence of an idealised surf zone flow field.

4.3.1 Approximating the hydrodynamics of the surfzone

Using the decomposition of Putrevu and Svendsen (1999), the instantaneous (depth and time dependent) flow is expressed as:

$$\tilde{\mathbf{u}}(x, y, z, t) = \overline{\mathbf{U}}(x, y, t) + \mathbf{U}^1(x, y, z, t) + \tilde{\mathbf{u}}^w(x, y, z, t) \quad (4.1)$$

$$w(x, y, z, t) = \tilde{w}^w(x, y, z, t) \quad (4.2)$$

where $\overline{\mathbf{U}}$ is as defined in Equation 3.2, \mathbf{U}^1 is the depth variable part of the wave-averaged current and $\tilde{\mathbf{u}}^w$ is the “wave” component. A model for a monochromatic wave field is constructed as follows. The incident wave velocity is $\tilde{\mathbf{u}}_w$ which is assumed to have a zero time average below trough level,

$$\overline{\tilde{\mathbf{u}}^w} = 0, \quad -h \leq z \leq \tilde{\eta}_t \quad (4.3)$$

In addition, total flux due to the depth varying part of the current, \mathbf{U}^1 , is equal and opposite to the flux due to the incident wave motion so that:

$$\int_{-h}^{\tilde{\eta}_t} \mathbf{U}^1 dz = - \overline{\int_{-h}^{\tilde{\eta}} \tilde{\mathbf{u}}^w dz} = - \overline{\int_{\tilde{\eta}_t}^{\tilde{\eta}} \tilde{\mathbf{u}}^w dz} \quad (4.4)$$

where $\tilde{\eta}_t$ is the elevation at the bottom of the wave trough.

Specification of the wave hydrodynamics, including breaking, at variable points in space and time requires some kind of wave theory and breaker model. For simplicity in investigation of the fundamental dynamics, first order cnoidal wave theory (Isobe, 1985) is used, with a crude breaker model. Cnoidal wave theory is superior to linear wave theory in the surf zone as it generates waves with short crests and long troughs with associated asymmetry in the orbital velocities. Pressure gradients, $\nabla P, \partial P / \partial z$ are also obtained from the first order cnoidal wave theory.

The breaker model follows the “roller” concept and simulates the effect of breaking as a region of fluid fixed on the front edge moving with the wave phase speed, as shown in Figure 4.4. The distribution of the roller is assumed to be elliptical and equally spaced above and below the (non-breaking) free surface. Following Kuriyama and Nakatsukasa (2000), the velocity inside the roller region then varies

linearly from the wave orbital speed, $u_{(cn)}$, to the wave phase speed, C :

$$\tilde{\mathbf{u}} = \left[u_{(cn)} + (C - u_{(cn)}) \frac{z - \eta + \eta_b}{2\eta_b} \right] \frac{\mathbf{k}}{|\mathbf{k}|}, \quad \eta - \eta_b < z < \eta + \eta_b \quad (4.5)$$

$$\eta_b = \pm \sqrt{\left(\frac{\gamma H^2 |\mathbf{k}|}{\alpha \pi^2} \right)^2 \left[1 - \left(\frac{\mathbf{k} \cdot \mathbf{x} - \omega t - 2\beta\pi}{\alpha \pi} \right)^2 \right]}, \quad (4.6)$$

$$2\beta\pi - \alpha\pi < \mathbf{k} \cdot \mathbf{x} - \omega t < 2\beta\pi + \alpha\pi$$

where H , \mathbf{k} and ω are the wave height, wave number vector and frequency. α , β and γ are adjustable parameters¹ which describe the length, position, and area of the roller.

The depth varying velocity component, \mathbf{U}^1 is determined from a slightly modified version of the undertow solution of Svendsen (1984), in which a boundary condition requiring that the undertow goes to zero at the trough level is used to avoid a discontinuity in the velocity field. Note that inclusion of undertow in the velocity field violates the basic assumptions of cnoidal wave theory, namely irrotationality, so strictly speaking is not self consistent.

In a particular simulation, constant wave-averaged currents and wave field parameters are used. Furthermore, modelling of the drifter assembly is restricted to the vertical plane aligned perpendicular the wave crests. This retains the dominant surf zone effect of drift induced by the wave motion and breaking while simplifying the necessary calculations, but does not represent the case of a current at an angle to the wave propagation. Extension to three dimensions is in principle straight forward, although more computationally expensive for the rigid body calculations.

4.3.2 A rigid body model for the drifter assembly

The drifter assembly experiences the instantaneous time and depth dependent velocities, \mathbf{u}, w and pressure gradients, $\partial p/\partial x, \partial p/\partial z$, associated with wave motion and the mean current as determined at its location. To model the motion of the drifter, the drifter assembly was treated as a connected series of rigid bodies, as shown in Figure 4.5. In the vertical plane, each assembly element (receiver, parachute or weight) obeys equations for its change of position/orientation and the conservation of linear and angular momentum:

$$\frac{dX}{dt} = U_e \quad (4.7)$$

$$\frac{dZ}{dt} = W_e \quad (4.8)$$

¹These symbols are redefined for this chapter only

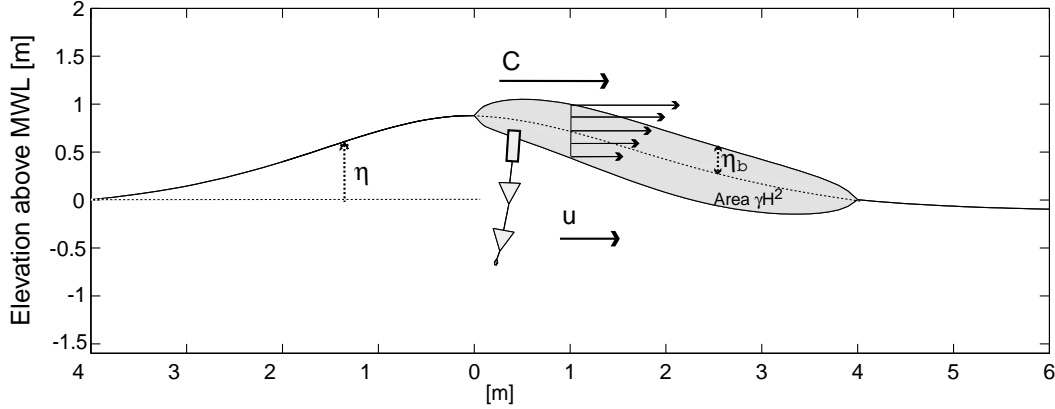


Figure 4.4: Schematic diagram of the drifter response model. The drifter assembly is modelled as a series of rigid bodies under the influence of the instantaneous hydrodynamics. The assembly shown consists of the receiver unit, two parachutes and one weight. The wave roller which simulates wave breaking is shown as the shaded region.

$$\frac{d\theta}{dt} = \frac{L}{I} \quad (4.9)$$

$$m \frac{dU_e}{dt} = P_x + D_x + T_x \quad (4.10)$$

$$m \frac{dW_e}{dt} = G + B + P_z + D_z + T_z \quad (4.11)$$

$$\frac{dH}{dt} = \tau^{(B)} + \tau^{(P)} + \tau^{(D)} + \tau^{(T)} \quad (4.12)$$

where X, Z are the position of the centre of gravity and θ is the orientation of the main axis of the element. U_e and W_e are the linear velocities of the element and m is its mass. P, D, T, G and B are the total pressure gradient, drag, tension (due to connecting tethers), gravity and buoyancy forces with subscripts indicating directional components. Hydrodynamic lift forces have been neglected. The change of angular momentum, L , is due to the torques, τ induced by the various forces; the symbols in brackets indicate the force responsible for the torque in each case and respectively correspond to buoyancy, pressure, drag, and tether tension. The rate of change of orientation, θ is directly determined by the angular momentum and the moment of inertia, I of the element. Equations 4.7 to 4.12 are integrated using a fourth order Runge-Kutta scheme².

The elements in the assembly are modelled as being either solid cylinders for the main drifter unit and the weight or hollow cones for the parachutes. Each element is discretised into n equally spaced control points along its main axis as shown in Figure 4.5. The pressure, drag and buoyancy forces are evaluated at each point to

²Some symbols are redefined for this section only

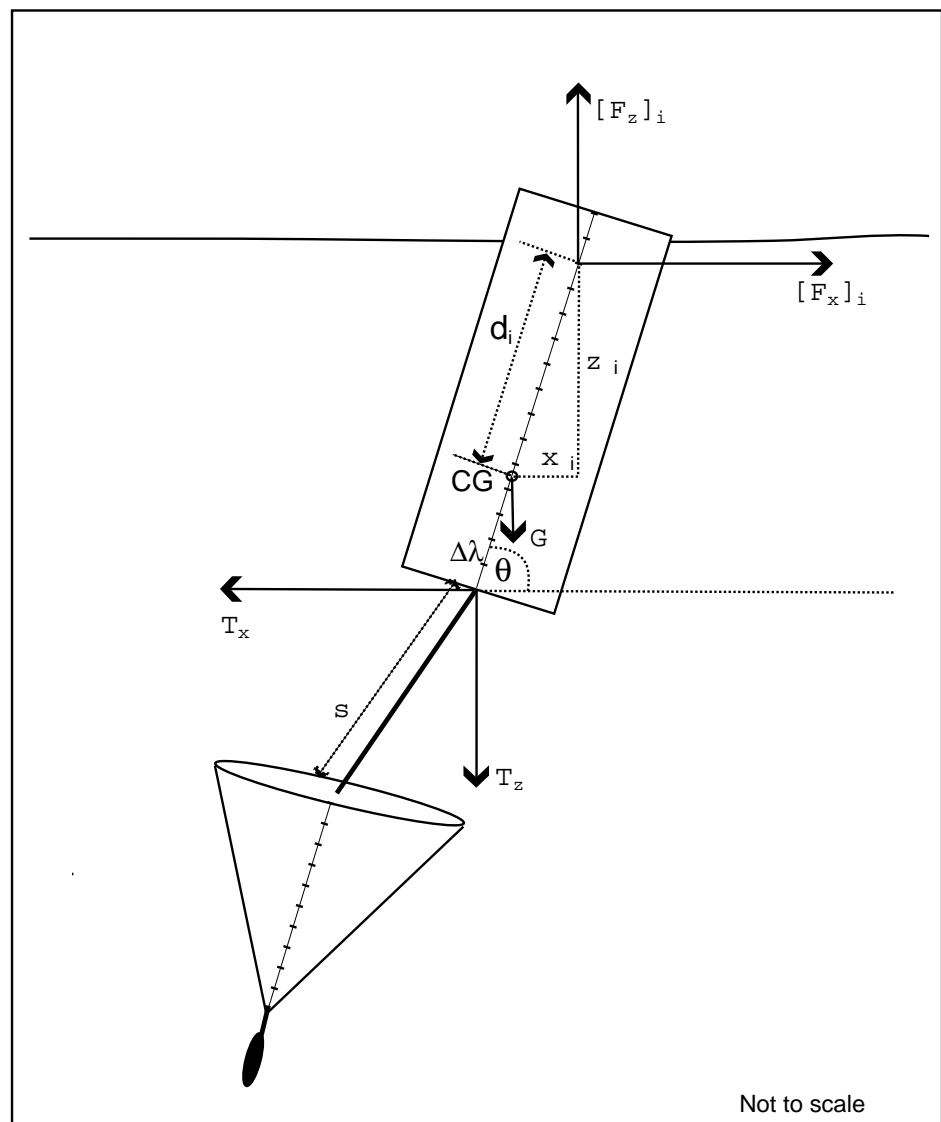


Figure 4.5: Forces acting on an element. $[F_x]_i$ and $[F_y]_i$ represent pressure, drag and buoyancy forces acting at one of the control points distance x_i, y_i from the centre of gravity (CG). T_x and T_y are tensions acting at the bottom of the element.

give a total linear force and torque:

$$F_x = \sum_{i=1}^n [F_x]_i d_i \Delta \lambda \quad (4.13)$$

$$F_z = \sum_{i=1}^n [F_z]_i d_i \Delta \lambda \quad (4.14)$$

$$\tau^{(F)} = \sum_{i=1}^n ([F_z]_i x_i - [F_x]_i z_i) d_i \Delta \lambda \quad (4.15)$$

where F can represent any of the forces, $[F]_i$ is the force at a control point, x_i and z_i are the position of each control point from the centre of gravity of the element and d_i is the diameter at the control point. The evaluation of the specific forces is as follows:

Pressure, P

$$[P_x]_i = \frac{\pi}{4} d_i \frac{\partial p}{\partial x} \quad (4.16)$$

$$[P_z]_i = \frac{\pi}{4} d_i \frac{\partial p}{\partial z} \quad (4.17)$$

Drag, D

$$[D_x]_i = C_d^x \rho_w (U_i - u) |U_i - u| \quad (4.18)$$

$$[D_z]_i = C_d^z \rho_w (W_i - w) |W_i - w| \quad (4.19)$$

Buoyancy, B

$$[B_x]_i = 0 \quad (4.20)$$

$$[B_z]_i = \rho_w \frac{\pi}{4} d_i, z_i < \eta(x_i) \quad (4.21)$$

Gravity, G

$$G = -m_e g \quad (4.22)$$

where m_e is the mass of the element.

The fields $\partial p/\partial x$, $\partial p/\partial z$ and u, w as well as the position of the free surface, η are determined by the hydrodynamic model and interpolated onto each control point. C_d^x and C_d^z are drag coefficients which depends on the orientation of the control point to the flow. In practice only the cylindrical drifter element breaks the surface and experiences buoyancy forces; the parachute elements are assumed to be neutrally buoyant and always below the surface. The drag coefficients are calculated by resolving drag coefficients for the perpendicular direction (flow at right angles to

main axis) and parallel direction determined by tow-tank testing:

$$C_d^x = C_d^\perp |\sin \theta| + C_d^\parallel |\cos \theta| \quad (4.23)$$

$$C_d^z = C_d^\perp |\cos \theta| + C_d^\parallel |\sin \theta| \quad (4.24)$$

$$C_d^\parallel = \begin{cases} C_d^\uparrow, & W_e \sin \theta > 0 \\ C_d^\downarrow, & W_e \sin \theta < 0 \end{cases} \quad (4.25)$$

For both elements $C_d^\perp = 0.001$, $C_d^\uparrow = 0.002$, and $C_d^\downarrow = 0.002/0.0001$ for the receiver/parachutes. ρ_w is the density of the water. The tether tensions and gravity force act at the element ends and centre of gravity respectively:

Tether tension, T

$$T_x = \mathcal{E} \left(\frac{s-L}{L} \right)^3 \cos \phi, \quad s > L, \quad 0 \text{ otherwise} \quad (4.26)$$

$$T_z = \mathcal{E} \left(\frac{s-L}{L} \right)^3 \sin \phi, \quad s > L, \quad 0 \text{ otherwise} \quad (4.27)$$

$$\tau(T) = \sum_{j=1}^{1 \text{ or } 2} ([T_z]_j x_j - [T_x]_j z_j) \quad (4.28)$$

where s is the separation between tether attachment points of two elements in the assembly, ϕ is the orientation and L the length of the tether. In the case of the torque term there may be two tethers for the parachute elements; x_j and z_j are the distance of the attachment points from the centre of gravity. \mathcal{E} is an elasticity constant, given a very high value of 10,000 N as in reality, the tethers between the parachutes are not made of an elastic material. Allowing a small amount of flex in the system does not alter the fundamental nature of the dynamics but greatly facilitates the numerical solution.

4.3.3 Simulation results

Figure 4.6 shows a series of visualisations of the model output for one 10 s wave period for a drifter assembly with two parachutes and for a receiver element alone. The wave and depth-averaged current, $\bar{\mathbf{U}}$, is zero in this case. As the drifter is hit by the roller, the receiver element is dragged in the direction of the wave propagation. The parachutes minimise the influence of the roller and effectively anchor the assembly to the orbital velocities deeper in the wave; this is particularly obvious after one second. The receiver element without parachutes is moved further by the breaking roller and is less effected by undertow than the two parachute arrangement. The net effect over a wave period is that the lone receiver undergoes significant displacement due to the wave while the parachute assembly shows minimal drift in the direction

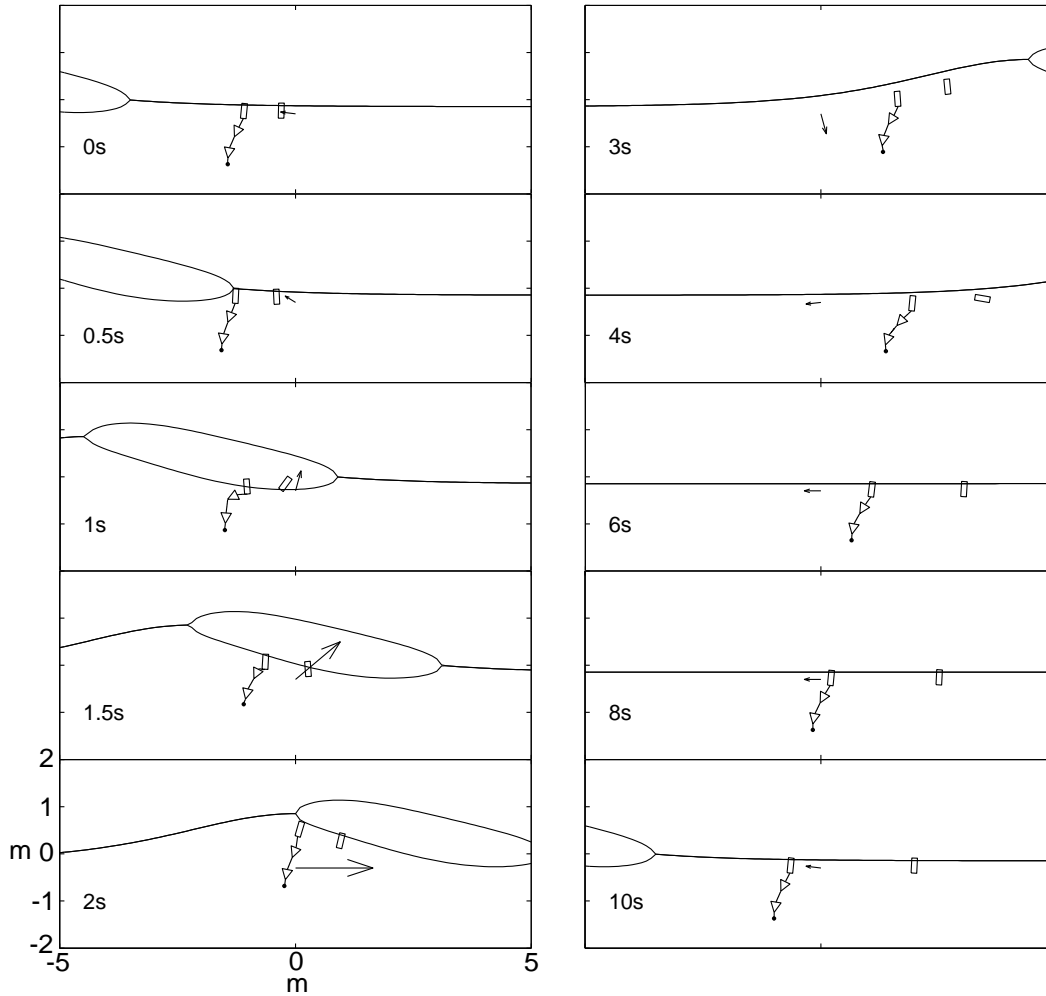


Figure 4.6: Visualisation of model output for an receiver unit alone and an assembly with two parachutes at a series of discrete times (indicated in the left corner of each frame).

of the wave. Qualitatively, the motion agrees very well with visual observations of the drifters in breaking waves.

A set of simulations for different drifter assemblies were carried out, varying the wave period, wave height and roller area for a range of mean currents between -1.0 ms^{-1} (offshore) and 1.0 ms^{-1} (onshore) in each case. The depth was determined from a breaking criteria of $H = 0.6h$ in each case. The roller model parameters were set so that the roller covered the region of the wave from the crest to the mean water level while the roller area was left as a free parameter. There is some correlation of estimated roller areas and Iribaren number (Kuriyama and Nakatsukasa, 2000) so variation of γ in a very crude way simulates different types of breaking waves. The range of parameters used are shown in Table 4.1. All combinations of parameters were tested except where the depth of the assembly exceeded the water depth (as

Table 4.1: Parameter values used for drifter simulations

Parameter	Values
Wave height [m]	[0.25, 0.5, 1.0, 2.0]
Wave period [s]	[5, 10]
Roller area (γ)	[2, 4, 6]
Parachutes	[0, 1, 2, 3]

determined by the breaking criterion).

Results from the full set of drifter simulations are shown in Figure 4.7. The results are plotted as an error between the wave-averaged velocity of the drifter receiver, \mathbf{U}_d , and the Eulerian depth and wave-averaged velocity, $\bar{\mathbf{U}}$. The size of this error usually does not show a linear relationship with the variation of parameters (current speed, wave height etc.). This reflects the complex nature of the dynamic response of the drifter. Examination of the results and the simulated motion of the drifter assembly reveals three sources of this error:

1. The surfing effect. The wave roller drags the drifter shoreward faster than the orbital velocities (as seen in Figure 4.6). This tends to be larger with larger waves.
2. Bias of vertical sampling. The presence of the parachutes tends to "over sample" the undertow in the lower part of the water column so that the mean motion is faster offshore than the Eulerian velocity. The effect tends to increase with a larger number of parachutes.
3. Bias of sampling of horizontal wave motion due to the current effect on wave shape. An onshore current leads to a longer wave, which, in the model used here, gives relatively longer troughs and short crests. Although the Eulerian mean mass flux is still the same as the depth-averaged current, the drifter spends more time influenced by the undertow in the trough section of the wave, and therefore tends to move offshore relative to $\bar{\mathbf{U}}$. The opposite happens with offshore current as the drifter spends relatively longer under the crest.

The first two effects oppose each other and the balance between these two determines whether the error is onshore or offshore; this is influenced by the number of parachutes. The third source of error operates to reduce the magnitude of the velocity while retaining the direction. This leads to a negative gradient of the error with respect to the Eulerian mean velocity. The mix of errors due to these processes largely determines the response characteristics for a given wave height, period, roller size and mean current.

In the short period waves ($T_p = 5s$), the undertow effect appears to dominate for an offshore directed mean current. In the long period waves ($T_p = 10s$), and in the short period waves with onshore current, the negative gradient of the error indicate that horizontal sampling bias is dominant. Roller size does not seem to affect the balance between surfing and undertow for the long period waves but larger rollers dramatically increase the undertow effect for short period waves with offshore current.

For waves of 1 m or less, the model indicates quite a good correspondence between the drifter and Eulerian depth and wave-averaged velocity if the right number of parachutes are used. The exception is strong offshore currents in short period waves, where the offshore velocity may be seriously overestimated. A general rule of thumb suggested by the modelling is to use an assembly length similar to the wave height, so one parachute for 0.75 m or less and two for 1.0 m ; the difference is relatively small suggesting that the number of parachutes is not crucial as long as it is at least one. For the smaller roller sizes, performance is quite acceptable for the 2 m wave height, but errors become large and unpredictable for the larger roller sizes. How well the model can simulate the dynamics at the largest wave sizes is also questionable and the solutions become unstable in one of the cases.

Clearly the basic assumptions in the wave hydrodynamic model are somewhat simplistic. In particular, the roller model is unlikely to capture the real effect of wave breaking very well. In the model, the surfing effect is due to a large increase in drag on the drifter. In the field, there can also be a catastrophic failure of the drogues, due to being overturned as described in Section 4.2.1.

The rigid body simulations for the drifter assembly itself should be quite accurate as it solves the equations of motion exactly. The only approximations, other than the normal modelling process of discretization, are in the formulation of the drag forces (and the neglect of lift forces). In addition the method is extremely flexible as the assembly can be embedded in any hydrodynamic field; for example use of LES results of breaking waves (e.g. Christensen and Deigaard, 2001) would provide highly realistic flow fields.

4.4 Measurement errors

There are errors inherent in both the position fixing of the GPS receiver and in calculation of velocities and accelerations from raw position data. Although the removal of SA has greatly improved the performance of non-differential GPS, there are still errors in the reported positions due to precision limits in hardware, satellite clock error, errors in the ‘known’ satellite positions, atmospheric effects on the speed

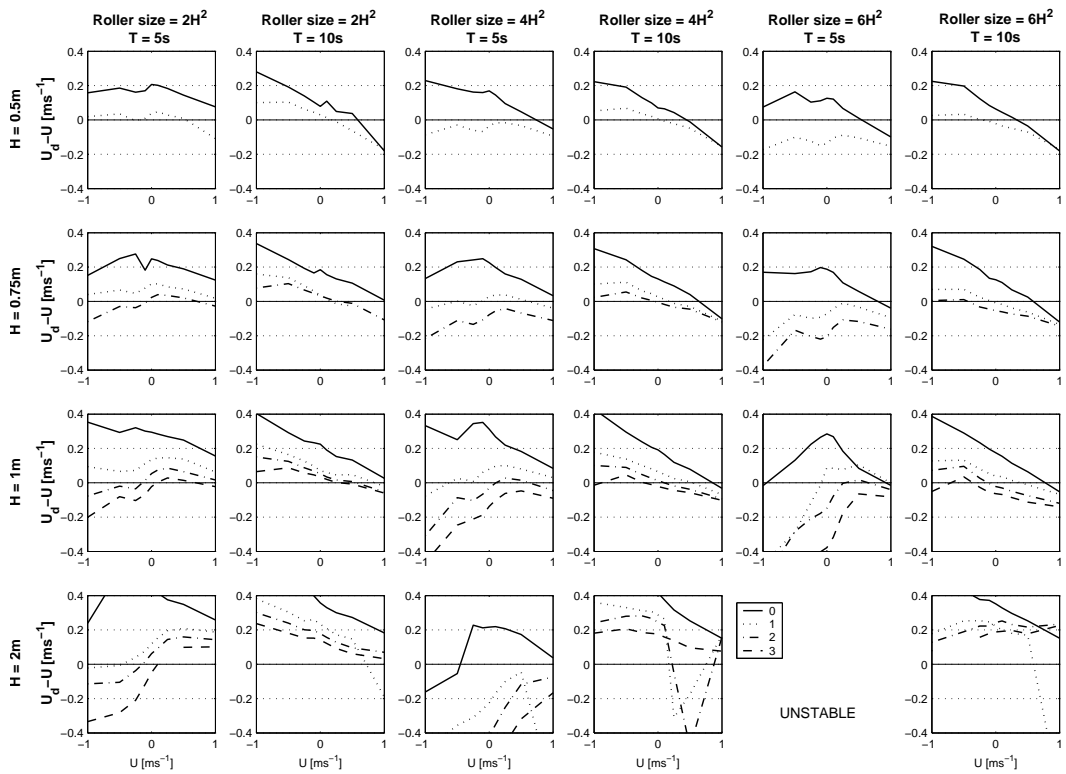


Figure 4.7: Results from the drifter simulation expressed as the difference between the mean drifter velocity averaged over three waves, and the mean current in the modelled hydrodynamics; positive results indicate a drifter moving shoreward faster than the depth-averaged current. In each subplot, the lines are for drifter assemblies with zero(solid), one(dotted), two(dot-dash) or three(dashed) parachutes. The columns are for a particular wave period and roller size, as labelled at the top. The rows correspond to different wave heights.

of light and multipath error (reflection of signals off large obstacles). Some of these errors are white noise while others, such as the atmospheric effects, produce position errors which oscillate with a preferred frequency. A distinction is made between absolute and relative error. The absolute deviation from the true geographic position is usually not important. However, the relative error which is an apparent change of position relative to an arbitrary datum which is not due to real motion (i.e. experienced by a stationary receiver) contaminates any calculations of the velocity and acceleration of a moving receiver.

To investigate the effect of relative position fixing error, a series of stationary tests was carried out. The data was obtained by simply placing the GPS unit in a wide open space and leaving to obtain position fixes for a period of time. The datalogger has a memory precision of $0^{\circ}0.0001'$ of latitude and longitude. At the test location latitude of $32^{\circ}S$ this corresponds to approximately 0.16 m of easting and 0.19 m of northing. Positions were converted to Universal Transverse Mercator (UTM) coordinates which facilitates later mathematical manipulation. Position data is collected at 1 Hz .

An example of output from the test receiver is shown in Figure 4.8 for a 8000 s stationary test. The standard deviation of displacement are 1.24 m and 1.98 m for Eastings and Northings. Over 95% of fixes fall within circles of radii 2.2 m and 3.6 m respectively. As shown in what follows, non-differential GPS position fixing is sufficient for accurately measuring motion with frequencies below about 0.05 Hz . Using differential correction, the relative RMS error can be greatly reduced, and effectively allows accurate velocity measurement for motions at frequencies of 1 Hz (Schmidt et al., 2003).

In the analysis that follows, it was assumed that to good approximation the position error is independent of the motion of the receiver and that these type of stationary tests are representative of the errors experienced by a moving receiver. Kirwen and Chang (1979) present an analysis of the effect of sampling rate and random position error on the calculation of both velocities and accelerations of individual drifters and this is included in Section 4.4.2.

4.4.1 Analysis of Position errors

The measured position, $\hat{\mathbf{x}}_i$ at time t_i is given by:

$$\hat{\mathbf{x}}_i = \mathbf{x}_i + \mathbf{e}_i \quad (4.29)$$

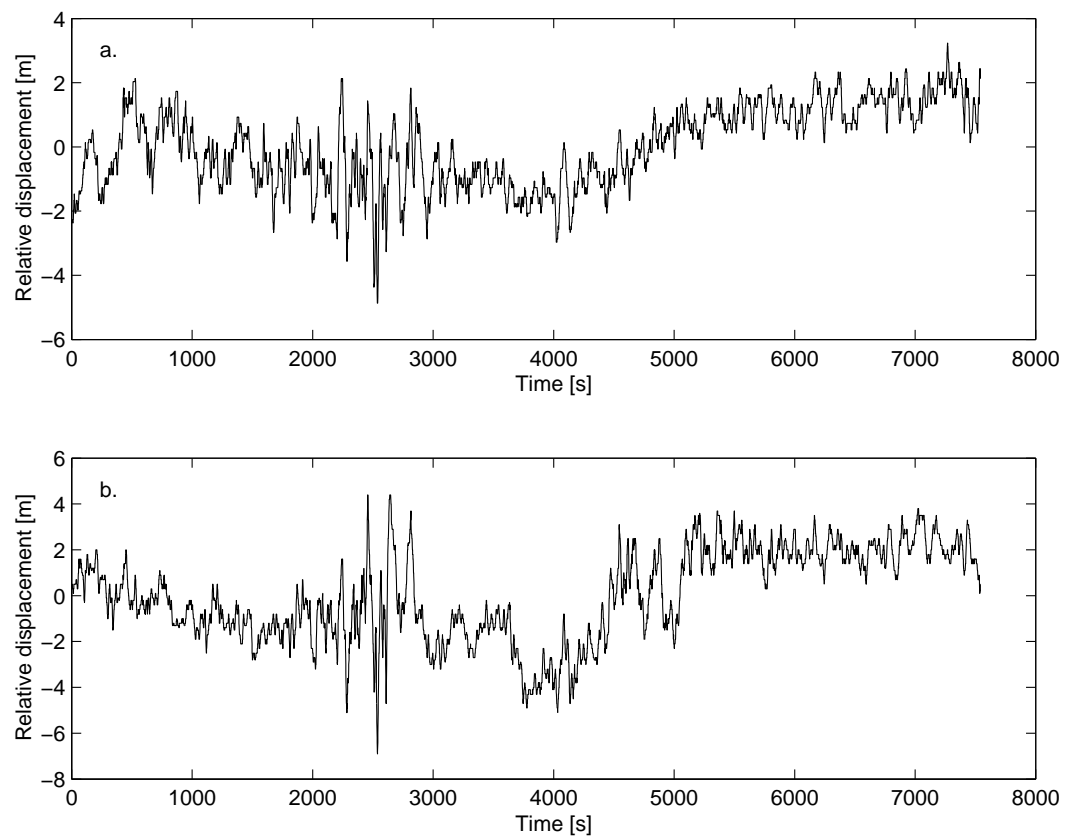


Figure 4.8: Raw data converted to UTM from a receiver unit left stationary for 3 hours.

where \mathbf{x}_i is the true position and \mathbf{e}_i is position fixing error, both observed at time t_i . \mathbf{x} and \mathbf{e} are assumed to be continuous variables observed at discrete times. Bold face indicates a horizontal vector quantity. No assumptions are made about the nature of the position fixing error except that $\widehat{\mathbf{e}} = \widehat{\mathbf{e}\mathbf{x}} = \mathbf{0}$ so that long time average of error is zero, and that the position error is uncorrelated with the true position. While the second assertion is not strictly true as the magnitude of certain position errors vary with latitude, this correlation is assumed to be negligible for the typical velocities considered here.

The true position and error are written as Fourier integrals,

$$\mathbf{x}(t) = \int_{-\infty}^{\infty} \mathbf{X}(f)e^{i2\pi ft} df \quad (4.30)$$

$$\mathbf{e}(t) = \int_{-\infty}^{\infty} \mathbf{E}(f)e^{i2\pi ft} df \quad (4.31)$$

where f is the frequency. The observed position in Equation (4.29) is rewritten in frequency space as:

$$\hat{\mathbf{x}}(t_i) = \int_{-\infty}^{\infty} \mathbf{Z}(f)e^{i2\pi ft_i} df = \int_{-\infty}^{\infty} (\mathbf{X} + \mathbf{E})e^{i2\pi ft_i} df \quad (4.32)$$

The power spectra of the raw data shown in Figure 4.8 is shown in Figure 4.9. The spectrum of stationary data, assumed to be representative of the positioning error, is coloured. In the surf zone, there are motions over a wide range of frequencies and it is necessary to determine how much different frequency ranges are affected by the positioning errors. Figure 4.10 show spectra of the displacement signal from a surfzone deployment with the stationary test spectra for the easting component. The measured signal power is approximately an order of magnitude larger than the stationary test data in the frequency range below 0.05 Hz; for frequencies higher than this the ratio increases. Filtering the position signal removes frequency bands which are not required, for example removing the incident wave motion to leave a wave-averaged signal. In addition filtering is often desirable to remove high frequency positioning errors prior to plotting trajectories.

4.4.2 Errors in velocity and acceleration calculations

The true velocity of the drifter, \mathbf{u}_d is:

$$\mathbf{u}_d(t) = \frac{d\mathbf{x}}{dt} = i2\pi f \int_{-\infty}^{\infty} \mathbf{X}e^{i2\pi ft} df \quad (4.33)$$

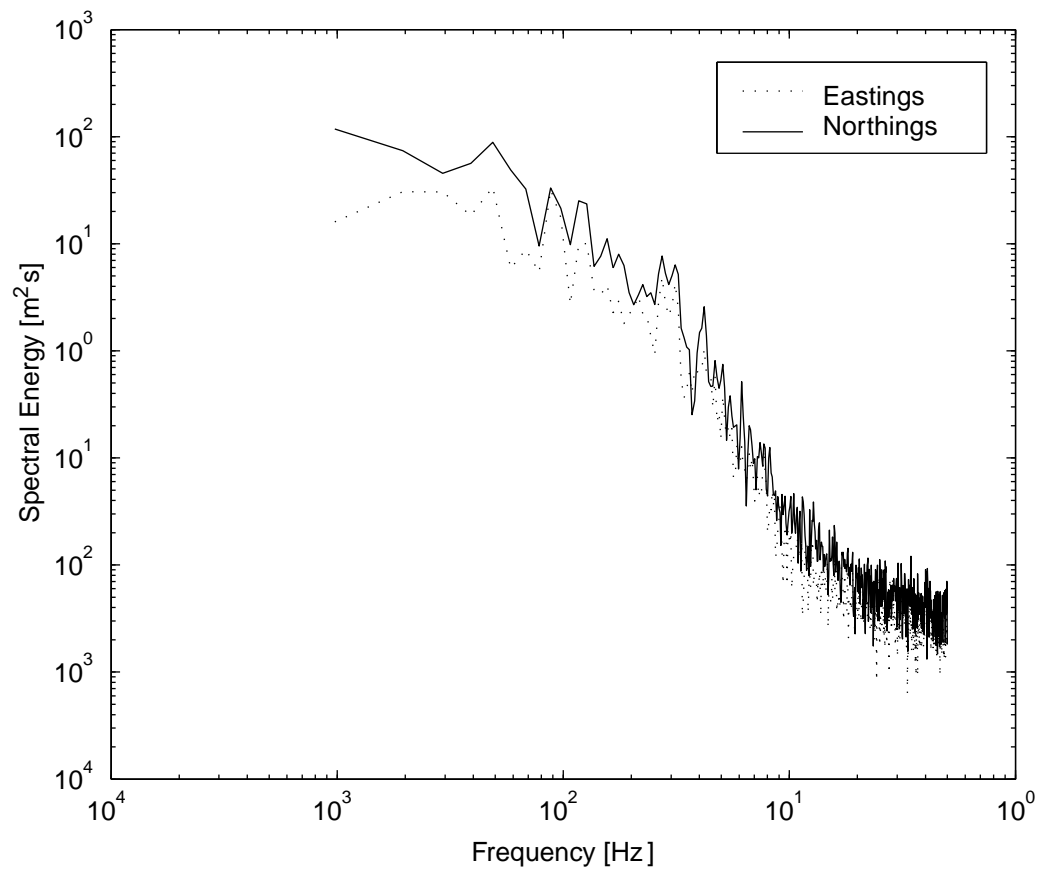


Figure 4.9: Power spectra of position signal for the stationary test.

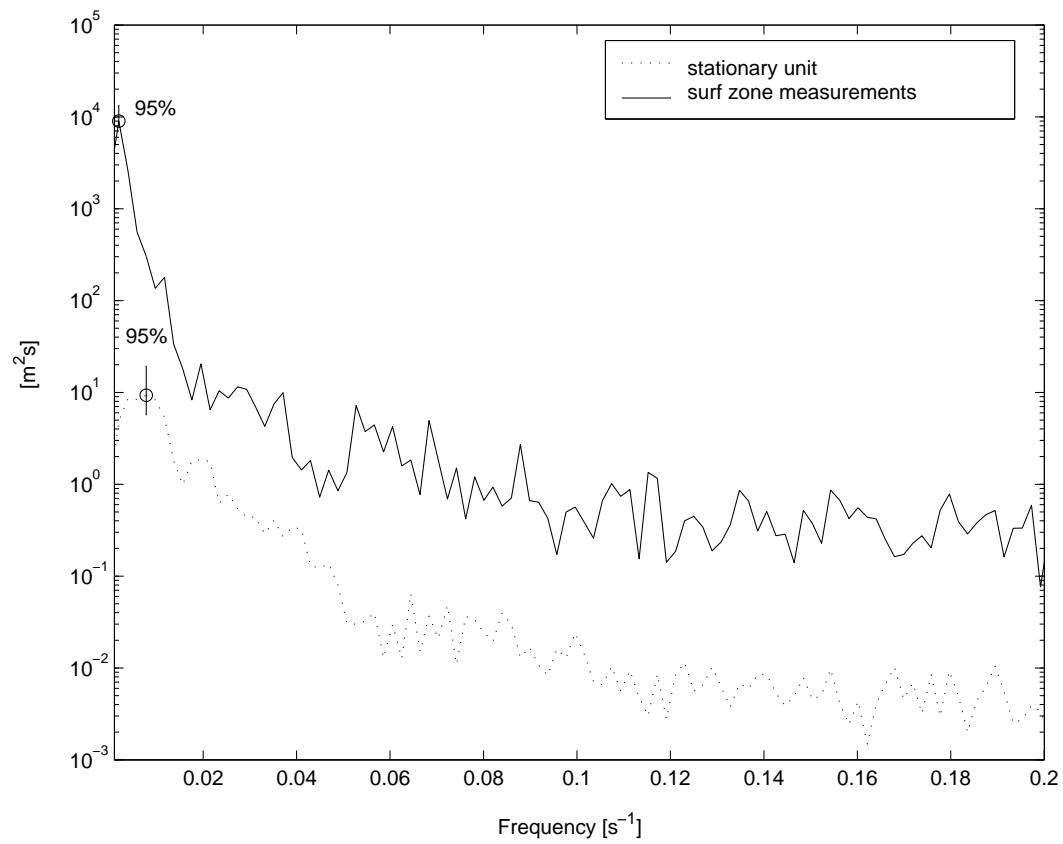


Figure 4.10: Power spectra of position signal for data from a surfzone deployment plotted with the power spectra from the stationary test.

Calculation of the velocity from drifter trajectory data is usually by centred differences to give an estimated velocity, $\hat{\mathbf{u}}_d$:

$$\hat{\mathbf{u}}_d(t_i) = \frac{\hat{\mathbf{x}}(t_{i+1}) - \hat{\mathbf{x}}(t_{i-1})}{2\Delta t} \quad (4.34)$$

which after substituting Equation 4.32 gives:

$$\hat{\mathbf{u}}_d(t_i) = \left[\int_{-\infty}^{\infty} (\mathbf{X} + \mathbf{E}) e^{i2\pi f t_{i+1}} df - \int_{-\infty}^{\infty} (\mathbf{X} + \mathbf{E}) e^{i2\pi f t_{i-1}} df \right] / 2\Delta t \quad (4.35)$$

where Δt is the time between consecutive observations, which is also assumed constant. This simplifies to:

$$\hat{\mathbf{u}}_d(t_i) = \frac{i}{\Delta t} \int_{-\infty}^{\infty} (\mathbf{X} + \mathbf{E}) \sin(2\pi f \Delta t) e^{i2\pi f t_i} df \quad (4.36)$$

The velocity error is therefore:

$$\mathcal{E}_{\mathbf{u}} = \mathbf{u}_d(t_i) - \hat{\mathbf{u}}_d(t_i) \quad (4.37)$$

$$= \int_{-\infty}^{\infty} i2\pi f \left\{ \mathbf{X} \left[1 - \frac{\sin(2\pi f \Delta t)}{2\pi f \Delta t} \right] - \mathbf{E} \left[\frac{\sin(2\pi f \Delta t)}{2\pi f \Delta t} \right] \right\} e^{i2\pi f t_i} df \quad (4.38)$$

The first term involves the true position Fourier coefficients, \mathbf{X} , and could be termed the finite differencing error (FDE) while the second term is due to the positioning errors, \mathbf{E} . Substituting for \mathbf{Z} , Equation 4.37 can be rewritten as:

$$\mathcal{E}_{\mathbf{u}} = \int_{-\infty}^{\infty} i2\pi f \left[C_{(u)} \mathbf{Z} - \mathbf{E} \right] e^{i2\pi f t_i} df \quad (4.39)$$

$$C_{(u)} = 1 - \frac{\sin(2\pi f \Delta t)}{2\pi f \Delta t} = 1 - \text{sinc}(2\pi f \Delta t) \quad (4.40)$$

which relates the velocity error to the components of the measured position. The FDE coefficient $C_{(u)}$ increases as the frequency of interest approaches the sampling frequency. This effect was highlighted by Kirwan and Chang (1979) and it approaches a maximum where $f\Delta t = 0.5$ (the Nyquist frequency) and the error is the same magnitude as the true signal.

The true acceleration of a drifter, \mathbf{a}_d , and the finite difference approximation from the measured position, $\hat{\mathbf{a}}_d$ are:

$$\mathbf{a}_d(t) = \frac{d^2 \mathbf{x}}{dt^2} = -4\pi^2 f^2 \int_{-\infty}^{\infty} \mathbf{X} e^{i2\pi f t} df \quad (4.41)$$

$$\hat{\mathbf{a}}_d(t_i) = \frac{\hat{\mathbf{x}}(t_{i+1}) - 2\hat{\mathbf{x}}(t_i) + \hat{\mathbf{x}}(t_{i-1}))}{2\Delta t^2} \quad (4.42)$$

Following a similar argument as for the velocity, the acceleration error is:

$$\mathcal{E}_{\mathbf{a}} = \int_{-\infty}^{\infty} -(2\pi f)^2 [C_{(a)}\mathbf{Z} - \mathbf{E}] e^{i2\pi ft_i} df \quad (4.43)$$

$$C_{(a)} = 1 - \text{sinc}^2(2\pi f \Delta t) \quad (4.44)$$

As with the FDE coefficient for the velocity, $C_{(a)}$ increases with frequency

The signal to noise ratio for each frequency is obtained by dividing the spectral powers of the signal and the error. The triangle inequality gives an upper bound for the error:

$$\mathcal{R}_{u/a}(f) = \frac{|\mathbf{Z}(f)|^2}{|C_{(u/a)}(f)\mathbf{Z}(f) - \mathbf{E}(f)|^2} \leq \frac{|\mathbf{Z}(f)|^2}{(|C_{(u/a)}(f)\mathbf{Z}(f)| + |\mathbf{E}(f)|)^2} \quad (4.45)$$

where the appropriate FDE coefficients are used for velocity (u) or acceleration (a). Signal to noise ratios calculated for the spectra shown in Figure 4.10 are shown in Figure 4.11. The general trend is a decrease of ratio towards higher frequencies mainly due to the increase of the FDE coefficients and also explains the more rapid decrease of the acceleration ratios; this ultimately limits the frequency of motions which can be reliably resolved. At the lower frequency end the FDE coefficients are very small, and here the increase in ratios is due to an increase in the measured displacement signal power coupled with the roll-off in the stationary error power spectrum below about 0.02 Hz .

4.5 Field validation

Direct validation of the drifters in the surf zone is somewhat problematic. This is because, in the absence of any "true" Lagrangian velocity information, it requires comparison of wave-averaged Lagrangian drifter velocities with fixed Eulerian data. Therefore the two instruments are not actually measuring the same thing. This is particularly the case in the surf zone as the speed of typical surf zone currents means that the two instruments are quickly separated. In addition, it is somewhat arbitrary to compare with Eulerian depth-averaged velocities; this is simply the quantity that would be convenient to measure.

Eulerian data for the validation was from a *Nortek Aquadopp* Acoustic Doppler Current Profiler (ADCP) set to sample 0.1 m bins at 1 Hz . The data were averaged over the depth, including only bins below the instantaneous free surface. Both the depth-averaged ADCP data and the drifter data were then filtered using a Butterworth 5th order lowpass filter with a cutoff frequency of $f_L = 0.05 Hz$. Because of

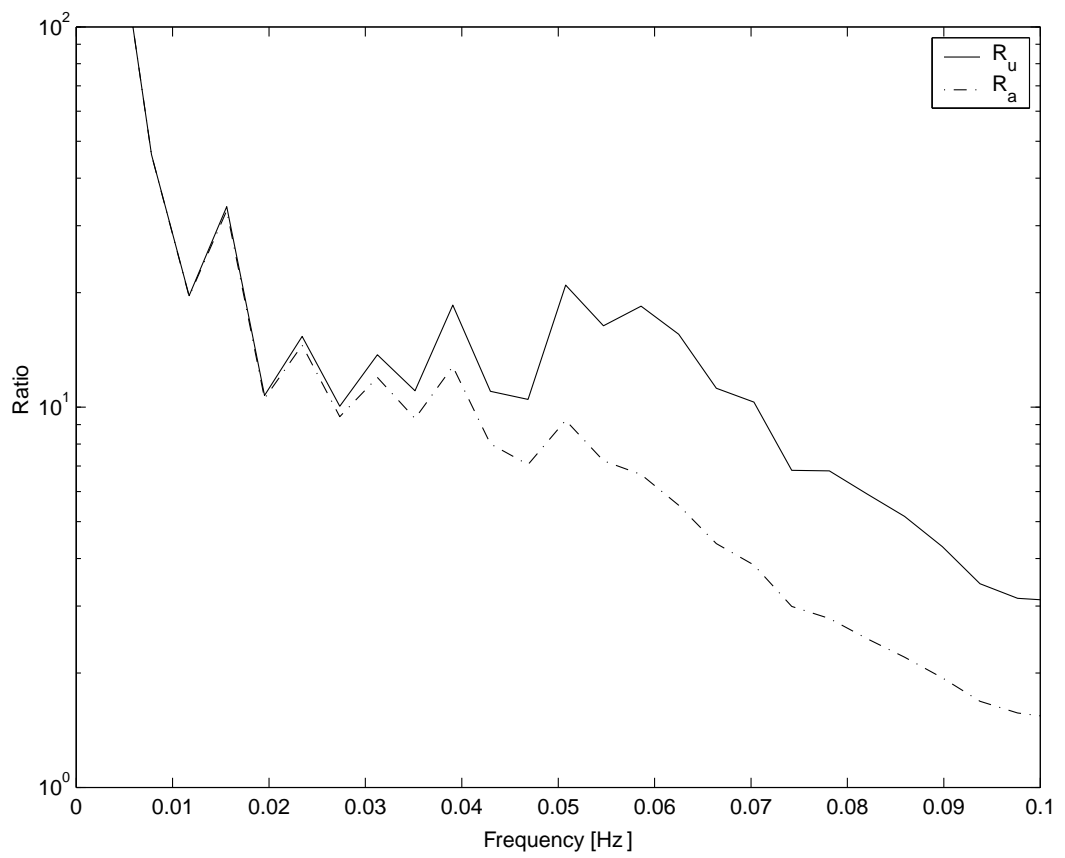


Figure 4.11: Signal to noise ratios calculated for measured surf zone data, assuming that stationary data approximates the positioning error.

Table 4.2: Summary statistics for comparison of filtered drifter and depth-averaged ADCP velocities. M , I and R^2 are the gradient, intercept and r-squared values from a linear regression of the drifter velocity against ADCP velocity, $V_{(drifter)} = M \cdot \bar{u}_{(ADCP)} + I$. The M_{fix} is a gradient for a linear regression with forced zero intercept. σ is the standard deviation of the difference between the measurements, $V_{(drifter)} - \bar{u}_{(ADCP)}$.

	M	$I[m s^{-1}]$	R^2	M_{fix}	$\sigma[m s^{-1}]$
Cross-shore	0.85	-0.02	0.59	0.91	0.16
Longshore	0.94	0.02	0.57	1.02	0.14

the rapid separation of the instruments, the drifter was repeatedly deployed in close proximity to the ADCP. The ADCP position was measured by leaving the drifter at the ADCP location for a few minutes; the ADCP and drifter velocities were then paired at the moment the drifter is closest to the ADCP if this was less than 5 m .

Two sources of data were used for the validation. First, a specific experiment in which a drifter was repeatedly deployed in the immediate vicinity of the ADCP. This experiment was carried out in relatively low energy swell dominated conditions with significant wave height, $H_{sig} \approx 0.6$ and peak spectral period $T_p = 14$ s . Secondly, data from experiments was collated where the drifters happen to pass by the ADCP. All data comes from experiments carried out on the metropolitan beaches in Perth, Western Australia. Conditions were a mixture of 1) swell dominated conditions (T_p typically 10-15 s) with light winds and minimal mean longshore currents and 2) local sea (T_p typically 5 s), driven by shore oblique seabreezes, which generates strong longshore currents. H_{sig} was between 0.2 m and 1.2 m .

All the validation data are shown in Figure 4.12. There is no obvious clustering of the different experiential conditions, suggesting that scatter is mostly due to errors inherent in comparing the two instruments. The apparent bias in one direction of the data is due in the cross-shore case to the tendency of cross-shore currents to consist of fast constrained offshore directed (negative) rip currents and slower diffuse onshore flow. In the longshore case, currents were predominantly in one direction at the experimental sites; the longshore component would be expected to be symmetric in any case. There is no obvious variation between one and two parachutes; the modelling suggests that there should be little difference for the conditions in which the data was collected. More data over a greater range of conditions would be required to properly check dependence on conditions and number of parachutes. As there is no obvious dependence on conditions, statistics are calculated for all the data together and these are shown in Table 4.5.

The best fit gradients suggest that the drifters slightly underestimate the depth-

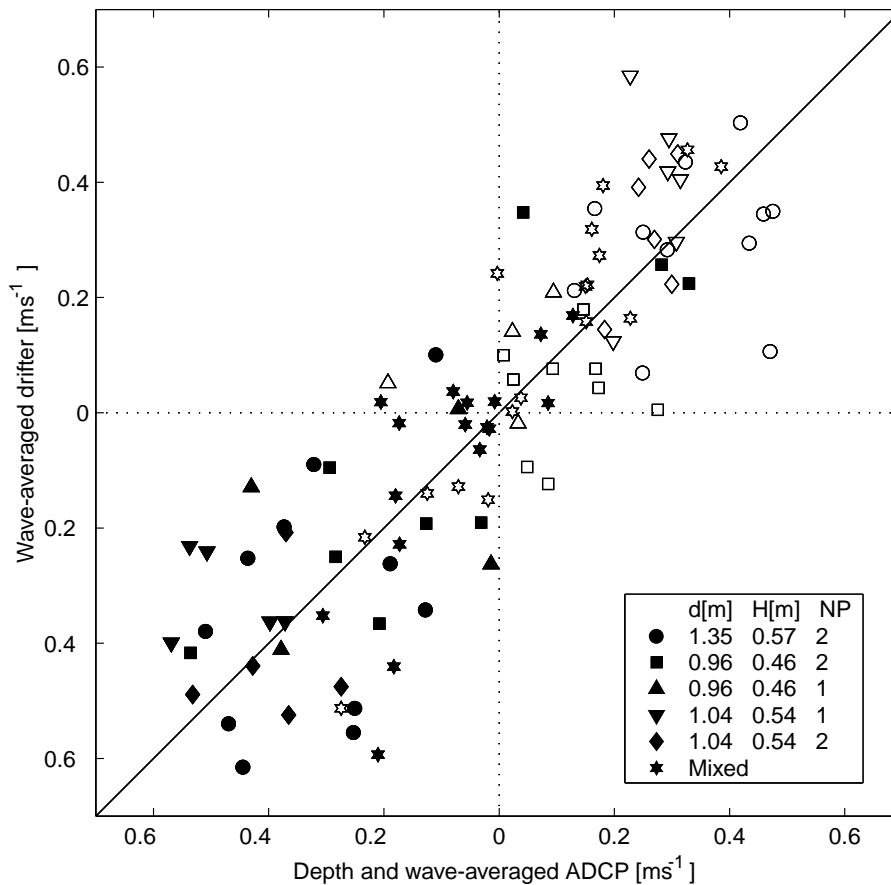


Figure 4.12: Drifter validation data. The solid symbols are cross-shore velocity components while empty symbols are longshore components. The depth (d), significant wave height (H), and number of parachutes are shown for each symbol for the validation experiment. The mixed values are from an ensemble of experimental data.

averaged velocity in both directions. Again this agrees well with the modelling results for the longer period waves. The low R^2 values and standard deviation reflect the scatter in the data. However, the best-fit agreement would seem to be remarkably good, especially in the cross-shore direction, where the influence of wave breaking might be expected to be unacceptably large.

For a similar validation procedure with their drifter, Schmidt et al. (2003) found very good agreement for longshore velocities (correlation coefficient 0.95 and RMS difference of 0.096 m s^{-1} inside surf zone). However, the cross-shore correlation was very poor; they attributed this to the fact that the drifter was measuring near surface velocities while the Eulerian instrument, near the bed, was measuring near bed velocities. This highlights the difficulties of comparing different types of surf zone measurements and the care required in assessing exactly what drifters are measuring. The type of drifter design, in terms of receiver and drogue arrangements, is also

clearly very important in determining response in the direction of wave propagation.

4.6 Summary and conclusions

Drifters specifically designed for use in the surf zone have been designed and validated. The receiver is a simple, low-cost design using non-differential GPS position fixing. A drogue consisting of a series of small parachutes prevents the drifter surfing in breaking waves. Simulations of drifter response in idealised surf zone waves predict that the drifter will perform well in low to medium energy surf zones. The quality of data obtained by the GPS drifters is good in terms of positioning accuracy and coverage. However, an analysis of positioning errors shows that only surf zone motions with frequencies of less than 0.05 Hz can be reliably resolved without differential correction. Despite the apparent difficulties of using drifters in the surf zone, the field validation was surprisingly successful, and while there is significant scatter in the data, the best fit for the combined data indicates that the drifter closely measures the depth and wave-averaged Eulerian current in low to moderate energy surf zones if drogued in an appropriate manner. While the units have not yet been used in high energy surf zones (H_s over 2 m), the type of high impact plunging waves experienced in the validation have tested resistance to surfing and sensitivity to submergence fairly vigorously.

Overall, drifters appear to have very significant potential as a valuable investigative tool for surf zone investigations. As surf zone drifters have to date received little attention, there is no doubt that design improvements could be made. In the context of the overall work described in this thesis, they have been used to make Lagrangian measurements of variable nearshore currents, which are presented in the next two chapters. The data is unique and provides information and insight which would be very hard to obtain with only Eulerian measurements.

Chapter 5

Field measurements of transient rip currents

5.1 Introduction

Rip currents are a generic name given to offshore directed flows which resemble plane jets with a strong constrained flow that broadens and forms a head region once it passes beyond the surf zone. The primary driving mechanisms for rip current circulation are believed to be longshore variations in the radiation stress gradient and setup. Detailed measurements of the forcing presented by Haller et al. (2002) show this to be the case as do model simulations which reproduce rip type circulations (Haas et al., 1999). Conservation of mass must also be satisfied, so that the offshore directed flow is balanced by an onshore flow which can be due to the wave induced flux (both from breaking and Stokes drift), or a diffuse onshore mean flow, or both.

Longshore variation of the radiation stress gradient is caused by differential wave transformation in the longshore direction. This may be due to:

1. Topographic variation (Bowen, 1969b).
2. Spatial variability of the incident wave field due to wave groups (Dalrymple, 1975).
3. Interaction of the incident wave field and the wave-averaged mean current (LeBlond and Tang, 1974; Dalrymple and Lozano, 1978; Murray and Reydelle, 2002).
4. Interaction of the incident wave field with lower frequency waves such as edge waves (Bowen, 1969b; Sasaki and Horikawa, 1978; Symonds and Ranasinghe, 2001).

The first mechanism leads to relatively fixed “topographic rips”. On sandy beaches, the positions where rip channels occur are likely to be determined by some or all of the hydrodynamic mechanisms and subsequently reinforced by feedback between the hydrodynamics and sediment transport as proposed by Hino (1975). There may be subsequent migration and morphological adjustment of these rip channels (Brander, 1999). Attempts to predict rip spacing (Hino, 1975; Short, 1985; Huntley and Short, 1992) have produced inconclusive results and suggest that where rip channels chose to form may be due to complex interactions. Topographic rip currents often have a continuous mean offshore flow which may “pulse” strongly (Cook, 1969; Bowman et al., 1988a,b; Aagaard et al., 1997).

Rip generation can, in theory, occur on a longshore uniform beach without topographic control. The radiation stress field is spatially and temporally variable due to one of the other three mechanisms above, leading to “transient rips” which occur in differing locations. Rip currents, which migrate in response to the variation of the incident wave field, are proposed as an alternative explanation for low frequency oscillations attributed to shear waves (Fowler and Dalrymple, 1991). While they have been generated in the laboratory (Fowler and Dalrymple, 1991), there is no conclusive proof that these transient type rip currents exist in the field and are completely unrelated to topography. Qualitative observation has been documented by Vos (1976) and Tang and Dalrymple (1989) measured migrating and pulsating rip currents, and noted the non-stationary nature of the nearshore circulation system. Murray et al. (2003) presented data of rip positions on a longshore uniform beach which do not show any preferred location. Another source of transient type rip currents has been observed in numerical model simulations of longshore currents, where shear wave instabilities are observed to produce jet-like currents which branch off the main flow and penetrate some distance offshore (Allen et al., 1996; Ozkan-Haller and Kirby, 1999).

Quantitative confirmation that transient rip position is entirely independent of topographic variation requires simultaneous measurement of topography and the flow field over a wide area, which is a formidable task. However, there seems to be sufficient indirect evidence for the existence of transient rip currents that can at least be said to not be “strongly” topographically controlled, and therefore distinct from rip currents which occur in well-defined rip channels. Transient rip currents are then, by definition, temporary features which develop in varying locations, have a specific lifetime and then decay.

Once initiated, a rip current develops into a distinct current system consisting of three main features (Figure 5.1):

1. A feeder region where the currents are directed towards the centre of the

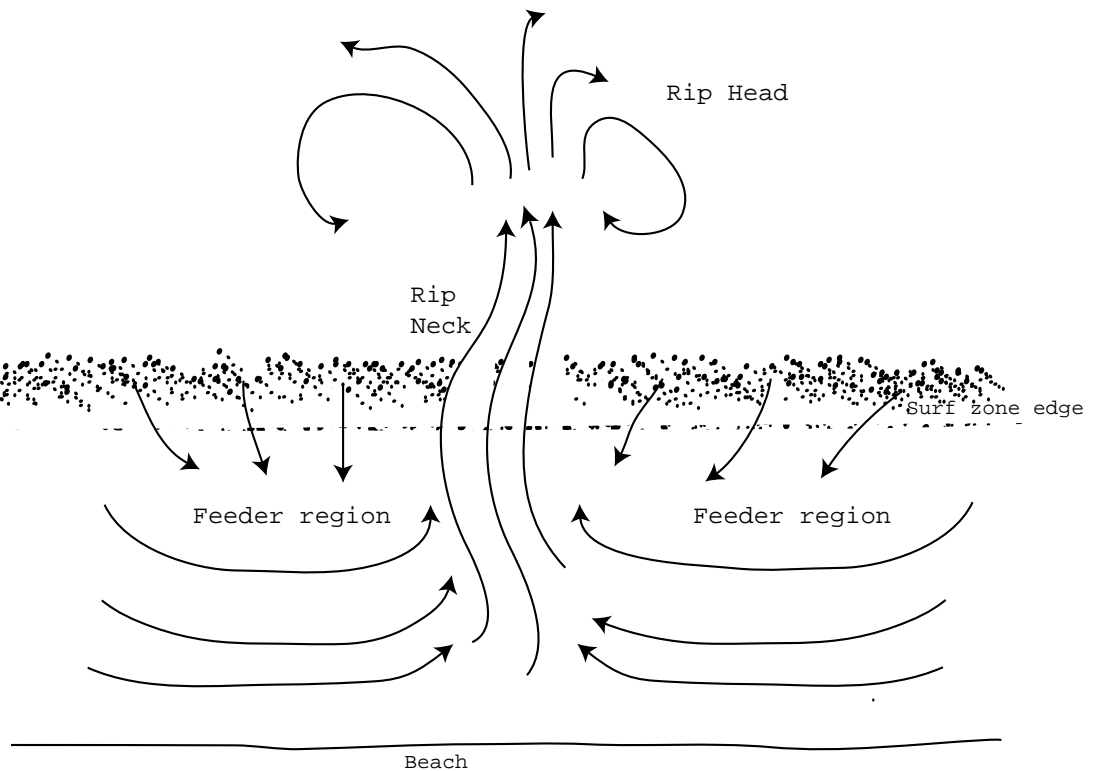


Figure 5.1: Schematic of the main features in rip current system.

rip and provide the volume flux for the offshore flow. Numerical modelling experiments suggest that in topographic rips, the extent of the feeder region is largely independent of rip spacing and that the rip is only supplied by a small local area (Svendsen et al., 2001); whether this is the case in transient rip currents is not known.

2. The rip neck which is the narrow offshore flowing section of the rip which usually has the highest current velocities and may extend a significant distance outside the surf zone. This may be directed perpendicular or obliquely to the shore, may have a meandering shape and may move around.
3. The rip head, which is the seaward end of the rip current, is often clearly visible as a sediment laden patch of water at the end of the narrower neck. This patch of water may persist as a coherent feature for some time after the rip flow has ceased. Distinct vortex features are often seen in this region.

While the exact arrangement in a rip system varies greatly, simple conservation of mass means that all rip currents must possess these three basic regions in some form.

Previous field work has examined the spatial structure and dynamics of rip current flow with arrays of current meters (Bowman et al., 1988a,b; Aagaard et al.,

1997), Lagrangian measurements with drifters (Shepard et al., 1941; Shepard and Inman, 1950; Sonu, 1972; Sasaki and Horikawa, 1975, 1978; Brander and Short, 2000; Schmidt et al., 2003), dye tracer (Sonu, 1972; Brander, 1999), video observations (Symonds et al., 1997) and side-scan sonar images (Smith and Largier, 1995). While the existing data have provided a good general understanding of the main characteristics of rip currents and typical current velocities, detailed dynamics of rip currents in the field remain poorly understood.

Rips and associated circulation cause spatial and temporal variation of the nearshore current field; however, their length scales across the rip neck are much smaller than the typical length scales of long waves at frequencies less than the incident wave field (hereafter collectively referred to as infragravity waves). Rip currents are associated with freely evolving vortical flow, which Peregrine (1998) pointed out is distinct from irrotational flows associated with infragravity waves. Vortical structures in the nearshore zone, while acknowledged to exist, have received little attention in the field mainly due to difficulties in observing them.

This chapter presents field investigations of small scale rip currents and the associated nearshore current structure on a medium energy swell dominated beach using Lagrangian and Eulerian techniques. The aim of the experiments were to improve the understanding of detailed dynamics of the offshore directed flows, believed to be transient type rip currents and concentrates on variability over short time (10 – 1000s) and space (10 – 100m) scales.

5.2 Field site and methodology

5.2.1 Field site

The field measurements were carried out on three days during (southern hemisphere) winter between 5th July and 20th September 2001, on Leighton beach, one of the metropolitan beaches of Perth, Western Australia. The site experiences diurnal microtidal tides with a mean spring tidal range of 0.6 *m*. Offshore reefs and islands significantly reduce the offshore swell height so that Leighton beach experiences low to moderate energy conditions with significant wave heights typically between 0.5 *m* and 1.2 *m* in winter. Weather conditions are dominated by the passage of fronts with onshore winds and locally generated seas separated by periods of predominantly offshore winds and a swell dominated wave climate. The beach undergoes rapid adjustment in response to the wave climate with erosion occurring during the passage of fronts followed by accretion during the swell dominated calm periods (Masselink and Pattiaratchi, 2002). The formation of a bar sometimes occurs at the field site in response to continued storm activity. However in 2001, storm conditions were

relatively mild and a fixed bar feature did not develop. The dates of the experiments were 5 July (*Experiment 1*), 13 September (*Experiment 2*) and 20 September (*Experiment 3*). Conditions for the experiments were chosen to be swell dominated. On the days of the measurements, the winds were offshore (from the NE) and hence there were no locally generated wind waves incident at the site.

5.2.2 Field methodology

Instrumentation consisted of a wave recorder, an upward looking Acoustic Doppler Current Profiler (ADCP) and four drifters with Global Positioning System (GPS) receivers. The positions of instrument deployments are shown in Figure 5.2. The aerial photograph is of the same area although not taken at the same time; note the rip current at the northern end of the beach. For *Experiment 1* only the drifters were used. The drifters themselves were described in Chapter 4.

The wave recorder was a *FSI Microtide* set to sample pressure at 4 Hz. This was deployed in around 2.5 m depth on a weighted disk on the seabed approximately 30 m seaward of the outer limit of wave breaking. The ADCP was a *Nortek Aquadopp Profiler* set to sample 0.1 m bins at 1 Hz. The instrument features a sensor head at a right angles to the main body so that the upper surface of the sensor can be positioned very close to the sea bed. The instrument was mounted flush on a cross shaped frame which, due to its low profile, is fixed and stable even when directly below breaking waves. The upper surface of the sensor was 0.05 m above the bed and with a blanking distance of 0.2 m this put the centre of the lowest bin at 0.3 m above the bed. The instrument was deployed just inside the breaker line.

Nearshore profiles were surveyed using a theodolite. The GPS receiver units were used to fix the instrument positions and survey the beach face by walking the bermline and the approximate MWL. A line of best fit was drawn along the MWL line and for subsequent analysis, the coordinate system rotated and translated to on/offshore and longshore axes with the longshore axis coincident with the best fit MWL line. The approximate position of the outer limit of the surf zone in each experiment was estimated visually relative to a fixed buoy (located with a GPS unit). The SE(*cross-shore*) and NE(*longshore*) directions are defined as positive x and y respectively, and x is measured from the MWL line. All position and velocity data is presented with respect to this rotated coordinate system.

Data from 14 deployments of three or four drifters was used in the analysis which follows. Each deployment was started in a rip neck (Figure 5.1) by releasing the drifters simultaneously at the same place once the rip current was observed to have been initiated. A deployment was terminated once all drifters were outside the surf zone and observed to be almost stationary or until one of the drifters beached

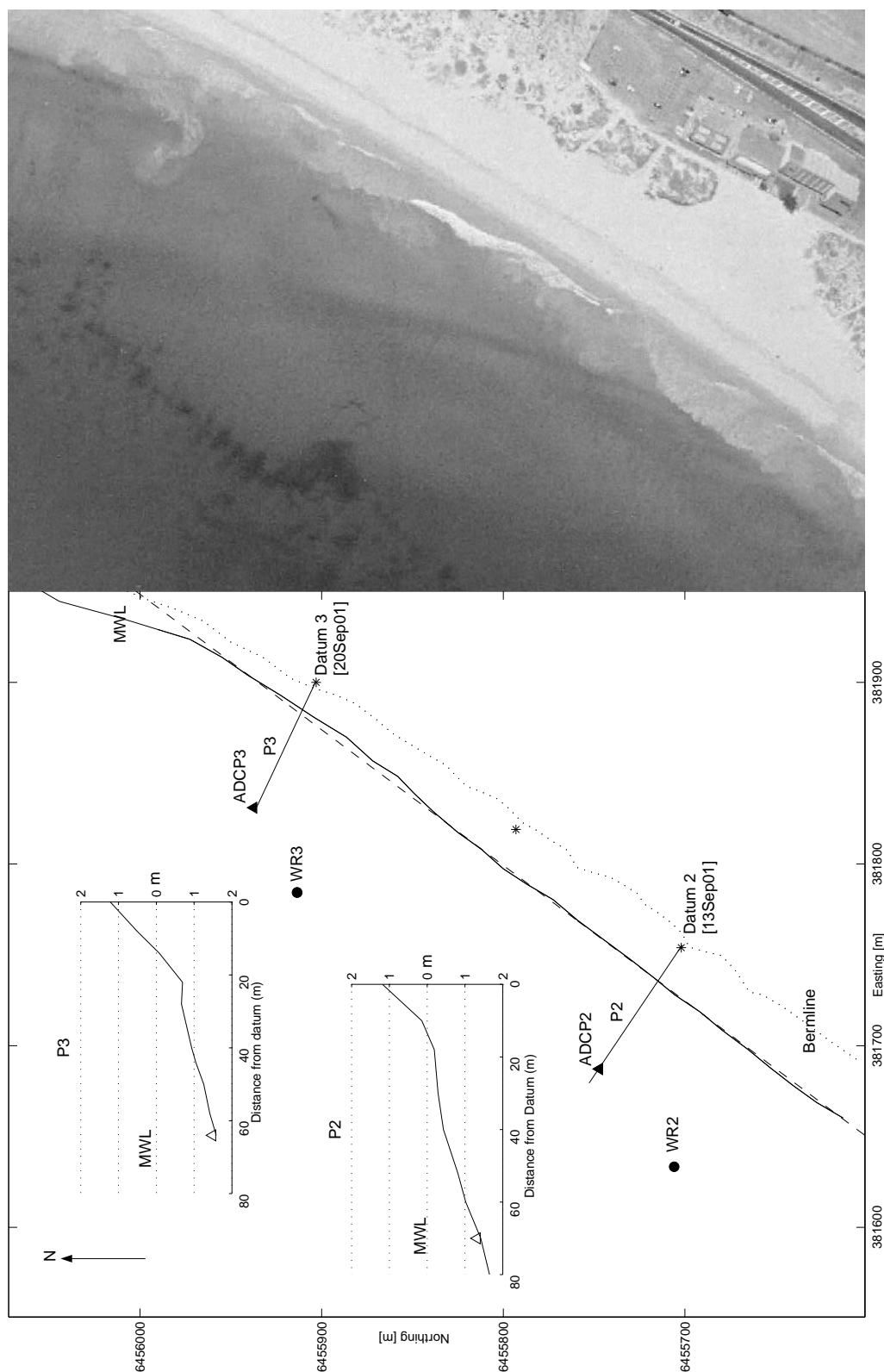


Figure 5.2: Plan of instrument deployment with aerial view of the field site. ADCP and WR(wave recorder) indicate positions of the instruments for the second and third experiments. Lines from the datum points show profile transect lines (P2 and P3). Mean water level(MWL) in plan view is mapped by walking with a GPS unit. MWL in beach profiles calculated from mean depth of water at the ADCP position. Dashed line is the best fit line of the shoreline used for the rotation of the coordinate axes for cross-shore and longshore orientation.

on the shore.

5.3 Eulerian measurements

5.3.1 Wave recorder

Spectra calculated for the periods spanning the drifter deployments on each day are shown in Figure 7.2. The spectra were calculated from a set of overlapping sections of 512 s (2048 datapoints) data segments which were linearly de-trended and tapered using a Hanning window with the final spectra an average of the set of Fourier transformations. Pressure data from the wave recorder were used for *Experiment 2* and *Experiment 3*. For *Experiment 1*, data from a wave rider 2 km to the north west of the field site was used. Corresponding to visual observations, the spectra indicate a narrow banded swell dominated sea on all three days. Significant wave heights were calculated as: $H_s = 4\sqrt{M_0}$ where M_0 is the zeroth spectral moment and were 1.02 m, 0.79 m and 1.03 m for the three experiments. While the calculated H_s is larger during *Experiment 1* than *Experiment 2*, this data was from an offshore source and included some locally generated waves; visual estimates of wave height were similar to *Experiment 2*.

The tidal influence during the measurement periods was very small. The mean water level measured by the wave recorder, defined here as the water level component passing a 0.0001 Hz filter, showed virtually no change for *Experiment 2* and a 10 cm variation for *Experiment 3* with high tide occurring at around 1330. While there is no direct tidal measurement for *Experiment 1*, the tidal predictions for Fremantle 2 km to the south indicate a tidal rise of only 0.18 m between 1121 (LW) and 1939 (HW) which spanned the period of the measurements. The aim was to collect data under very similar hydrodynamic conditions so that some generic conclusions about the hydrodynamic regime under narrow banded swell dominated conditions can be made.

5.3.2 ADCP

Three hour mean ADCP data spanning the period of deployments on each day are shown in Figure 5.4. The measured current in any bins above the instantaneous measured water level were set to zero. The mean water level was determined from the instrument pressure sensor data assuming hydrostatic pressure; this procedure will tend to slightly underestimate the water (or rather air-foam interface) level under the crest of breaking waves due to bubbles and a decreased pressure due to strong vertical accelerations. The mean current velocities are low but exhibit a classic undertow profile with onshore flow at the mean water level and offshore flow

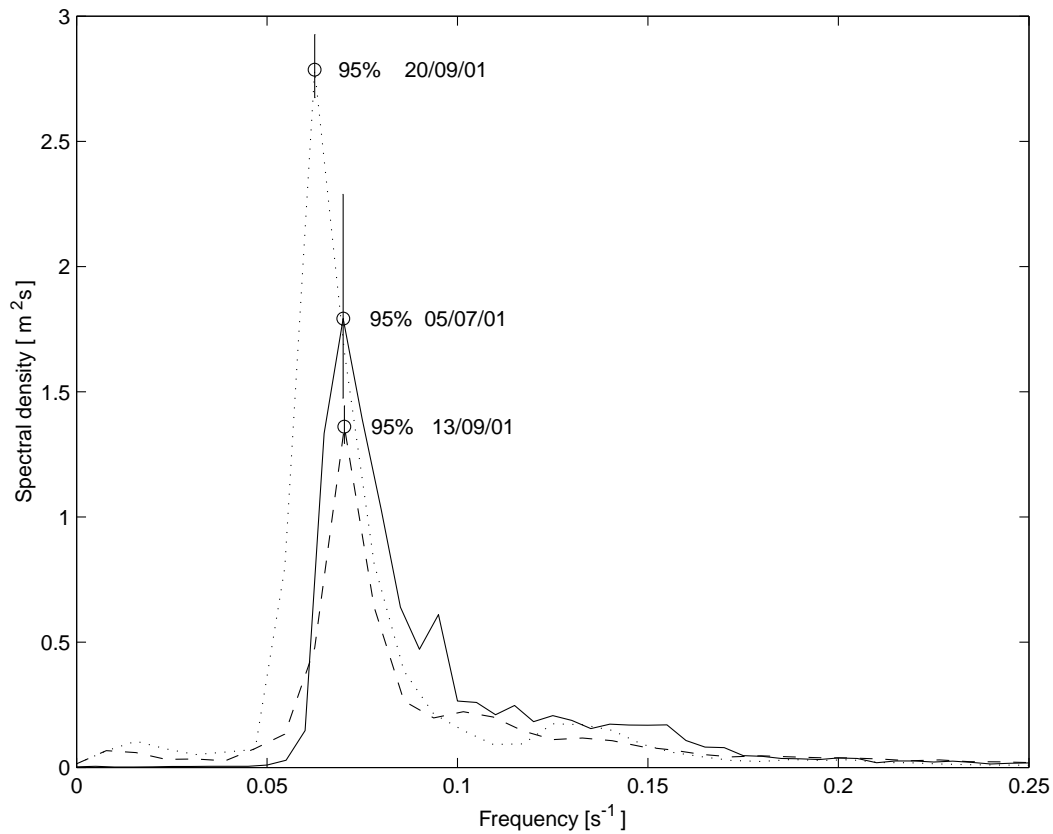


Figure 5.3: Spectra calculated from an offshore wave buoy data from *Experiment 1* (5 July, solid line) and the wave recorder data from *Experiment 2* (13 September, dashed line) and *Experiment 3* (20 September, dotted line).

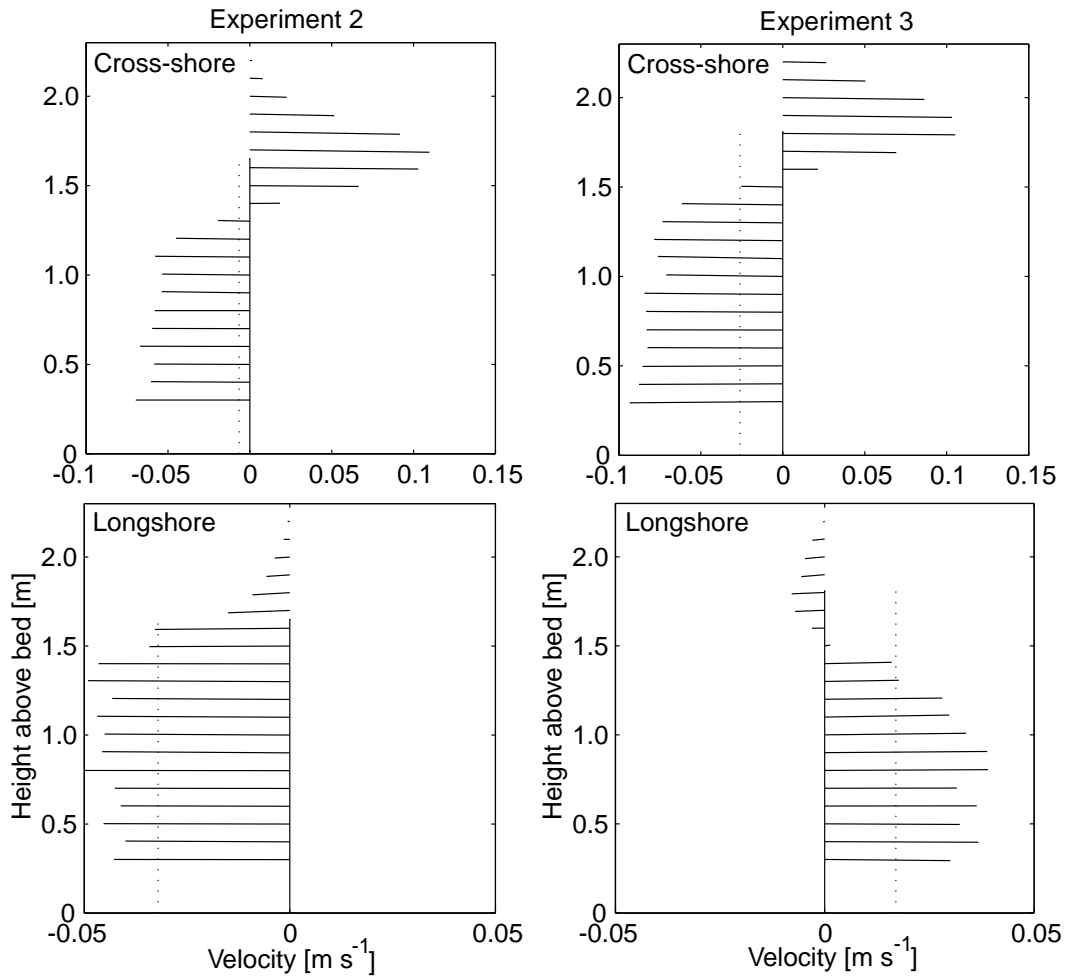


Figure 5.4: Three hour means of ADCP data of cross-shore and longshore velocity for *Experiment 2* and *Experiment 3*. The cross and longshore velocity components are shown for each depth bin. The height of the solid vertical line corresponds to the mean depth. The depth-averaged velocity is indicated with a dotted line.

in the lower part of the water column. Below the level of transition between onshore and offshore flow, there is little vertical variation with depth. The higher cross-shore current magnitudes for *Experiment 3* are due to the larger wave heights on this day. The longshore current is in different directions on the two days and shows greater vertical variation for *Experiment 3*. Depth-averaged flow velocities are small and directed offshore in both cases but in different longshore directions.

Figure 5.5 shows spectra, calculated as for the wave recorder with overlapping sections of 1024s (1024 datapoints), of the ADCP pressure and depth-averaged velocity for same three hour sections of *Experiment 2* and *Experiment 3* as used for the means shown in Figure 5.4. To characterise the low frequency flow climate during the experiments, ratios of kinetic and potential energy were estimated using the

method of Lippmann et al. (1999). The ratio is defined in terms of variances of velocities and surface elevation:

$$R = \frac{h (\langle u^2 \rangle + \langle v^2 \rangle)}{g \langle \eta^2 \rangle} \quad (5.1)$$

where u, v, η are depth-averaged velocities and pressure at the ADCP. Variances are calculated by integrating the spectra in Figure 5.5 in the range $f = 0.0025 - 0.05 Hz$. Values of R are 1.29 for *Experiment 2* and 1.57 for *Experiment 3*. A ratio of 1 would correspond to an equipartition of kinetic and potential energy consistent with gravity wave modes while for non-divergent motions $R \gg 1$. The estimated values indicate that there is a significant amount of energy, 22% and 36% respectively, not associated with free infragravity wave modes. As expected from the relative increase of the current variance at lower frequencies in the spectra, the ratios increase as the frequency band is shifted to $f = 0.0025 - 0.01 Hz$ where the ratios are 1.78(43%) and 2.86(65%). It is worth noting that estimates of non-infragravity energy due shear waves using Equation 5.1 were found to be biased high by Noyes et al. (2002) when compared to methods based on longshore current meter arrays. Nevertheless, the important implication of the ratios is that while the current variance is dominated by infragravity motion, there is a significant other mode of nearshore current variability present.

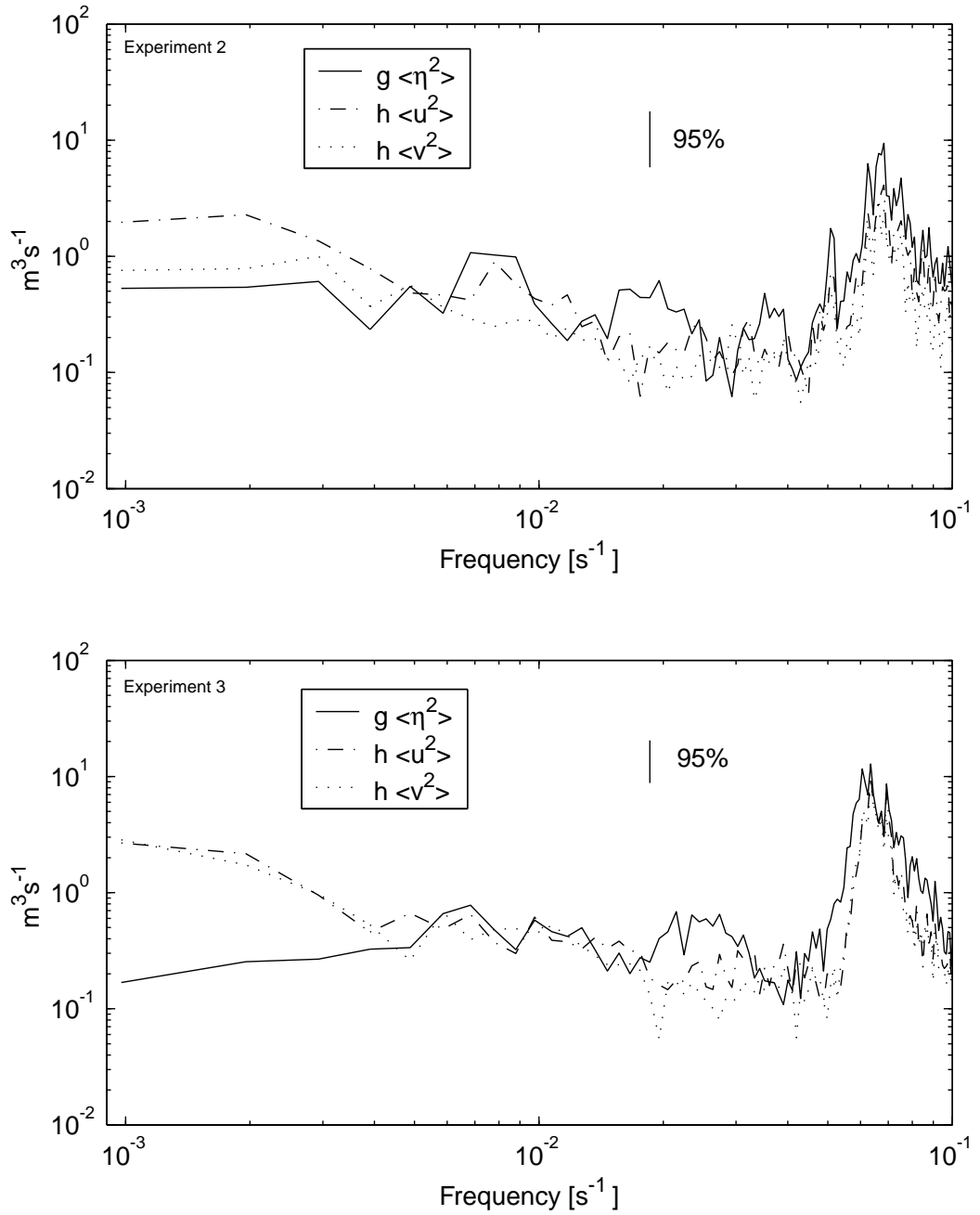


Figure 5.5: Spectra of pressure and depth-averaged velocity from three hours of ADCP measurements spanning the period of drifter deployments for *Experiment 2* (top) and *Experiment 3* (bottom). The spectral density of the current components and surface elevation has been multiplied by the mean depth, h , and gravitational acceleration, g , respectively so that they correspond to estimates of potential and kinetic energy contributions. Note that the spectra are not variance-preserving.

5.4 Descriptive analysis of the rip currents

Four of the rip events are discussed and analysed in more detail in what follows. The individual plots are all rotated to the on/offshore coordinate system. The four rip events were chosen because they represent the two main types of rip flow observed. In addition, in these deployments the drifters, which were deployed in a cluster, remained in the rip neck in each case; this is beneficial for quantitative analysis described in Section 5.5. The duration of the data presented for each event is 800 s except for *RE2a* which lasts for 1800 s. The first two rip events, *RE3a* and *RE3b* shown are from *Experiment 3* and both show “classic” rip currents flowing almost directly offshore. Visual observations were of very well defined rip currents occurring in different locations approximately every 5 minutes. The third and fourth rips, *RE2a* and *RE2b*, are from *Experiment 2* where the rip currents were less well defined, flowed obliquely to the shore and appeared for a longer duration. The reasons for the difference in rip flow between *Experiment 2* and *Experiment 3* are not clear. The records from the wave recorder for the periods of the four rip events are shown in Figure 5.6. The incident wave field has a smaller significant wave height and is less groupy in *Experiment 2* than *Experiment 3*. There may also be an associated difference in the directional characteristics of the wave field, but no data is available to investigate this.

During *Experiment 2*, the drifters also moved back onshore relatively quickly, so it was practical to leave them to complete a circuit of the rip current circulation and flow back out in a second rip which subsequently developed. In contrast, the rip currents in *Experiment 3* moved the drifters further and more directly offshore, from where they moved onshore very slowly; for practical reasons (to conduct more than one deployment per day) the drifters were recovered before they completed a circuit of the circulation system. The rip events during *Experiment 1* were very similar in nature to those in *Experiment 3* with narrow, well defined necks perpendicular to the shore. In *Experiment 1* all drifters tended to move longshore towards the south after moving offshore in the rips, indicating there was some continuous longshore current, but there is no current meter data from this day to corroborate this. Data from this day are not discussed in detail but are included in the analysis of relative dispersion and length scales.

5.4.1 Rip event 3a (Figure 5.7)

The trajectories show a well defined offshore flow which appears to spread and dissipate outside the surf zone. A “classic” rip current neck and head region can be seen. The trajectories show all the characteristics of a plane jet being ejected

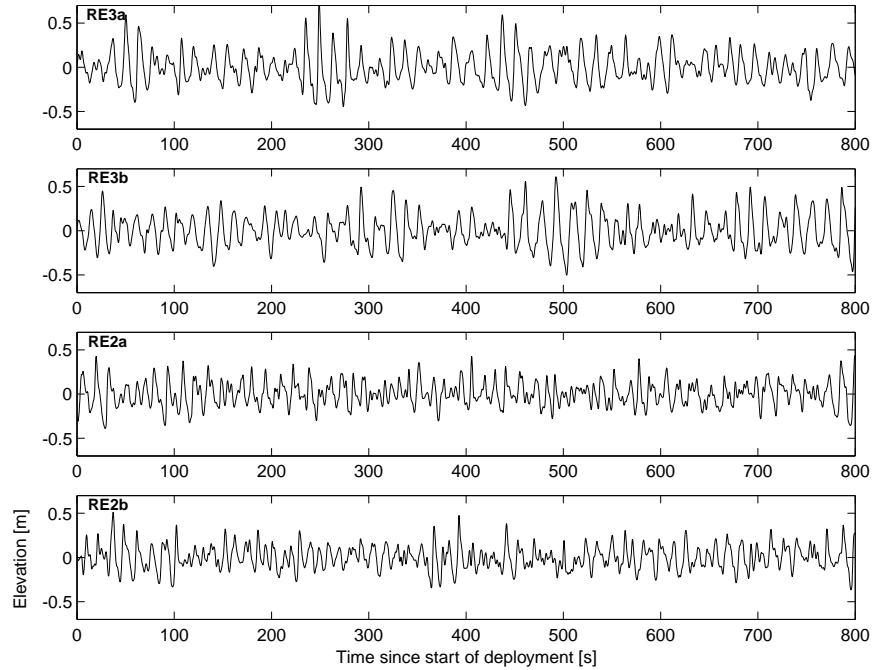


Figure 5.6: Wave records from the wave recorder for the duration spanning the rip events except for *RE2a* where only the first 800 *s* are shown.

from the surf zone. There is little longshore spreading in the neck section indicating a constrained jet-like flow, while in the head the drifters rapidly spread, consistent with the visually observed mushroom shape at the offshore limit. For the first 120 *s* (subplot *a.*) flow is strongly offshore with instantaneous velocities up to 1.1 m s^{-1} and an average speed of 0.5 m s^{-1} . There is significant variability within a very narrow section, with two of the drifters turning shorewards in a meander while the others are not affected. At 120 *s* (subplot *b.*) two of the drifters almost stop while the other two continue moving offshore, again showing significant variability over a very short distance. One drifter ends up outside the jet region and is left behind, indicating very little offshore flow outside of a tightly constrained region. Once 100 - 110 *m* offshore, the trajectories spread out with the outer two drifters turning back shoreward. Drifter velocities decelerate rapidly in the head region; at around 300 *s* (subplot *c.*), now some 100 *m* offshore, the drifters are almost stationary.

The spatial gradients of the velocities across the rip neck and the diverging region of the head are strong; the ADCP measurements (not shown), from 20 *m* alongshore show some mean offshore flow as the drifters pass, but less than half the average velocity of the drifters, indicating the region of strong offshore flow is tightly constrained.

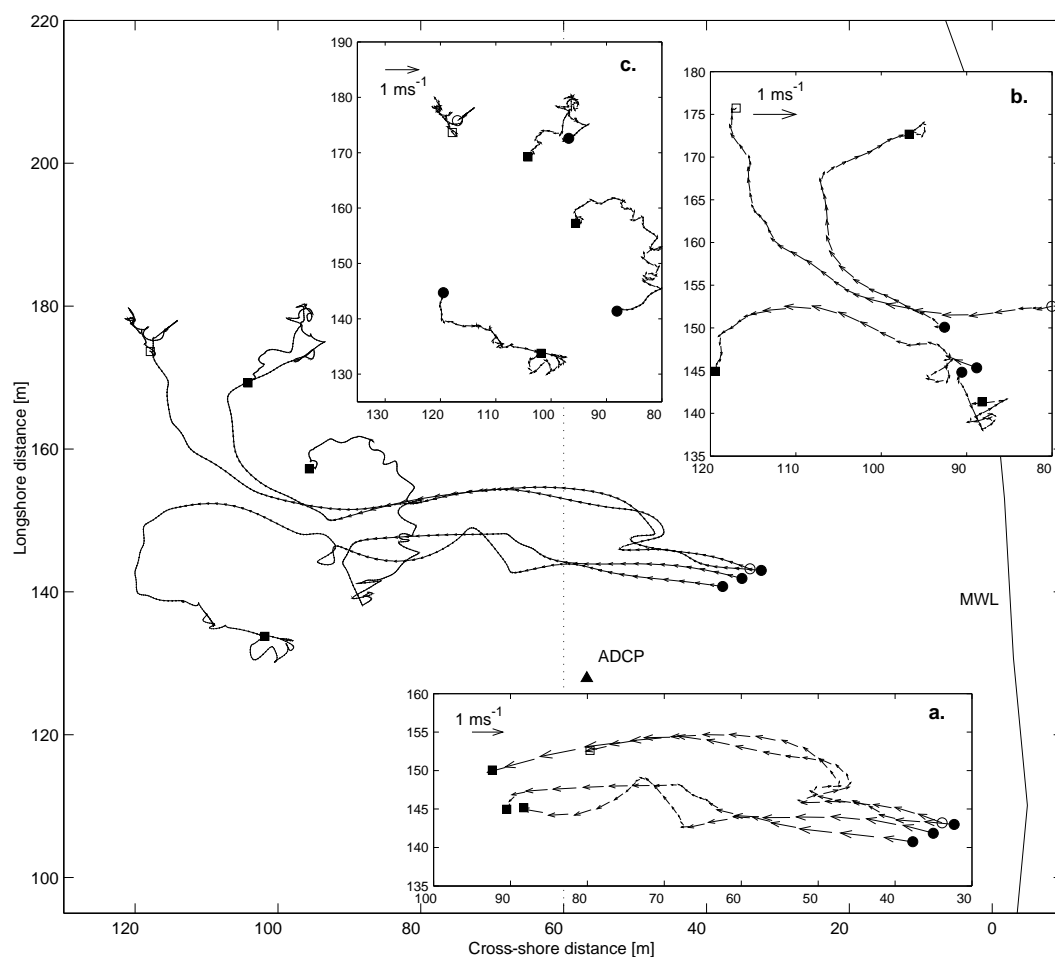


Figure 5.7: Velocity vectors for Rip Event 3a. The vector arrows are plotted at 5 second intervals. The main plot shows the tracks from the whole deployment, while the subplots show shorter sections (*a*. $T = 1 - 120 s$, *b*. $T = 121 - 300 s$, *c*. $T = 301 - 800 s$) Circles indicate the start of each segment, squares indicate the end. The approximate outer limit of the surf zone is indicated in the main plot with a dotted line, and the position of the ADCP with a filled triangle.

5.4.2 Rip event 3b (Figure 5.8)

The general features of this rip current are similar to *RE3a*. Again there is a well defined neck region and a head region. For 60 s after deployment (subplot *a.*) all drifters move offshore with peak speeds of 0.7 ms^{-1} and a mean speed of 0.5 ms^{-1} . After moving offshore initially, the trajectories of two drifters is interrupted by a surfing event and the trajectory of the third turns shorewards again. Between 110 and 200 s (subplot *b.*) all the drifters turn back towards shore at some point and one has a net motion shoreward over this period. It appears that the rip flow is retarded and then pulses a second time, carrying the drifters well outside the surf zone. The fact that two of the drifters are surfing indicates the presence of particularly large breaking waves which would provide a strong local forcing in the shoreward direction. From 200 to 300 s (subplot *c.*) all drifters move offshore in a well defined rip neck with mean speed of 0.4 ms^{-1} and peak speed up to 1.0 ms^{-1} . After 300 s the flow begins to spread and the outer two drifters turn back shorewards. As with *RE3a*, the trajectories diverge in the head region although the flow patterns are more complex.

One drifter describes almost two complete rotations in what appears to be a well defined vortex structure. An estimate of the rotation rate of the first loop is 0.01 s^{-1} while for the second it is 0.0025 s^{-1} indicating that the eddy is spinning down. Elliptical orbits of this type can be caused by mode 0 edge waves, which have circular horizontal particle orbits. However, the edge wave amplitudes required to generate the observed orbital excursions, about 0.3 m at the ADCP and 0.2 m at the wave recorder, are not present in the surface elevation records.

The ADCP measurements during the rip (Figure 5.9), from about 20 m along-shore, show almost no indication of the rip, supporting the visual observation of a narrow region of offshore flow. However, sustained offshore flow was recorded by the ADCP 480 - 660 s after the deployment of the drifters. This is most likely another rip occurring later at the ADCP position; an offshore flow of this magnitude and duration which was homogeneous longshore would completely drain the surf zone. There is little variation of the current strength below the flow reversal centred around mean water level and the shape of the undertow profile is apparently maintained and shifted towards negative (offshore) velocities. The rip seen in the ADCP data is initially shore perpendicular then swings to become oblique to the shore at the ADCP location.

5.4.3 Rip event 2a (Figure 5.10)

This rip event has a different kind of structure from from *RE3a* and *RE3b*. The offshore flow is oblique to the shore following a reversal at the initiation of the rip. All

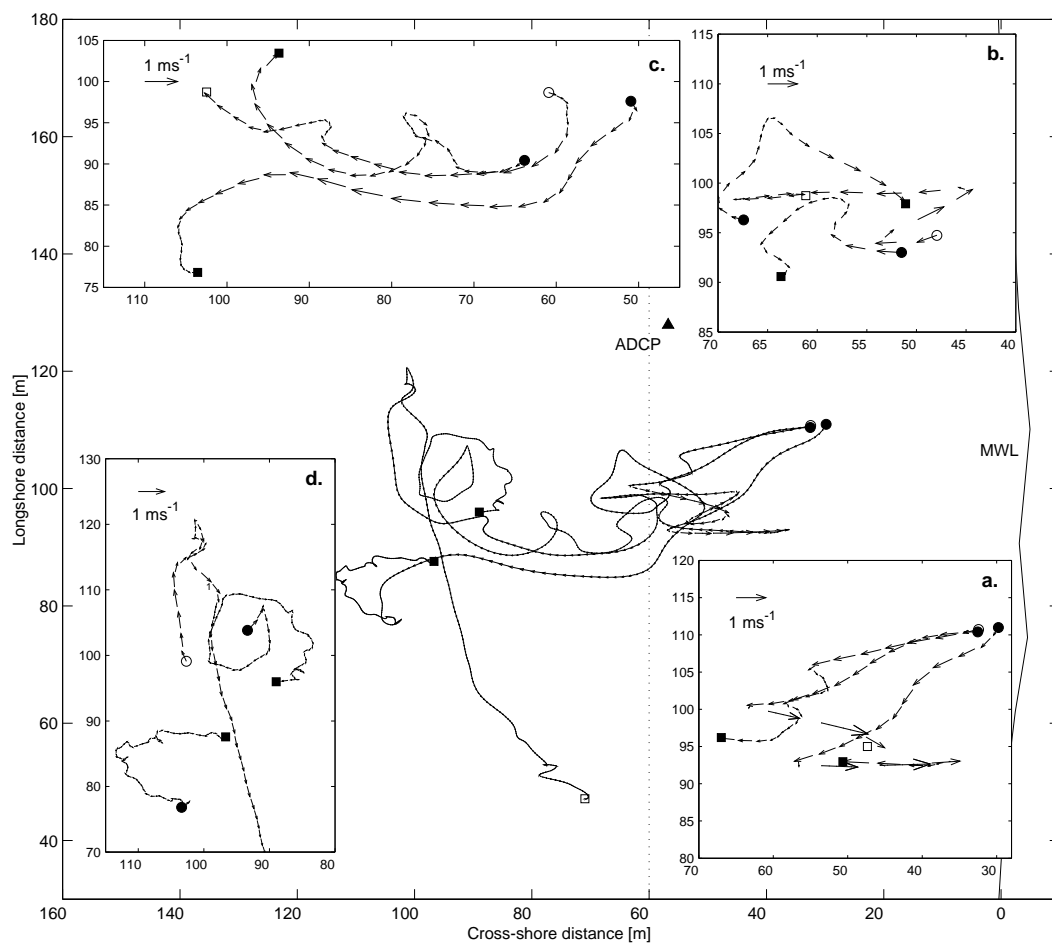


Figure 5.8: Velocity vectors for Rip Event 3b. The vector arrows are plotted at 5 s intervals. The main plot shows the tracks from the whole deployment, while the subplots show shorter sections (*a.* T = 1 - 110 s, *b.* T = 111 - 200 s, *c.* T = 201 - 360 s, *d.* T = 361 - 800 s). Circles indicate the start of each segment, squares indicate the end. The approximate outer limit of the surf zone is indicated in the main plot with a dotted line, and the position of the ADCP with a filled triangle.

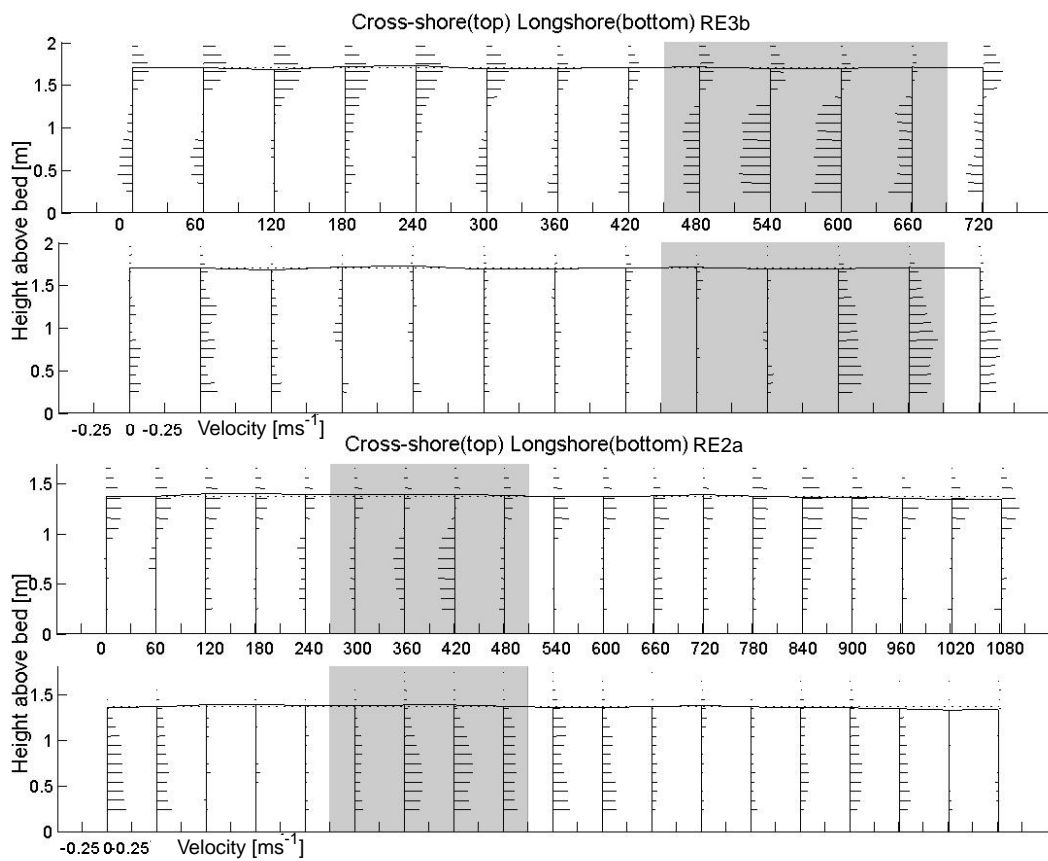


Figure 5.9: ADCP profiles during rip events 2 and 3. Velocities and water depth are averaged in 120 s blocks centred around the time indicated below each profile. The vertical bins have also been averaged with the adjacent bins in each case. The shaded areas in each case highlight periods of sustained offshore flow consistent with a rip current.

the drifters initially move directly offshore for about 50 s before turning shoreward again (subplot *a.*). Speeds in both directions peak at about 0.7 ms^{-1} . At about 100 s all drifters then move obliquely offshore northwards, with mean current speeds of 0.55 ms^{-1} and peak speeds of 0.9 ms^{-1} during the following 100 s. Once outside the surf zone the drifters turn shoreward and mean speeds slow to 0.2 ms^{-1} but they remain in a constrained cluster and do not spread here. The flow then appears to become unsteady and meanders increasingly with the trajectories becoming less coherent (subplot *b.*). Eventually the drifters split at around 600 s (subplot *c.*) with two describing large looping trajectories rotating in opposite directions. The trajectories appear to describe a rip current which undergoes a large meander while still a coherent jet before spreading in a head type feature; note the qualitative similarity with the rip shown in the photograph of the field site (Figure 5.2).

Two of the drifters subsequently move back well inside the surf zone. One of these does so in a surfing event while the other drifts back in a large loop with a mean speed of 0.1 ms^{-1} presumably due to the net onshore flow which must be present. Both then appear, at different times, to be caught in a second rip event which transports them back offshore again this time in an obliquely south longshore direction with speeds peaking at 0.7 ms^{-1} (subplot *d.*). These two drifters follow the type of trajectories expected in a complete rip current cell where a diffuse onshore flow in the feeder region supplies the rip necks. This general circulation appears to be present even though the rip currents themselves are apparently transient in time and space.

As the drifter passes near the ADCP about 360 s after deployment, offshore and longshore flow is seen in the ADCP data, presented in Figure 5.9. Significant offshore mean flow occurs for two 60 s averaging periods and northward longshore flow persists for longer. Prior to this there is little mean flow, indicating a transient phenomena. Note that the direction of the rip flow is also in the opposite direction to the long time mean flow shown in Figure 5.4. Again, here, ADCP data indicates little variation of horizontal velocity with depth.

5.4.4 Rip event 2b (Figure 5.11)

An oblique rip current is observed which shares several features with *RE2a*. Firstly there is the initial reversal of direction, in what appears to be an eddy structure (subplot *a.*) with mean speed of 0.3 ms^{-1} and a rotation rate of about 0.006 s^{-1} . As in Section 5.4.2 the edge wave required to generate an orbit of this kind is not seen in the elevation records. Following this, all drifters move obliquely offshore with mean speed of 0.4 ms^{-1} and peak speeds of 0.9 ms^{-1} , the flow again becoming increasingly unsteady with distance. However, unlike *RE2a*, there is no significant

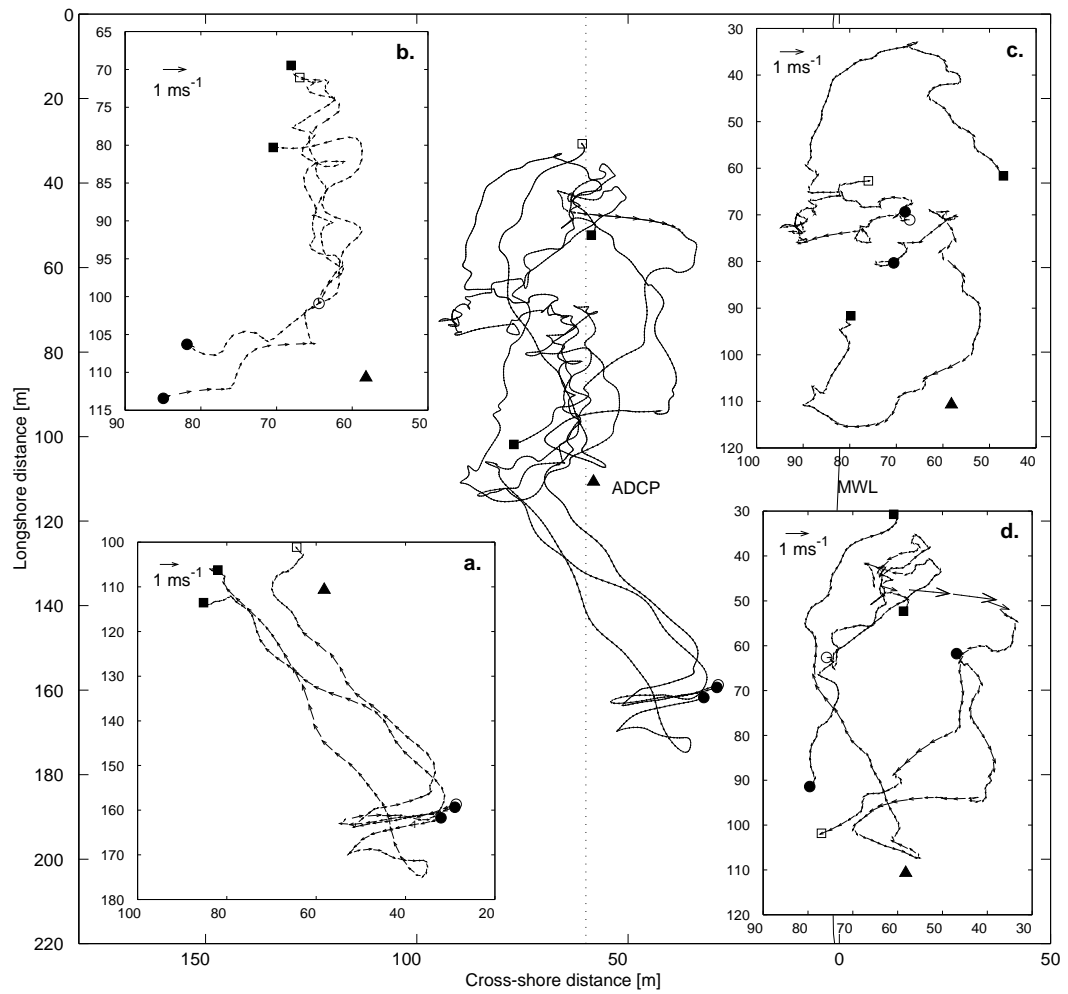


Figure 5.10: Velocity vectors for Rip Event 2a. The vector arrows are plotted at 5 second intervals. The main plot shows the tracks from the whole deployment, while the subplots show shorter sections (*a.* $T = 1 - 300$ s, *b.* $T = 301 - 600$ s, *c.* $T = 601 - 1200$ s, *d.* $T = 1201 - 1800$ s) Circles indicate the start of each segment, squares indicate the end. The approximate outer limit of the surf zone is indicated in the main plot with a dotted line, and the position of the ADCP with a filled triangle.

large scale meander in this case. Once outside the surf zone, the trajectories diverge and there is a reversal of direction with all drifters moving back inshore in the opposite alongshore direction from the initial rip. One of the drifters surfs inshore and subsequently moves offshore again, presumably into another rip current, this time oriented obliquely in the opposite longshore direction.

Note that although *RE2a* and *RE2b* are similar in their shape and may appear to be constrained by the same topography, this rip event occurs 60 *m* longshore from *RE2a*. This distance is the same scale as the width of the surf zone so it seems unlikely that this can be due to a topographic rip channel. The latter stages of *RE2a* (around 1200 *s*) show drifters in the same region as the initial section of this rip event but moving in the opposite longshore direction. In addition, while *RE2a* and *RE2b* are immediately either side of the ADCP position, the depth-averaged longshore velocity as measured by the ADCP is in fact towards the south, in the opposite direction to the two rip events. If *RE2a* and *RE2b* were manifestations of the same topographic rip, this should be seen in the long time average current measured by the ADCP.

5.5 Analysis of drifter clusters

The position of the centroids and the area spanned by simultaneous drifter positions or “clusters” are shown in Figure 5.12. The position of the cluster centroid, x_o, y_o is given by:

$$x_o(t) = \frac{1}{n} \sum_{i=1}^n x_i(t) \quad y_o(t) = \frac{1}{n} \sum_{i=1}^n y_i(t) \quad (5.2)$$

where x_i, y_i is the position of one of n individual drifters. The velocity of the cluster is the rate of change of x_o, y_o calculated by centred differences and is equivalent to the mean of the individual drifter velocities. The velocities of the cluster centroids are shown in Figure 5.13. In each case, the approximate time when the cluster centroid crossed the edge of the surf zone, and the time at which the rip neck ended, are shown. In addition, periods where one of the drifters is caught in a surfing event is indicated by a shaded region. While the net movement is offshore, there are significant fluctuations and changes in the on/offshore direction. In general, as would be expected, velocities are higher inside the surf zone and in the rip neck. Means, minimums (maximum offshore directed), maximums, and standard deviation of the velocity records from the rip neck section are shown in Table 5.5.

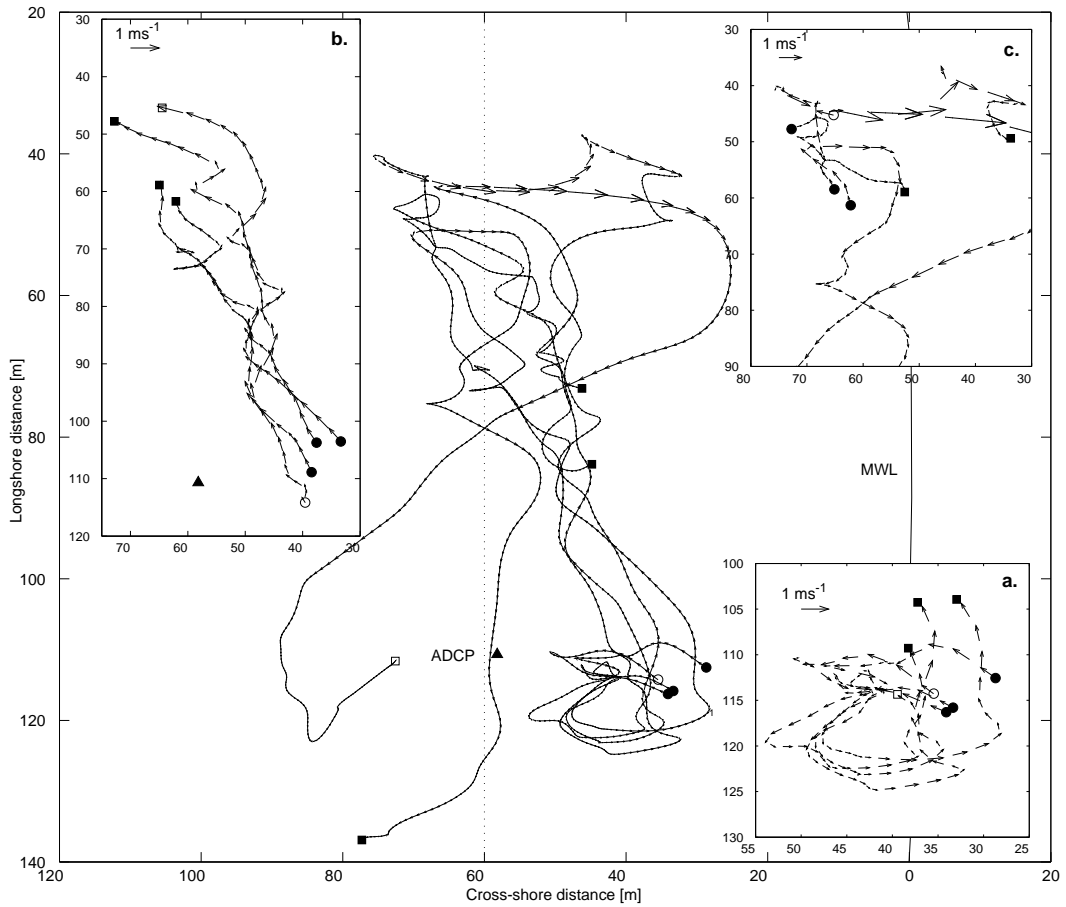


Figure 5.11: Velocity vectors for Rip Event 2b. The vector arrows are plotted at 5 second intervals. The main plot shows the tracks from the whole deployment, while the subplots show shorter sections (*a.* $T = 1 - 200s$, *b.* $T = 201 - 400s$, *c.* $T = 401 - 600s$). Circles indicate the start of each segment, squares indicate the end. The approximate outer limit of the surf zone is indicated in the main plot with a dotted line, and the position of the ADCP with a filled triangle.

Table 5.1: Summary statistics of the cluster velocities in the rip neck for *RE3a-4*. For the cross-shore component, \bar{U} is the mean over the duration of the rip neck, U_{min} and U_{max} are minimum and maximum values and σ_U is the standard deviation. Corresponding values are shown for the longshore component, V .

[ms^{-1}]	Cross-shore				Longshore			
	\bar{U}	U_{min}	U_{max}	σ_U	\bar{V}	V_{min}	V_{max}	σ_V
RE3a	-0.33	-0.90	0.12	0.27	0.06	-0.15	0.22	0.10
RE3b	-0.20	-0.59	0.46	0.26	-0.06	-0.30	0.31	0.13
RE2a	-0.06	-0.62	0.50	0.23	0.13	-0.22	0.52	0.16
RE2b	-0.07	-0.56	0.58	0.24	0.09	-0.30	0.51	0.22

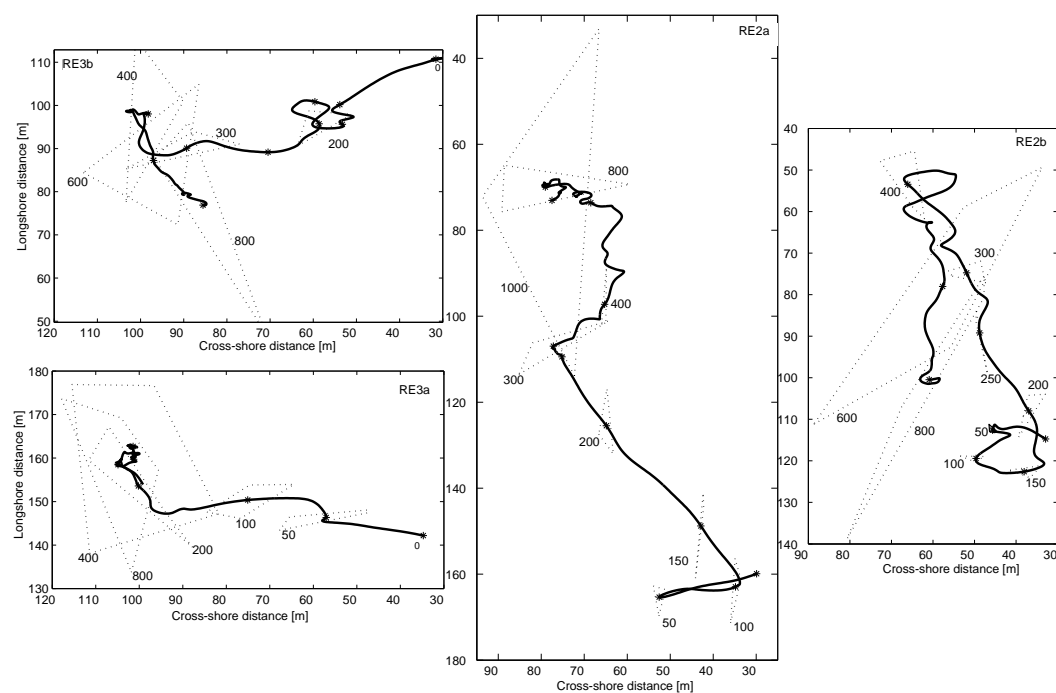


Figure 5.12: Trajectory of the cluster centroids and area spanned by the cluster for the four rip events. The polygons vertices are formed by the individual drifters. The number by each cluster polygon is the time in seconds since the start of the deployment.

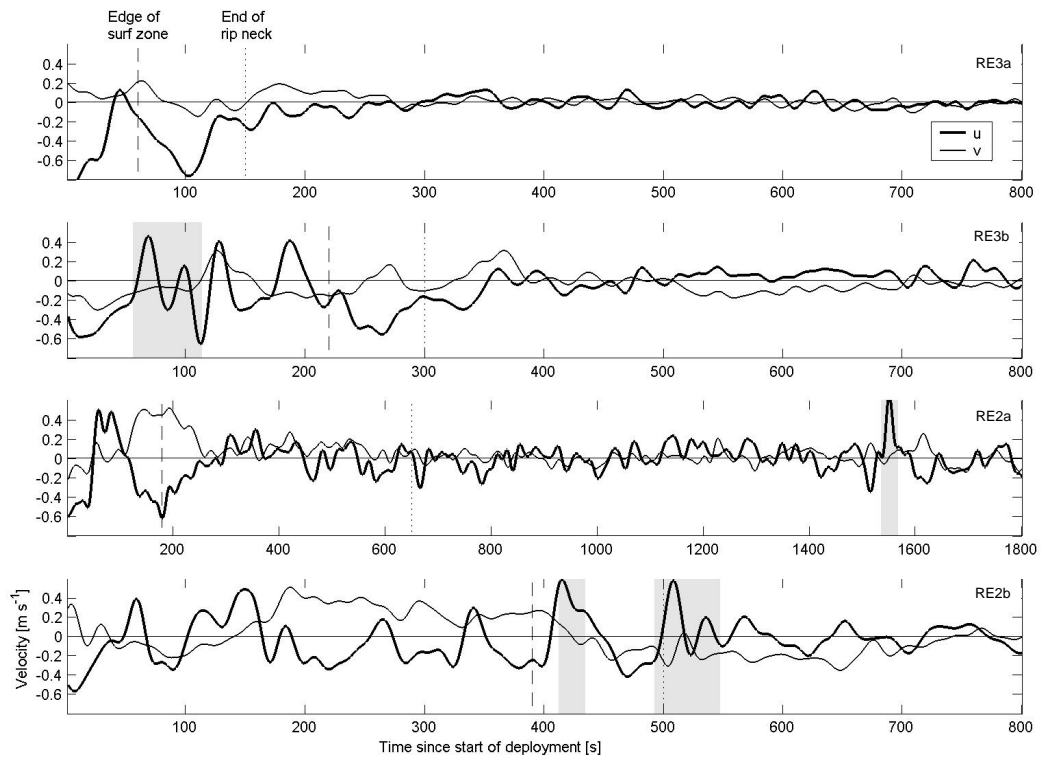


Figure 5.13: Velocity of the cluster centroid for the four rip events. The shaded regions mark periods in the data affected by the surfing of one or more of the drifters. Note that the timeseries RE2a is longer than the others.

5.5.1 Dynamics of the clusters in the rip neck

The acceleration of a fluid column (or to be more precise, a volume spanning the water depth which moves at the depth-averaged velocity) is governed by:

$$\frac{D\bar{\mathbf{U}}}{Dt} = -g\nabla\bar{\eta} + \bar{\mathbf{S}} + \bar{\mathbf{L}} + \bar{\mathbf{B}} \quad (5.3)$$

where $\bar{\mathbf{U}}$ is the current as defined in Equation 3.2. The term \mathbf{S} is the forcing due to wave motions with frequencies greater than 0.05 Hz; this is not the same as the classic radiation stress, because of the random nature of the wave field. \mathbf{L} contains all of the lateral momentum mixing (including shear dispersion mechanism, Svendsen and Putrevu (1994)) and \mathbf{B} is the bottom shear stress. Surface stresses due to wind have been neglected. This is essentially a shallow water equation with terms for the forcing and mixing due to the incident waves.

Assuming that the drifters move with a velocity close to $\bar{\mathbf{U}}$ as expressed in Equation 3.2, the mean forcing acting across the cluster equals the acceleration of the centroid. By considering clusters, the forcing is occurring over the same length scale as the cluster; smaller scale relative accelerations between individual drifters in a cluster are not considered. While it is impossible to directly determine the relative contribution of each term, the total forcing can be directly estimated as the Lagrangian acceleration is a total derivative of velocity. Haller et al. (2002) show that the nonlinear terms in an Eulerian frame are of comparable magnitude to the radiation stress gradient and setup gradient in a laboratory rip channel. Obtaining the spatial gradients of Eulerian velocity required to evaluate the nonlinear terms is difficult in the field as a high sensor density is required.

The accelerations of the clusters were calculated from the second order centred differences of the centroid position and is shown for the neck region of the four rip events in Figure 5.14. Both cross-shore and longshore components of acceleration continually change direction indicating oscillatory forcing. This is presumably caused both by variable wave forcing, which leads to an imbalance between the short wave forcing and setup gradient and by surface elevation gradients associated with free infragravity waves. The wave field shows significant groupiness (Figure 5.6) during the rip events, especially in *RE3a* and *RE3b*. The rip current records are unfortunately too short to demonstrate dependence of the acceleration on the short wave envelope with any statistical certainty. Another source of the fluctuations observed in the rip flows may be self-instability. Haller and Dalrymple (2001) have investigated this phenomena for laboratory generated topographic rip currents and find that it explains much of the variability of the rip current velocities. The meandering in the latter section of the rip neck in *RE2a* (Figure 10b.) and *RE2b*

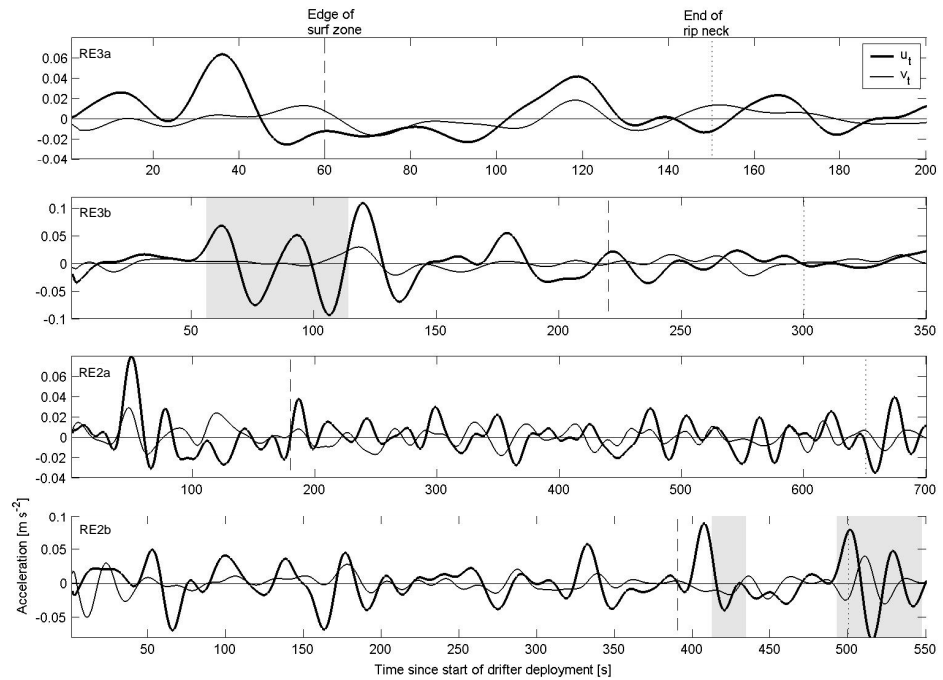


Figure 5.14: Acceleration of the cluster centroid in the neck region for the four rip events. The shaded regions mark periods in the data affected by the surfing of one or more of the drifters. Note that the timeseries RE2a is longer than the others.

(Figure 11b.) suggests an instability mechanism. Means, minimums, maximums and standard deviation of the cluster accelerations in the rip neck region are summarised in Table 5.2.

A conceptual model for the transient rip currents is of a slow evolution (over the order of 100's of seconds) of a forced jet-like flow which is then modulated by higher frequency wave group forcing, infragravity waves and self-instability of the flow. Substantial momentum is input at the start of the rip neck, and this must be sufficient to generate a rip, as temporally variable forcing appears to occur continuously, but transient rip development occurs sporadically at variable locations. As the drifters traverse the rip neck, there appears to be subsequent accelerations of the rip flow as seaward motion is retarded and then resumed. How much of the stop-start behaviour is caused by large modulations due to infragravity waves, and how much by changes in the underlying rip flow, is impossible to ascertain from the data. Similarly, it is not clear what is responsible for the longshore accelerations which cause changes of direction seen in *RE2a* and *RE2b*. The eventual deceleration of the neck section of the rip currents outside the surf zone must be partially caused by bottom friction and lateral mixing.

Table 5.2: Summary statistics of the cluster accelerations in the rip neck for *RE3a-4*. For the cross-shore component, \overline{U}_t is the mean over the duration of the rip neck, $U_{t_{min}}$ and $U_{t_{max}}$ are minimum and maximum values and σ_{U_t} is the standard deviation. Corresponding values are shown for the longshore component, V_t .

$[ms^{-2}]$ $\times 10^{-2}$	Cross-shore				Longshore			
	\overline{U}_t	$U_{t_{min}}$	$U_{t_{max}}$	σ_{U_t}	\overline{V}_t	$V_{t_{min}}$	$V_{t_{max}}$	σ_{V_t}
RE3a	0.41	-2.56	6.35	2.01	-0.05	-1.69	1.82	0.81
RE3b	0.10	-14.9	10.9	3.15	0.10	-2.26	7.62	1.06
RE2a	0.09	-3.54	7.98	1.69	0.03	-1.82	2.90	0.86
RE2b	0.08	-8.36	27.1	3.16	-0.09	-16.1	4.04	1.58

5.5.2 Cluster dispersion

Following List et al. (1990), the variance of the drifter positions with respect to the cluster centroid is:

$$\sigma_x^2(t) = \frac{\sum_{i=1}^n [x_i(t) - x_o(t)]^2}{n-1} \quad \sigma_y^2(t) = \frac{\sum_{i=1}^n [y_i(t) - y_o(t)]^2}{n-1} \quad (5.4)$$

where n is the number of drifters. The total dispersion of the drifter clusters can then be expressed as:

$$\sigma^2(t) = \frac{\sigma_x^2(t) + \sigma_y^2(t)}{2} \quad (5.5)$$

The calculated values of σ , σ_x and σ_y are shown in Figure 5.15. A relative dispersion coefficient can be defined by:

$$K(t) = \frac{1}{2} \frac{\partial \sigma^2(t)}{\partial t} \quad (5.6)$$

which can be approximated directly from the values of σ^2 . Directionally dependent values, K_x and K_y can be calculated from σ_x and σ_y respectively.

The clusters in each case show little or no spreading of the cluster within the rip neck region followed a period of expansion in the head region. It is useful to estimate the dispersion in the head region. To obtain an approximate values for these numbers the gradients of the best fit lines to the dispersion values during the head expansion are used. The period of head expansion is defined as being from the end of the rip neck to the first main peak of the total dispersion. These lines and the respective values of K, K_x, K_y are shown in Figure 5.15. Although somewhat *ad hoc*, this gives an estimation of the dispersion in the rip head region, and is a bulk estimate calculated in a similar manner to the surf zone dispersion experiments with dye by Inman et al. (1971). In each case the longshore component of the dispersion coefficient is larger than the cross-shore during expansion of the

rip head. The total dispersion values, K , are between 1.29 and $3.88 \text{ m}^2\text{s}^{-1}$. These values are similar to those found by Inman et al. (1971) for *inside* the surf zone over similar length scales. Prior to, and following the rip head expansion, dispersion rates are much lower. The presence of the rip head therefore appears, unsurprisingly, to dramatically enhance mixing outside the surf zone. By contrast, the neck region appears to locally suppress horizontal dispersion when compared to the values of Inman et al. (1971). Note, however, that low dispersion rates are implicit in the selection of the four rip events as deployments where the cluster remains together in the rip neck.

The dispersion coefficient is sometimes negative which is partly due to the fact that the data is only a single realisation rather than an ensemble average (List et al., 1990). In addition, List et al. (1990) also point out that as a cluster moves into deeper water, continuity means that the surface area of a fluid column has to contract. It is also worth pointing out here that the drifters will not measure shear dispersion in the same way as a dye would. This is because they are a connected body spanning the water column and cannot be sheared and mixed vertically like a dye. Much of what Inman et al. (1971) were measuring in the cross-shore direction is probably due to such a shear dispersion mechanism, so the results may not be comparable. Note, however, that the momentum mixing mechanism described by Svendsen and Putrevu (1994) *does* affect the drifter trajectories as the shape of the current field, which determines the drifter trajectories, is affected by this mixing.

Values of σ_x, σ_y and the associated K_x, K_y are calculated for the clusters in 14 deployments, including the four considered in detail. There are a total of 13,067 data points, which after filtering corresponds to 653 separate samples. The dispersion values are averaged in 1 m bins of σ_x and σ_y . The dependence of K_x, K_y on σ_x, σ_y for inside and outside the surf zone are plotted in Figure 5.16 and least squares lines of best fit are calculated for each case. For both inside and outside the surf zone, the longshore dispersion shows a clear power law relationship with the longshore spread of the cluster. There is considerably more scatter in the cross-shore dispersion values and a number of negative values which are not shown in the log plots, however there still appears to be some dependence on the length scale of the cluster. The apparently counter intuitive lower dispersion of the cross-shore component is at least partially explained by the drifters inability to measure shear dispersion. The dispersion is apparently of similar magnitude inside and outside the surf zone when averaged over the whole data set. This is contrary to the relative rip neck/head dispersion seen in *RE3a-3b*, but is due to the fact that the cluster did not remain together in the rip neck in some of the other rip events, and in these cases experiences rapid spreading.

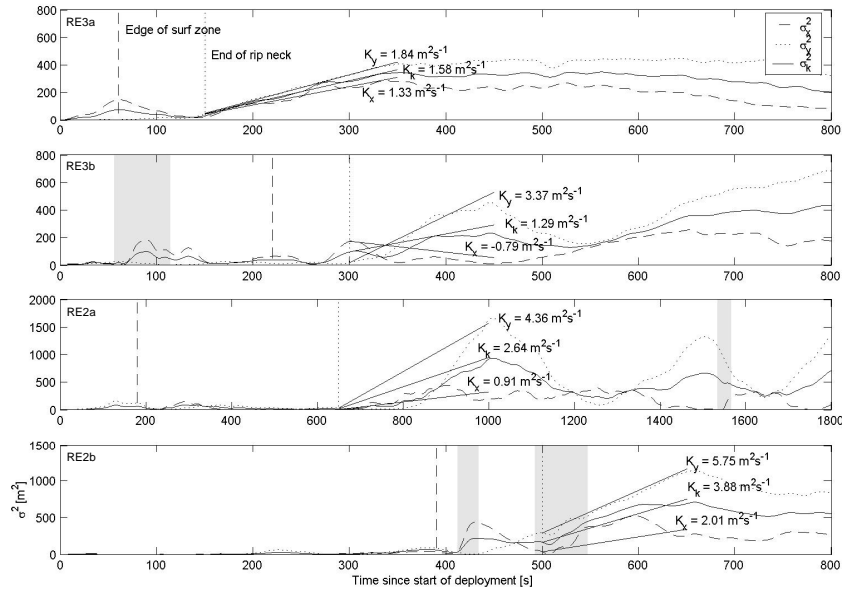


Figure 5.15: Dispersion of the clusters for the four rip events. The time at which the cluster centroid crosses the approximate location of both the outer edge of the surf zone and the end of the rip neck are shown. Periods where one of the drifters was caught in a surfing event is indicated by the grey shading.

A $4/3$ power law relationship for the dispersion, $K = \alpha r^{4/3}$, was first predicted by Richardson (1926) (and further explained later by Batchelor (1952)) for a pair of particles separated by r in a homogeneous, stationary turbulent flow if sufficient time has elapsed that their positions are independent of their initial separation. However, given that the data here is neither stationary nor homogeneous, is close to a boundary, and that the entire flow field was not sampled uniformly, it is surprising that the dispersion of the clusters should show a power law relationship with an exponent close to $4/3$. However, Okubo (1974) discusses the fact that other theories of turbulent dispersion lead to the same $4/3$ power law result without the rather strict assumptions in the classical analysis of Batchelor (1952). Scale dependence close to the $4/3$ relationship is seen over a remarkably large range of scales (1000 km to 10 m) in the ocean (Okubo, 1974). A scale dependence indicates caution is needed when comparing measured dispersion values in the nearshore. For example, values for K of $0.03 m^2 s^{-1}$ found by Rodriguez et al. (1995) compare well with the smaller scales in Figure 5.16, but are orders of magnitude different for the larger scales. This also implies that when modelling surf zone processes, appropriate diffusion coefficients are dependent on the model grid scale.

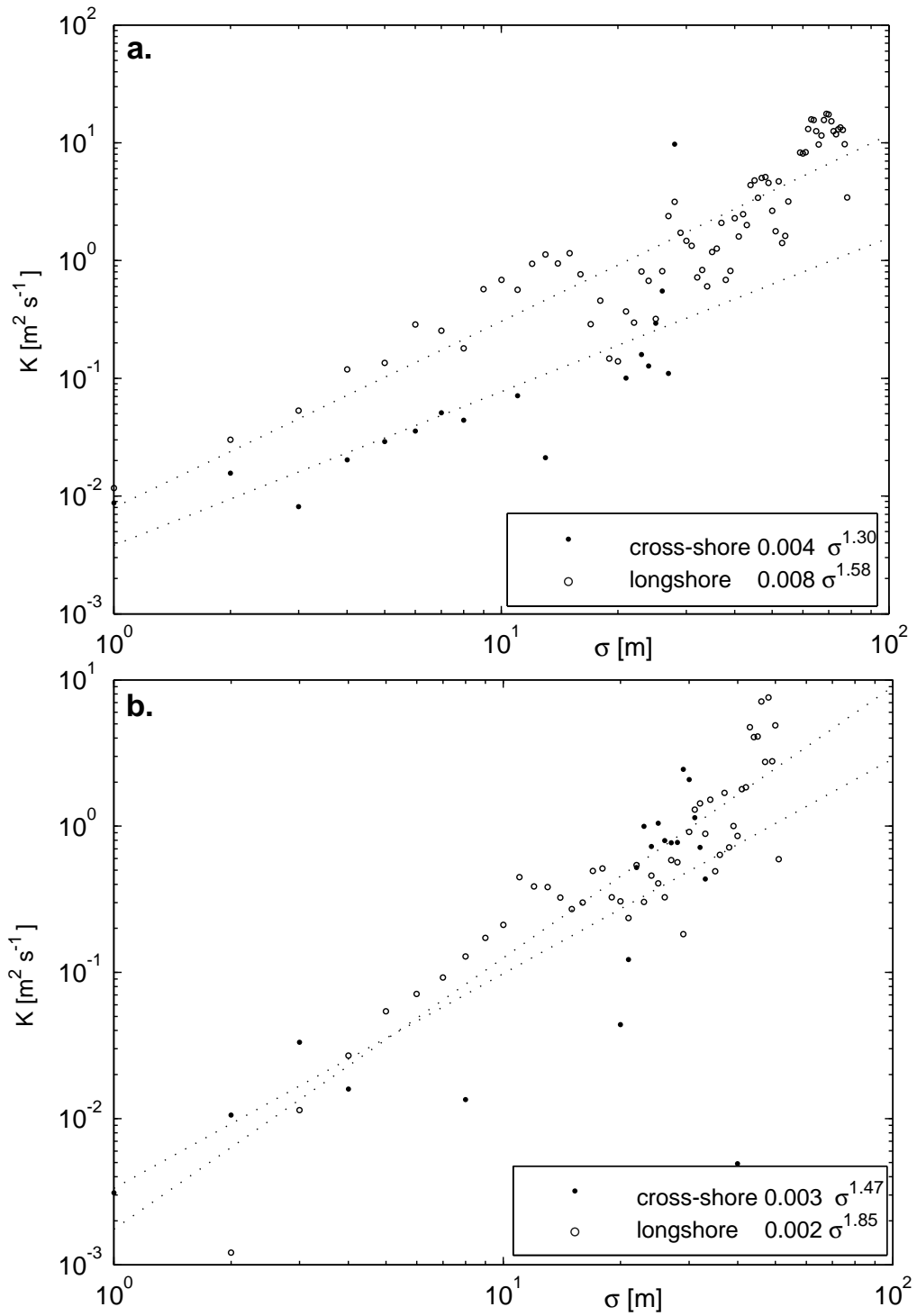


Figure 5.16: Cross-shore (●) and longshore (○) dispersion coefficients averaged in one meter bins of standard deviation of cross-shore and longshore separation for *a.* inside the surf zone and *b.* outside the surf zone. The line shown are the least squares fit and the equation of each line is shown in the legends.

5.6 Spatial variability of the current field

In order to derive quantitative spatial information from Lagrangian data, single or particle pair statistics are normally used to describe the dispersion and velocity correlations. This type of analysis has been used extensively with oceanic drifter data, examples include Davis (1985); Paduan and Niiler (1993). While there have been dye experiments conducted in the surf zone (e.g. Sonu, 1972; Inman et al., 1971; Brander, 1999), there has been no analysis of drifter field data, that the author is aware of, using particle statistics. The calculation of cluster dispersion presented in the last section is equivalent to the rate of particle pair separation. What follows is a first attempt to estimate spatial length scales with Lagrangian trajectories in the nearshore zone.

The velocity covariance of a pair of fluid columns moving with the depth-averaged velocity which, as in Section 5.5.1, is assumed to be sufficiently well sampled by the drifters is given by:

$$C_{ij}(\mathbf{r}, \mathbf{r}') = \langle u_i[\mathbf{r}(t_0, \mathbf{r}_0)] u'_j[\mathbf{r}'(t_0, \mathbf{r}'_0)] \rangle \quad (5.7)$$

where \mathbf{r} is a displacement vector, and u_i a velocity vector component of a column which started at \mathbf{r}_0 , primes indicate quantities associated with a second column. The $\langle . \rangle$ indicates ensemble averaging over many particle pair realisations but in practice ergodicity is assumed to allow temporal averaging to be used. The very nature of the experiment has preferentially sampled the rip events which will bias the calculation of C_{ij} so that it describes particular times and longshore locations within the flow field. The amount of data is small for this type of analysis so the results have limited statistical validity. However, useful information can still be gained about typical length scales.

As the rip currents do not appear to have preferred longshore positions, it was assumed that C_{ij} is a function of the longshore separation, $y' - y$, rather than absolute position. Dependence on cross-shore location is retained as the flow field is expected to be non-homogeneous across the surf zone. Following the method of Davis (1985), the mean current and the covariance of observation pairs are averaged in discrete spatial bins which is equivalent to the covariance of a velocity which has been spatially filtered with a lowpass cutoff of the same size as the averaging bins (for a proof see Appendix in Davis (1985)). Bins of 5 m are used for the cross-shore position and for the longshore separation. The covariance estimate, $\hat{C}_{ij}(\zeta_1, \zeta_2, \xi)$, is the average covariance calculated for all pairs of simultaneous observations with cross-shore locations in bins centred at ζ_1 and ζ_2 and with longshore separation in the bin with centre at ξ .

The longshore covariance function, $L_{ij}(y)$ for each cross-shore zone spanning x_1 to x_2 of:

$$L_{ij}(y; x_1, x_2) = \frac{\sum_n \hat{C}_{ij}(x_n, x_n, y) N(x_n, x_n, y)}{\sum_n N(x_n, x_n, y)}; \quad x_1 \leq x_n < x_2 \quad (5.8)$$

where N is the number of pairs in each covariance estimate. Because the quantity of data in some of the longshore separation bins is small, $L_{ij}(y; x_m, x_n)$ is also smoothed with a 1-2-1 kernel. Smoothed longshore covariance functions for cross-shore zones of $x_1 = 35m$ to $x_2 = 65m$ (inside the surf zone) and $x_1 = 65m$ to $x_2 = 95m$ (outside the surf zone) are calculated and normalised by $L_{ij}(0; x_m, x_n)$. The covariance of velocities with cross-shore separation from a particular cross-shore location, x_c give a cross-shore covariance function, $M_{ij}(|x - x_c|; x_c)$:

$$M_{ij}(|x - x_c|; x_c) = \frac{\hat{C}_{ij}(x_c, x_c + x, 0) N(x_c, x_c + x, 0) + \hat{C}_{ij}(x_c, x_c - x, 0) N(x_c, x_c - x, 0)}{N(x_c, x_c + x, 0) + N(x_c, x_c - x, 0)} \quad (5.9)$$

The cross-shore covariance functions are calculated for $x_c = 50m$ and $x_c = 70m$, then smoothed with a 1-2-1 kernel and normalised by $M_{ij}(0; x_c)$.

Correlation functions calculated separately for nine deployments from *Experiment 1* and *Experiment 3* and five deployments from *Experiment 2* in view of the different type of rip flows observed; results are shown in Figure 5.17. The limited amount of data means some of the curves have somewhat unusual shapes and caution is required in how much can be reliably determined from the results. It is important to realise that the structure of the correlation functions will be partially determined by infragravity motion. However, the sampling bias of times and locations where transient rip currents were occurring means that the displacement at which the correlation falls to zero is useful as a reasonable estimate of length scales of the rip flows.

Data from *Experiment 1* and *3* show a longshore de-correlation length scale of around 20 - 30 m . This is consistent with the observation in Section 5.4.1 of a significant difference between drifter velocities and ADCP data 20 m alongshore. The de-correlation length in the cross-shore direction is slightly longer at around 30 - 40 m , which would be expected for a cross-shore jet type flow. The de-correlation lengths from inside and outside of the surf zone are similar. The curves for *Experiment 2* show similar length scales to *Experiment 1* and *3*, but in the opposite sense with longshore scales of 30 - 40 m and cross-shore scales of 20 - 30 m ; this would be expected as the rip currents were oriented obliquely to the shore. Again in this case, inside and outside of the surf zone are similar in terms of de-correlation

lengths. The fact that short cross-shore scales are somewhat shorter than the width of the surf zone in *Experiment 2* (*RE2a* and *RE2b*) indicate that the flow is a jet-like flow as opposed to a continuous (across the surf zone) longshore flow. The strong negative cross-shore correlations of $\langle vv \rangle$ in *Experiment 2* (Figure 5.17c.) appear due to "over-sampling" of pairs of drifters moving in opposite longshore directions at the end of the rip necks. This is an artifact of the small number of data and the sampling of a small number of individual rip current events. Given the limitations of the data it is hard to draw any conclusions regarding the difference between $\langle uu \rangle$ and $\langle vv \rangle$ correlation estimates.

5.7 Discussion

The data shown in Figure 5.4 shows that the long time average of depth-averaged velocity is close to zero in both the longshore and cross-shore direction. This is what would be expected for the experimental conditions with waves perpendicular to a longshore uniform beach. However, what the drifter trajectories have also shown is an active varying horizontal circulation which occurs over timescales greater than the incident wave period. Much of the fluctuations in the trajectories will be due to infragravity waves, which are the dominant source of the total current variance. However, there is separate part of the velocity field associated with another type of motion as indicated by the energy ratios calculated in Section 5.3. The non-infragravity flow mode must be rotational and non-divergent, as are shear waves. The tendency of nearshore flows on beaches with gentle slopes to be two-dimensional, rotational and contain discrete eddies has been highlighted by Peregrine (1998), who also discusses how random breaking waves can generate vorticity even with a mean perpendicular incidence on a longshore uniform beach. Given the lack of longshore current, the variable rotational flow measured here does not derive its vorticity from the longshore current shear, and cannot be classified as shear waves. Rather, this rotational flow mode could be thought of as "infragravity turbulence", with vorticity introduced by the spatial variability of a random incident wave field, and which includes discrete vortices and transient rip currents seen in the drifter trajectories.

It seems likely that discrete vortex features are important in the rip generation mechanism. In their drifter measurements of a rip current reoccurring in the same location (and therefore presumably topographic), Schmidt et al. (2003) show the presence of a persistent eddy within the surf zone at the shoreward end of offshore flow in the rip neck. Numerical experiments of topographic rip currents (Chen et al., 1999; Haas et al., 2003) clearly show the generation and subsequent shedding of vortex pairs from the edges of the rip channels. Despite the lack of a bar with

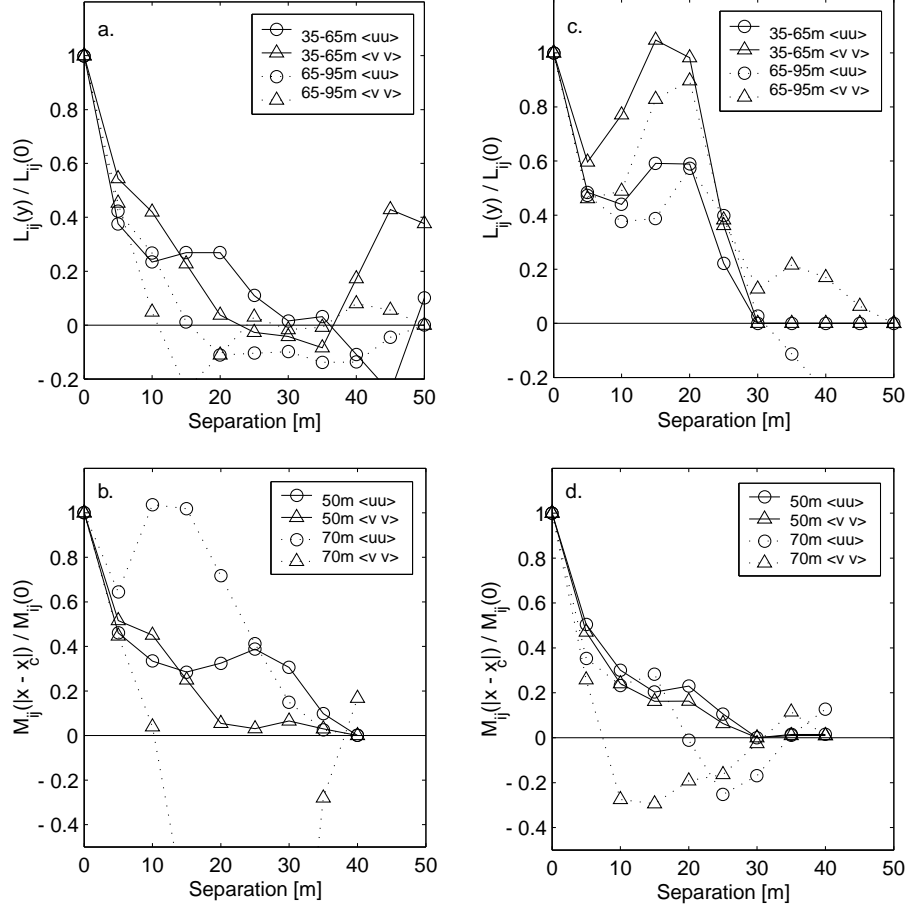


Figure 5.17: Spatial correlations calculated from all deployments. *a.* Longshore correlation for *Experiment 1* and *3*. *b.* Cross-shore correlation for *Experiment 1* and *3*. *c.* Longshore correlation for *Experiment 2*. *d.* Cross-shore correlation for *Experiment 2*. Longshore correlations are for cross-shore zones of $x_1 = 35m$ to $x_2 = 65m$ (solid line; inside the surf zone) and $x_1 = 65m$ to $x_2 = 95m$ (dashed line; outside the surf zone). Cross-shore covariance functions $M_{ij}(|x-x_c|)$ are normalised by $M_{ij}(0)$ for cross-shore reference positions, x_c , of $50m$ (solid line; inside the surf zone) and $70m$ (dashed line; outside the surf zone). In *b.* the section of the axis below -0.5 is omitted to retain clarity in the positive half; the correlation reaches a minimum of -3.0 at a cross-shore separation of $25m$.

rip channels, the start of the deployment shown in RE2b (Figure 5.11) clearly shows a vortex feature which appears similar to this type of starting vortex. Although the rip itself is somewhat oblique to the shore this suggests the initial stages of transient rip flow may be similar in that a vortex is involved at the landward (inlet) end. Bühler and Jacobson (2001) point out that transient rip currents could in principle be generated through the formation of counter rotating vortex pairs which propagate offshore. Bühler and Jacobson (2001) also point out that single vortices with opposite rotations will tend to propagate longshore, collide and form a vortex pair; thus generation of a vortex pair during a particular forcing event itself may not be necessary. Up-scale evolution of vortex energy, inherent to two-dimensional turbulence, may also lead to vortices large enough to produce a rip current being generated through the merging of smaller vortices. Infragravity waves will modulate the relative vorticity of vortices by vortex stretching, which may cause a pumping mechanism which enhances offshore propagation. Lagrangian data provides a means to resolve discrete surf zone current eddies in the field and further investigation should lead to a better understanding of the evolution of eddies and their role in rip current formation.

It is not possible to conclusively prove that the circulation in the data are not topographically controlled as a complete bathymetry for the field site is not available; the evidence here is somewhat circumstantial. However, Boussinesq modelling of circulation on a plane beach of the same slope and with a similar random wave field shows the development of complex circulation and narrow offshore jets at the same scales as the rip currents described in this paper. These results, which will be presented elsewhere, are further evidence that this type of circulation does not need to be topographically controlled.

5.8 Summary and conclusions

Measurements using Lagrangian and Eulerian techniques on a swell dominated beach show a complex nearshore current field. Estimates of energy ratios using the method of Lippmann et al. (1999) show that while the infragravity wave energy is dominant, there is a significant variable component of the current field not related to infragravity motion. One well defined feature of this variable non-infragravity current field is the ejection of transient rip currents from inside the surf zone that are not topographically controlled. The overall appearance of drifter trajectories suggest that the rip currents behave like a shallow plane jet, consisting of a constrained neck region that flows into an spreading head region. Lagrangian measurements reveal the following characteristics of the rip dynamics:

1. Substantial momentum is imparted to the rip flow at the start of the rip neck.
2. There is continuous modulation of the current field at infragravity wave frequencies.
3. The rip neck region is constrained and has short (20 - 30 *m*) length scales across the main axis of the flow.
4. The rip head appears to be a region of enhanced mixing with relative dispersion coefficients between 1.29 and 3.88 m^2s^{-1} .
5. Discrete vortices are seen both at the initiation of one of the rip currents and in the head region of another.

The estimates of dispersion indicate that transient rip currents should greatly enhance mixing in the region outside the surf zone. An evaluation of all of the data appears to show scale dependence with best fit power laws ranging between 1.30 and 1.85. These values are close to the 4/3 power law found over a large range of scales in the ocean, and suggest that in some way the variable nearshore current field may have similarities with large scale horizontal oceanic turbulence. The existence of a predictable scale dependence has some very useful implications for modelling nearshore dispersion of material, and imply that eddy viscosities used in turbulence closure schemes may also be scale dependent. Further investigation is desirable to see if this is ubiquitous in the nearshore.

Chapter 6

Field measurements of longshore currents

6.1 Introduction

A series of drifter deployments were carried out over three days to measure the strong longshore currents driven by summer seabreeze on the same section of Scarborough beach, Perth, WA. The purpose of these experiments were largely to test the drifters in strong longshore currents. The analysis carried out on the trajectories is not as extensive as that in Chapter 5, as the emphasis of the thesis is on variable currents in the absence of quasi-steady currents. However, the results should serve to highlight the potential of the instruments and the results qualitatively show the highly variable nature of the longshore current system. The results of estimates of cluster dispersion imply that variable currents are important in lateral mixing of the quasi-steady longshore current momentum.

6.2 Field site and methodology

6.2.1 Field site

Field measurements were carried out on three days during (southern hemisphere) summer on 30 January (*E1*), 31 January (*E2*) and 13 February 2003 (*E3*), on Scarborough beach, one of the metropolitan beaches of Perth, Western Australia. The site experiences diurnal microtidal tides with a mean spring tidal range of 0.6 *m*. Strong seabreezes (typical windspeed 10 ms^{-1}) from the SSW are oblique to the N-S oriented shoreline. The locally generated sea (period 4-5 *s*) drives strong northward longshore currents.

Table 6.1: Significant wave heights for swell ($0.02 < f < 0.125$), sea ($0.125 < f < 1.0$) and combined ($0.02 < f < 1.0$)

Exp	$H_{sig}[m]$		
	Swell	Sea	Combined
E1	0.56	0.68	0.86
E2	0.52	0.77	0.93
E3	0.55	1.02	1.16

6.2.2 Field methodology and incident wave conditions

The instrumentation consisted of an InterOcean S4 wave recorder, an upward looking ADCP and four GPS drifters. The positions of instrument deployments are shown in Figure 6.1. The ADCP was deployed near the outer edge of the surf zone. The S4, which measures pressure and horizontal velocity, was deployed 1.0 m above the bed in approximately 3 m of depth outside the surf zone. The instrument was attached to a post extending from a fixed weighted disk which sits flat on the bed, ensuring no movement due to the wave action.

As in Chapter 5, the beach is surveyed with a theodolite and the GPS units and the coordinate system is rotated and translated to an on/offshore and longshore axes with the longshore axis coincident with the best fit MWL line. The survey shows a steep beach face slope of 0.25. Due to the energetic wave conditions it was impossible to accurately survey at depth greater than about 0.5 m . The beach slope calculated from the position and depth of the ADCP, was 0.03 from the MWL to the ADCP location. There was no visible significant offshore bar, however exact shape of the profile is unknown.

Drifter deployments were carried out for each experiment using the four drifters. There were 6 deployments between 1510 and 1730 for *E1*, 7 deployments between 1530 and 1745 for *E2*, and 7 deployments between 1300 and 1520 for *E3*. The same cluster of four drifters was repeatedly deployed from a similar starting location and allowed to travel about 500 m along the beach. Drifters were recovered at the end of the 500 m or when they moved a significant distance outside the surf zone.

Directional spectra from the S4 for a 20 minute period near the end of each deployment period, calculated using the Extended Maximum Entropy Method (Hashimoto et al., 1993), are shown in Figure 7.2. In each experiment, the presence of two regions of wave energy are seen. Swell, centred about a frequency of around 0.1 Hz and perpendicular to the beach, was narrow banded both in frequency and direction. The locally generated sea, generated by the seabreeze, was more spread in frequency and direction with most energy between 0.2 and 0.3 Hz and obliquely

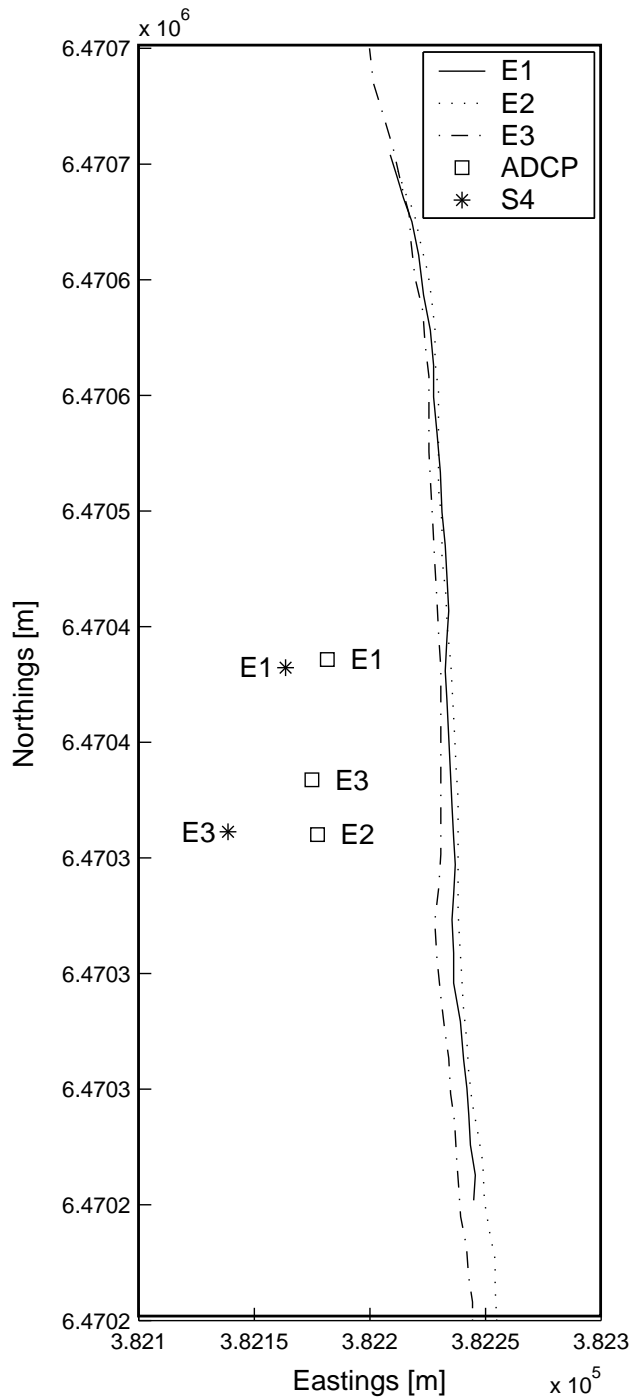


Figure 6.1: Plan of instrument deployment. The positions of the ADCP and S4 are indicated in each case. The mean water level (MWL) mapped with a GPS unit is shown in each case.

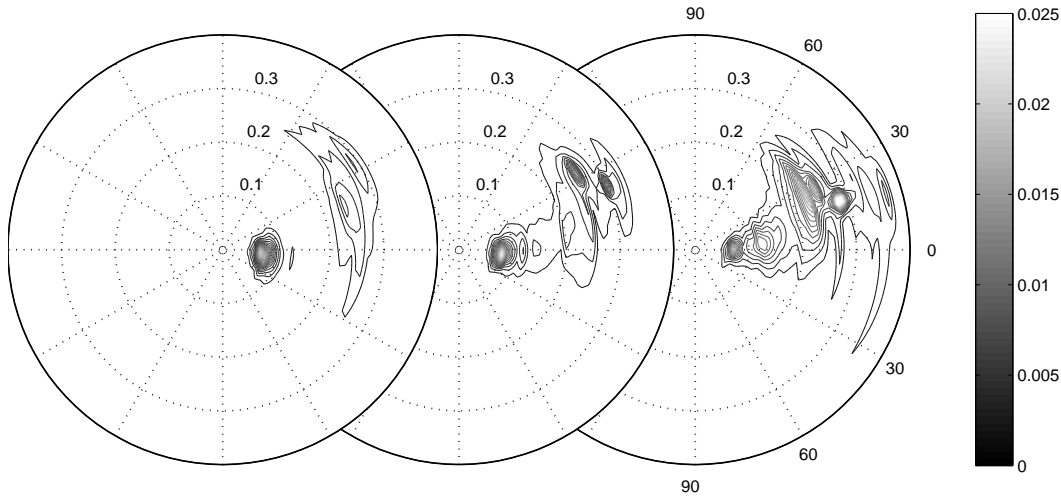


Figure 6.2: Directional spectra calculated for the three experiments (left to right, *E1* to *E3*). The directions are the angle of wave propagation relative to the x -axis.

incident from the SW. Significant wave heights for the swell/sea components and total are shown in Table 6.2.2. In each case, the local sea was the dominant energy component.

The tidal influence during the measurement periods was small. The mean water level measured by the S4, defined as the water level component passing a 0.0005 Hz filter, showed a tidal rise of 0.15, 0.25 and 0.1 m for the three experiments.

6.3 ADCP data

Mean ADCP data, calculated as in Chapter 5, during the period of deployments on each day, are shown in Figure 6.3. The total averaging times vary as there were data retrieval problems in *E1*, and in *E3* the instrument was buried in the second half of the deployment. The longshore current component exhibits nearly constant velocity below the mean water level, decreasing around the mean water level. The vertical structure is qualitatively very similar to the predicted profile shape of Garcez Faria et al. (1998). The reversal of mean flow in the cross-shore direction, associated with the undertow, combines with the longshore profile to produce a spiral shape, as predicted by Quasi-3D models (Van Dongeren et al., 1994).

Spectra calculated as in Section 5.3.2 of the ADCP data of surface elevation, and depth-averaged velocity components are shown in Figure 6.3 and provide frequency dependent estimates of the amount of potential and kinetic energy associated with the variable current. At higher frequencies around the incident wave frequencies, there is close to equi-partition of energy, while there is a clear excess of kinetic energy

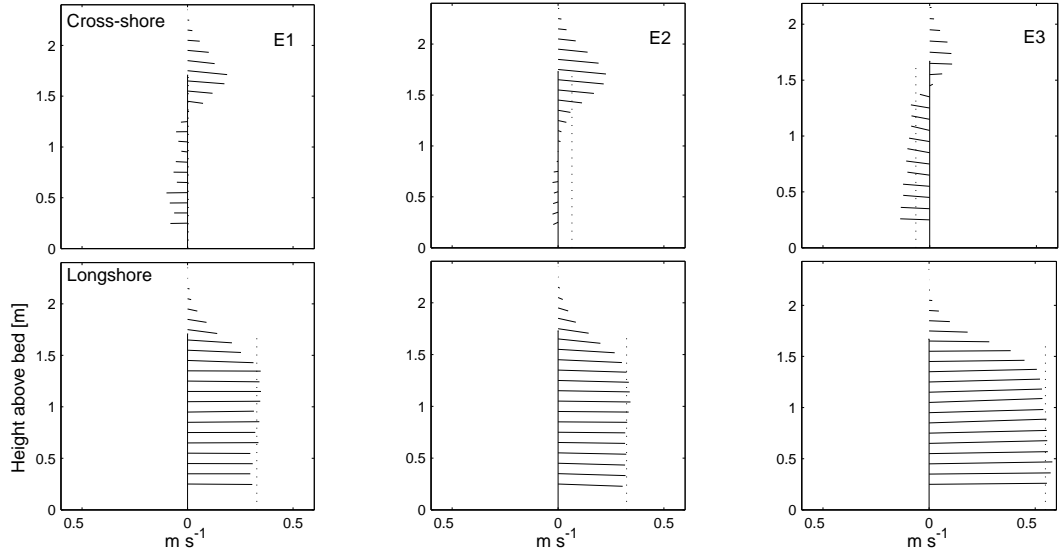


Figure 6.3: Mean ADCP data of cross-shore and longshore velocity for a. *E1* 1000 s from 1445 b. *E2* 10000 s from 1510 and c. *E3* 4000 s from 1320. The cross and longshore velocity components are shown for each depth bin. The height of the solid vertical line corresponds to the mean depth. The depth-averaged velocity is indicated with a dotted line.

towards the lower frequencies. The ratio of kinetic and potential energy estimates for $f = 0.0025 - 0.05 \text{ Hz}$, as defined in Section 5.3.2 are 2.42 and 3.22 for *E2* and *E3* respectively. This corresponds to 59% and 69% of the kinetic energy belonging to non-divergent motions. For the lower frequency range of $f = 0.0025 - 0.01 \text{ Hz}$, almost all of the energy is non-divergent with ratios of 7.82(87%) and 7.28(86%).

6.4 Drifter trajectories

Ensemble plots of the drifter trajectories for each experiment are shown in Figure 6.5. A general feature of the trajectories is significant meandering. Some of the shoreward motions are caused by surfing; these periods are easily identified and excluded from any analysis. Drifters deployed together tended to spread rapidly and thereafter usually follow different paths. However, the trajectories in the first and third experiments in particular show some tendency to cluster in particular locations, suggesting that there may be some topographic control with inhomogeneity in the longshore direction.

The drifter velocities were calculated and averaged in spatial bins of 10 m and 20 m in the cross-shore and longshore direction respectively, generating a map of the velocity field shown in Figure 6.6. Averaging along all the bins in the longshore direction gives a mean cross-shore profile of the longshore velocity field. The velocity

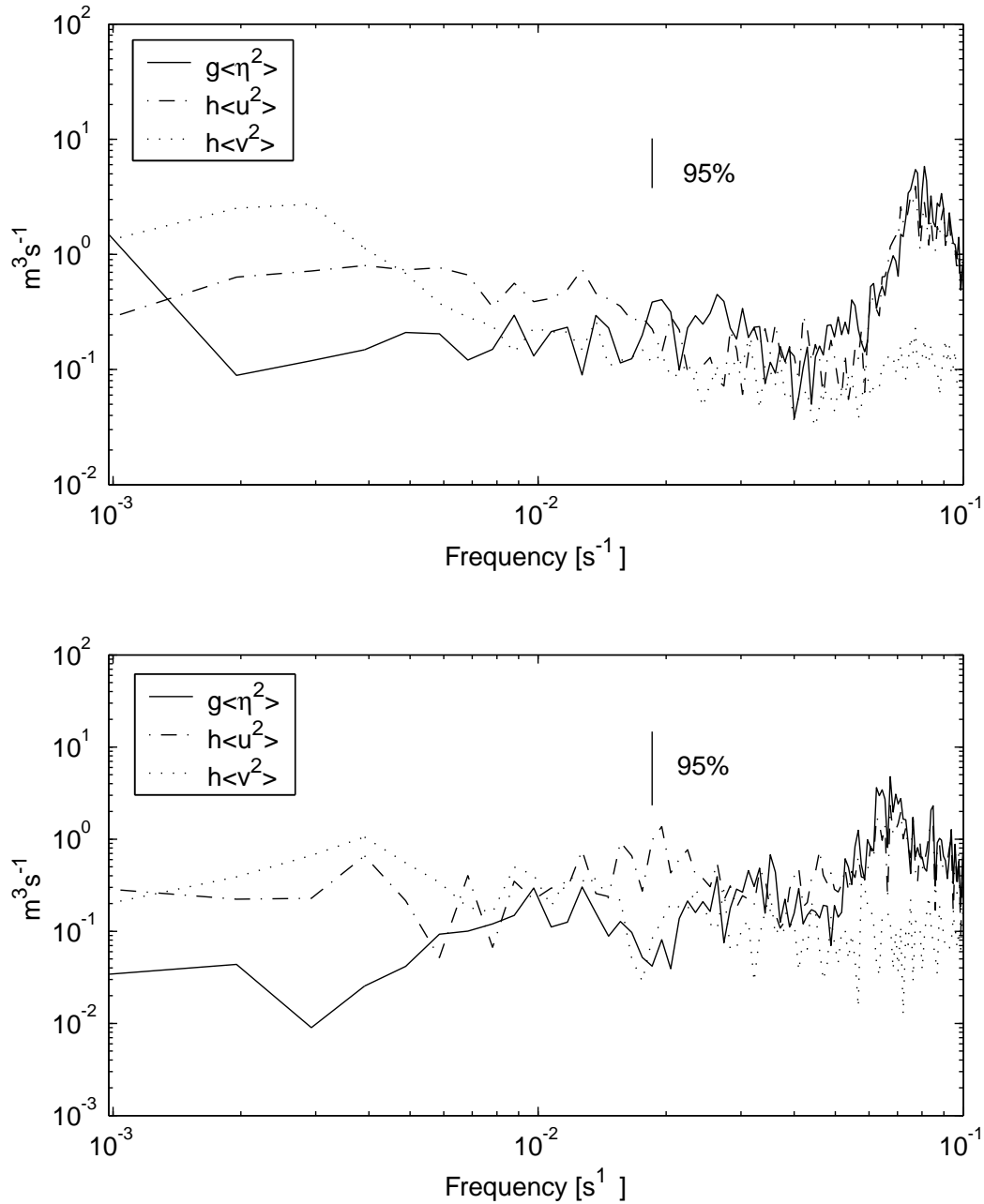


Figure 6.4: Spectra of pressure and depth-averaged velocity from ADCP measurements spanning the period of drifter deployments for a. *Experiment 2* 10000 s from 1510(top) and b. *Experiment 3* 4000 s from 1320(bottom). The spectral density of the current components and surface elevation has been multiplied by the mean depth, h , and gravitational acceleration, g , respectively so that they correspond to estimates of potential and kinetic energy contributions. Note that the spectra are not variance-preserving.

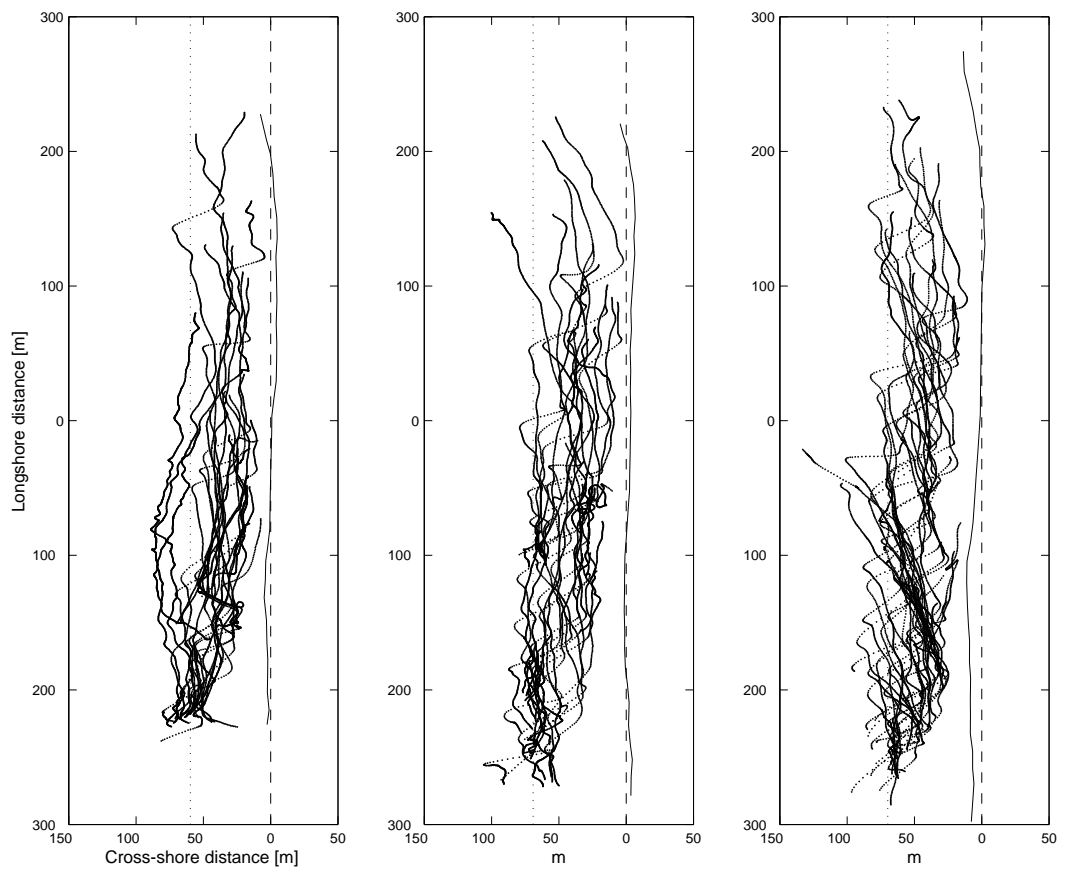


Figure 6.5: Ensemble trajectories of drifter deployments for each experiment.

profiles show a maximum approximately two-thirds of the distance from the shoreline to the outer edge of the surf zone, similar to measurements in other experiments on plane beaches with Eulerian instruments (e.g. Thornton and Guza, 1986). The peak velocities of the measured profiles are 0.75, 0.77 and 0.9 $m s^{-1}$ for *E1-E3*. The depth-averaged longshore velocity from the ADCP shows close correspondence with the profile velocity for the first two experiments. Agreement in the third is less good but may be partially explained by the apparent presence of a topographically fixed offshore directed flow seen in the clustering of the trajectories and obliquely oriented mean current vectors between $y = -200 m$ and $y = -50 m$. This suggests that the velocities may not be very uniform longshore and the ADCP may be in a region of slower flow just beyond the strongest flow.

To examine the variable part of the drifter velocities, \mathbf{u} , the long time mean (quasi-steady) longshore current was removed from the measured velocities, $\hat{\mathbf{u}}$, so that:

$$\mathbf{u}(x, y) = \hat{\mathbf{u}}(x, y) - \mathbf{U}_o(x) \quad (6.1)$$

To avoid discontinuities and physically unrealistic jumps in the profile, the quasi-steady longshore current profile, $\mathbf{U}_o(x) = [0, V_o(x)]$ was assumed to be the best fit 3rd order polynomial to each set of measured longshore velocity profile, as shown in Figure 6.6. The variable part of the trajectory, \mathbf{x} , can then be reconstructed by numerically integrating:

$$\mathbf{x}(t) = \int_0^t \mathbf{u}(t') dt' \quad (6.2)$$

Two examples of a trajectory with the mean longshore velocity removed are shown in Figure 6.7. The residual trajectories can be seen to quickly separate from their starting point, following meandering trajectories in both longshore directions. Note that drifters at different cross-shore locations were also separating in the longshore direction due to different quasi-steady velocities at those points. The residual trajectories show that the variable current has a complex spatial structure including sections where trajectories loop back on themselves. Other trajectories (not shown) also have flow reversal features with length scales of 10 to 30 m . Figure 6.8 shows RMS values of \mathbf{u} as a function cross-shore location. Overall, the variable cross-shore current appears to become more energetic away from the shoreline, while the longshore component doesn't show any clear trend except a significant increase towards the shoreline in *E3*. In view of estimated KE/PE ratios, it is inevitable that a large component of the variable (residual) displacements are caused by the rotational currents.

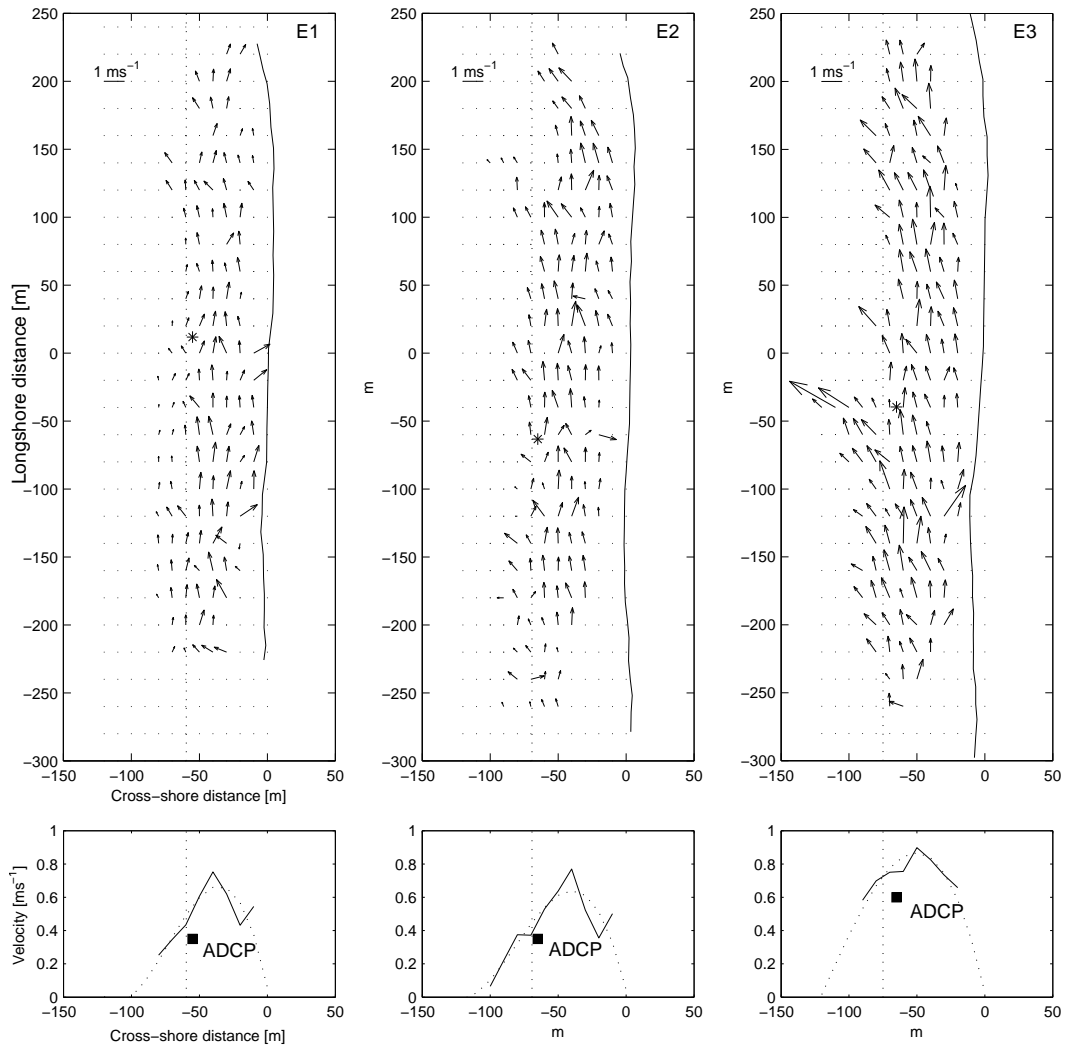


Figure 6.6: Averaged velocity from the ensemble of trajectories in each longshore current experiment. The position of the ADCP is shown by an asterisk and the approximate edge of the surf zone is indicated by the dotted line. The lower figures in each case is longshore velocity averaged over all drifter data in the longshore direction. The solid squares are time and depth-averaged ADCP measurements from that cross-shore location. The dotted line is the best fit 3rd order polynomial.

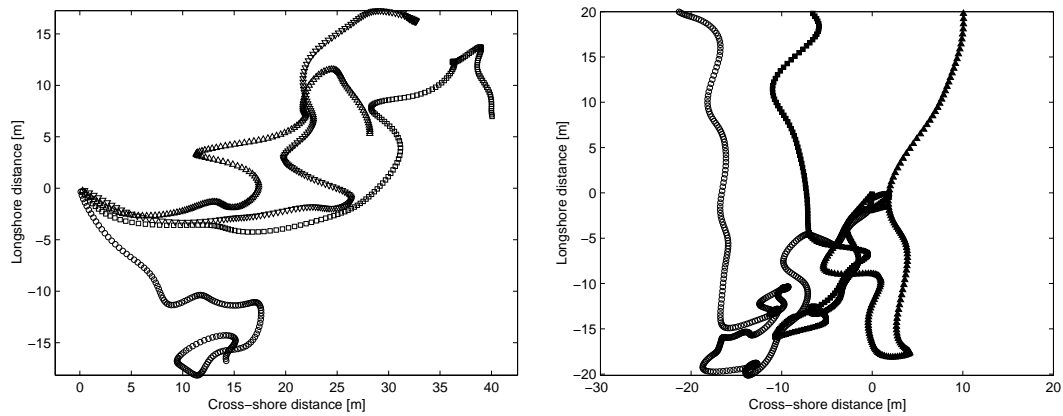


Figure 6.7: Residual drifter trajectories from two deployments with displacement due to quasi-steady longshore current removed. The trajectories all start at $[0, 0]$.

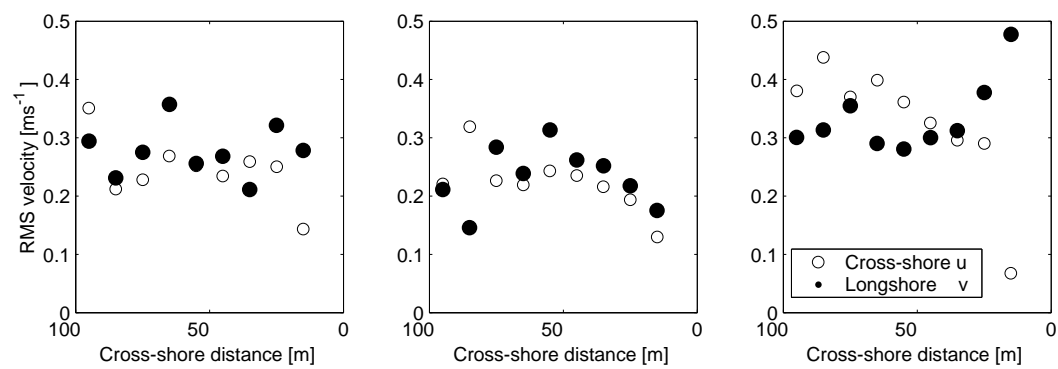


Figure 6.8: RMS velocities of the variable part of the drifter velocity after the quasi-steady

6.5 Cluster dispersion

Values of σ_x, σ_y and the associated K_x, K_y were calculated for all the clusters in each experiment, which contained a total of 2580, 2238, and 2359 data points respectively, which after filtering correspond to 129, 112, and 118 independent samples. Dispersion values were averaged in 1 m bins of σ_x and σ_y . The dependence of K_x, K_y on σ_x, σ_y are plotted in Figure 6.9 and least squares lines of best fit are calculated for each case.

There is a large amount of scatter in the data points, however, as in Chapter 5, there appears to be a definite scale dependence of the dispersion. The dispersion is less in the cross-shore direction than the longshore. The power law exponents of the best fit lines varies considerably, between 1.57 and 2.41. For the combined data set, the cross-shore and longshore exponents are 2.41 and 1.92 respectively. These can be compared with exponents for inside the surf zone from Chapter 5 of 1.30 and 1.58 for cross-shore and longshore directions. The scatter in the data cautions against relying too closely on the values of the power law exponents, particularly for the cross-shore direction. However, they are apparently much higher than those estimated in Chapter 5 or a value (for dispersion in isotropic homogeneous turbulence) of $4/3$.

It might be expected that there would be a shear dispersion mechanism in the longshore direction, as drifters separated in the cross-shore direction are partially separated by differences between the longshore current strength at the different cross-shore locations. Unlike the lateral mixing which occurs due to the *vertical* non-uniformity of the current, in this case the drifters can be “mixed” across the cross-shore gradient of the longshore velocity. Note that this does not help to explain the high power law exponents observed, as in an ideal unbounded shear flow, shear dispersion leads to stream-wise scale dependent dispersion with a power law of $4/3$ (Fischer et al., 1979, Chapter 4). It should also be noted that for particle pairs in a shear flow (even when homogeneous), their dispersion will depend on the orientation of the separation vector and that a scale dependence will depend on the cross-shore *and* longshore separation.

Specific values for dispersion for a 10 m separation from the combined data are $K_x = 0.2 \text{ m}^2\text{s}^{-1}, K_y = 0.3 \text{ m}^2\text{s}^{-1}$. The only other direct dispersion measurements in longshore current the author is aware of were reported by Takewaka et al. (2003) for a longshore current with a measured velocity of 0.3 ms^{-1} , driven by a wave field with significant wave height of 0.56 m and peak period of 6.5 s . Comparison is difficult, as they calculate their dispersion coefficient for a dye cloud assuming a Fickian diffusion process. However, their estimated cross-shore dispersion value of $K_x = 0.025 \text{ m}^2\text{s}^{-1}$ for when the cloud size was less than 5 m is consistent with $K_x = 0.039 \text{ m}^2\text{s}^{-1}$ calculated from a $\sigma_x = 5 \text{ m}$ separation.

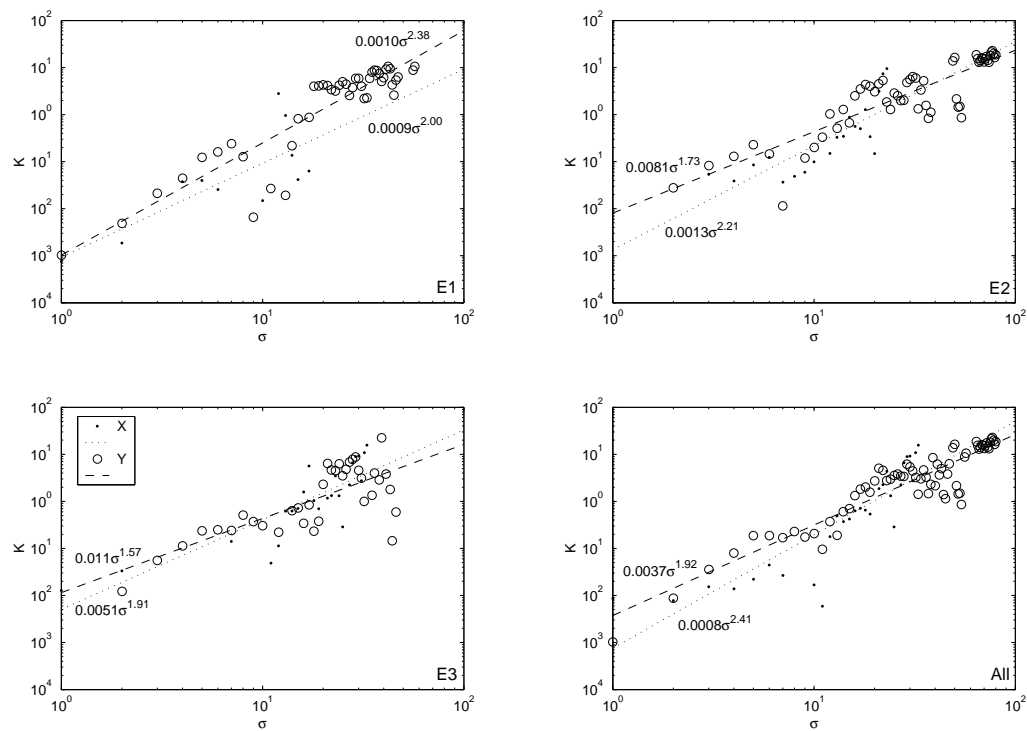


Figure 6.9: Cross-shore (\bullet) and longshore (\circ) dispersion coefficients averaged in one metre bins of standard deviation of cross-shore and longshore separation for the three experiments (E1, E2, E3) and all data combined (All). The lines shown are the least squares fit for the cross-shore (\cdots) and longshore direction ($---$) and the equation of each line is shown.

6.6 Discussion

The quasi-steady longshore current profile was calculated from all drifter deployments in a particular experiment, and therefore defined as constant for the (approximately) three hour duration of deployments in each case. However, local sea increased in size to some extent over the duration of each experiment as the sea state developed in response to the seabreeze. This leads to a problem in defining the quasi-steady current (and is the reason for the qualifier "quasi") for the purpose of extracting the variable current. This means that many of the residual trajectories show significant longshore displacements, with earlier deployments having a displacement in the opposite direction to the quasi-steady current. Reducing the temporal averaging window by using less deployments for calculating the quasi-steady current profile leads to uncertainty due to less data at each cross-shore location. An obvious solution is a combination of a cross-shore Eulerian current meter array and Lagrangian drifters.

The difficulty alluded to in drawing firm conclusions regarding hydrodynamic processes from trajectories is partially due to the lack of knowledge regarding how Lagrangian tracers should behave in the complex mixture of hydrodynamics. Model simulations of longshore current instabilities show a complex turbulent kind of motion (e.g. Allen et al., 1996; Ozkan-Haller and Kirby, 1999). To the authors knowledge, no virtual particle tracking has been reported from these types of models, so the kind of trajectories expected is unknown, however the vorticity plots presented from these works suggest that the trajectories will be very convoluted and should exhibit reversals of direction of the type seen in the residual plots.

The variable currents have important implications for the cross-shore distribution of the longshore current. The momentum equation for the longshore current distribution is (Equation 3.11 with $\mathbf{U}_o = V(x)$ on a longshore uniform beach),

$$S_o^y + L_o^y + B_o^y + T^y = 0 \quad (6.3)$$

so that the longshore incident wave forcing is balanced by bottom friction and lateral mixing of momentum. As described in Section 3.2.3, \mathbf{L} is due to both (small-scale) turbulent mixing and the shear dispersion mechanism. However, the last term represents the cross-shore redistribution of momentum due to the variable current component as discussed in Section 3.3. Results from Quasi-3D modelling of longshore currents, carried out by Zhao et al. (2003), show that mixing caused by the variable currents (shear waves) have a similar magnitude in the longshore momentum balance to the Q3D dispersion terms.

However, the scale dependence of K_x and K_y indicates (as with the nearshore

dispersion for perpendicular incident waves described in Chapter 5) that horizontal dispersion is non-Fickian and apparently caused by whole range of scales up to the length scale of the surf zone width. The drifters were not mixed cross-shore due to the three-dimensional shear dispersion effect, and the other (potentially scale dependent) mixing mechanism due to the infragravity waves are too weak to account for the estimates of K_x and K_y (this is considered in more detail in Section 8.3.3). So at the larger scales ($\mathcal{O}10\text{ m}$), the horizontal dispersion measured by the drifters must be dominated by the variable rotational component of the current.

If the variable current is largely caused by shear instability then, in analogy to a wall bounded shear flow, it is tempting to model T^y using a closure of the type:

$$T^y = -u \overbrace{\frac{\partial v}{\partial x}} \approx \frac{\partial}{\partial x} \nu_u \frac{\partial V}{\partial x} \quad (6.4)$$

where ν_u is an eddy viscosity associated with the variable current rather than ν_t , associated with small scale turbulence. This is expected to have magnitude $\nu_u \sim \mathcal{U}^R \ell$, where ℓ is a mixing length. In practice, the assumptions leading to Equation 6.4 are violated if the mixing length, the integral scale over which the variable current causing the mixing remains correlated, is comparable to the cross-shore length scale of the mean flow itself (Tennekes and Lumley, 1972). This is apparently the case here, with the trajectories exhibiting coherent features of ($\mathcal{O}10\text{ m}$), and because the scale dependence continues up to the surf zone width. However, it is interesting to get an idea of the potential magnitude of the mixing as a comparative eddy viscosity. Assuming $\nu_u^{(x)} \approx K_x$ at the scale of the appropriate scale, the data indicates $\nu_u \sim 1.0\text{ m}^2\text{ s}^{-1}$ for a mixing length of 10 m . This is similar in magnitude to the “equivalent eddy viscosity” estimated for the shear dispersion mechanism and are consistent with the large eddy viscosities required to match observations. Therefore, if the preceding analysis is valid at least in terms of an order of magnitude, the drifter data support the proposition that variable currents generated due to shear waves or variable wave forcing are a major mixing mechanism responsible for shaping the quasi-steady current distribution.

6.7 Summary and conclusions

The longshore current driven by an obliquely incident locally generated sea has been measured with drifters and a fixed ADCP. Repeated deployments of the drifters allow the spatial distribution of the longshore current to be mapped, assuming stationarity of the mean longshore current. The cross-shore profile of quasi-steady longshore current velocity show maximum velocities of between 0.75 m s^{-1} and 0.9 m s^{-1} ,

approximately two-thirds of the distance from the shoreline to the outer limit of the surf zone. The variable part of the drifter trajectories, calculated by de-trending the measured trajectories with the displacement due to the quasi-steady current, are complex and include loops and regions of flow reversal with length scales of 10 to 30 m .

The dispersion of the drifter clusters shows an apparent scale dependence, with best fit power law exponents for the combined data of 2.41 and 1.92 for K_x and K_y . The energetic nature of the variable part of the currents and the estimated values for K_x imply that the variable current field may have an important role in determining the cross-shore distribution of the quasi-steady longshore current.

Chapter 7

Numerical modelling

7.1 Introduction

Transient rip currents are narrow offshore flows generated in the surf zone. Unlike rip currents that are associated with a topographic rip channel, “transient” rip currents are spatially and temporally variable, and are temporary features which develop, have a specific lifetime and then decay. Rip currents occur when the offshore directed pressure gradient locally exceeds the onshore directed momentum transfer due to the incident waves. This is due to longshore inhomogeneities in the gradient of momentum flux, which can be caused by differential wave transformation over variable topography, as occurs over a rip channel in a longshore bar. However, the nearshore wave field can possess longshore variations in the onshore momentum flux on a plane, featureless beach; this can be caused by:

1. Interaction of the incident wave field and the wave-averaged mean current (Dalrymple and Lozano, 1978; LeBlond and Tang, 1974).
2. Interaction of the incident wave field with lower frequency waves such as edge waves (Bowen, 1969b; Sasaki and Horikawa, 1978; Symonds and Ranasinghe, 2001).
3. The inherent spatial variability of the incident wave field (Dalrymple, 1975; Tang and Dalrymple, 1989; Peregrine, 1998).

Although transient rip currents have been generated in the laboratory using intersecting wave trains (Fowler and Dalrymple, 1991), there has been no conclusive proof that these transient rip currents exist in the field. Tang and Dalrymple (1989) made measurements of nearshore circulation, including (transient) rips, that was spatially and temporally variable and concluded that it was largely driven by the

variability of the incident wave field. Chapter 5 described measurements of transient rip currents where the swell was perpendicularly incident on a beach without an offshore bar or significant longshore variation. The trajectories showed narrow (length scales 20-30 m) offshore directed flows with typical flow speeds 0.2-0.5 ms^{-1} occurring at variable locations. The Lagrangian velocities showed that forcing occurs mainly at the start of the rip neck and that the neck subsequently spread into head region. Eulerian measurements from the same experiment strongly supported the assertion that the rip currents did not persist at one location.

The usual definition of the nearshore current in theoretical description of nearshore circulation is the net flow after averaging over the incident short wave motion. Vertical averaging then defines a wave and depth-averaged current vector, $\bar{\mathbf{U}}$ which is governed by:

$$\frac{\partial \bar{\eta}}{\partial t} + \nabla \cdot [(\bar{\eta} + h)\bar{\mathbf{U}}] = 0 \quad (7.1)$$

$$\frac{\partial \bar{\mathbf{U}}}{\partial t} + (\bar{\mathbf{U}} \cdot \nabla)\bar{\mathbf{U}} = -g\nabla\bar{\eta} + \bar{\mathbf{S}} + \bar{\mathbf{L}} + \bar{\mathbf{B}} \quad (7.2)$$

where h is the still water depth, $\bar{\eta}$ is the wave-averaged surface elevation, $\bar{\mathbf{S}}$ is short wave forcing, $\bar{\mathbf{L}}$ is a term to describe lateral mixing, and $\bar{\mathbf{B}}$ is bottom friction. Equations 7.1 and 7.2 are a set of forced shallow water equations, and with various simplifications are the theoretical basis for most descriptions of nearshore flow at frequencies below that of the incident waves. Specification of $\bar{\mathbf{S}}$ requires knowledge of the momentum transfer from the incident waves. Using existing wave theories the effect of shoaling, refraction and diffraction (including wave-current interaction) can be included to provide a spatially variable forcing term; however, the spatial variation is due to either variable mean water depth or interaction with the current. If there is feedback between the mean current/elevation field and the determination of the wave forcing, the first two transient rip generation mechanisms on a plane beach can be represented. Although progress is being made on more realistic wave-drivers (Kennedy and Kirby, 2003), at present wave-averaged modelling of current motions cannot capture the spatially and temporally variable nature of a random wave field, and thus excludes the third generation mechanism.

Numerical modelling of topographically generated rip currents have been undertaken by several researchers. This has followed two approaches, the first using the wave-averaged equations which, as discussed above, rely on a parameterisation of the incident wave field. Recent examples are the simulations carried out by Haas et al. (2003) of the rip current laboratory experiments of Haller et al. (1997), and the modelling investigation of Yu and Slinn (2003). As the spatial variation in the forcing term is largely due to differential wave breaking due to variable topography,

this type of model performs well for topographic rips and the examples cited showed generation of unsteady rip flows in good agreement with the measurements.

An alternative approach uses a phase-resolving description in which individual waves are simulated. Chen et al. (1999) used a Boussinesq (phase-resolving) model to simulate the same laboratory experiments of Haller et al. (1997); this model also reproduced the experiments well. Boussinesq-type equations reduce the three-dimensional flow problem for surface waves to two horizontal dimensions by assuming a polynomial distribution for the velocity field in the vertical. This makes them less computationally demanding to solve than a fully three-dimensional set of equations, while still resolving the instantaneous surface and including an approximation of non-hydrostatic pressure. The ability to simulate surface waves accurately from intermediate depth to shallow water makes Boussinesq models potentially very useful tools for investigating nearshore dynamics and explains the amount of research effort that has been spent on deriving and refining Boussinesq models (for a recent review of Boussinesq-type equations, see Madsen and Schaffer (1998)). Simulation of a random wave field is possible, thereby implicitly including a spatially and temporally variable forcing of the wave-averaged currents. Furthermore, it also includes generation of vertical vorticity due to discontinuities in individual wave crests, something Peregrine (1998) has proposed as an important source of surf zone vorticity. Despite their potential for simulating complex hydrodynamics associated with random wave fields, Boussinesq type models have received relatively little use for nearshore process research on open beaches; exceptions are Chen et al. (2001) and Kirby and Chen (2003) who simulated longshore currents at field scale.

In this chapter, a modelling investigation of transient rip currents is carried out using a Boussinesq model. The model demonstrates that rotational wave-averaged flow can be generated simply by the action of a random wave field on a plane beach. This rotational flow includes coherent wave-averaged flow structures such as vortices and transient rips. By carrying out a series of simulations using different beach slopes and wave spectra, the effect of different beach slopes and wave fields on the frequency, intensity and direction of transient rip currents and the total cross-shore flux due to rotational flow was investigated. The generation mechanism of transient rip currents is investigated in detail using the modelling results. Finally, the general characteristics of the rotational component of the flow field, in terms of energy ratios and velocity spectra, are presented.

7.2 Model implementation

The simulations were carried out using a modified version of *Funwave*, an open source distribution of a model developed at *The Center for Applied Coastal Research, University of Delaware*. The model is based on the fully nonlinear Boussinesq equations of Wei et al. (1995), with an additional term to include vertical vorticity conservation at second order in the dispersive parameter as described by Chen et al. (2001). For completeness, and for the context of the subgrid parameters detailed later, a brief outline of the model is presented, including the governing equations, treatment of wave breaking, subgrid mixing and boundary conditions. Detailed description of the model subgrid schemes are described in Kirby et al. (1998a), Kennedy et al. (2000) and Chen et al. (2000).

The equation for the conservation of mass is:

$$\beta \tilde{\eta}_t + \nabla \cdot \mathbf{M} + F_s = 0 \quad (7.3)$$

$$\begin{aligned} \mathbf{M} = \Lambda \left[\tilde{\mathbf{u}}^{(r)} + \left(\frac{z_r^2}{2} - \frac{1}{6}(h^2 - h\tilde{\eta} + \tilde{\eta}^2) \right) \nabla(\nabla \cdot \tilde{\mathbf{u}}^{(r)}) \right. \\ \left. + \left(z_r + \frac{1}{2}(h - \tilde{\eta}) \right) \nabla(\nabla \cdot (h\tilde{\mathbf{u}}^{(r)})) \right] \end{aligned} \quad (7.4)$$

where $\tilde{\mathbf{u}}^{(r)}$ is the horizontal velocity vector at a reference depth of $z_r = -0.531h$. Subscript t denotes time differentiation. The still water depth is h and $\tilde{\eta}$ is the instantaneous surface elevation. The parameters β and Λ account for the presence of a slot in the vicinity of the shoreline as discussed below. The term F_s is a source function which operates along a strip in the seaward region of the domain; this effectively adds and subtracts mass from this strip, thereby generating waves.

The momentum equation is:

$$\tilde{\mathbf{u}}_t^{(r)} + (\tilde{\mathbf{u}}^{(r)} \cdot \nabla) \tilde{\mathbf{u}}^{(r)} + g \nabla \tilde{\eta} + \mathbf{\Gamma}_1 + \mathbf{\Gamma}_2 + \mathbf{\Gamma}_3 - \mathbf{F}_{br} - \mathbf{F}_m + \mathbf{F}_b = 0 \quad (7.5)$$

The terms while \mathbf{F}_{br} , \mathbf{F}_m and \mathbf{F}_b account for wave breaking, lateral momentum mixing and bottom friction. $\mathbf{\Gamma}_1$ and $\mathbf{\Gamma}_2$ are dispersive terms:

$$\mathbf{\Gamma}_1 = \frac{z_r^2}{2} \nabla(\nabla \cdot \tilde{\mathbf{u}}^{(r)}) + z_r \nabla(\nabla \cdot (h\tilde{\mathbf{u}}^{(r)})) - \nabla \left[\frac{\eta^2}{2} \nabla \cdot \tilde{\mathbf{u}}_t^{(r)} + \eta \nabla \cdot (h\tilde{\mathbf{u}}_t^{(r)}) \right] \quad (7.6)$$

$$\begin{aligned} \mathbf{\Gamma}_2 = \nabla \left\{ (z_r - \eta)(\tilde{\mathbf{u}}^{(r)} \cdot \nabla) [\nabla \cdot (h\tilde{\mathbf{u}}^{(r)})] + \frac{1}{2}(z_r^2 - \eta^2)(\tilde{\mathbf{u}}^{(r)} \cdot \nabla)(\nabla \cdot \tilde{\mathbf{u}}^{(r)}) \right\} \\ + \frac{1}{2} \nabla \left\{ [\nabla \cdot (h\tilde{\mathbf{u}}^{(r)}) + \eta \nabla \cdot \tilde{\mathbf{u}}^{(r)}]^2 \right\} \end{aligned} \quad (7.7)$$

and $\mathbf{\Gamma}_3$ is a second order correction to the vorticity (Chen et al., 2001):

$$\mathbf{\Gamma}_3 = \tilde{\mathbf{u}}^{(r)} \times \left[\nabla \times \left\{ (z_r - z) \nabla [\nabla \cdot (h \tilde{\mathbf{u}}^{(r)})] + \left(\frac{z_r^2}{2} - \frac{z^2}{2} \right) \nabla (\nabla \cdot \tilde{\mathbf{u}}^{(r)}) \right\} \right] \quad (7.8)$$

\times and $\nabla \times$ are the two-dimensional cross product and curl. A quasi fourth-order finite difference scheme (Wei et al., 1995) is used to solve Equations 7.3 and 7.5.

Wave breaking is modelled with an eddy viscosity formulation which redistributes momentum and dissipates energy locally at the front face of the wave. The breaking term is given by:

$$\mathbf{F}_{br} = \frac{1}{(h + \eta)} \left\{ \nabla \cdot \nabla [\nu_b (h + \eta) \tilde{\mathbf{u}}^{(r)}] + \nabla (\nabla \cdot [\nu_b (h + \eta) \tilde{\mathbf{u}}^{(r)}]) \right\} \quad (7.9)$$

$$\nu_b = BL^2 |(h + \eta) \nabla \cdot \mathbf{M}| \quad (7.10)$$

where L is a mixing length coefficient and set at 1.2, and B varies between 0 and 1 and represents the intensity of breaking. Breaking begins when $\eta_t \geq 0.35\sqrt{gh}$ and stops when $\eta_t < 0.15\sqrt{gh}$

Sub-grid turbulent mixing is included using a Smagorinsky (1963) model which calculates an eddy viscosity based on the wave-averaged currents. The term \mathbf{F}_m in the momentum equation is identical to Equation 7.9 but with the viscosity, ν_b replaced by:

$$\nu_t = c_m \Delta x \Delta y \left[\left(\frac{\partial U^r}{\partial x} \right)^2 + \left(\frac{\partial V^r}{\partial y} \right)^2 + \frac{1}{2} \left(\frac{\partial U^r}{\partial y} + \frac{\partial V^r}{\partial x} \right)^2 \right]^{\frac{1}{2}} \quad (7.11)$$

where U^r and V^r are mean velocity components averaged in blocks of two peak wave periods.

Bottom friction is approximated with a quadratic law:

$$\mathbf{F}_b = \frac{f_b}{h + \eta} \tilde{\mathbf{u}}^{(r)} |\tilde{\mathbf{u}}^{(r)}| \quad (7.12)$$

The seaward boundary and landward boundary have a sponge layer region which absorbs any outgoing waves. The run-up at the shoreline is modelled using a slot technique, in which the beach is made semi-permeable and the solution domain includes the region where the beach is above the still water level. The incident wave field is input in the seaward region of the domain using a source function method (Wei et al., 1999) in which mass is effectively added and removed, thereby generating an arbitrary wave spectrum.

Following Chen et al. (2001), the spectra are represented in 100 bins of equal energy. To match the periodic boundary conditions, the directional bins at each

frequency are then determined by the requirement that the longshore wave-number components are integer of the longshore length. The end result is a matrix of spectral densities with associated frequencies and directions.

At the source line, the amplitude for the source function input is generated by summing the components:

$$a^S(y, t) = \sum_{i=1}^{i=n_f} \sum_{j=1}^{j=n_d} \Phi^S(i, j) \cos [k_i \sin(\theta_j)y - 2\pi f_i t + \phi_{ij} + \phi_{ij}^* t] \quad (7.13)$$

where f_i is the frequency, θ_j the direction relative to the x-axis, Φ_{ij}^S the spectral density and ϕ_{ij} a random phase component for the $[i, j]^{th}$ component¹. The $\phi_{ij}^* t$ term is an additional random time-dependent phase change which prevents a longshore stationary wave field from being generated. This addition term, and the discretization for the periodic domain are detailed below in Section 7.2.1. For each simulation using the same spectrum, the source input is identical, as the random seed is kept the same.

The open source code was modified to include the boundary conditions discussed above, input of an arbitrary random wave field by the source function method of Wei et al. (1999), and the vorticity correction (Chen et al., 2001) of the original momentum equation of Wei et al. (1995). The original Fortran code was also parallelised to run on a high performance computer.

Quite extensive testing and validation of *Funwave* has been reported in Kennedy et al. (2000) and Chen et al. (2001). The simulations of laboratory rip currents by Chen et al. (1999) showed good agreement with measured data, at least for topographic rips. The evidence is that the model reproduces nearshore hydrodynamics well, and the model is used here as an investigative tool without further validation.

7.2.1 Discretization of wave spectra

The amplitude for an arbitrary spectrum can be reconstructed from a spectral matrix, Φ_{ij}^S of n_ω discrete frequency and n_θ directional bins by:

$$a^S(y, t) = \sum_{i=1}^{i=n_\omega} \sum_{j=1}^{j=n_\theta} \Phi_{ij} \cos [k_i \sin \theta_j - \omega_i t + \phi_{ij}] \quad (7.14)$$

For a directionally symmetric spectrum with central direction perpendicular to the source line as is the case with spectrums used for the simulations, each spectral bin $[i, j]$ in Equation 7.2.1 exists as one member of a pair of opposite directions. Denoting directional index pairs by $[i, j^+]$ and $[i, j^-]$ so that $\theta_{j^+} = -\theta_{j^-}$, Equation 7.2.1 can

¹ ϕ and ψ are redefined for this section only

be rewritten as:

$$a^S(y, t) = \sum_{i=1}^{i=n_\omega} \sum_{j=1}^{j=n_{\theta+}} \Phi_{ij+} \cos [k_i \sin \theta_{j+} - \omega_i t + \phi_{ij+}] + \Phi_{ij-} \cos [k_i \sin \theta_{j-} - \omega_i t + \phi_{ij-}] \quad (7.15)$$

which, as $\sin \theta_{j+} + \sin \theta_{j-} = 0$ and $\Phi_{ij+}^S = \Phi_{ij-}^S$ is equivalent to:

$$a^S(y, t) = \sum_{i=1}^{i=n_\omega} \sum_{j=1}^{j=n_{\theta+}} 2\Phi_{ij+}^S \cos [\omega_i t + \varphi_{ij+}] \cos [k_i \sin \theta_{j+} + \psi_{ij+}] \quad (7.16)$$

where $\varphi_{ij+} = (\phi_{ij+} + \phi_{ij-})/2$ and $\psi_{ij+} = (\phi_{ij+} - \phi_{ij-})/2$. Equation 7.2.1 can be seen to represent a sum of longshore fixed standing waves. Note that Equation 7.2.1 is strictly only valid for symmetric discretizations of the spectrum, i.e when each (ω_i, θ_j) bin in the spectral matrix has a corresponding (ω_i, θ_{-j}) . Note also that this effect is not specific to a periodic domain. While there is no proof, it is intuitively expected, and found in practice, that the end result is also the same for sufficiently fine nonsymmetric discretizations of a symmetric spectrum.

The problem with a perfectly symmetrical spectrum, as seen by Equation 7.2.1, is that the wave field becomes unrealistically fixed relative to longshore position on the beach. As a result, areas of high and low waves, and hence radiation stress, also become fixed. When investigating forcing due to a random wave field on an otherwise homogeneous longshore domain, this is highly undesirable. In reality, of course, the spectrum is not perfectly symmetrical and changes in time, and as a result additional terms arise in the phase of both of the cosine functions in Equation 7.2.1 which act to move the wave field around. To simulate this in the source function an additional time dependent random term was included in the phase function, χ_{ij} so that Equation 7.2.1 becomes:

$$a^S(y, t) = \sum_{i=1}^{i=n_\omega} \sum_{j=1}^{j=n_d} \Phi_{ij}^S \cos [k_i \sin(\theta_j)y - (\omega_i + \chi_{ij})t + \phi_{ij}] \quad (7.17)$$

This modifies Equation 7.2.1 to:

$$a^S(y, t) = \sum_{i=1}^{i=n_\omega} \sum_{j=1}^{j=n_{\theta+}} 2\Phi_{ij+}^S \cos [\omega_i t - \varphi_{ij+}^* t + \varphi_{ij+}] \cos [k_i \sin \theta_{j+} - \psi_{ij+}^* t + \psi_{ij+}] \quad (7.18)$$

where $\varphi_{ij+}^* = (\chi_{ij+} + \chi_{ij-})/2$ and $\psi_{ij+}^* = (\chi_{ij+} - \chi_{ij-})/2$. Now the source line "standing waves" move alongshore with a celerity of $\psi_{ij+}^*/k_i \sin \theta_{j+}$. Note that it also introduces a slight frequency shift in the fundamental wave as well, thus technically violating the dispersion relation. However, since the dispersion relation would not

be satisfied perfectly in the domain in any case, small values of χ_{ij} do not appear to cause problems for the source function and the waves presumably relax to their Boussinesq solution almost immediately. It was found that $\chi_{ij} = 0.1N\omega$, with N a uniformly distributed random number between 0 and 1, works well.

In order to satisfy the periodic boundary conditions there must be an integer number of wavelengths in the cross-shore direction:

$$k_i \sin \theta_j = \frac{2\pi p}{L} = pk_D \quad (7.19)$$

where p is an integer and k_D is the wavenumber of the longshore domain length. The dispersion relation is assumed to be valid at the source line so that: $\omega_i = gk_i \tanh k_i h$. In practice the spectrum, $S(\omega_i, \theta_j)$ is first discretised into bins to give the frequencies, then the dispersion relation is inverted numerically to give a set of k_i . Note that p in Equation 7.2.1 can be negative or zero, and to keep notation simple so that $p = j$, corresponding to the j^+ and j^- indices above. Then for each k_i , θ_j is determined by inverting Equation 7.2.1 so that:

$$\theta_j = \arcsin \left(\frac{pk_D}{k_i} \right); p = j \quad (7.20)$$

Once the structure of the frequency/directional bins is set up, the spectral function, Equation 7.24 can then be mapped onto the spectral matrix. The amplitudes of the individual components are given by:

$$\Phi_{ij}^S = \sqrt{2\Phi(\omega_i, H, \theta_j)\Delta\omega_i\Delta\theta_j} \quad (7.21)$$

where $\Delta\omega_i$ and $\Delta\theta_j$ are the bin dimensions for each component.

The longshore variance of the source line amplitudes were checked for the periodic case and a non-periodic source line without the restriction of Equation 7.2.1:

$$\mathcal{V}_1 = \frac{1}{n} \sum_{i=1}^n \text{Var} [a(y, t_i)] \quad (7.22)$$

$$\mathcal{V}_2 = \text{Var} \left[\sqrt{\frac{1}{n} \sum_{i=1}^n a(y, t_i)^2} \right] \quad (7.23)$$

where a is the amplitude at the source function for longshore position y at timestep t_i , and the variance is along the y variable in each case. For spectra N10 which should experience the greatest effect of having to satisfy Equation 7.2.1, the time averaged longshore variances are $\mathcal{V}_1 = 4.9 \times 10^{-6}$ for the periodic case, and $\mathcal{V}_1 = 3.6 \times 10^{-6}$ for a non-periodic source line. For \mathcal{V}_2 , which a measure of the longshore variability of wave energy averaged over the whole simulation, values are 1.9×10^{-5} and 1.4×10^{-5} . So

while the need to map to integer longshore wave lengths has increased the longshore variability, it has not done so dramatically. More importantly, the small values for \mathcal{V}_2 show that fixed longshore locations of high and low waves have not been generated.

7.3 Experiments

7.3.1 Model domain

The domain for all the numerical experiments was a plane beach of varying slope as shown in Figure 7.1. The coordinate axes are oriented with x directed cross-shore towards the shoreline, and y longshore. The grid spacing in the cross-shore and longshore directions were 2 m and 3 m respectively. For each slope, the outer wave generation region was kept the same, 7 m deep and 160 m long. The source line was located at $x = 60$ m. The domain is 1191 m long in the longshore direction while the cross-shore length extends to beyond the limit of wave uprush and depends on the slope.

The slot width used for the shoreline run-up was $\delta = 0.04$ and the shape parameter $\lambda = 10$ which is rather too large for accurate simulation of wave run-up (Kennedy et al., 2000). This was the smallest slot size that could be used while maintaining numerical stability for all the simulations, and for the sake of consistency between runs, the same value was used throughout. However, tests of different slot widths indicated that the resulting error affects only the swash zone; the setup further out is very similar so the error is unlikely to be important for the fundamental mechanisms occurring away from the swash zone.

7.3.2 Wave spectra

The input wave spectra were directional spread TMA spectra (Bouws et al., 1985). A one-dimensional TMA spectrum was constructed for depth H with a peak frequency of f_p :

$$\begin{aligned}\Phi(f, H) &= \alpha g^2 (2\pi)^{-4} f^{-5} \Psi_1(f, H) \Psi_2(f/f_p) \Psi_3(f, f_p, \gamma, \mu_a, \mu_b) \\ \Psi_1(f, H) &= \frac{\left[k(f, H)^{-3} \frac{\partial k(f, H)}{\partial f} \right]}{\left[k(f, \infty)^{-3} \frac{\partial k(f, \infty)}{\partial f} \right]} \\ \Psi_2(f/f_p) &= \exp \left[-5/4 (f/f_p)^{-4} \right] \\ \Psi_3(f, f_p, \gamma, \omega_a, \omega_b) &= \exp \left[\ln(\gamma) \exp(-(f - f_p)^2 / 2\mu^2 f_p^2) \right]\end{aligned}$$

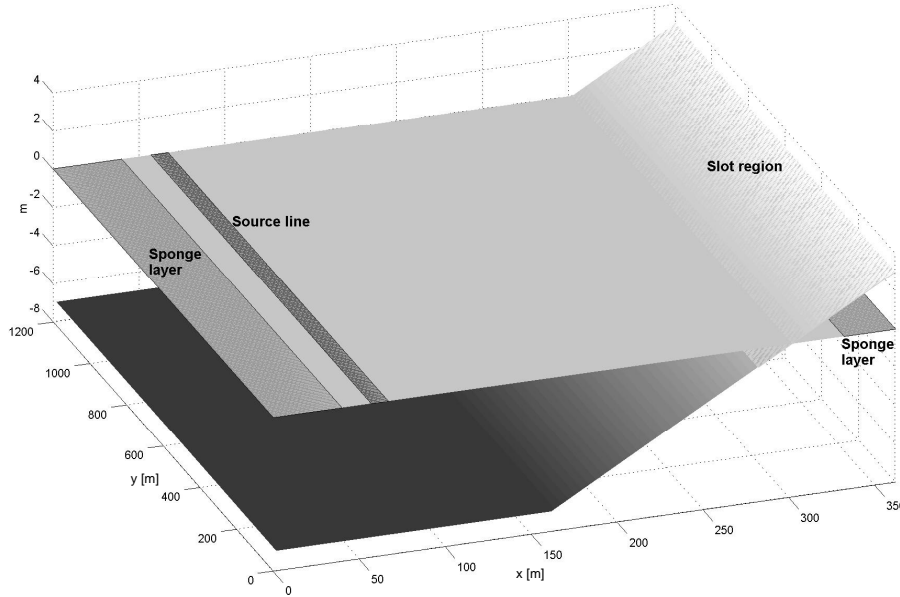


Figure 7.1: Model domain

$$\mu = \begin{cases} \mu_a & f_p \geq f \\ \mu_b & f_p < f \end{cases}$$

where k is the wavenumber for a particular depth and frequency. The dispersion relation, $\omega^2 = gk \tanh(kh)$ is assumed to be valid. Parameters used are: $\gamma = 2$ $\alpha = 0.014$ $\omega_a = 0.07$ $\omega_b = 0.09$.

The 1D frequency spectra were converted to directional spectra using a directional spreading function (Mitsuyasu, 1975):

$$\Phi(f, H, \theta) = \Phi(f, H)G(\theta) \quad (7.24)$$

$$G(\theta) = \sum_i w_i \cos^{2\Sigma_i} \left(\frac{\theta - \theta_i}{2} \right) \quad (7.25)$$

where θ is the peak direction of each directional mode and w_i are weights of each mode so that $\int G(\theta)d\theta = 1$. All the simulations described here have a single directional mode with $\theta_1 = 0$. The value of Σ was varied to produce a spectrum with wide or narrow spreading.

For the simulations, four different spectra were generated and the parameters for these are shown in Table 7.1. The spectra are shown in the left hand column in Figure 7.2. The RMS wave height in each case was set at 0.7 m. Spectrum N10 is an ideal representation of swell with narrow spreading and N7 is shorter period waves with narrow spreading. Spectrum W5 corresponds to an idealised locally generated, directionally spread sea, while W7 is a longer period directionally spread

Table 7.1: Parameters used for wave spectra. The main direction, θ_1 , is measured relative to the x-axis. Frequencies are in 50 bins of equal energy bounded by f_{min} and f_{max} . The RMS wave height for all the spectra is 1.0 m.

Spectra	$T_p(s)$	$f_p(Hz)$	$f_{min}(Hz)$	$f_{max}(Hz)$	θ_1	Σ_1
N10	10	0.1	0.02	0.3	0	100
N7	7	0.143	0.05	0.4	0	100
W7	7	0.143	0.05	0.4	0	10
W5	5	0.2	0.1	0.5	0	10
VN10	10	0.1	0.02	0.3	0	1000

sea. The intention was to compare the effects of period and spreading while using spectra which are still reasonable for natural conditions. The right hand column of Figure 7.2 shows the spectrum calculated from simulated data just shoreward of the source line generation region at $x = 100$ m, $y = 600$ m. Surface elevation, and the two velocity components were used to estimate the directional spectrum using the Extended Maximum Likelihood Method (Isobe et al., 1984) as if they were measured field data. The estimation method cannot retrieve the directional spectrum perfectly, but correspondence with the input spectra is good.

7.3.3 Simulation runs

The model parameters used for the simulations were all identical except for the turbulent mixing coefficient and bottom friction coefficient. Closely following the values of Chen et al. (2001) for field scale simulation of longshore currents, values of $c_m = 0.2$ and $f_b = 0.001$ were used for the main set of simulations. The time step was set to 0.1 s for all runs and each simulation ran for 50000 time steps or 5000 s, with the exception of runs 13-16 which were only run for 10000 time-steps (1000 s). All times in the text or figures are relative to $t = 0$ s at the (cold) start of the simulations.

A total of 17 runs were carried out. Runs 1-12 tested each beach slope with each spectra and are the main experimental simulations. Runs 13-16 were carried out to check the influence of the turbulent mixing coefficient and bottom friction coefficient for the same conditions as run 5. Finally, run 17 was for a spectra with an unrealistically narrow spread on the 0.03 beach slope. This wave field has a spread of frequencies but with so little directional spreading that all waves are effectively perpendicular to the beach; the small amount of spreading induces a small alongshore perturbation. The model runs are summarised in Table 7.2.

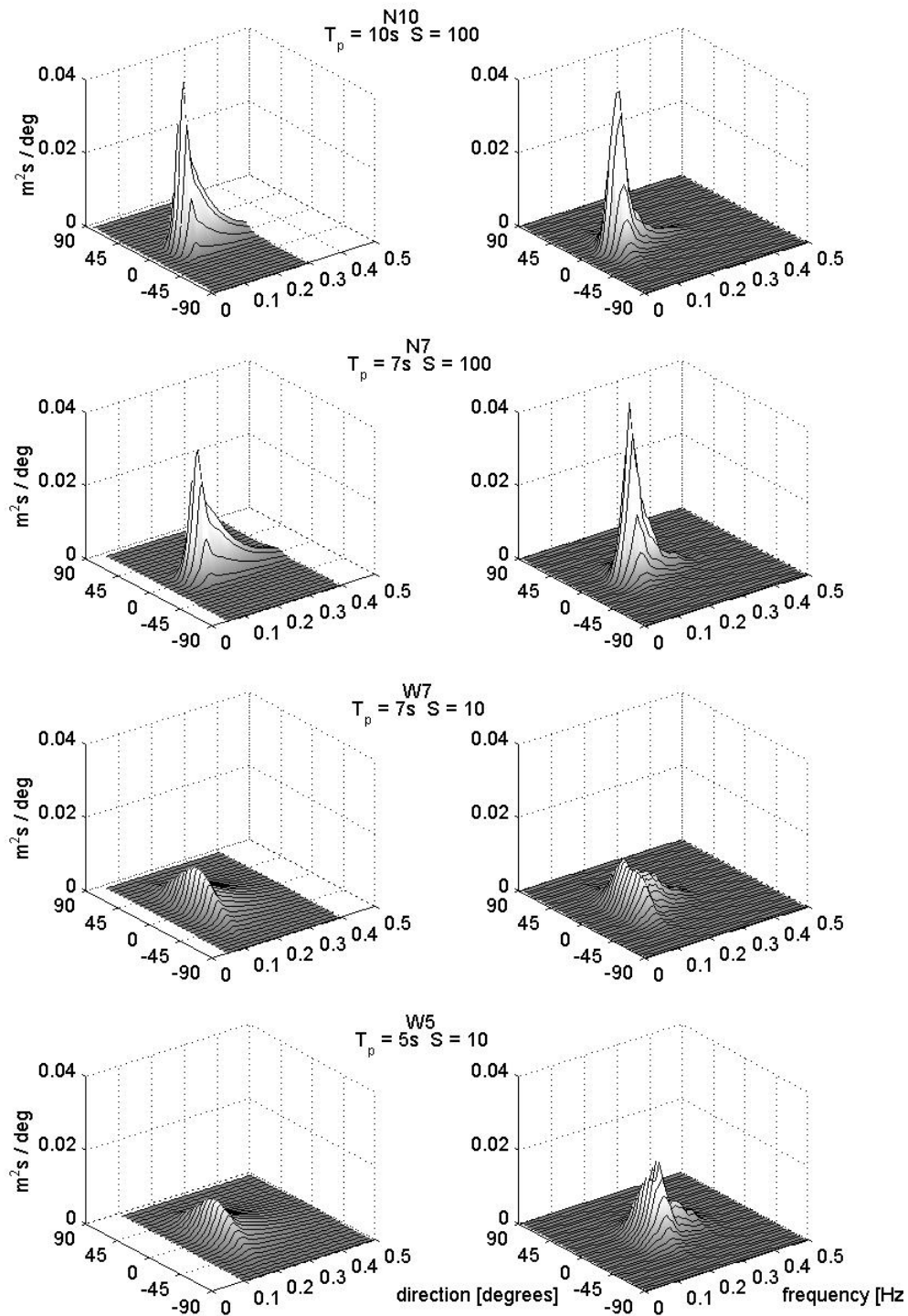


Figure 7.2: Directional spectra used in the simulations. Directions are measured anticlockwise from the x-axis. The left column are the ETMA spectra input at the source line. The right column are the directional spectra estimated from the simulated surface elevation and velocities 50 m shoreward of the source line.

Table 7.2: Simulation runs carried out. T_p is the peak period of the spectra, Σ_1 is the spectra directional spreading parameter, f_b is the bottom friction coefficient and c_m is the subgrid mixing coefficient.

Run	Abbrev.	Slope	Spectra	f_b	c_m
1	0.05N10	0.05	N10	0.001	0.2
2	0.05N7	0.05	N7	0.001	0.2
3	0.05W7	0.05	W7	0.001	0.2
4	0.05W5	0.05	W5	0.001	0.2
5	0.03N10	0.03	N10	0.001	0.2
6	0.03N7	0.03	N7	0.001	0.2
7	0.03W7	0.03	W7	0.001	0.2
8	0.03W5	0.03	W5	0.001	0.2
9	0.015N10	0.015	N10	0.001	0.2
10	0.015N7	0.015	N7	0.001	0.2
11	0.015W7	0.015	W7	0.001	0.2
12	0.015W5	0.015	W5	0.001	0.2
13	-	0.03	N10	0.01	0.2
14	-	0.03	N10	0.0001	0.2
15	-	0.03	N10	0.001	2.0
16	-	0.03	N10	0.001	0.02
17	-	0.03	VN10	0.001	0.2

7.4 Results

The model solution is a time-series of instantaneous surface elevation and velocities at the reference height. The instantaneous mass flux, \mathbf{M} , was also retrieved. From the instantaneous mass flux and elevations, a wave-averaged mass flux, $\overline{\mathbf{M}}$, and surface elevation, $\overline{\eta}$ is defined, where the overline indicates averaging the instantaneous values over blocks of two peak wave periods, T_p . A depth and wave-averaged velocity is then given by $\overline{\mathbf{U}} = \overline{\mathbf{M}}/(\overline{\eta} + d)$. To avoid infinite depth average current at the shoreline, $\overline{\mathbf{U}} = \mathbf{u}^{(r)}$ for $\overline{\eta} + d < 0.2$, justified on physical grounds by the fact that any resolvable waves will be shallow water waves at this depth. The vorticity of the currents is defined as $\overline{\zeta} = \nabla \times \overline{\mathbf{U}}$. Unless stated otherwise, the terms current and vorticity will refer to the depth and wave-averaged definitions. The averaging is effectively a filtering operation with lowpass cutoff of $f = 1/2T_p$. It is important to note that the wave-averaged fields retain temporal resolution by averaging over $2T_p$ only, but that they cannot be directly related to the wave-averaged current in the classic wave-averaged equations, due to violation of the usual assumption that $\overline{\mathbf{U}(\mathbf{u} - \overline{\mathbf{U}})} = \mathbf{0}$.

Figure 7.3 shows a snapshot of the instantaneous surface elevation for run 5 (slope 0.03 and narrow spectrum with peak period 10 s). The waves can be seen to shoal and become increasing asymmetric as they approach the shore, eventually

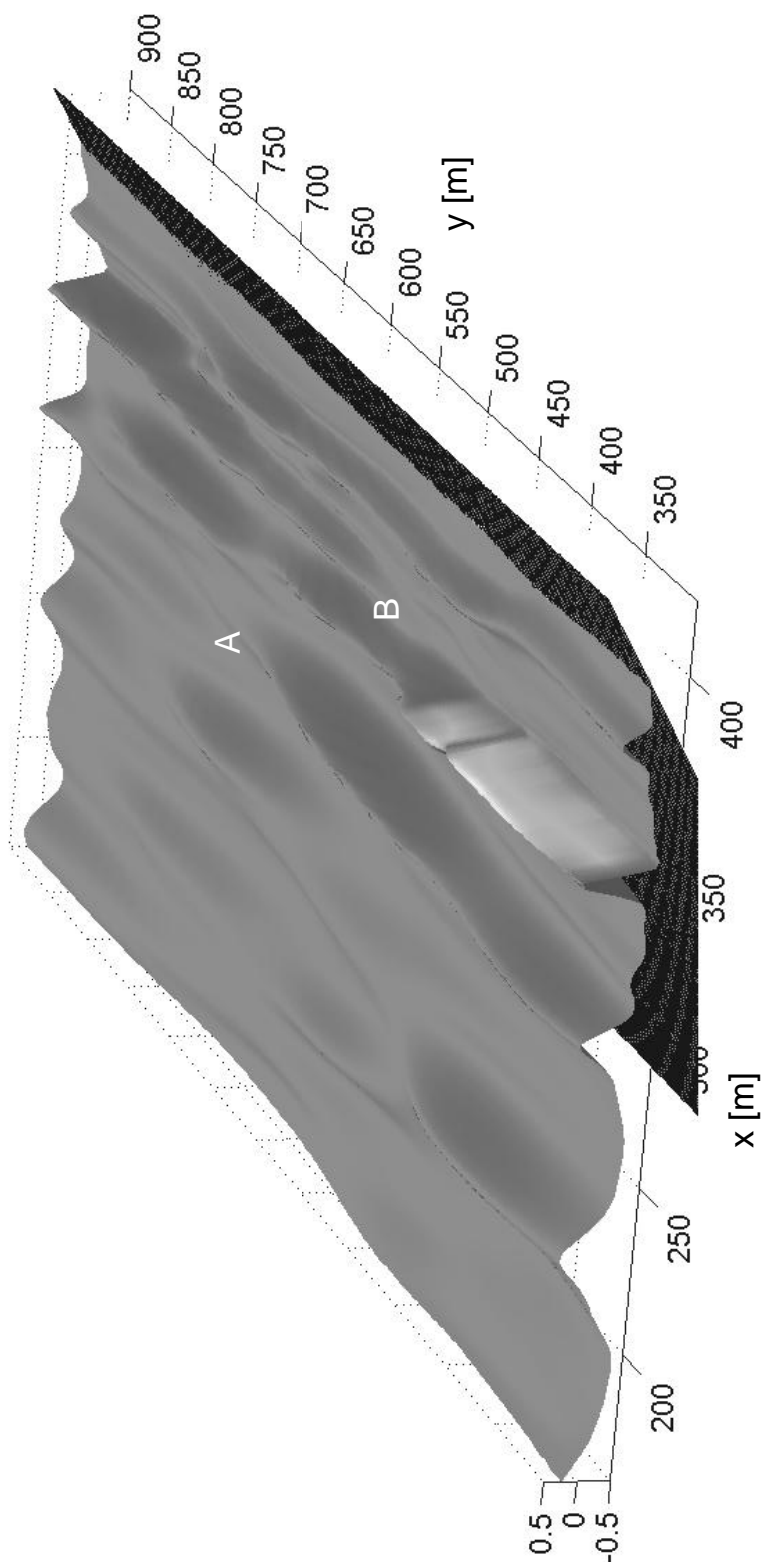


Figure 7.3: Instantaneous surface elevation for run 5 at $t = 4160$ s for the centre of the longshore extent of the domain. The light coloured region at the front edge of one of the crest is a region of intense breaking. Two types of discontinuities in wave crests are indicated: A. End point of an individual wave crest. B. Merging of separate wave crests.

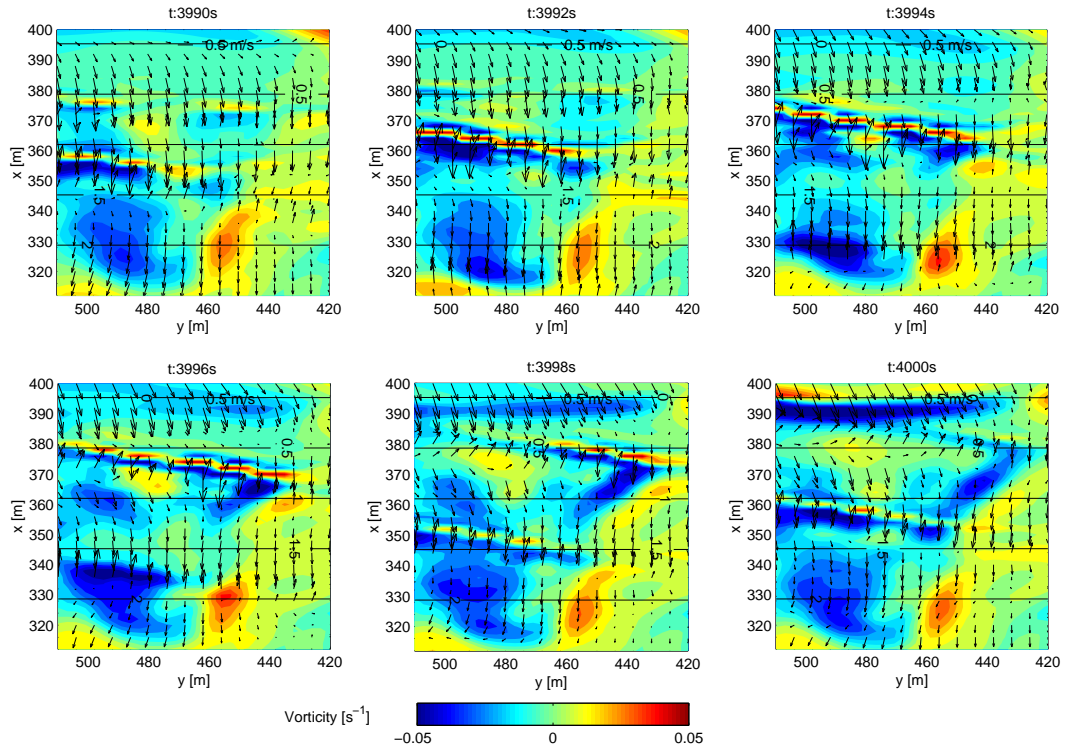


Figure 7.4: Series of snapshots of a instantaneous velocity and vorticity. The lines of adjacent positive and negative vorticity are caused by breaking wave crests. The arrow in the frame for $t = 3998s$ is to highlight the shedding of negative vorticity from the end of the wave crest.

decreasing in height as they break near the shoreline. The wave crests are not continuous, possessing two types of discontinuity: regions where two or more wave crests meet and areas at which a wave crest ends. The instantaneous velocities are dominated by the wave orbital velocities. However, the vorticity of the instantaneous flow is very persistent, being advected and modulated due to vortex stretching by the passing waves, but varying over a much longer timescale. This is seen in a series of snapshots of instantaneous vorticity and velocity in Figure 7.4; although there is significant local influence as the incident wave moves through, the net result is a relatively small change to the vorticity field. Also noticeable in the series of snapshots is the shedding of vorticity from the ends of breaking wave crests.

The currents show complex flow patterns in all of the runs except run 17. Figure 7.6 shows mean flow vectors and vorticity (these are for the same time as the instantaneous surface in Figure 7.3). The existence of discrete vortices and more complex features, like transient rip currents, are seen in all of the wave and depth-averaged current fields. The transient rip currents appear as narrow regions of off-shore flow which penetrate offshore and are associated with a vortex pair in the head.

The offshore penetration of the rip currents is limited, reaching the 4 m contour in some of the beach slope/spectra conditions, but not beyond. The rip currents are oriented at varying angles to the shore but always have opposite regions of vorticity along the rip neck and a vortex pair in the head region.

Figure 7.5 shows the trajectories of virtual particles released in the transient rip feature shown in Figure 7.6. The trajectories were calculated by integrating the drifter position forward in time with the instantaneous model velocities, \mathbf{u} . Small velocity fluctuations, consistent with the subgrid eddy viscosity, were also added to simulate subgrid turbulence. With a directionally narrow swell and a beach slope of 0.03, the conditions are qualitatively similar to those during the drifter deployments described in Chapter 5. The virtual trajectories are very similar to measured trajectories in transient rip currents (Figures 5.7 and 5.8). This provides some qualitative validation that the fundamental dynamics of the transient rip currents are reproduced in the model.

The vorticity field has vortices and vorticity gradients at a range of scales; there are similarities with the vortical flow seen in nonlinear simulations of longshore current instabilities (Allen et al., 1996; Ozkan-Haller and Kirby, 1999). The presence of low frequency waves can also be seen in the current fields as linear regions of similar flow velocities, but being irrotational, are not seen in the vorticity plots. While the existence of both rotational and long wave currents is ubiquitous, there is significant difference in the appearance of the current field for the different spectra and beach slopes. To illustrate this, the central sections from six different simulations (in order, runs 5, 6, 7, 8, 1, 9) are shown in Figure 7.7. These compare the four spectra on the intermediate beach slope, 0.03, and the three beach slopes for the narrow 10 s peak period spectra, N10. Qualitative differences between the wave spectra are of fewer, but better defined, vortical features for the narrow spread spectra, N10 and N7 compared to W7 and W5. However, the wide spread spectra appear to generate a more even spread of smaller vortices. There is a clear difference between beach slopes for the N10 spectra, as the shallower slope, 0.015 has larger and more intense vortical structures than 0.03, whereas the steep slope, 0.05, has no discernable rotational features at the same vorticity shading scale.

As determined from the distribution of breaking and shoaling of mean wave heights, the average breakpoint position is between 2.0 m and 1.5 m depth, further offshore for the longer period waves. The furthest offshore extent of wave breaking in each case is around the 2.5 m depth contour and based on this, the maximum surf zone widths are 50 m , 83 m , 167 m for the beach slope of 0.05, 0.03 and 0.015 respectively. Depth contours are used as a relative measure of cross-shore location for different beach slopes and spectra,

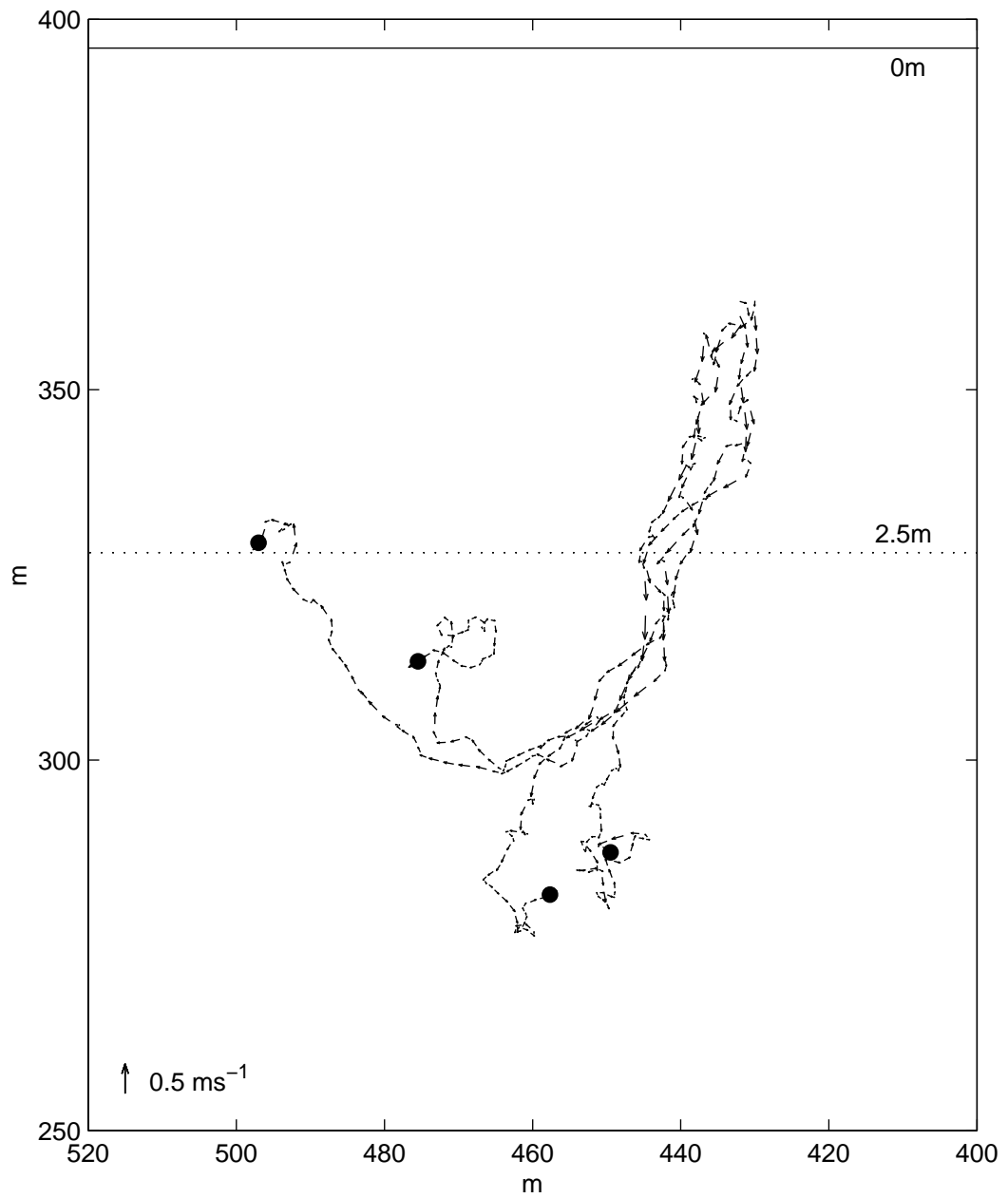


Figure 7.5: Virtual drifter tracks from a deployment lasting 600 s of a cluster of drifters started at from $[x = 360 \text{ m}, y = 430 \text{ m}]$ at $t = 4160 \text{ s}$ during run 5(0.03N10).

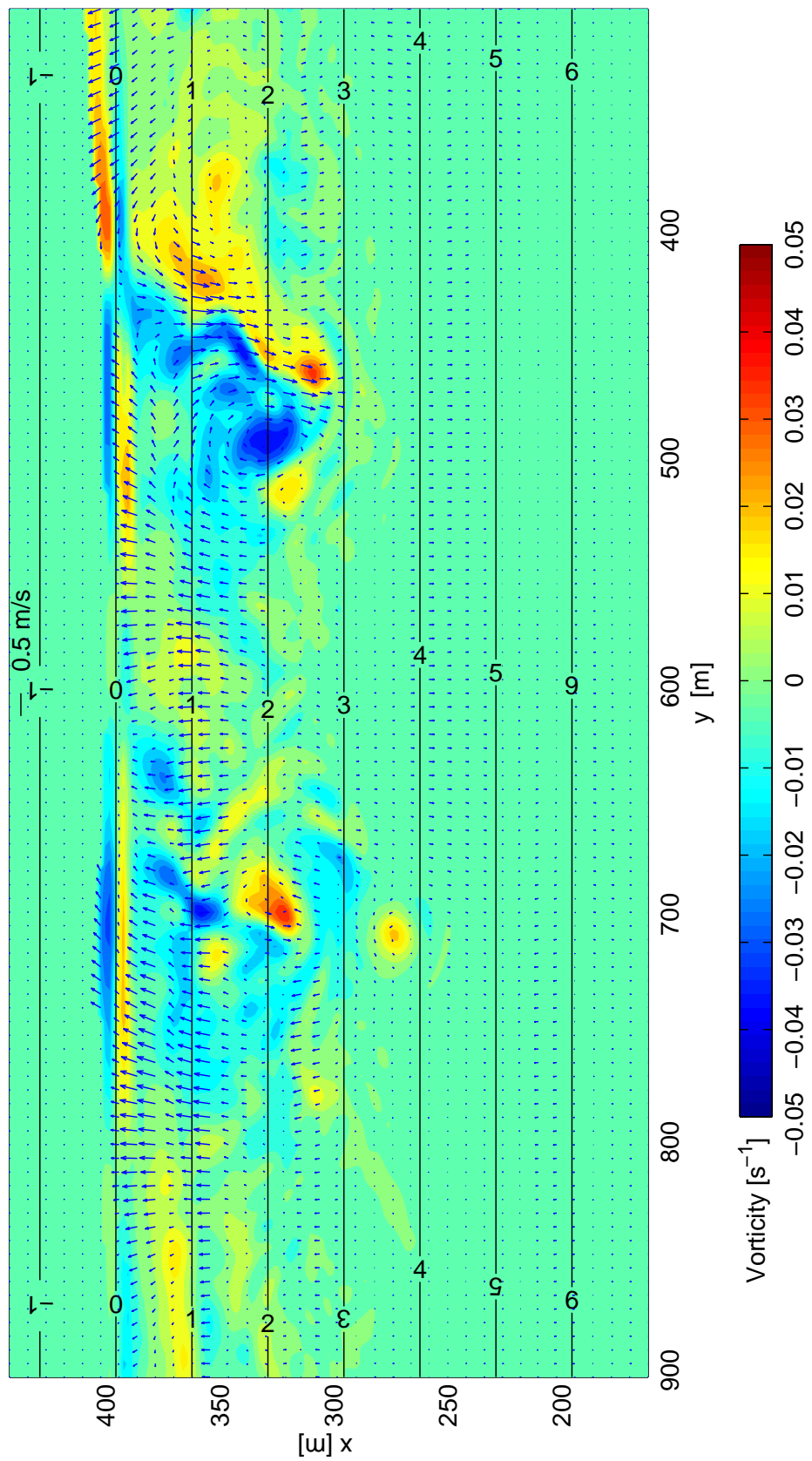


Figure 7.6: Wave and depth-averaged current for run 5 at $t = 4160s$ for the centre of the longshore extent of the domain. A rip current (A.) and discrete vortices (B.) can be seen, clearly associated with regions of strong vorticity.

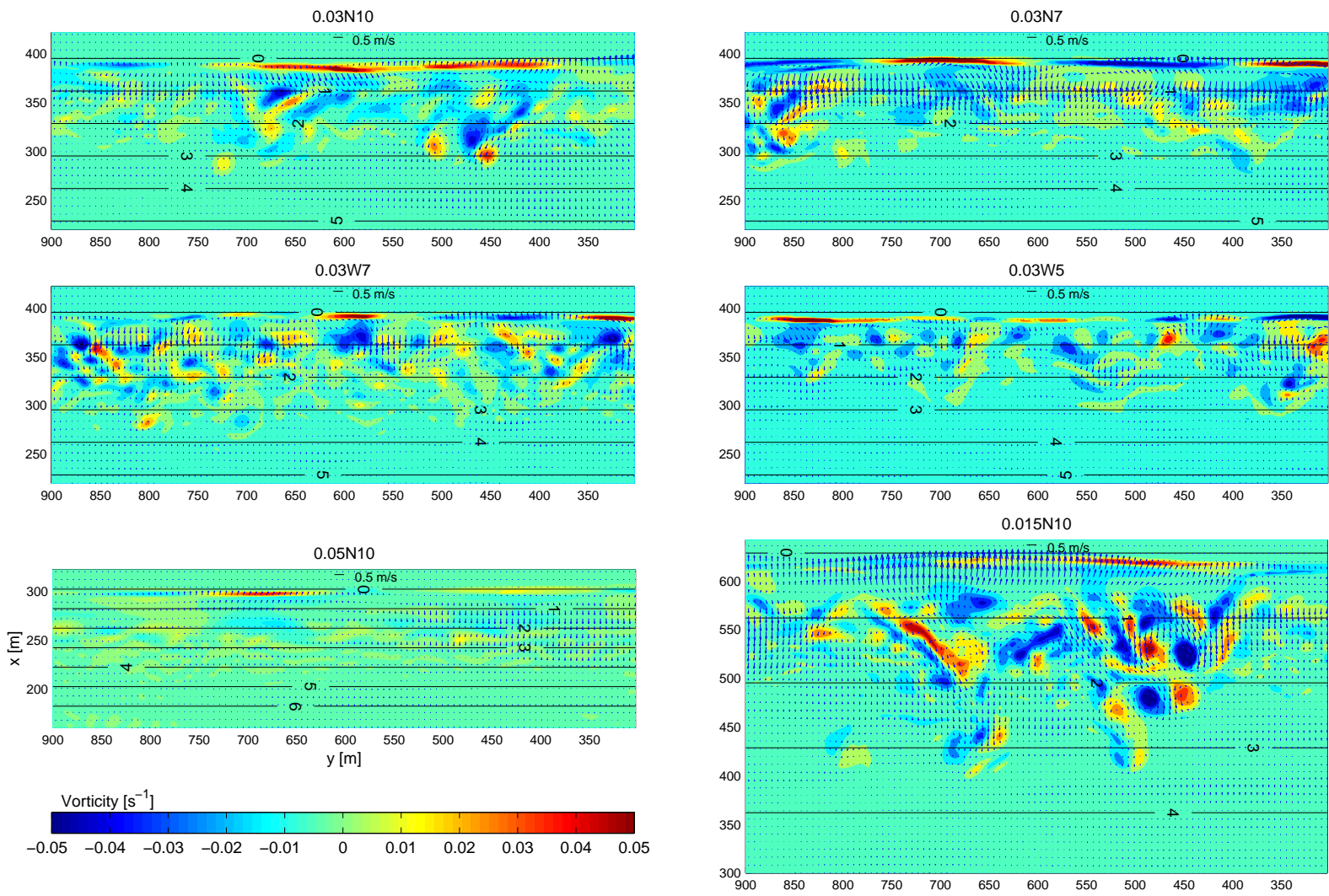


Figure 7.7: Comparison of currents and vorticity for run 5 (0.03N10), 6 (0.03N7), 7 (0.03W7), 8 (0.03W5), 1 (0.05N10) and 9 (0.015N10) at $t = 4700$ s

7.4.1 Longshore timeseries

It is interesting to examine the change of velocity and vorticity distribution along a particular depth contour as a time series. Following Allen et al. (1996) and Ozkan-Haller and Kirby (1999), contour plots of velocity and vorticity as a function of longshore distance and time were produced. These type of (y, t) plots are useful for identifying rip events and discrete vortex features. The (y, t) velocity plots (Figure 7.8) show a mixture of the cross-shore long wave component which appear as bands and rip currents and vortices which appear as isolated regions of cross-shore flow. The vorticity plots are the best way to identify vortical features such as eddies and transient rips, as the long wave velocity signal, being irrotational, is effectively excluded. Rip currents and vortex pairs aligned alongshore appear as adjacent regions with opposite rotation whereas isolated vortices produce a signature with only positive or negative vorticity. The rip current in Figure 7.6 is clearly seen as two strips of opposite signed vorticity. The gradient of a vortical feature in (y, t) space is its longshore propagation velocity. Most of the rip currents seen in Figure 7.8 show little longshore movement during their lifetimes, but some do propagate longshore at up to 0.1 m s^{-1} .

The persistence of patches of vorticity is seen throughout the (y, t) plots, and associated narrow (in the longshore dimension) regions of offshore velocity can be discerned running through the cross-shore velocity plots. This is common to all the time-series for the runs although there are differences between the spectra and beach slopes (Figure 7.9); as would be expected from the snapshots in Figure 7.7 of instantaneous vorticity, there are clear differences of frequency, spacing, intensity and duration of the vorticity patches. A quantitative comparison of the transient rip populations is carried out in Section 7.5.

Spectra of frequency and longshore wavenumber were calculated from the 2D Fourier transform from (y, t) to $k - \omega$ space. The spectra for the mean elevation and current along the 2.0 m isobath (Figure 7.10) show the presence of infragravity waves, which exist at frequencies above the zeroth mode edge wave dispersion line, and another region of energy which lies along the wavenumber axis at low frequencies. The second region cannot be due to infragravity waves as it is well outside the zeroth mode edge wave dispersion curve (Oltman-Shay et al., 1989) and the absence of energy in the surface elevation spectrum indicates a non-divergent motion. Shear waves, the only known mechanism for generating non-divergent *wave* motions, would not normally be expected in the absence of longshore current. Furthermore, there is no evidence of a well defined linear dispersion in $k - \omega$ space as is usually observed in shear waves (Oltman-Shay et al., 1989; Allen et al., 1996; Ozkan-Haller and Kirby, 1999). The obvious conclusion is that this energy is due to the rotational motions

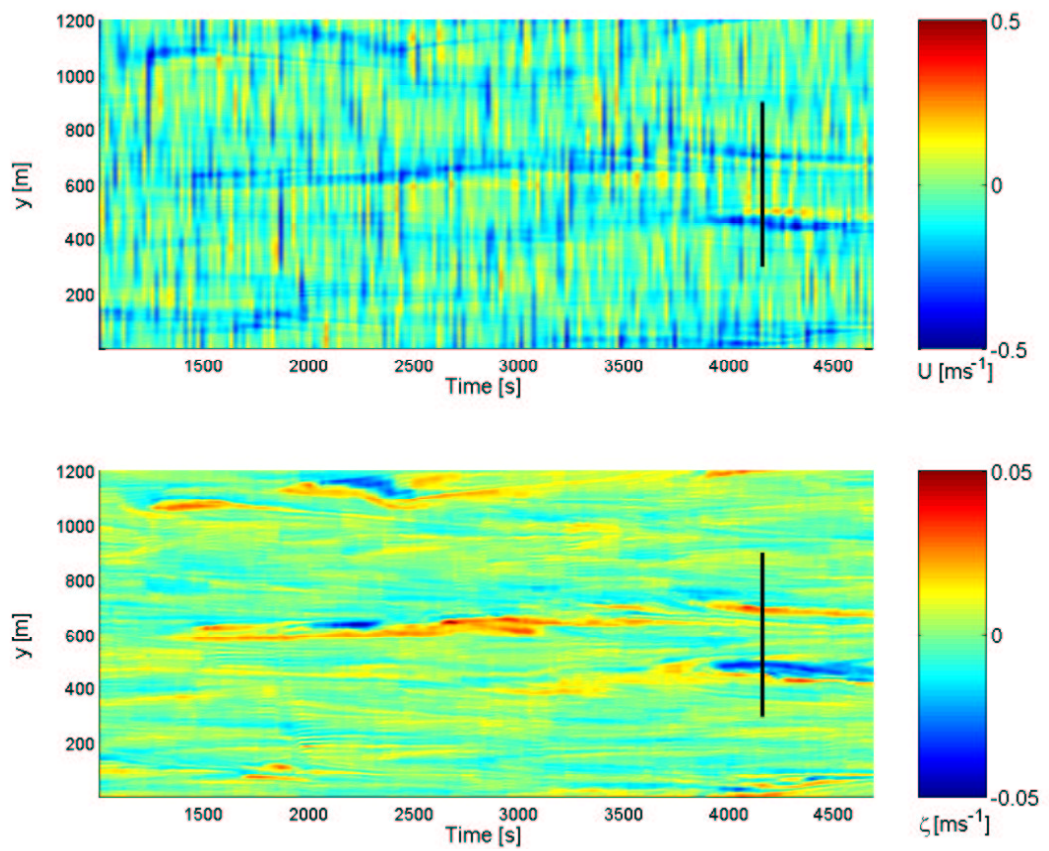


Figure 7.8: Time-series of the cross-shore velocity and vorticity along the 2.0 m isobath for run5 (0.03N10). The solid lines correspond to the snapshot of Figure 7.6.

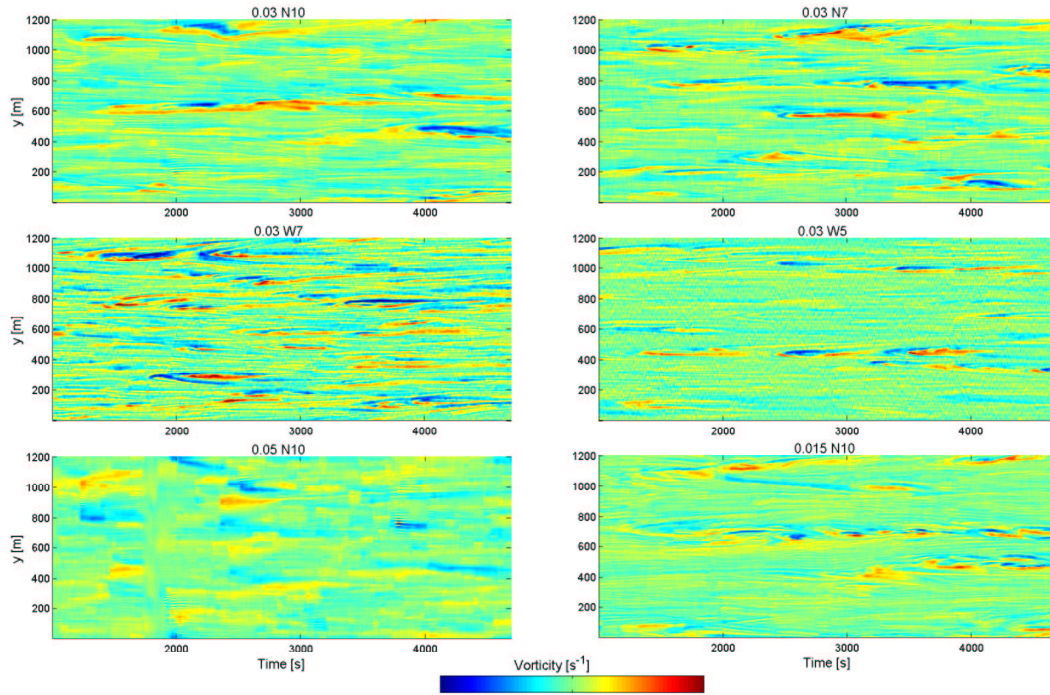


Figure 7.9: Longshore vorticity time-series on 2 m isobath for run 5 (0.03N10), 6 (0.03N7), 7 (0.03W7), 8 (0.03W5), 1 (0.05N10) and 9 (0.015N10).

associated with vortices and transient rip currents, and the important point is that these motions are apparently distinct from infragravity or shear waves.

7.5 Comparison of transient rip occurrence

The snapshots of velocity and vorticity and the (y, t) plots show clear differences between beach slopes and wave spectra. As a measure of transient rip activity, the frequency, duration, intensity of individual rip currents were obtained for each beach slope/spectra regime.

To obtain the data on individual rip events, a rip must be identified in time and space. This is not easy to do objectively and requires a careful definition of what constitutes a transient rip as distinct from other flow features. The key features of a rip current are defined to be:

1. Offshore flow of at least 0.15 m s^{-1} across the outer edge of the surf zone.
2. Constrained offshore flow and associated opposite signed regions of high vorticity.
3. A period of continuous offshore flow exceeding 120 seconds.

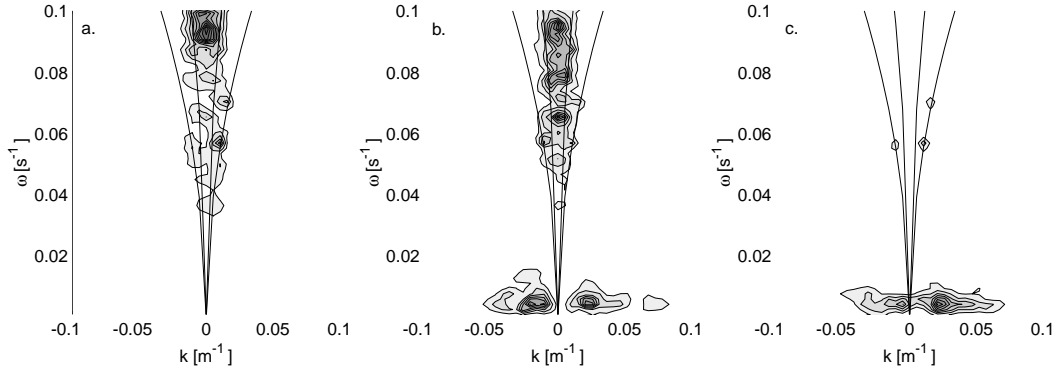


Figure 7.10: Wavenumber-frequency spectra on the 2.0 m isobath for run 5(0.03N10). *a.* \bar{u} (contours $10^4 m^3 s$) *b.* \bar{U} (contours $10^4 m^3 s^{-1}$) *c.* \bar{V} (contours $10^4 m^3 s^{-1}$). The lines are the dispersion relations for the first two edge wave modes.

Criterion 3 distinguishes a rip from a passing vortex couple which could in theory exist without the jet region of a rip current. The rip currents were identified from the (y, t) plots (e.g. Figure 7.8). To ensure consistency between different conditions, an algorithm was used to generate templates of regions which satisfy criterion 1 and 2 in (y, t) space.

The rip identification algorithm is based on the principle that due to the regions of opposite signed vorticity, there is a strong vorticity gradient across the rip neck as shown in Figure 7.11. For a particular depth with location x_D , there are vorticity and velocity values $\bar{U}(y_i, t_j; x_D)$ and $\bar{\zeta}(y_i, t_j; x_D)$ at longshore location y_i for each averaging period at time t_j . The longshore timeseries plots Figure 7.8) are of $\bar{U}(y_i, t_j; x_D)$ and $\bar{\zeta}(y_i, t_j; x_D)$. The procedure to identify rip currents is:

1. For a minimum offshore velocity of U_T and a vorticity gradient threshold of $(\partial\bar{\zeta}/\partial y)_T$, mark $[y_i, t_j]$ bins where:

$$\bar{U}(y_i, t_j; x_D) \leq U_T \quad (7.26)$$

$$\left[\bar{\zeta}(y_i + 1, t_j; x_D) - \bar{\zeta}(y_i - 1, t_j; x_D) \right] / 2\Delta x \leq (\partial\bar{\zeta}/\partial y)_T \quad (7.27)$$

2. Define individual patches as a set of marked bins which are connected.
3. Discard all patches with total duration of less than 120 s .

The values of $U_T = -0.15 \text{ ms}^{-1}$ and $(\partial\bar{\zeta}/\partial y)_T = 0.0015$ were used. These values were found by tuning the performance of the algorithm so that well defined, jet-like vortical flows were found; this part of the procedure is subjective, but once the values are set, the algorithm was consistent between the different runs.

To satisfy criterion 3, a rip is defined as an unbroken template in (y, t) space

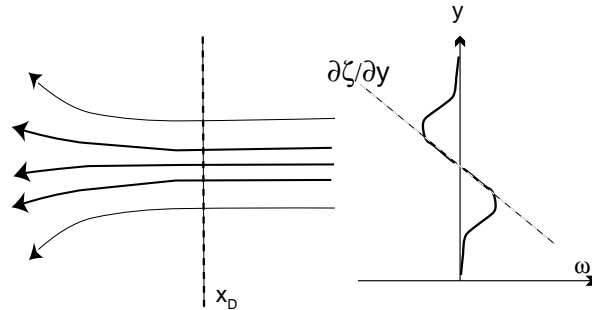


Figure 7.11: Vorticity distribution across a rip current. In the coordinate system of the simulations, there is a negative gradient across the rip neck.

with a duration of at least 120 seconds. From the series of templates, a number of statistics can then be generated:

- Duration - total length in time of the template.
- Mean current - mean offshore velocity over area covered by the template.
- Maximum current - maximum offshore velocity covered in the template.
- Maximum width - widest point of the template along the y direction.

The period of the simulation runs from 1000 s to 4600 s was used to calculate statistics for the rip currents for runs 1 to 12. As the outer limit of breaking is around the 2.5 m isobath, this is set as an appropriate reference to investigate the rip current activity.

Figure 7.12 shows the duration and mean offshore velocity of all the rip events passing the criteria across the 2.5 m isobath. It should be noted that the cross-shore horizontal distance to the 2.5 m isobath is of course dependent on the beach slope. There is significant variation of the number, duration and intensity of rip events between different spectra and beach slopes. There is an obvious increase in the duration and strength of rip currents for the long period narrow spread waves as the beach slope decreases. This corresponds well with the observations of Murray et al. (2003) (and pers. comm.) who found an increase of transient rip activity with decreasing beach slope for swell dominated conditions. By contrast, for the

shorter period waves with wide spreading (W7 and W5), there is a decrease in rip frequency, strength and duration with decreasing beach slope. As would be expected, the rip activity corresponds closely to the rotational cross-shore flux. For the 0.015 slope there is a dramatic decrease in rip occurrence and strength from the swell dominated conditions to shorter period wave fields. Again this agrees in general terms with Murray et al. (2003), who found that for a beach with slope of 0.02, rip activity decreases as the standard deviation of wave height increases (in other words as the sea state becomes "messier"). There is no consistent effect of spreading, as differences between N7 and W7 vary with beach slope.

The mean and maximum velocity and widths of the transient rip population are shown in Figure 7.13. The mean value for the offshore velocity is surprisingly constant, but this may be partly related to the way in which a rip is defined and identified. The rip current widths show how short the typical longshore length scales are, and the mean appears to decrease for spectra with lower peak period and increased spreading. While caution is required in relating specific values to field measurements, as they are somewhat determined by the rip selection process itself, the velocities and rip widths for 0.03N10 are consistent with measurements in Chapter 5 of velocities and length scales in transient rip currents on a beach with slope 0.0325 in swell dominated conditions.

7.6 Transient rip generation

The generation of an individual rip is shown in Figure 7.14. The main sequence of features is common to all rip events seen in the data:

1. Two patches of vorticity within the surf zone with opposite rotations such that the patch in the positive y direction has a negative (clockwise) rotation.
2. Intensification of vorticity in each patch leading to a well defined vortex pair.
3. Propagation of the vortex pair offshore.
4. Further intensification of the vortex pair and movement of the vortices towards each other.
5. The formation of a rip neck behind the head region containing the vortex pair.
6. Shedding and dissipation of one or both vortices as the rip decays.

In the example shown in Figure 7.14, a secondary vortex pair appears to be formed from the edges of the rip neck and maintains the rip as the first pair breaks off. The

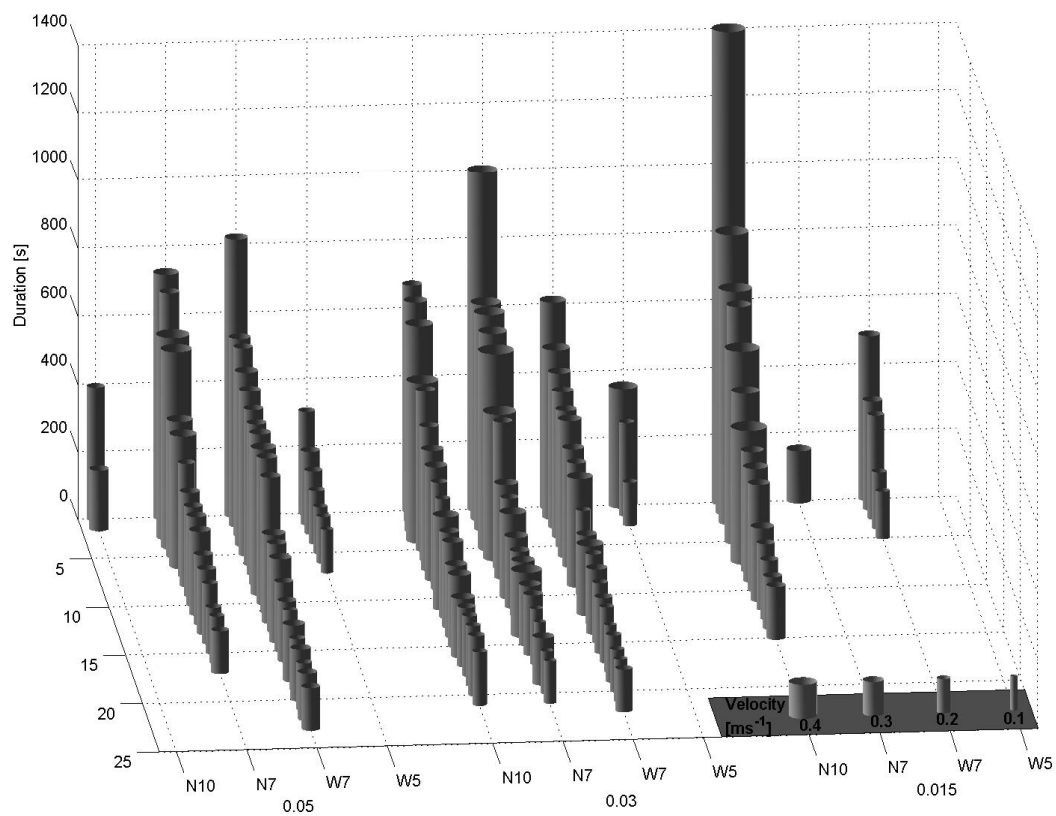


Figure 7.12: Rip currents crossing the 2.5 m isobath for runs 1 to 12. Each column represents one continuous rip current, showing mean velocity and duration as indicated by width and height.

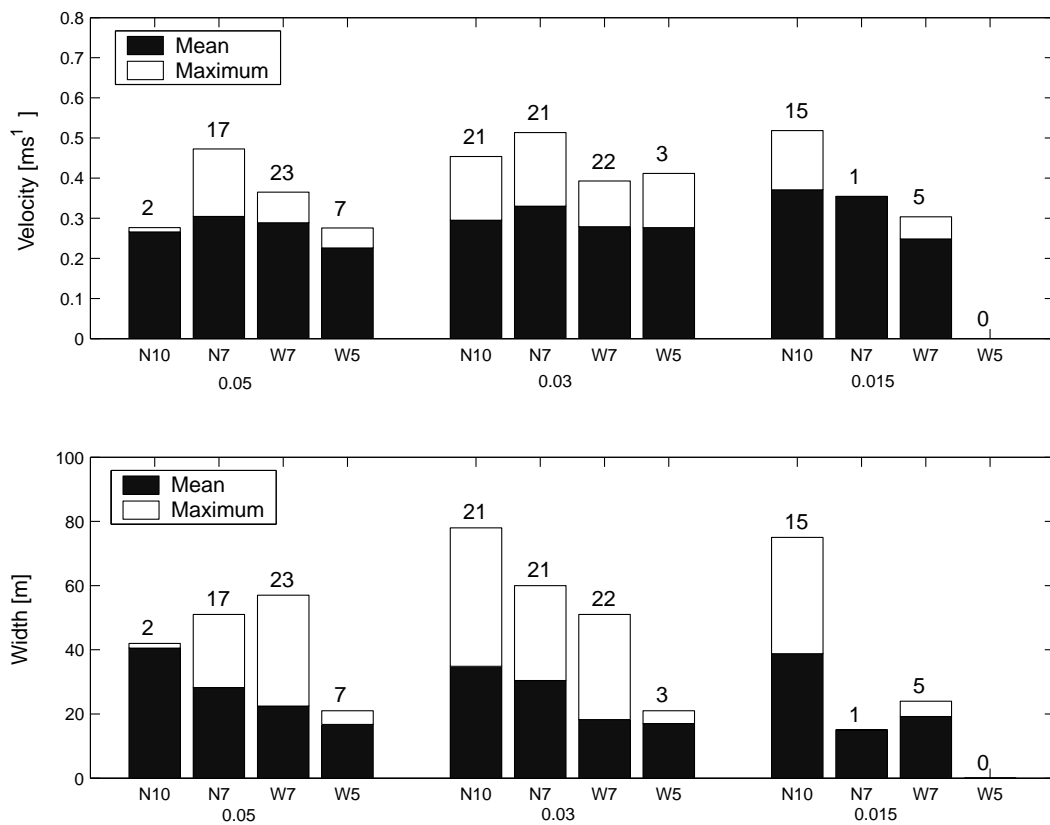


Figure 7.13: Mean and maximum offshore velocity(top) and longshore width(bottom) of rip currents crossing the 2.5 m isobath for runs 1 to 12. The number of individual rip currents in each case are indicated at the top of each bar.

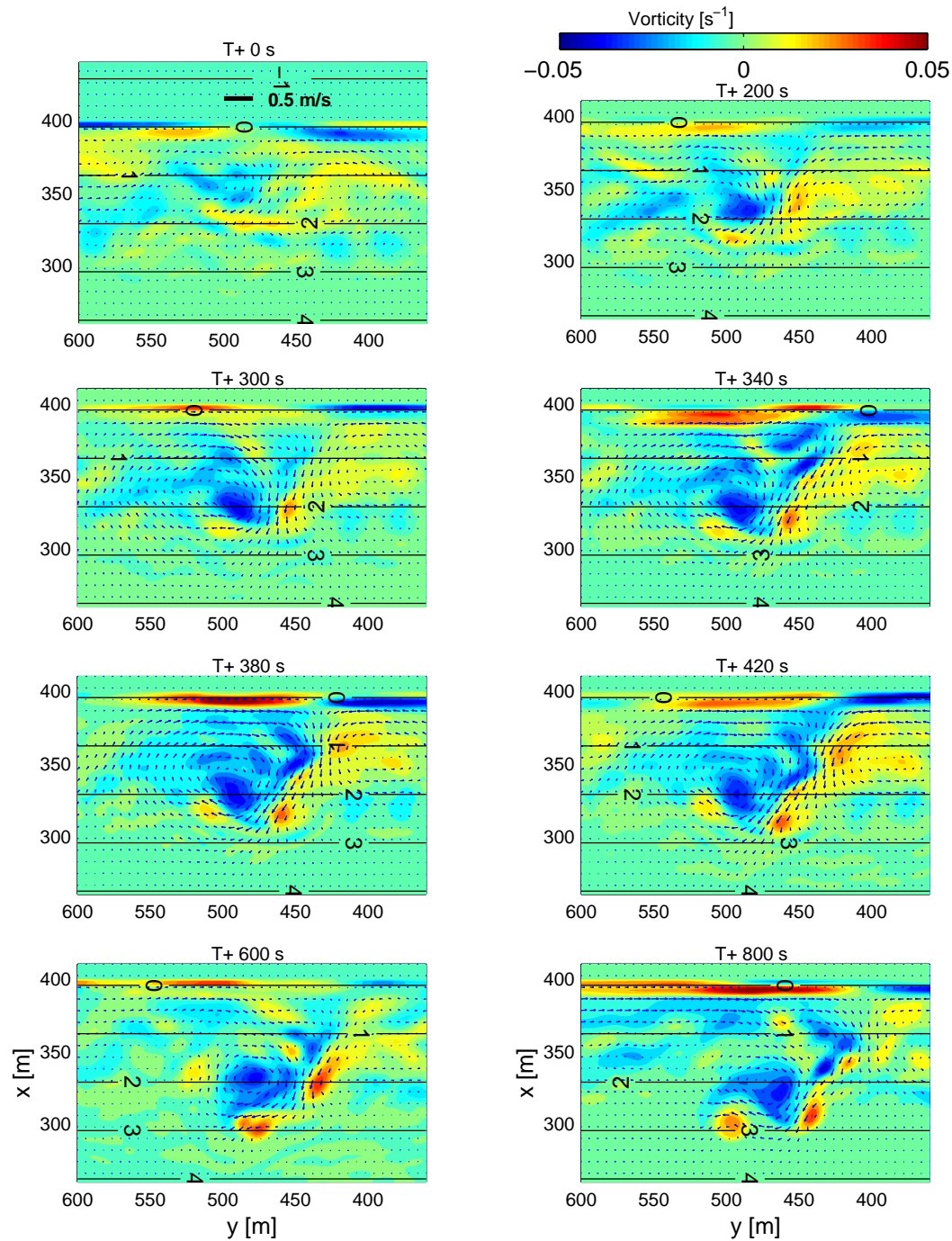


Figure 7.14: Snapshots of the velocity and vorticity field for a section of run 5 (0.03N10) from time $t = 3740$ s showing the development of a transient rip current.

distance of penetration of the rip current beyond the surf zone is limited to just beyond the 3 m contour.

The fundamental behaviour of idealised patches of vorticity in a wedge shaped domain is relatively well understood and has been discussed by Peregrine (1998) and Bühler and Jacobson (2001) in reference to the surf zone. Individual vortices will tend to propagate longshore and the propagation direction means that the two patches seen in the initial stages of rip generation will tend to be driven together. A vortex pair rotating as seen here will also tend to propagate offshore into deeper water. As the vortex pair moves offshore, conservation of potential vorticity (with $f = 0$) also means that streamlines will be squeezed together; this was proposed as the reason for offshore intensification of rip neck flow by Arthur (1962). The formation and shedding of vortex pairs from the edges of rip channels is also seen in simulations of topographic rip currents (e.g. Chen et al., 1999; Haas et al., 2003). Generation of vortex pairs occurs at the edges of the rip channel and they are subsequently advected offshore so that the rip periodically sheds vortex pairs into the region offshore of the bar. The fundamental dynamics of the vortex pairs, once initiated, appear to be qualitatively similar.

While the behaviour of the vortex pairs is as would be expected, there are two important questions to address. Firstly, what determines the spin-up of the patches of opposite vorticity on a plane beach which initiate the rip generation? Second, but related to the first question, is there a feedback mechanism between the rip currents and the incident waves?

7.6.1 Vorticity balance

The dynamics of the vorticity are governed by the curl of Equation 7.2,

$$\frac{\partial \bar{\zeta}}{\partial t} + (\bar{\mathbf{U}} \cdot \nabla) \bar{\zeta} = \bar{\zeta} \bar{\mathbf{U}} \cdot \frac{\nabla(\bar{\eta} + h)}{\bar{\eta} + h} + \nabla \times (\bar{\mathbf{S}} + \bar{\mathbf{L}} + \bar{\mathbf{B}}) \quad (7.28)$$

which can also be written as an equation for the potential vorticity:

$$\frac{D}{Dt} \left(\frac{\bar{\zeta}}{\bar{\eta} + h} \right) = \frac{1}{\bar{\eta} + h} \nabla \times (\bar{\mathbf{S}} + \bar{\mathbf{L}} + \bar{\mathbf{B}}) \quad (7.29)$$

New vorticity is provided to the current field through the $\nabla \times \mathbf{S}$ term in Equation 7.28. The lack of vorticity in run 17 strongly suggests that the directional spreading of the wave field is necessary to input the ambient vorticity necessary to generate coherent vortical features. Furthermore, the similarity of the rip positions for the same wave field (identical at the source line) but different beach slopes (0.03 and 0.015) seen in Figure 7.9 suggests that wave/edge wave interaction is not a dom-

inant factor in determining rip position as different slopes would lead to a different edge wave climate. Therefore, the inherent spatial variability (and hence breaking) of a random directionally spread wave field appears to be the dominant determination of $\nabla \times \mathbf{S}$ and hence where rip currents form. It is clear that the shedding of vorticity from breaking wave crests (Figure 7.4) supplies new vorticity to the current field. This is the mechanism proposed by Peregrine (1998) in which a discontinuous bore generates vorticity at its end.

In the timeseries of vorticity evolution, snapshots of which are shown in Figure 7.14, patches of existing vorticity can be seen to move around and coalesce within the surf zone. In addition, there is advection of vorticity from the shoreline boundary deeper into the surf zone. The advective change of local vorticity is represented by the term $(\bar{\mathbf{U}} \cdot \nabla)\bar{\zeta}$ in Equation 7.28.

Isolating the exact spin-up mechanism is difficult due to the apparent importance of both vorticity generation by the incident wave forcing and redistribution of existing vorticity by advection. However, it is useful to estimate the relative magnitude of terms in Equation 7.28. All of the terms except $\nabla \times \mathbf{S}$ can be easily evaluated directly from the model results. The term $\nabla \times \mathbf{S}$ can in principle be calculated directly. However, this is quite complex and it is easier to simply assume it is the residual in the local rate of change of vorticity once the other terms have been accounted for. Figure 7.15 shows the relative magnitude of the nonlinear, stretching and forcing terms for varying cross-shore locations for the period ($t = 3740 - 4540$ s) and longshore extent ($y = 360 - 600$ m) of Figure 7.14. The incident wave forcing term is the largest in the inner surf zone and decreases offshore, indicating that the main vorticity input from the incident wave field occurs in the inner surf zone. The nonlinear terms are also important in the inner surf zone and are increasingly dominant moving offshore. The stretching term is smaller and reduces offshore, corresponding to the decrease in $\nabla h/h$; however this term is important as it intensifies seaward moving vorticity as discussed previously.

The bottom friction term, $\nabla \times \mathbf{B}$, acts to dissipate vorticity and the lateral mixing term, $\nabla \times \mathbf{L}$, will tend to smear out vorticity gradients and discourage the formation of coherent features such as vortices. These terms are an order of magnitude smaller than the others, but act to spin down the transient rip flow.

7.6.2 Feedback

Rips are often seen to re-emerge from the same place as a previous rip. The persistence of the long narrow regions (in y, t space) of high vorticity associated with the rip currents are seen in Figure 7.8. This appears to be because remnant patches of vorticity encourage the spin-up of new vortex patches in the same location, as seen

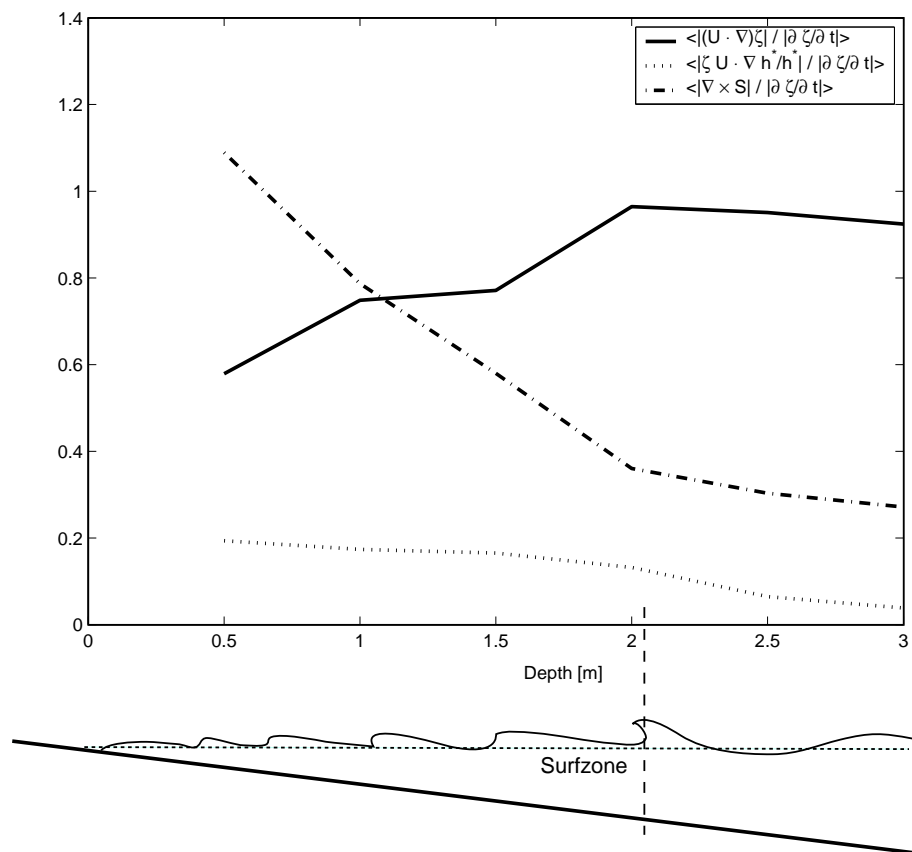


Figure 7.15: Magnitude of terms in vorticity balance relative to the local rate of change of vorticity. The ratios of the absolute values of terms are calculated and then averaged over the temporal and longshore extent in Figure 7.14 for cross-shore locations corresponding to the depth shown.

in the sequence in Figure 7.14 and 7.15. In (y, t) plots of the incident wave height distribution in the surf zone (not shown), there is a clearly discernable signature of the rip currents, indicating that there is some feedback on the incident wave field. Observation of individual wave crests are of refraction towards the rip current and a local increase of crest height, in a similar manner to the observations of Chen et al. (1999) for monochromatic waves propagating over a topographic rip.

To test the dependence of $\nabla \times \mathbf{S}$ on the existing vorticity, a correlation coefficient for $y - t$ space is defined by:

$$C = \frac{\sum_{j=1}^{nt} \sum_{i=1}^{ny} P_1(y_i, t_j) P_2(y_i, t_j)}{\left(\sum_{j=1}^{nt} \sum_{i=1}^{ny} P_1(y_i, t_j)^2 \sum_{j=1}^{nt} \sum_{i=1}^{ny} P_2(y_i, t_j)^2 \right)^{1/2}} \quad (7.30)$$

where $P_1 = \nabla \times \mathbf{S}$ and $P_2 = \bar{\zeta}$ are the values of two parameters. The 95% confidence intervals were calculated and account for the spatial autocorrelation of the parameters (Clifford et al., 1989). Correlations for varying cross-shore locations are shown for the whole domain over the period $t = 1000 - 4500$ s in Figure 7.16. While the correlation is not strong, it is significant, and indicates positive feedback between existing vorticity and forcing torque due to the incident wave field at all cross-shore locations to the 3 m depth contour. This feedback is apparently strong enough to sustain the rip flow or to encourage re-development sometime later at the same location.

The lack of rip currents in run 17 indicates that for the frictional and mixing parameters used for the simulations, the feedback mechanism by itself is not unstable. An analysis by Falqués et al. (1999) found the setup in the wave-averaged equations to be unstable to a idealised shore perpendicular wave field if there feedback due to refraction of the incoming wave field. However, the results of run 17, effectively a slightly perturbed plane wave field with a spread of frequencies, show the opposite (refraction is implicitly included in the Boussinesq equations). The results here indicate that a certain amount of directional spreading, and the associated spatial gradients in forcing of the wave-averaged current, is required to provide sufficient vorticity to initiate the rip generation process.

To summarise the rip generation mechanism a proposed conceptual model is shown in Figure 7.17. The key feature is the formation of a vortex pair which propagates offshore. The generation of the regions of opposite signed vorticity is due both to direct input of vorticity from the incident wave field and advection of existing vorticity. A positive feedback means that new vorticity tends to be injected so as to enhance the existing vorticity distribution; this appears to lead to persistence and repeated development of rip currents at the same location.

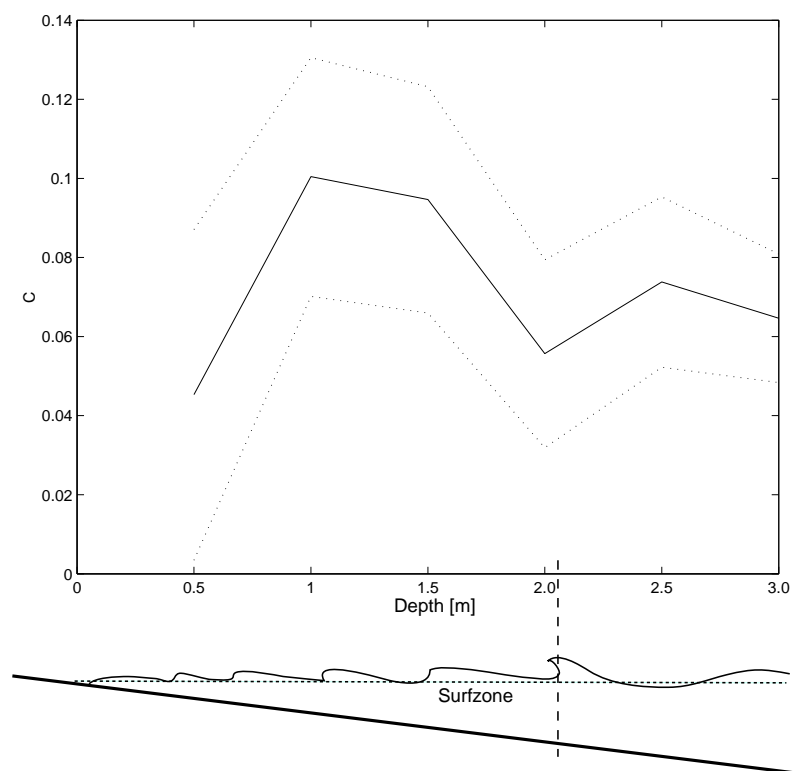


Figure 7.16: Correlation coefficient of $\nabla \times \mathbf{S}$ and $\bar{\zeta}$ for the whole domain for $t = 1000 - 4500s$. The dotted lines are 95 % confidence intervals.

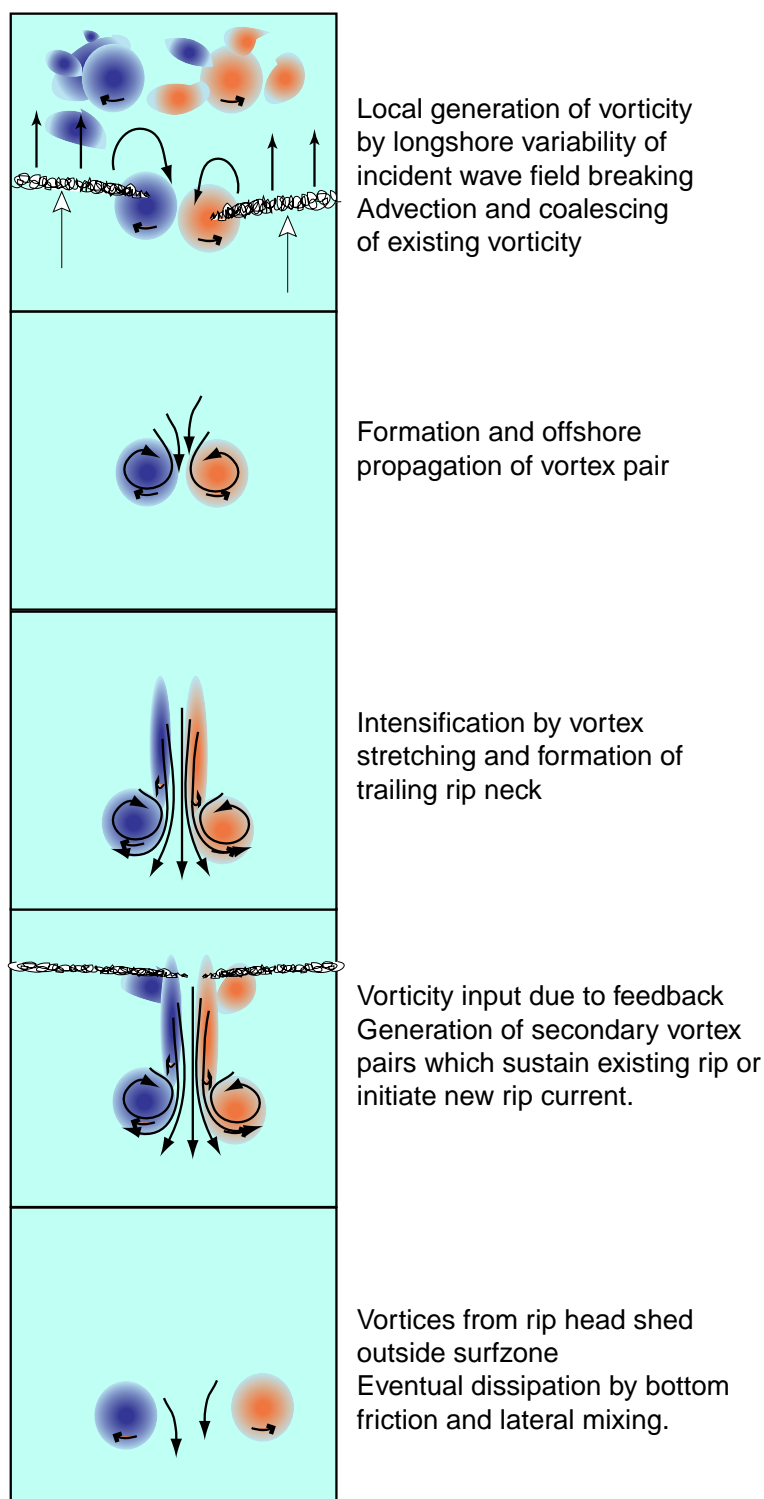


Figure 7.17: Conceptual model of transient rip generation.

7.7 The rotational flow field

The transient rip currents are well defined features which are part of the rotational component the flow field. It is interesting to characterise the rotational flow component in a general way both in terms of its energy content and its wavenumber spectra. The nearshore current field can be considered to consist of an horizontally irrotational, divergent component associated with infragravity waves and a rotational component associated with eddies and transient rips. The plots of velocity and vorticity (Figure 7.8) and the $k-\omega$ spectra clearly show the distinction between the two types of motion.

7.7.1 Partitioning the flow field

A Helmholtz decomposition uniquely partitions a vector field into a rotational, non divergent part and an irrotational part. While the basic idea is straightforward, the exact definition of the partition is more arbitrary as the decomposition can be applied to $\overline{\mathbf{U}}, \overline{\mathbf{M}}$ or $h^*\overline{\mathbf{U}}$ where h^* is MWL total depth (including long time average setup). By using $h^*\overline{\mathbf{U}}^2$ so that,

$$h^*\overline{\mathbf{U}} = h^*\mathbf{u}^D + h^*\mathbf{u}^R; \nabla \times h^*\mathbf{u}^D = 0 \quad \nabla \cdot h^*\mathbf{u}^R = 0 \quad (7.31)$$

the two modes separate very naturally in the linearised equations. The surface elevation is associated with the divergent component in the linearised continuity equation as

$$\frac{\partial \overline{\eta}}{\partial t} = -\nabla \cdot h^*\mathbf{u}^D \quad (7.32)$$

and the velocity in the rotational component is equivalent to the velocity under the rigid-lid approximation. Defining a transport stream function, ψ so that $\partial\psi/\partial y = -h^*\overline{U}^R$, $\partial\psi/\partial x = h^*\overline{V}^R$, means that:

$$\nabla \times h^*\overline{\mathbf{U}} = \nabla \times h^*\mathbf{u}^R = \nabla^2\psi \quad (7.33)$$

As $\nabla \times h^*\overline{\mathbf{U}}$ is known directly from the model results, a poisson equation for ψ can be solved, thereby extracting \mathbf{u}^R from the total velocity field. In practice a minimum depth must applied to prevent \mathbf{u}^R becoming infinite at the shoreline. Note that $\nabla \times \mathbf{u}^R \neq \overline{\zeta}$, but rather is related by:

$$\nabla \times \mathbf{u}^R = \overline{\zeta} + \frac{\nabla h^*}{h^*} \times \mathbf{u}^D \quad (7.34)$$

²As $\widehat{\overline{\mathbf{U}}} = 0$, $\overline{\mathbf{U}} = \mathbf{u}$ defined in Chapter 3.

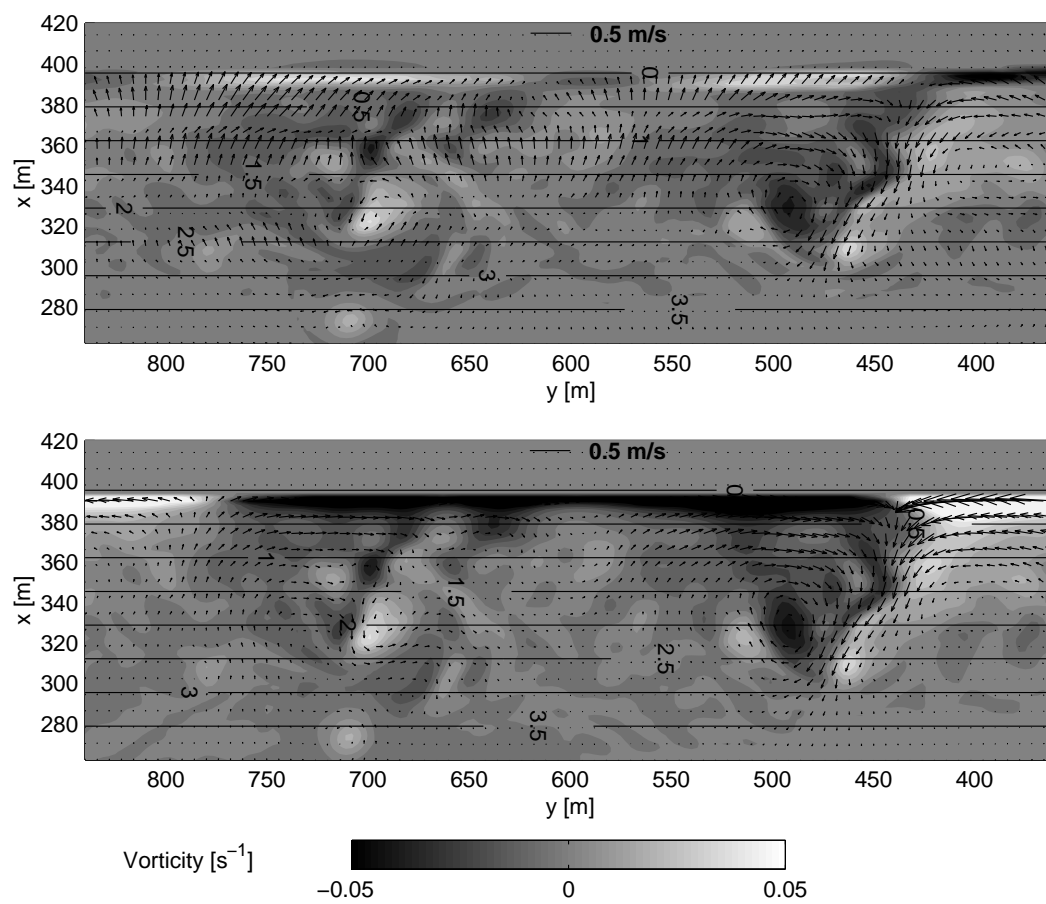


Figure 7.18: Total, $\bar{\mathbf{U}}$ (top) and rotational component, \mathbf{u}^R (bottom) flow field for a section of run 5 at $t = 4160\text{s}$. The shading in the bottom figure is $\nabla \times \mathbf{u}^R$

The results from the partition of a section of Figure 7.6 are shown in Figure 7.18. The main flow of the transient rip current is rotational, non-divergent flow and removal of the divergent part of the velocity field has excluded gravity wave motions which are present in the full velocity field as linear regions of on or offshore velocity.

7.7.2 Cross-shore flux

The total offshore directed flux was calculated for each run as measure of the exchange across a particular offshore location. The flux is defined as the mean of the negative x components of flux across a particular depth contour, x_d :

$$Q = \frac{-1}{LT} \int_t^{t+T} \int_0^L \min [\bar{U}(x_d, y', t'), 0] dy' dt' \quad (7.35)$$

and specific values for u^R and u^D are calculated.

The flux from the period of the simulation for $t = 1000 - 4600$ s across the 2.0 m depth contour is shown in Figure 7.19. The rotational flux contribution is significant in all the runs and in some cases greater than the divergent, irrotational part. This implies that the rotational flow field is important for determining mixing across the outer edge of the surf zone. Note that the contribution of the general rotational flow is still significant even when no well defined transient rip currents have been identified (such as with 0.015W5).

The influence of beach slope on the total rotational flux appears to depend on the wave spectra. Reflecting the trends in the transient rip population, there is an increase with decreasing beach slope for N10 while for the wide spread spectra, W7 and W5 the opposite is true. In each case, W5 has a lower flux than W7. N7 does not show an increase between 0.05 and 0.03, but an overall decrease for the shallowest slope. Shallower slopes apparently favour rotational flow for narrow spread spectra, while for wide spread spectra, steeper slopes generate more flow. The reason for this is not clear, but it indicates that the influence of the slope on vorticity generation by the wave field and its subsequent evolution is not linear.

7.7.3 Energy partition

A longshore average kinetic energy of the current for a particular cross-shore location, x_c , is defined by:

$$E_K(x_c) = \frac{h}{2L} \int_0^L \langle \bar{U}^2 \rangle + \langle \bar{V}^2 \rangle dy \quad (7.36)$$

where L is the length of the domain and $\langle .^2 \rangle$ is the variance for the period $t = 1000 - 4600$ s. A kinetic energy, E_K^R , is also calculated for the rotational

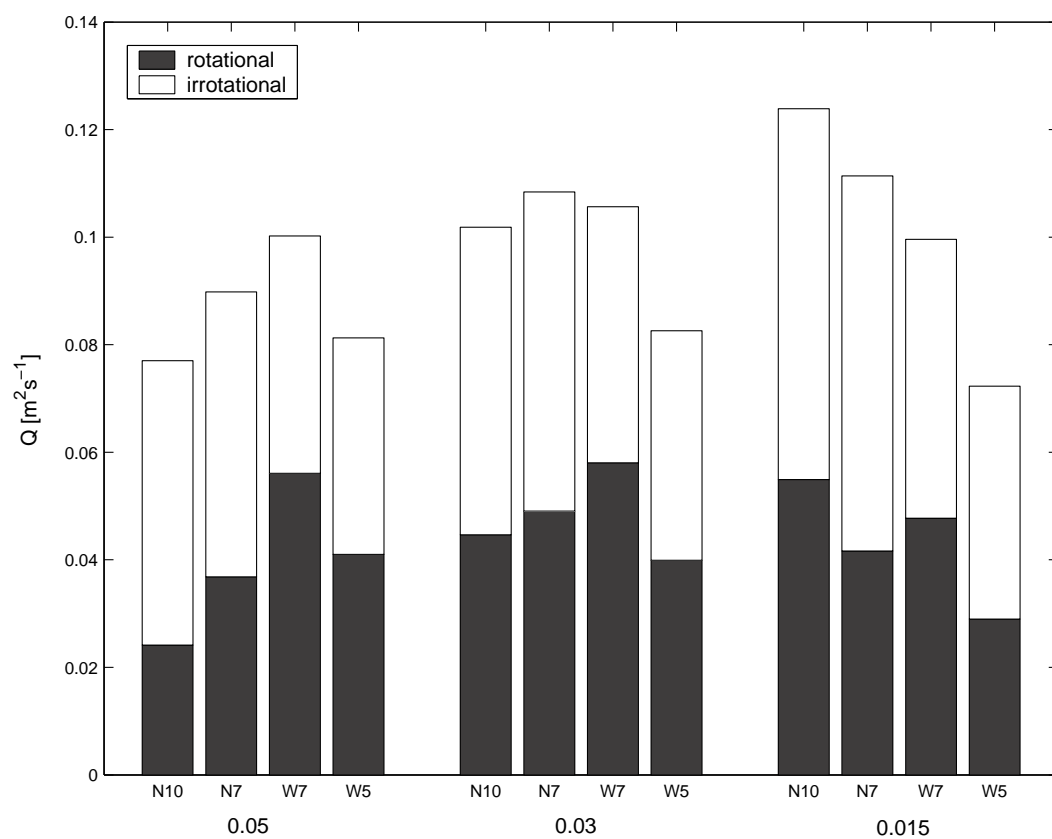


Figure 7.19: Mean offshore directed flux per unit longshore distance at the 2 m depth contour for the rotational (u^R) and irrotational (u^D) flow. The spectra and beach slopes are indicated under each bar.

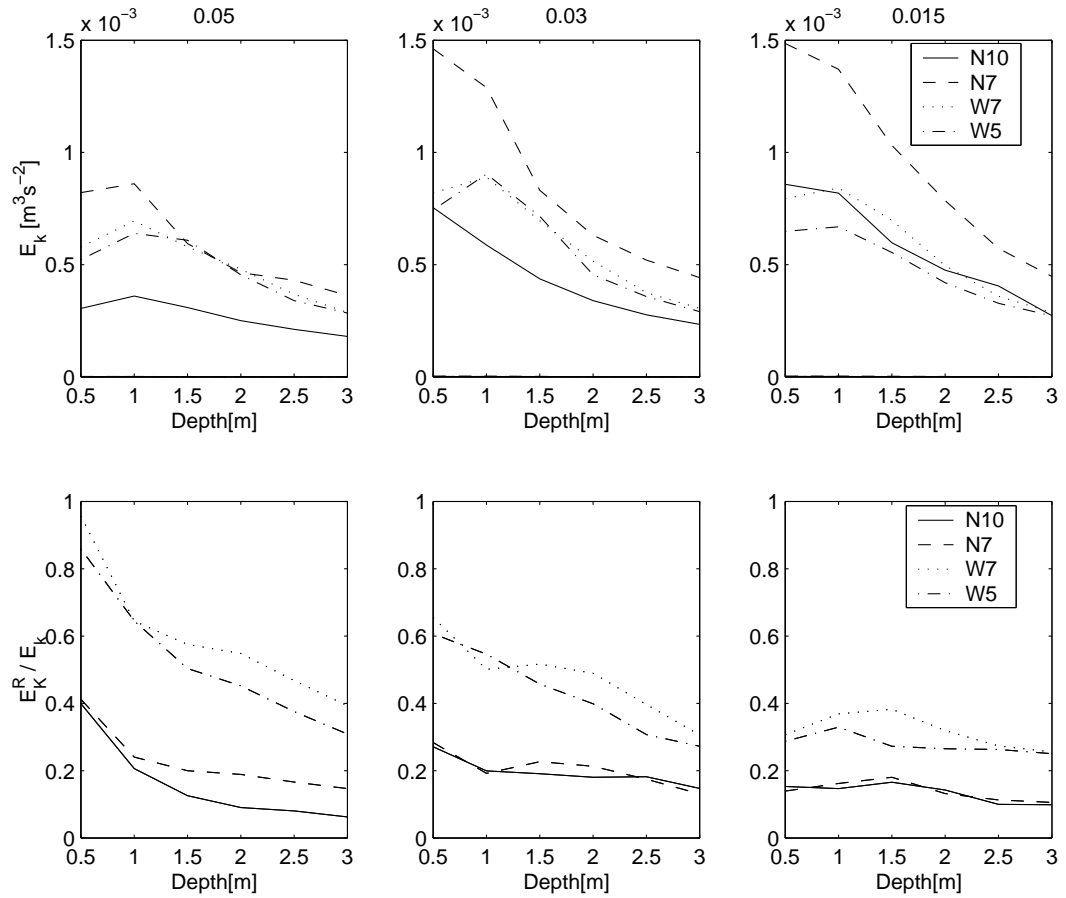


Figure 7.20: Fraction of rotational energy for runs 1-4 (a.) 5-8 (b.) and 9-12 (c.) at each 0.5 m depth contour from 0.5 m to 3.0 m depth.

component. The ratio $R_1 = \frac{E_K^R}{E_K}$ is then a measure of the fraction of rotational kinetic energy. Figure 7.20 shows the total kinetic energy and ratios for runs 1-12.

The ratios indicate that the rotational energy is a significant proportion of total kinetic energy, and is dominant near the shore line for the wide spreading spectra, W7 and W5, on the steeper slopes. The rotational energy ratios show general trends with varying beach slope and spectra:

1. The peak moves further shoreward with decreasing wave period. This may correspond to the shoreward shift of the breakpoint with decreasing period.
2. The peak moves to shallower depths with decreasing beach slope.
3. In each case, ratios increase in the same sequence of spectra N10-N7-W5-W7, so there is general increase with decreasing period with the exception of W7 which shows the highest ratios.

Some caution is required in interpreting the apparent decrease of rotational energy ratios with decreasing beach slope due to the modelling of the shoreline. As the run-up is not correctly represented, much of the energy that would normally be reflected from the steeper beach slope will pass into the beach. Therefore there may be significant amounts of missing reflected irrotational energy. However, it is interesting that while the total energy, E_K , of the wide spread spectra, W7 and W5, are similar for the beach slopes, the narrow spread spectra, N10 and N7, show a significant increase near the shore with decreasing beach slope. This increase for spectra N10 and N7 is in the irrotational energy fraction and is relatively larger close to the shore, indicating that it is edge wave energy; this suggests that the narrow spread spectra are more effective at generating edge waves on shallower beach slopes.

7.7.4 Longshore wavenumber spectra

Wavenumber spectra of the rotational current components \bar{U}^R and \bar{V}^R were calculated by averaging a timeseries of longshore wavenumber spectra calculated along a particular depth contour. This is equivalent to integrating the $k - \omega$ spectra over all frequencies. The data used is from the range $t = 1000 - 4600$ s. Spectra were also calculated for the input wave amplitudes at the offshore source line.

Figure 7.21 shows the spectra of u^R, v^R for different beach slopes and incident wave spectra at the 1.5 m depth contour. Assuming the longshore variability of the incident wave forcing, \mathbf{S} , is related to the longshore distribution of wave heights, spectra of $\sqrt{(\tilde{\eta} - \bar{\eta})^2}$ are an indication of the wavenumber distribution of the nearshore current forcing. As the instantaneous surface is not available for all the runs, the spectra were calculated for the source line input function. The first moment of the source line spectra, $Phi(k)$, which is calculated as $k_m = \sum_i k_i \Phi(k_i) / \sum_i \Phi(k_i)$, is also shown as an indication of the centroid of forcing in wavenumber space. As the wave periods decrease and spreading increases, k_m becomes larger, corresponding to a decrease in the longer forcing length scale.

All of the wavenumber spectra show a similar shape, with a peak at less than the length scale of the domain and a decrease of energy towards higher wavenumbers. Thus all of the rotational motion for different beach slopes and incident wave spectra share the same basic statistical character. The general shape of the rotational current spectra appears to reflect to some extent the wave amplitude spectra, with the more peaked (rounded) wave spectra corresponding to narrow (wide) directional spreading and the general position of the spectral peaks, of u^R in particular, close to k_m . A close correspondence of spectral shape might be expected if the rotational flow evolution was a linear function of the forcing. However, the relative importance of the nonlinear terms found in Section 7.6.1 suggests that there may also be an

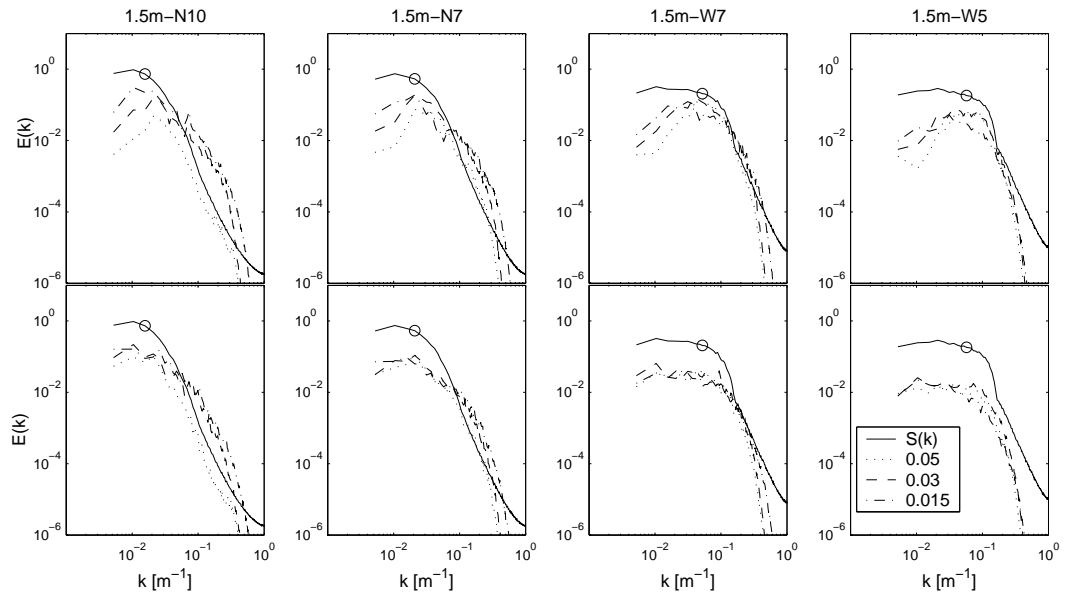


Figure 7.21: Longshore wavenumber spectra for variable slopes at 1.5 m depth contour. The top set of spectra is for the cross-shore rotational velocity component, U^R , the bottom for the longshore component, V^R . The solid line is the spectra for the source line amplitude in each case and the open circle indicates the position of

independent transfer of energy between scales.

Significant differences between the spectra for u^R, v^R indicate strong anisotropy, as would be expected in the presence of the sloping bottom and shoreline boundary. Spectra at varying cross-shore locations, shown in Figure 7.22 for the the intermediate slope (0.03) show a significant increase of longshore component energy and strong anisotropy at the position closest to the shore; this corresponds to vortical structures becoming elongated along depth contours closer to the shoreline.

7.8 Effect of bottom friction and subgrid mixing

A detailed investigation of the effect of the bottom friction and lateral mixing was not carried out. However for completeness, the bottom friction and lateral mixing parameters were varied by an order of magnitude in runs 13-16 to qualitatively understand how important these variations might be. The flow fields for run 5 and 13-16 after 10000 time-steps is shown in Figure 7.23. These runs are all with the same slope of 0.03 and spectra (peak period of 10 seconds and a spreading parameter of 100) to show the effect of varying the bottom friction coefficient and subgrid mixing coefficient.

The effect of increasing both parameters is to reduce both the magnitudes and gradients of the discrete flow features. An order of magnitude increase of the bottom

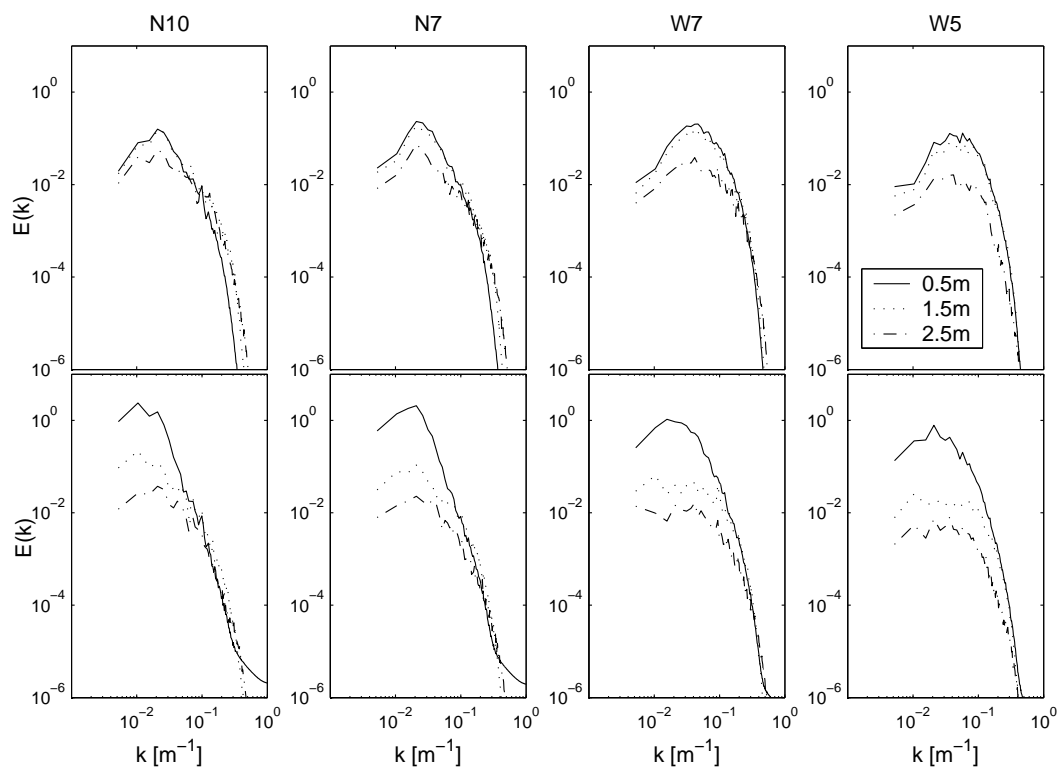


Figure 7.22: Longshore wavenumber spectra for variable cross-shore positions. The top set of spectra is for the cross-shore rotational velocity component, U^R , the bottom for the longshore component, V^R . The solid line is the spectra for the source line amplitude in each case.

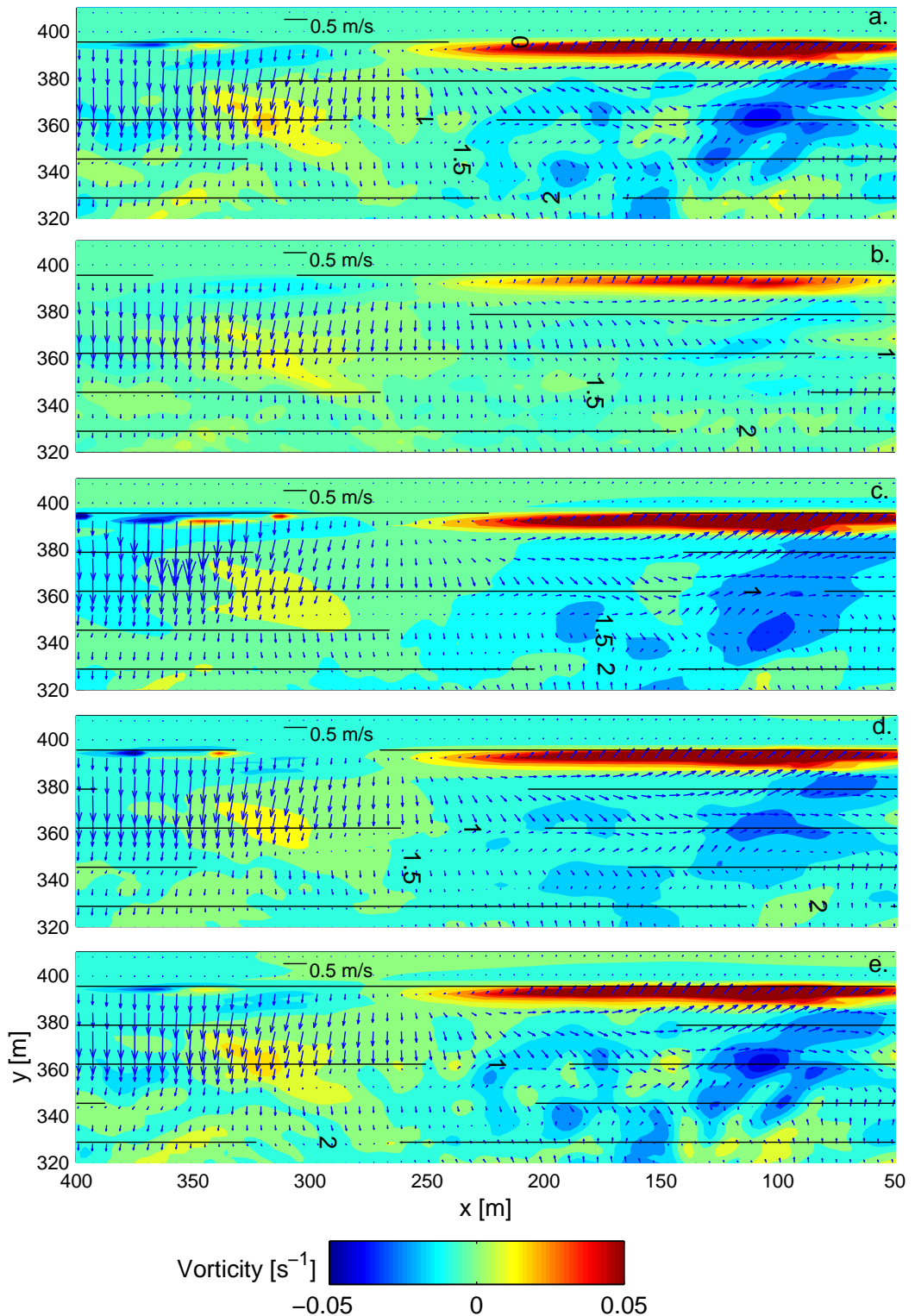


Figure 7.23: Velocity field from runs 5, 13-16 (top to bottom) 1000 s after the start of the simulation for the spectra N10 and beach slope 0.03 but with varying friction and mixing parameters (f_b and c_m). From the top to bottom the friction and turbulent mixing parameters are a. $f_b = 0.001, c_m = 0.2$, b. $f_b = 0.01, c_m = 0.2$, c. $f_b = 0.0001, c_m = 0.2$, d. $f_b = 0.001, c_m = 2.0$, e. $f_b = 0.001, c_m = 0.02$

friction coefficient is more significant than an equivalent increase of mixing coefficient; a value of $f_b = 0.01$ largely suppresses the development of any transient rips, while with $c_m = 2.0$, the central rip feature is still apparent. The effect of the bottom friction is similarly more pronounced for the reduced parameter values; while the same basic flow features are seen, they have taken on different shapes and are more intense. Decreasing the subgrid mixing parameter appears to have the least effect of all the variations, with the same flow pattern seen, but with slightly enhanced vorticity gradients, as would be expected with a reduced lateral mixing.

Sensitivity of modelled rip currents to bottom friction and lateral mixing (including quasi-3D mixing effect) was tested by Haas et al. (2003). These comparisons were for wave-averaged model simulations of tank scale rip currents and found that both increased bottom friction and lateral mixing tend to stabilise the rip currents and decrease peak current speeds. In numerical wave-averaged experiments of rip currents formed over an idealised bar/trough topography, Yu and Slinn (2003) found bottom friction less important and that wave-current interaction was dominant in determining the flow patterns.

The significant differences, albeit for order of magnitude differences in values, highlight the importance of using the correct parameters for any accurate simulations of real situations. The results generated with the parameters used for the main simulations may not be entirely accurate for the precise prediction of velocities. However, the fact that the general shape and features of the flow field remains unaltered suggests that fundamental mechanisms discussed in Section 7.6 are unaltered by varying parameters. Furthermore, it seems reasonable to assume that the quantitative comparison in Section 7.5 and 7.7 should remain valid in a *relative* sense.

7.9 Discussion

While the model provides a highly detailed simulation of nearshore hydrodynamics, it is important to acknowledge its limitations. The Boussinesq equations do not include undertow; the main influence of this is the absence of enhanced lateral mixing of momentum (Svendsen and Putrevu, 1994), particularly in the cross-shore direction. As highlighted in the preceding section, uncertainties in parameter values for the subgrid closures will have significant effects. The breaking model is crude in terms of its representation of the overturning process and transfer of momentum. The use of a slot at the shoreline means that some wave energy penetrates the beach and run-up and to some extent setup is underestimated. For the shortest period waves in particular, the grid scale is really too coarse for resolving the finer details

of the wave shape. Finally, the domains and spectra are highly idealised; plane beaches are not really present in nature, and there will always be some topographic influence on the current field. This investigation should be viewed as a process study of nearshore currents, forced variably in time and space in a manner consistent with real ocean wave fields, rather than any attempt reproduce real current structures and wave fields in a highly accurate manner. While the transient rip currents in the model are qualitatively consistent with field measurements, the specific results in Section 7.5 concerning the occurrence of transient rip currents in varying conditions are of most value relative to each other, and should be treated with caution.

As suggested by Peregrine (1998), flow in the nearshore may have the character of two dimensional turbulence. The rotational flow component of the wave-averaged nearshore currents may have similarities with forced quasi two-dimensional turbulence ("quasi" as the flow is not truly two-dimensional) in a wedge shaped domain. The magnitude of the terms in the vorticity equation (which have similar relative magnitudes if the analysis in Section 7.6.1 is extended to the whole domain) suggest that nonlinear transfer of vorticity is of similar importance to the incident forcing. The rotational flow response would then be the combined effect of a (linear) response to the forcing at a range of scales and re-adjustment of energy between scales by nonlinear turbulent type mechanisms. Unfortunately, identification of nonlinear energy transfer between scales, which is the key characteristic of turbulence, is made difficult by the presence of a whole range of forcing scales.

If turbulent type mechanisms are important, the "transient rips" may be a coherent jet structure that naturally arises in variably forced two-dimensional turbulence (Danilov and Gurarie, 2001). It is possible that the incident forcing need not have a particular form, and that just "stirring" at an appropriate range of length scales leads to spontaneous formation of jets which are ejected offshore. The tendency of two-dimensional turbulence to form larger vortices from smaller vortices may explain observations in the model results of the agglomeration of small vorticity patches into larger ones. It would be useful to investigate the development of (quasi) two-dimensional non-rotating turbulence in a sloping domain with idealised forcing of varying longshore length scales. The author is not aware of any work which deals with the fundamental behaviour of this kind of flow as it differs from forced two-dimensional turbulence due to the nonlinear stretching term. Although relatively small in the vorticity balance in most of the surf zone (although note that it becomes infinite as the water depth tends to zero), the stretching term makes the flow both anisotropic and inhomogeneous and imparts a cross-shore asymmetry to the vorticity evolution.

Beyond the fundamental behaviour of the rotational component, there is also the

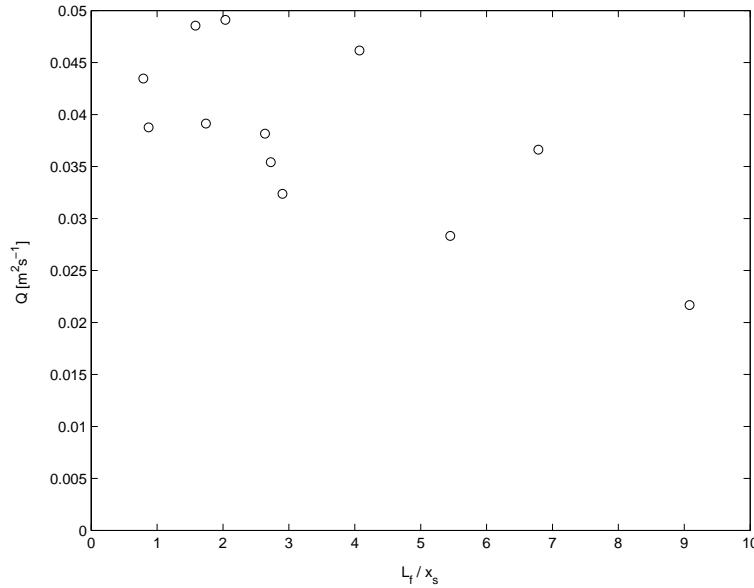


Figure 7.24: Rotational current flux dependence of the ratio of forcing length scale, $L_f = 2\pi/k_m$, and surf zone width, x_s .

question of interaction between the rotational and divergent current components. As shown by Kirby et al. (1998b), edge and shear wave modes can form resonant sets. The spectra in Figure 7.10 suggest that in the absence of shear waves, the rotational and divergent components are well separated in wavenumber-frequency space, which may mean that they can be decoupled and treated separately. However, this needs further investigation.

The rip populations and cross-shore rotational fluxes are apparently dependent on the combination of beach slope and spectra and do not show a simple dependence on either in isolation. For a given spectra, there is an optimum beach slope, and shallower or steeper slopes decrease the activity. Both the spectra and slopes have length scales associated with them. For the slope, this is the width of the surf zone, $x_s = [50 \text{ m}, 83 \text{ m}, 167 \text{ m}]$. For the spectra, this is the length scale of the variability in longshore forcing; this is less easy to define explicitly, but $L_f = 2\pi/k_m$ should be appropriate. The rotational flux shows a general decrease as L_f/x_s increases (Figure 7.24), suggesting that there may be an optimum relationship between the spatial variability of the incident wave field and the beach slope. This would be another motivation to study idealised forced quasi two-dimensional turbulence, to confirm whether these two length scales are the fundamental governing parameters for the (forced) rotational flow field.

The implication of the results for larger scale coastal processes is mainly the significant cross-shore flux that appears to occur due to rotational current motion

and would mediate exchange of sediment and other material. This is in addition to cross-shore mass flux due to undertow or fixed rip currents but is entirely missing in a wave-averaged description. The comparative results suggest that the magnitude of exchange across the outer edge of the surf zone is dependent both on beach slope and wave field, but not necessarily in a simple way. Further work is required to find suitable simple parameterisations of variable wave climates and beach morphologies to calculate the cross-shore fluxes due to transient circulation of the kind described here.

7.10 Summary and conclusions

Boussinesq model simulations of directionally spread random waves with the mean direction perpendicular to a plane beach show the development of an active horizontally rotational current field not associated with infragravity waves. The rotational flow field is similar in appearance to 2D turbulence and occurs in the absence of any mean longshore flow. Coherent features observed in the rotational flow field include transient rip currents and discrete vortices, which occur variably in space and time. The exact nature of the flow field depends on the beach slope and the incident wave spectra. The frequency, duration, and intensity of the transient rip currents similarly depend on both the beach slope and the incident wave spectra but not in a simple way, with the optimum beach slope apparently depending on the wave spectra.

The transient rip currents are associated with a vortex pair which is generated within the surf zone and subsequently propagates offshore. Analysis of the vorticity balance show that the main vorticity input occurs within the inner surf zone. The vorticity dynamics during the evolution of the transient rip currents are dominated by the advection terms, and this makes it hard to identify the precise source of vorticity input from the incident wave field. However, observations of vorticity associated with discontinuities in wave crests show that this mechanism is important. The directional spreading of the wave field is necessary to initiate the transient rip currents, although their development and maintenance appears to involve a feedback mechanism, which explains the observation of repeated ejection from nearby locations.

The proportion of total energy contained in the non-divergent, rotational portion of the flow field is significant. Longshore wavenumber spectra indicate that the spatial distribution of rotational energy is strongly influenced by the wave height distribution, in turn a direct function of the incident wave spectra. The total rotational flux across the outer edge of the surf zone shows the same general trends as the

rip current population, dependent on slope and wave spectra. The total flux out of the surf zone due to the rotational motion is of similar magnitude to that associated with irrotational (infragravity) motion, and is therefore presumably important, but to date not included, in determination of cross-shore fluxes of sediment and other material.

Chapter 8

Discussion and Conclusions

8.1 Introduction

This chapter brings together the different aspects of the overall work. The first section summarises the original contribution of the work, and is followed by a discussion of ideas and unanswered questions. Next there are specific suggestions for future work and finally a summary of the important conclusions.

8.2 Original contribution

The contribution of the preceding four chapters, which form the main part of the original work, can be summarised as:

- The design and validation of a drifter for surf zone use. The Lagrangian data from this instrument reveals spatial patterns of nearshore currents. Unlike with Eulerian data, no assumption of a wave-like current structure is necessary to gain spatial information, and features like transient rips and large scale vortices can be directly observed. Lagrangian data from several drifters at once also allows the direct estimation of (scale dependent) dispersion rates due to horizontal currents, in the nearshore zone. The drifters have been shown to be effective for measuring currents in both perpendicular incident waves, and in the presence of strong longshore current.
- Field measurements of transient rips were made which showed their spatial structure, measured their flow velocities and estimated their mixing effect. Transient rips were found to be distinct from infragravity waves due to their spatial length scales, and Eulerian data corroborated this, indicating significant amounts of variable rotational current energy, even without any longshore current.

- Longshore current measurements showed that the drifters can be used to profile the cross-shore distribution of the quasi-steady longshore current system.
- Dispersion rates as a function of horizontal scale have been estimated for the perpendicular wave case and in longshore currents. To the author's knowledge this has never been investigated previously in the nearshore, and the data indicate a surprisingly strong scale dependency.
- A Boussinesq model has been used to simulate a random wave field, consistent with real oceanic spectra, with mean direction perpendicular to a plane beach. The model generates an active rotational current field. This supports both the assertion that transient rips exist in the absence of topographic control, and the proposition implied by the field data that rotational variable currents are a general feature of the nearshore current climate. Investigation of different beach slopes and wave fields showed that the amount of transient rip activity depended on both, but not necessarily in a simple way. The model showed that the vorticity balance is also quite complex with both the incident wave forcing and nonlinearity being important, and that feedback exists between the currents and the incident wave field. As in the field, the general rotational current field in the model was found to have significant amounts of energy. The longshore wavenumber spectra of the variable rotational currents also appeared to be somewhat universal in shape and imply the existence of a continuous range of scales similar to two-dimensional turbulence.

In terms of techniques and methods, both the design of the drifter and the analysis methods for Lagrangian data are innovations (in terms of their use in the nearshore zone), that will hopefully continue to be developed and more widely used. The results of the Boussinesq modelling have highlighted the importance of using models that can resolve random wave fields in order to capture the variable aspect current field, otherwise missing from phase-averaged models.

8.3 Questions and ideas

8.3.1 Incident wave field feedback

The analysis in Section 7.6 showed that the Boussinesq modelling results indicate a positive feedback between the incident wave forcing and existing vorticity that appears to enhance transient rip generation and maintenance. Although not strong, the feedback is significant across the surf zone and the region outside (Figure 7.16).

In terms of rip generation, the exact nature of the feedback mechanism between the waves and current is somewhat subtle. It is well known that waves are re-

fracted by a wave-averaged current, and wave focussing over established rip currents is observed in the modelling results. Dalrymple and Lozano (1978) showed that a coupled model of currents driven by a wave field, that is in turn refracted by the current, generates periodic rip current cells on a longshore uniform topography. Studies of topographic rip currents have highlighted that there is not positive feedback throughout a rip current system. Recent numerical modelling by Haas et al. (2003) and Yu and Slinn (2003) show negative feedback due to refractive focussing of wave energy, and hence higher opposing radiation stress gradients when breaking, along the rip current neck. However, analysis of tank experiment data by Haller et al. (2002) showed positive feedback on longshore feeder currents and hence rip current strength. Refractive focussing and dissipation by breaking further offshore leads to less wave breaking in the inner rip neck region and the net force driving feeder currents is therefore enhanced. The result is positive feedback in the inner region and negative feedback further offshore.

A positive feedback mechanism in which incident wave energy dissipation is enhanced due to strong offshore flows was proposed by Murray and Reydellet (2002), and a simple cellular automata model based on this idea generates transient rip currents in the absence of topographic variability. While their exact physical mechanism for the dissipation is questionable, enhanced breaking of waves in the region of rip currents is observed in the field. Like refraction, this would be expected to redistribute the effective incident wave forcing so that it opposes the rip flow offshore, and reinforces it inshore. A dissipative feedback exists in a real way in the Boussinesq model used in this work because of the Smagorinsky scheme (Equation 7.11) which generates higher viscosities (and hence wave dissipation) in regions of strong shear which exist in the transient rip currents.

Recently, Bühler and McIntyre (2003) discovered a new interaction between a wave field and a background wave-averaged current field. The "remote recoil" involves the refraction of the wave field by the rotational current field and a corresponding force felt by the rotational flow, even beyond the region of horizontal overlap (hence "remote"), and in the absence of wave breaking. This is clearly a relevant interaction mechanism in real nearshore current and wave fields. There would be a cumulative effect of the interaction of the spatially inhomogeneous wave field with the spatially inhomogeneous current field; how this would influence the overall coupled hydrodynamics is, at present, unknown.

Neither a refractive or dissipative feedback associated with rip currents appears to account for a uniformly positive feedback on the vorticity field as observed. This may be partly because the overall vorticity field is considered rather than only the regions of strong offshore directed flows. Another reason may be that the Dalrymple

and Lozano (1978) equations and the models used by Haas et al. (2003) and Yu and Slinn (2003) all assume a depth dependent breaking criteria, leading to a constant wave height gradient regardless of the presence of the current flow. However, what is observed visually in the field, and in the numerical model, is a modification to wave breaking in the presence of strong opposing currents. This is likely to influence the transfer of momentum from the incident waves, and may be highly nonlinear with respect to individual incident waves, and thus not represented by a wave-averaged radiation stress type of formulation.

While feedback between the incident waves is deterministic in its mechanism, it does not necessarily reduce the “randomness” of the overall response. Models like those of Dalrymple and Lozano (1978) and Falqués et al. (1999) predict evenly spaced rip currents under their idealised assumptions. However, in nature, feedback co-exists with variable forcing inherent in the wave field and strong nonlinearity of the variable rotational currents themselves. Therefore, while they may capture much of the essential physics of the feedback mechanism, a predictable, deterministic system does not evolve.

8.3.2 Three-dimensional effects

The current work focused on the depth-averaged nearshore currents. In the theoretical description, the effect of the depth variation of the currents was conveniently included the terms for lateral mixing and wave forcing following Putrevu and Svendsen (1999). The lateral mixing effect in particular might then be assumed to smear out vorticity gradients in the variable flow field, presumably damping the formation of features like transient rips. As reviewed in Chapter 2, Zhao et al. (2003) found significant damping of shear waves in a Q3D model. In addition, the vorticity dynamics are influenced by introducing vortex tilting which transfers vertical vorticity into horizontal; as pointed out by Zhao et al. (2003), this is not physically a dissipative mechanism, although it acts as such in the depth integrated equations.

As the magnitude and orientation of three dimensional effects are largely determined by the incident wave field, they will vary spatially. In addition, they will be implicitly altered by feedback between currents and the incident wave field. How spatially and temporally variable three dimensional effects would interact with the variable current field is not understood. Analysis of the three way feedback between variable currents, 3D effects and the incident wave field is challenging even with a detailed numerical model. However, due to the mainly dissipative nature of the 3D effects, it is probably reasonable to suggest that they are not involved a strong positive feedback mechanism in the generation of rotational features such as transient rips.

Another aspect of the three-dimensionality of the flow is the observation by some previous researchers that rip currents are stronger near the surface outside the surfzone (Shepard and Inman, 1950; Bowman et al., 1988b). This has also been observed by Haas and Svendsen (2002) in laboratory experiments. Whether this applies to transient rip currents is unknown. The ADCP measurements from the outer surf zone in Chapter 5 show little vertical variation of the transient rip flow other than that associated with the undertow (also present in the absence of rip flow); Haas and Svendsen (2002) similarly found little depth variation in their topographic rip channels. However, it is possible that further offshore the flow may develop a significant vertical variation. Mathematically this can be incorporated in the depth-averaged equations as three dimensional effects in the mixing and forcing terms as with undertow, however this has obvious implications for what the drifters are measuring and how close those measurements are to a depth-averaged velocity.

8.3.3 Infragravity turbulence

In Chapter 5, the term “infragravity turbulence” was suggested to describe the overall spatially variable rotational flow field. This section considers in more detail the possible similarities with classic ideas of turbulence. The idea of nearshore current motion has turbulent nature is not new. Peregrine (1998) suggests: “... it may be more constructive to think of the flow in the surf zone as being a strip of two-dimensional turbulence along the coastline.” It is hard not to attribute the ragged and fractal nature of the suspended sediment at the outer edge of a typical surf zone (which persists over many incident waves) at least partially to a horizontal turbulent type motion.

Turbulent dispersion?

The dispersion of drifter clusters in the experiments described in Chapters 5 and 6 showed a scale dependence of the type:

$$K = C_1 \sigma^\alpha \quad (8.1)$$

where the power law exponents, α , were in the range 1.3 to 1.85. Considering the rate of dispersion of two particles separated by r ,

$$K = \frac{1}{2} \left\langle \frac{dr^2}{dt} \right\rangle = \left\langle r \frac{dr}{dt} \right\rangle = \langle r \delta v \rangle \quad (8.2)$$

where δv is the separation velocity. As $K \sim r^\alpha$, this implies that $\delta v \sim r^{1-\alpha}$. So where $\alpha > 1$ larger separations imply larger separation velocity.

If the particles are in a turbulent velocity field with particles being advected by eddies with diameter r and rotational velocity δv , the power law for the dispersion can be equated to the spectral slope of the wavenumber energy spectrum (Monin and Yaglom, 1975); the classic $E \sim k^{-5/3}$ slope equates to the $K \sim r^{4/3}$ slope of Richardson (1926). As discussed in Chapter 5, oceanic observations of dispersion with power laws close to $4/3$ have been attributed to large scale horizontal turbulence (Okubo, 1974) and the range of dispersion exponents observed appear to be consistent with the drifters separating in two-dimensional turbulence. The exponents measured in the nearshore in this work are somewhat larger.

Other than the uncertainty in the estimation of the power law from the data, there are some caveats to an interpretation of the scale dependent dispersion being due to horizontal currents with a turbulent nature. Two-dimensional isotropic homogeneous turbulence with Kolmogorov scaling implies a $4/3$ power law, as do analyses of turbulent dispersion with rather less strict assumptions. However, the converse cannot be inferred; a $4/3$ power law for particle pair dispersion does not necessarily imply a particular flow regime. Particle pair dispersion in deep water surface gravity waves, caused by differential Stoke's drift in an spatially variable wave field, have been shown to lead to power laws of $\alpha = 7/6$ (Eguiluz et al., 2002). Herterich and Hasselmann (1982) showed that this may partially account for the Okubo's observed scale dependent dispersion over oceanic length scales $< 100 m$. However, it is unlikely to account for the nearshore dispersion here. Other than the fact that the drifters do not actually appear move with the Stoke's drift velocity, the actual values for surface gravity wave dispersion rates are at least an order of magnitude smaller (assuming they are similar in shallow and deep water) than those observed here. Another possible (related) relative dispersion mechanism is due to infragravity wave "Stoke's drift", which as in the deep wave short gravity wave case would be spatially variable. To the author's knowledge, there is no theoretical work on particle dispersion in infragravity waves, however, estimates of net displacements over typical infragravity wave periods suggest that this effect should be smaller than observed separation velocities.

Forcing and nonlinearity

The modelling described in Chapter 7 supports an interpretation of the field measurements of dispersion as due to a turbulent type velocity field. The existence of rotational flow at a range of scales is seen visually in the model flow fields, and in spectra of the longshore wavenumbers of the rotational flow. It was proposed in Section 7.9 that the rotational flow is a (linear) response to the forcing at a range of scales and a nonlinear turbulent type transfer of energy between scales. The

equation for the rotational flow derived in Chapter 3 for the general case is:

$$\frac{\partial \mathbf{u}^R}{\partial t} + \Pi^R [(\mathbf{u}^R \cdot \nabla) \mathbf{u}^R] = -g\nabla\eta^R + \mathbf{S}^R + \mathbf{L}^R + \mathbf{B}^R + \mathbf{N}[\mathbf{U}_o] + \mathbf{N}[\mathbf{u}^D] \quad (8.3)$$

where $\mathbf{N}[\mathbf{U}_o]$ and $\mathbf{N}[\mathbf{u}^D]$ represent all the terms involving interaction between the rotational and quasi-steady/divergent current components. Writing in non-dimensional variables with the same parameter notation as defined in Chapter 3, and assuming all terms of order α , β or any combination is small leaves,

$$\frac{\partial \mathbf{u}'^R}{\partial t} + \Pi^R [(\mathbf{u}'^R \cdot \nabla) \mathbf{u}'^R] = \frac{0.1\gamma^2\kappa\vartheta^R}{(Fr^R)^2} \mathbf{S}'^R + \frac{\gamma^2 h^*}{Fr^R \mathcal{L}} \mathbf{L}'^R + f_w \gamma \sigma \tau^R \mathbf{B}'^R + \mathcal{O}[\alpha, \beta] \quad (8.4)$$

Physically this just implies that the rotational currents can be considered in isolation, influenced by the incident wave forcing, mixing and bottom friction.

Assuming that the \mathbf{L} and \mathbf{B} act only as dissipative mechanisms, the dynamics are determined by the size of \mathbf{S} . At each limit there is a governing equation,

$$\frac{\partial \mathbf{u}^R}{\partial t} + \Pi^R [(\mathbf{u}^R \cdot \nabla) \mathbf{u}^R] = \mathbf{L}^R + \mathbf{B}^R \quad \frac{0.1\gamma^2\kappa\vartheta^R}{(Fr^R)^2} \ll 1 \quad (8.5a)$$

$$\frac{\partial \mathbf{u}^R}{\partial t} = \mathbf{S}^R + \mathbf{L}^R + \mathbf{B}^R \quad \frac{0.1\gamma^2\kappa\vartheta^R}{(Fr^R)^2} \gg 1 \quad (8.5b)$$

Between these limits there is an intermediate situation where both nonlinear and forcing terms are important. It is interesting to note that the size of \mathbf{S} is dependent on $\kappa = s\mathcal{L}/h^*$, so when the relative change of water depth is small (large overall depth/shallow slope, \mathbf{S} is small and the nonlinear terms dominate, and vice versa. This is exactly what is seen in the numerical modelling results shown in Figure 7.15 in Section 7.6.1. The modelling results also indicate that for surf zone conditions, $0.1\gamma^2\kappa\vartheta^R/(Fr^R)^2 \sim 1$, so both nonlinearity and forcing are important.

Characteristics of turbulence

Is the name "turbulence" appropriate for the variable rotational flow? It can be argued the rotational flow field seen in the numerical modelling results satisfies all of the defining criteria of turbulence (given by Kantha and Clayson, 2000):

- Irregularity
- Three-dimensionality (in the sense of vortex stretching)
- Vorticity
- Strong diffusivity

- Dissipation
- Nonlinear
- Broad spectrum
- Anisotropy of large scales
- Loss of memory

Ultimately, whether the term “turbulent” is applied, is a matter of terminology and/or definition. However, it does imply a conceptual shift in how the rotational part of the nearshore current system might be studied and understood. With turbulence comes randomness and strong nonlinearity, which make deterministic approaches to prediction difficult. However, there may be some universality from a statistical viewpoint that may allow techniques usually applied to turbulence to also be relevant for nearshore currents.

Nearshore current classification

A final proposition is that infragravity turbulence could be considered as a fundamental general class of nearshore current motion along with infragravity waves (free and forced), shear waves, and quasi-steady current systems such as topographic rip currents and longshore currents. Like shear waves, it possesses vorticity but is distinct in not having a wave-like structure. Its vorticity is derived from variable incident wave forcing or a background vorticity gradient, and in this sense overlaps with, or is generated by, shear waves as they become highly nonlinear. Under this general classification, transient rip currents are then a specific, well defined feature of infragravity turbulence which occur under the appropriate conditions. Figure 8.1 is a revised version of the summary diagram of nearshore processes presented in Section 1.1.

8.3.4 Nearshore mixing

Dispersion of material in the nearshore zone is not really well understood. Much can be inferred from the studies which have been aimed at understanding the mixing of momentum. However, there are few direct field investigations of dispersion in the nearshore zone. Inman et al. (1971), Rodriguez et al. (1995) and Takewaka et al. (2003) made measurements of dye dispersion and obtained diffusion coefficients. Each of these studies has assumed that Fickian dispersion is a good approximation in the surf zone. For turbulent mixing to be Fickian in nature, and for the change

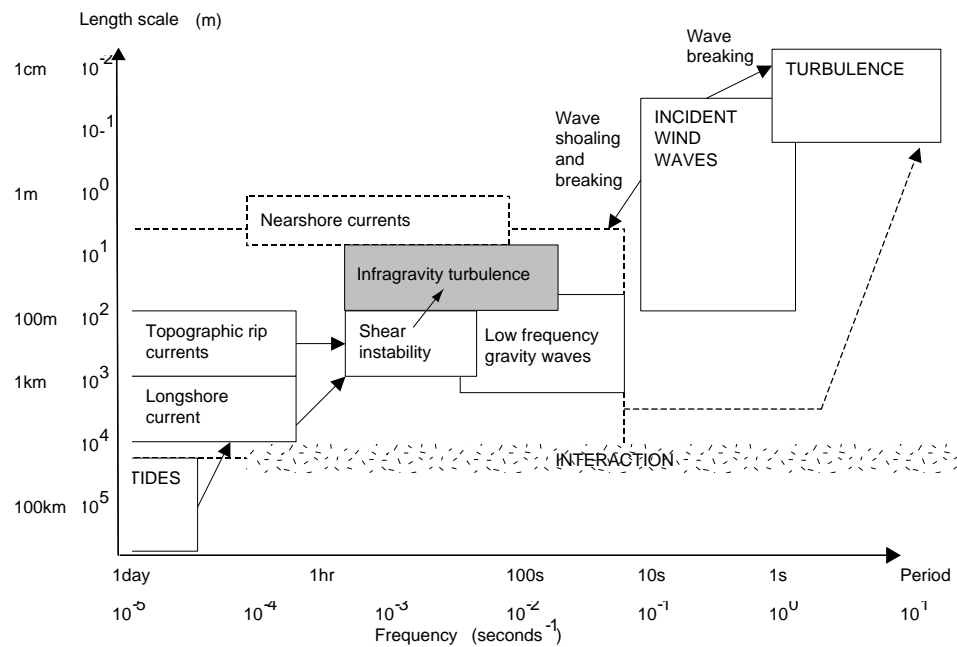


Figure 8.1: Hydrodynamic processes in the nearshore zone with infragravity turbulence introduced as a fundamental class of motion.

of concentration, C , due to mixing to therefore be described by:

$$\frac{\partial C}{\partial t} = \nabla \cdot \kappa_C \nabla C \quad (8.6)$$

where κ_C is a (not necessarily isotropic) diffusion coefficient tensor, then the length scale of the dispersing patch needs to be much larger than the Lagrangian scales (Fischer et al., 1979, Chapter 3). However, the dispersion of drifters estimated in Chapters 5 and 6 show a scale dependence up to the scale of the surf zone width. Both this and the spatial length scale estimates in Section 5.6 imply coherent structures and therefore Lagrangian length scales in the variable currents are of the same order as the surf zone width. This calls into question the use of Equation 8.6 to describe surf zone diffusion, in particular for localised suspension and horizontal diffusion of sediment. Of course, it is desirable to be able to use Equation 8.6, but further investigation is clearly required before it can be considered uniformly valid in the nearshore.

A complication to theoretical understanding of dispersion in the nearshore zone is that the depth varies. This means that nearshore processes are usually far from homogeneous (especially in the cross-shore direction) or isotropic. Inhomogeneity means that dispersion of a particle pair depends not only on separation but also their orientation and cross-shore position. As mentioned in Chapter 6, the presence of a quasi-steady current shear adds another dispersive mechanism. Depth variation is of course the reason for the inhomogeneity but also introduces a continuity requirement for fluid columns to stretch as they move offshore. This will tend to induce a negative dispersion for particle pairs which opposes their tendency to separate in a disorganised current field.

Use of drifters provides a way to assess the lateral dispersion caused by the depth-averaged current velocities. Dye, by contrast, is also mixed by shear dispersion and incident wave breaking; a drifter sampling optimally has zero net displacement over an incident wave cycle, whereas dye will be dispersed by small scale turbulence of the breaking. As noted in §5.5.2 and §6.5, when compared at the same spatial scale, the dispersion coefficient of the drifters are similar to values from the dye experiments. However, such comparisons are not in the same conditions; a combination dye/drifter experiment would be able to separate relative contributions of the depth-averaged horizontal currents and other mixing mechanisms.

The outstanding issue in terms of a wider context and application of results is to gain a better understanding of the transfer of material across the nearshore zone. Other than the obvious application of sediment transport, ongoing development of earth models will require parameterisations for exchange rates across the land/ocean interface. Currently there is little understanding of the net flux of material from the

surf zone to the region outside due to horizontal currents, especially on longshore uniform beaches.

8.4 Further work

Two main areas for further work have emerged as being important. The first is a better fundamental, theoretical understanding of transient rotational flow (infragravity turbulence). The second is further field investigation of variable rotational currents, in particular transient rips.

8.4.1 Idealised infragravity turbulence

The Boussinesq model has the advantage of being able to simulate real wave fields and implicitly includes most of the important hydrodynamics, such as wave nonlinearity, wave-current interaction and wave run-up. However, its complexity makes understanding the fundamental dynamics difficult. An investigation of the behaviour of Equation 8.3 for idealised (spatially varying) wave forcing and without divergent or quasi-steady currents needs to be carried out to identify the fundamental behaviour of the forced rotational flow in a wedge shaped domain. Analytical approaches will probably be limited by the nonlinearity, but numerical solutions of Equation 8.3 are straight forward. This would answer questions like:

- Whether transient rip currents arise from sufficiently energetic rotational flow or whether some feedback on the wave forcing is necessary.
- If transient rip currents occur without feedback, is there a uniform relationship between simple length scales (such as forcing and bottom slope) the generation of transient rips?
- How does the variation of bottom friction and lateral mixing influence vorticity generation?

Extensions to the simplest case could include feedback with the incident wave forcing, infragravity waves, quasi-steady currents and complex topography. As a further note regarding analysis of rotational/divergent interaction, a possible avenue for analytical investigation is a “weakly divergent” formulation of the rotational current equations, in analogy to “weakly compressible” equations for gas dynamics (e.g. Zank and Matthaeus, 1991).

Given the apparently turbulent nature of rotational currents, a spectral approach may prove the most appropriate for the overall rotational flow field. Kirby et al. (1998b) have proposed this for combined infragravity and shear waves. It may be

able relate the incident wave field and variable wave-averaged current in spectral space (which may also be relevant to forced infragravity waves). In the same way as the 4/3 power law is implied by a particular spectral shape of the mixing flow, a predictable spectral form for the variable currents (if it exists) should give some direct insight into dispersion rates.

8.4.2 Field work

Field work is invaluable for understanding nearshore hydrodynamics in real conditions. Specific areas of field work which are highly desirable are:

- Further detailed Lagrangian measurements of transient rip currents, perhaps with larger numbers of drifters deployed at intervals, to get spatial maps of the flow development of transient rips. This would help to observe and better understand the initial spin-up mechanism in the field, and to verify that a Boussinesq model captures the essential dynamics properly.
- Further detailed Lagrangian measurements of longshore currents, again using larger numbers of drifters. This would hopefully unambiguously observe vortices and other variable flow features associated with shear waves; modelling of particle trajectories in numerical simulations are required to support this.
- Lagrangian measurements of dispersion in varying conditions to verify whether a scale dependence of dispersion is ubiquitous. As a complement to theoretical work, this would also help in developing a general theory of nearshore dispersion.
- Field surveying of transient rip occurrence to verify and extend model predictions of their frequency, strength and duration for varying wave conditions and cross-shore profiles. Even visual estimates would provide valuable data.
- Continued development of surf zone drifters to reduce surfing and improve performance in high energy conditions. The eventual limitation may be safe deployment and recovery in large surf zones.

8.5 Conclusions

Wave-averaged, variable, rotational currents are ubiquitous in the nearshore. These rotational currents are well known in the presence of longshore currents as shear waves. However, both field measurements and modelling presented in this work have demonstrated that there are also variable rotational currents in the absence of longshore currents. The development of a surf zone drifter has made Lagrangian

measurements possible, which have provided a unique insight into their dynamics. The use of a Boussinesq model has allowed transient currents associated with random wave fields to be simulated.

Within the rotational flow field, transient rip currents are well defined structures that can develop purely due to the inhomogeneity of the incident wave field. Lagrangian measurements have shown them to be similar to jets, originating in the surf zone and spreading in the region outside. As the field data suggested, the numerical modelling showed that a vortex pair is associated with the evolution of the rip and head region. The field data also suggested that transient rip currents were not isolated, but rather part of an overall rotational flow field with significant energy, that co-exists with infragravity waves. This was confirmed by the numerical model which generated currents with significant vorticity at a range of scales, and discrete features such as vortices.

An important aspect of the rotational currents which have been observed and modelled is their role in nearshore mixing. A scale dependence up to the length scale of the surf zone width indicates a range of mixing scales and questions the validity of eddy diffusivity closures for small time and length scales. Estimated dispersion coefficients indicate strong lateral mixing due to the rotational flow field. Transient rip currents provide a connection in the absence of topographic rip currents between the surf zone and the region outside.

In many ways, more questions have been generated than answered, and there is clearly a long way to go in understanding nearshore currents. It is hoped that this work has made some contribution in identifying and understanding variable, rotational nearshore currents, which (it is suggested) exists as general class of motion that includes, but is not exclusively, nonlinear shear waves and transient rips. In view of its appearance, range of scales, nonlinearity and strong contribution to mixing, the name "infragravity turbulence" is suggested as a general classification. A conceptual shift from thinking of variable nearshore currents solely in terms of low frequency waves and rip currents may be necessary in order to fully encapsulate the rich array of hydrodynamics occurring in the nearshore zone.

References

- Aagaard, T., Greenwood, B., and Nielsen, J. (1997). Mean currents and sediment transport in a rip channel. *Marine Geology*, 140:25–45.
- Allen, J., Newberger, P., and Holman, R. (1996). Nonlinear shear instabilities of alongshore currents on plane beaches. *J. Fluid Mech.*, 310:181–213.
- Arthur, R. (1962). A note on the dynamics of rip currents. *J. Geophys. Res.*, 67:2777–2779.
- Batchelor, G. (1952). Diffusion in a field of homogeneous turbulence. ii the relative motion of particles. *Proc. Camb. Phil. Soc.*, 48:345–363.
- Bouws, E., Günther, H., Rosenthal, W., and Vincent, C. (1985). Similarity of the wind wave spectrum in finite depth 1. spectral form. *J. Geophys. Res.*, 90(C1):975–986.
- Bowen, A. (1969a). The generation of longshore currents on a plane beach. *J. Marine Res.*, 27:206–215.
- Bowen, A. (1969b). Rip currents 1. theoretical investigations. *J. Geophys. Res.*, 74(23):5479–5490.
- Bowen, A. and Holman, R. (1989). Shear instabilities of the mean longshore current, 1. Theory. *J. Geophys. Res.*, 94(C12):18083–18032.
- Bowen, A. and Inman, D. (1974). Nearshore mixing due to waves and wave-induced currents. In *Rapp. P.-v. Réunion. Cons. int. Explor. Mer*, volume 167, pages 6–12. Bianco Luna A/S, Copenhagen.
- Bowman, D., Arad, D., Rosen, D., Kit, E., Goldbery, R., and Slavicz, A. (1988a). Flow characteristics along the rip current system under low energy conditions. *Marine Geology*, 82:149–167.
- Bowman, D., Rosen, D., Kit, E., Arad, D., and Slavicz, A. (1988b). Flow characteristics at the rip current neck under low energy conditions. *Marine Geology*, 79:41–54.
- Brander, R. (1999). Field observations on the morphodynamic evolution of a low-energy rip current system. *Marine Geology*, 157:199–217.
- Brander, R. and Short, A. (2000). Morphodynamics of a large-scale rip current system at Muriwai Beach, New Zealand. *Marine Geology*, 165:27–39.

- Bühler, O. and Jacobson, T. (2001). Wave-driven currents and vortex dynamics on barred beaches. *J. Fluid Mech.*, 449:313–339.
- Bühler, O. and McIntyre, M. (2003). Remote recoil: a new wavemean interaction effect. *J. Fluid Mech.*, 492:207230.
- Chen, Q., Dalrymple, R., Kirby, J., Kennedy, A., and Haller, M. (1999). Boussinesq modelling of a rip current system. *J. Geophys. Res.*, 104:20617–20637.
- Chen, Q., Kirby, J., Dalrymple, R., Kennedy, A., and Chawla, A. (2000). Boussinesq modeling of wave transformation, breaking and runup. II: 2d. *J. Wtrwy., Port, Coast. and Ocean Eng.*, 126(1):48–56.
- Chen, Q., Kirby, J., Dalrymple, R., Kennedy, A., Thornton, E., and Shi, F. (2001). Boussinesq modelling of waves and longshore currents under field conditions. In *Proc 27th Int. Conf. on Coast. Eng.*, pages 651 – 663.
- Christensen, E. and Deigaard, R. (2001). Large eddy simulation of breaking waves. *Coast. Eng.*, 42:53–86.
- Clifford, P., Richardson, S., and Hemon, D. (1989). Assessing the significance of the correlation between two spatial processes. *Biometrics*, 45(1):123–134.
- Cook, D. (1969). The occurrence and geological work of rip currents off southern California. *Marine Geology*, 9:173–186.
- Dalrymple, R. (1975). A mechanism for rip current generation on an open coast. *J. Geophys. Res.*, 80:3485–3487.
- Dalrymple, R. (1978). Rip currents and their causes. In *Proc. 16th Int. Conf. On Coast. Eng.*, volume 2, pages 1414–1427. ASCE.
- Dalrymple, R. and Lozano, C. (1978). Wave current interaction models for rip currents. *J. Geophys. Res.*, 83(C12):6063.
- Danilov, S. and Gurarie, D. (2001). Forced two-dimensional turbulence in spectral and physical space. *Physical Review E*, 63:061208.
- Davis, R. (1985). Drifter observations of coastal surface currents during code: The statistical and dynamical views. *J. Geophys. Res.*, 90(C3):4756–4772.
- Eckart, C. (1951). Surface waves on water of variable depth. Technical report, Scripps Institution of Oceanography, La Jolla ,CA.
- Egüiluz, V., Levinsen, M., and Alstrøm, P. (2002). Weak wave turbulence scaling theory for diffusion and relative diffusion in turbulent surface waves. *Europhysics Letters*, 58(4):517–523.
- Elgar, S., Herbers, T., and Guza, R. (1994). Reflection of ocean surface gravity waves from a natural beach. *J. Phys. Ocean.*, 24:1503–1511.

- Falqués, A., Montoto, A., and Vila, D. (1999). A note on hydrodynamic instabilities and horizontal circulation in the surf zone. *J. Geophys. Res.*, 104(C9):20,605–20,615.
- Fedderson, F. (1998). Weakly nonlinear shear waves. *J. Fluid Mech.*, 372:71–91.
- Fischer, H., List, E., Koh, R., Imberger, J., and Brooks, N. (1979). *Mixing in Inland and Coastal Waters*. Academic Press, New York, NY.
- Fowler, R. and Dalrymple, R. (1991). Wave group forced nearshore circulation. In *Proc 22nd Int. Conf. on Coast. Eng.*, volume 1, pages 729–742.
- Garcez Faria, A., Thornton, E., Stanton, T., Soares, C., and Lippmann, T. (1998). Vertical profiles of longshore currents and related bed shear stress and bottom roughness. *J. Geophys. Res.*, 103(C2):3217 – 3232.
- Guza, R. and Thornton, E. (1985). Observations of surf beat. *J. Geophys. Res.*, 90(C2):3163–3174.
- Haas, K. and Svendsen, I. (2002). Laboratory measurements of the vertical structure of rip currents. *J. Geophys. Res.*, 107(C5):10.1029/2001JC000911.
- Haas, K., Svendsen, I., and Haller, M. (1999). Numerical modelling of nearshore circulation on a barred beach with rip channels. In *Proc 26th Int. Conf. on Coast. Eng.*, volume 1, pages 801–814.
- Haas, K., Svendsen, I., Haller, M., and Zhao, Q. (2003). Quasi-three-dimensional modeling of rip current systems. *J. Geophys. Res.*, 108(C7):3217.
- Haller, M. and Dalrymple, R. (2001). Rip current instabilities. *J. Fluid Mech.*, 433:161–192.
- Haller, M., Dalrymple, R., and Svendsen, I. (1997). Experimental modeling of a rip current system. In *Proc. 3rd Int. Symp. Ocean Wave Measurement and Analysis*, pages 750–764.
- Haller, M., Dalrymple, R., and Svendsen, I. (2002). Experimental study of nearshore dynamics on a barred beach with rip channels. *J. Geophys. Res.*, 107(C6):10.1029/2001JC000955.
- Hashimoto, N., Nagai, T., and Asai, T. (1993). Modification of the extended maximum entropy principle for estimating directional spectrum in incident and reflected wave field. *Rept. of P.H.R.I.*, 32(4):25–47.
- Herterich, K. and Hasselmann, K. (1982). The horizontal diffusion of tracers by surface waves. *J. Phys. Ocean.*, 12:704–711.
- Hino, M. (1975). Theory on the formation of rip current and cuspidal coast. In *Proc. 14th Int. Conf. On Coast. Eng.*, volume 1, pages 901–919. ASCE.
- Holland, K., Holman, R., Lippmann, T., Stanley, J., and Plant, N. (1997). Practical use of video imagery in nearshore oceanographic field studies. *IEEE Journal of Oceanic Engineering (special issue on image processing for oceanic applications)*, 22(1):8192.

- Howd, P., Bowen, A., and Holman, R. (1992). Edge waves in the presence of strong longshore currents. *J. Geophys. Res.*, 97(C7):11,357 – 11,371.
- Howd, P., Oltman-Shay, J., and Holman, R. (1991). Wave variance partitioning in the trough of a barred beach. *J. Geophys. Res.*, 96(C7):12,781 – 12,795.
- Huntley, D., Guza, R., and Thornton, E. (1981). Field observations of surf beat. part 1: Progressive Edge Waves. *J. Geophys. Res.*, 86(C7):6451–6466.
- Huntley, D. and Short, A. (1992). On the spacing between observed rip currents. *Coast. Eng.*, 07:211–225.
- Inman, D., Tait, R., and Nordstrom, C. (1971). Mixing in the surf zone. *J. Geophys. Res.*, 76:3493–3514.
- Isobe, M. (1985). Calculation and application of first-order cnoidal wave theory. *Coast. Eng.*, 9:309–325.
- Isobe, M., Kondo, K., and Horikawa, K. (1984). Extension of MLM for estimating directional wave spectrum. paper no.A-6. 15pp. In *Proc. Symp. on Description and Modeling of Directional Seas*.
- Kantha, L. and Clayson, C. (2000). *Small scale processes in geophysical research*, volume 67 of *International Geophysics Series*. Academic Press, San Diego, California.
- Kennedy, A., Chen, Q., Kirby, J., and Dalrymple, R. (2000). Boussinesq modeling of wave transformation, breaking and runup. i:1d. *J. Wtrwy., Port, Coast. and Ocean Eng.*, 126(1):39–47.
- Kennedy, A. B. and Kirby, J. T. (2003). An unsteady wave driver for narrow-banded waves: modeling nearshore circulation driven by wave groups. *Coast. Eng.*, 48:257275.
- Kirby, J. and Chen, Q. (2003). Examining the low frequency predictions of a boussinesq wave model. In *Proc. 28th Int. Conf. On Coast. Eng.*, volume 1, pages 1075–1087. World Scientific, Singapore.
- Kirby, J., Wei, G., Chen, Q., Kennedy, A., and Dalrymple, R. (1998a). Funwave 1.0; fully nonlinear boussinesq wave model documentation and user’s manual. Technical Report CACR-98-06, Center for Applied Coastal Research, University of Delaware, Newark, DE 19716.
- Kirby, J. T., Putrevu, U., and Özkan Haller, H. T. (1998b). Evolution equations for edge waves and shear waves on longshore uniform beaches. In *Proc. 26th Int. Conf. On Coast. Eng.*, volume 1, pages 203–216. ASCE.
- Kirwan, A. and Chang, M.-S. (1979). Effect of sampling rate and random position error on analysis of drifter data. *J. Phys. Ocean.*, 9:382–387.
- Kirwen, A. and Chang, M.-S. (1979). Effect of sampling rate and random position error on analysis of drifter data. *J. Phys. Ocean.*, 9:382–387.

- Kuriyama, Y. and Nakatsukasa, T. (2000). A one-dimensional model for undertow and longshore current on a barred beach. *Coast. Eng.*, 40:39–58.
- LeBlond, P. and Tang, C. (1974). On energy coupling between waves and rip currents. *J. Geophys. Res.*, 79:811–816.
- Li, L. and Dalrymple, R. (1998). Instabilities of the undertow. *J. Fluid Mech.*, 369:175–190.
- Lippmann, T., Herbers, T., and Thornton, E. (1999). Gravity and shear wave contributions to nearshore infragravity motions. *J. Phys. Ocean.*, 29:231–239.
- Lippmann, T., Holman, R., and Bowen, A. (1997). Generation of edge waves in shallow water. *J. Geophys. Res.*, 102(C4):8663–8679.
- List, E., Gartrell, G., and Winant, C. (1990). Diffusion and dispersion in coastal waters. *J. Hydraulic Eng.*, 116(10):1158–1179.
- Liu, P.-F. and Mei, C. (1976). Water motion on a beach in the presence of a breakwater, I and II. *J. Geophys. Res.*, 81:3079–3094.
- Longuet-Higgins, M. (1970a). Longshore currents generated by obliquely incident waves. *J. Geophys. Res.*, 75:6778–6789.
- Longuet-Higgins, M. (1970b). Longshore currents generated by obliquely incident waves. *J. Geophys. Res.*, 75:6790–6801.
- Longuet-Higgins, M. and Stewart, R. (1962). Radiation stress and mass transport in water waves, with application to surf-beats. *J. Fluid Mech.*, 13:481–504.
- Longuet-Higgins, M. and Stewart, R. (1963). A note on wave setup. *J. Marine Res.*, 21:4–10.
- Longuet-Higgins, M. and Stewart, R. (1964). Radiation stress and mass transport in water waves; a physical discussion, with applications. *Deep-Sea Research*, 11:529–562.
- Madsen, P. and Schaffer, H. (1998). Higher-order boussinesq-type equations for surface gravity waves: Derivation and analysis. *Phil. Trans. Roy. Soc. Lond.*, A356:3123–3184.
- Majda, A. and Bertozzi, A. (2002). *Vorticity and incompressible flow*. Cambridge texts in applied mathematics. Cambridge university press, The Edinburgh Building, Cambridge, UK.
- Masselink, G. and Pattiaratchi, C. (2002). Seasonal variation in nearshore processes and beach morphology along the sheltered coastline of perth, western australia. *Marine Geology*, 172:242–263.
- Mei, C. (1989). *The Applied Dynamics of Ocean Surface Waves*, volume 1 of *Advanced Series on Ocean Engineering*. World Scientific, Siugapore.
- Mei, C. and Angelides, D. (1977). Longshore circulation around a conical island. *Coast. Eng.*, 1:31–42.

- Mitsuyasu, H. (1975). Observation of the directional wave spectrum of ocean waves using a cloverleaf buoy. *J. Phys. Oceanogr.*, 5:750–760.
- Monin, A. and Yaglom, A. (1975). *Statistical fluid mechanics*, volume 2. MIT Press, Cambridge, MA, USA.
- Murray, A., LeBars, M., and Guillon, C. (2003). Tests of a new hypothesis for non-bathymetrically driven rip currents. *J. Coast. Res.*, 19:269 – 277.
- Murray, A. and Reydellet, G. (2002). A rip current model based on a hypothesized wave/current interaction. *J. Coast. Res.*, 17(3):517–530.
- Noyes, J., Guza, R., Elgar, S., and Herbers, T. (2002). Comparison of methods for estimating nearshore shear wave variance. *J. Atmos. Ocean. Tech.*, 19:136–143.
- Okayasu, A. and Katayama, H. (1992). Distribution of undertow and long wave component velocity due to random waves. In *Proc. 23rd Int. Conf. On Coast. Eng.*, volume 1, pages 883–891. ASCE.
- Okubo, A. (1974). Some speculations on oceanic diffusion diagrams. In *Rapp. P.-v. Réunion. Cons. int. Explor. Mer*, volume 167, pages 77 – 85. Bianco Luna A/S, Copenhagen.
- Oltman-Shay, J. and Guza, R. (1987). Infragravity wave observations on two california beaches. *J. Phys. Ocean.*, 77(5):644–663.
- Oltman-Shay, J., Howd, P., and Birkemeier (1989). Shear instabilities of the mean longshore current 2. field observations. *J. Geophys. Res.*, 94(C12):25–45.
- Ozkan-Haller, H. and Kirby, J. (1999). Nonlinear evolution of shear instabilities of the longshore current: a comparison of observations and computations. *J. Geophys. Res.*, 104(C11):25953–25984.
- Paduan, J. and Niiler, P. (1993). Structure of velocity and temperature in the northeast Pacific as measured with lagrangian drifters in fall 1987. *J. Phys. Ocean.*, 23:585–600.
- Peregrine, D. (1998). Surf zone currents. *Theoret. Comput. Fluid Dynamics*, 10:295–309.
- Putrevu, U. and Svendsen, I. (1995). Infragravity velocity profiles in the surf zone. *J. Geophys. Res.*, 100(C6):16131–16142.
- Putrevu, U. and Svendsen, I. (1999). Three-dimensional dispersion of momentum in wave-induced nearshore currents. *Eur. J. Mech. B/Fluids*, 18(3):409–427.
- Richardson, L. (1926). Atmospheric diffusion shown on a distance-neighbour graph. *Proc. Roy. Soc.*, A110:709–727.
- Rodriguez, A., A. Snchez-Arcilla, A., Redondo, J., Bahia, E., and Sierra, J. (1995). Pollutant dispersion in the nearshore region: modelling and measurements. *Water Science and Technology*, 32(9-10):169–178.

- Sasaki, T. and Horikawa, K. (1975). Nearshore current system on a gently sloping bottom. *Coast. Eng. Japan*, 18:123–142.
- Sasaki, T. and Horikawa, K. (1978). Observation of nearshore current and edge waves. In *Proc. 16th Int. Conf. On Coast. Eng.*, pages 791–809. ASCE.
- Sasaki, T., Igarashi, H., and Harakai, S. (1981). Nearshore currents on a partially rocky shore. In *Proc. 17th Int. Conf. On Coast. Eng.*, volume 2, pages 1071–1090. ASCE.
- Schäffer, H. (1993). Infragravity waves induced by short wave groups. *J. Fluid Mech.*, 247:551–588.
- Schäffer, H. (1994). Edge waves forced by short wave groups. *J. Fluid Mech.*, 259:125–148.
- Schäffer, H. and Svendsen, I. (1988). Surf beat generation on a mild slope beach. In *Proc. 21st Int. Conf. On Coast. Eng.*, volume 1, pages 1058–1072. ASCE.
- Schmidt, W., Woodward, B., Millikan, K., Guza, R., Raubenheimer, B., and Elgar, S. (2003). A GPS-tracked surf zone drifter. *J. Atmos. Ocean. Tech.*, 20:1069–1075.
- Shepard, F., Emery, K., and LaFond, E. (1941). Rip currents: A process of geological importance. *J. Geology*, 49:337–369.
- Shepard, F. and Inman, D. (1950). Nearshore water circulation related to bottom topography and wave refraction. *Trans. A.G.U.*, 31:196–213.
- Sheremet, A., Guza, R., Elgar, S., and Herbers, T. (2001). Estimating infragravity wave properties from pressure-current meter array observations. In *Proc. 27th Int. Conf. On Coast. Eng.*, volume 2, pages 1476–1489. ASCE.
- Short, A. (1985). Rip-current spacing and persistence, Narrabeen Beach, Australia. *Marine Geology*, 65:47–71.
- Short, A. and Hogan, C. (1994). Rip currents and beach hazards: Their impact on public safety and implications for coastal management. *J. Coastal Res.*, SI.12:197–209.
- Slinn, D., Allen, J., Newberger, P., and Holman, R. (1998). Nonlinear shear instabilities of alongshore currents over barred beaches. *J. Geophys. Res.*, 103:18,357–18,379.
- Smagorinsky, J. (1963). General circulation experiments with the primitive equations. *Mon. Weather Rev.*, 93:99–165.
- Smith, J. and Largier, J. (1995). Observations of nearshore circulation: Rip currents. *J. Geophys. Res.*, 100(C6):10967–10975.
- Sonu, C. (1972). Field observations of nearshore circulation and meandering currents. *J. Geophys. Res.*, 77:3232–3247.
- Svendsen, I. (1984). Mass flux and undertow in a surf zone. *Coast. Eng.*, 8:347–365.

- Svendsen, I., Haas, K., and Zhao, Q. (2001). Analysis of rip current systems. In *Proc. 27th Int. Conf. Coast. Eng.* ASCE.
- Svendsen, I. and Putrevu, U. (1994). Nearshore mixing and dispersion. *Proc. Roy. Soc. Lond.*, A545:561–576.
- Svendsen, I. and Putrevu, U. (1997). *Surf-Zone Hydrodynamics*, pages 1–75. Number 2 in *Advances in Coastal and Ocean Engineering*. World Scientific, Singapore.
- Symonds, G., Holman, R., and Bruno, B. (1997). Rip currents. In *Coastal Dynamics '97*, pages 584–593. ASCE.
- Symonds, G., Huntley, D., and Bowen, A. (1982). Two-dimensional surf-beat: Long wave generation by a time varying break point. *J. Geophys. Res.*, 87(C1):492–498.
- Symonds, G. and Ranasinghe, R. (2001). On the formation of rip currents on a plane beach. In *Proc. 27th Int. Conf. On Coast. Eng.*, volume 1, pages 468–481. ASCE.
- Takewaka, S., Misaki, S., and Nakamura, T. (2003). Dye diffusion experiment in a longshore current field. *Coast. Eng. J.*, 45(3):471–489.
- Tang, E.-S. and Dalrymple, R. (1989). *Nearshore circulation: Rip currents and wave groups*, pages 205–230. *Advances in Coastal and Ocean Engineering*. Plenum Press, New York.
- Taylor, G. (1954). The dispersion of matter in a turbulent flow through a pipe. *Proc. Roy. Soc. Lond.*, A219:446–468.
- Tennekes, H. and Lumley, J. (1972). *A first course in turbulence*. The MIT Press, Cambridge, Massachusetts.
- Thornton, E. and Guza, R. (1986). Surf zone longshore currents and random waves: Field data and models. *J. Phys. Ocean.*, 16(7):1165–1178.
- Ting, F. and Kirby, J. (1994). Observation of undertow and turbulence in a laboratory surf zone. *Coast. Eng.*, 24:51–80.
- Ursell, F. (1952). Edge waves on a sloping beach. *Proc. Roy. Soc. Lond.*, A214:79–97.
- Van Dongeren, A., Sancho, F., Svendsen, I., and Putrevu, U. (1994). SHORECIRC: A quasi-3d nearshore model. In *Proc. 24th Int. Conf. On Coast. Eng.*, volume 2, pages 2741–2754. ASCE.
- Van Dongeren, A. and Svendsen, I. (2000). Nonlinear and 3d effects in leaky infragravity waves. *Coast. Eng.*, 41:467–496.
- Vos, R. (1976). Observations on the formation and location of transient rip currents. *Sediment. Geol.*, 16:15–19.
- Wei, G., Kirby, J., and Grilli, S.T. Nd Subraymanya, R. (1995). A fully non-linear boussinesq model for surface waves: I. highly non-linear, unsteady waves. *J. Fluid Mech.*, 294:71–92.

- Wei, G., Kirby, J., and Sinha, A. (1999). Generation of waves in boussinesq models using a source function method. *Coast. Eng.*, 36:271–299.
- Yu, J. and Slinn, D. (2003). Effects of wave-current interaction on rip currents. *J. Geophys. Res.*, 108(C3):3088, doi: 10.1029/2001JC001105.
- Zank, G. and Matthaeus, W. (1991). The equations of nearly incompressible fluids. 1. hydrodynamics, turbulence and waves. *Phys. Fluids A.*, 3(1):69–82.
- Zhao, Q., Svendsen, I., and Haas, K. (2003). Three-dimensional effects in shear waves. *J. Geophys. Res.*, 108(C8):3270.

Appendix A

Models and scales for the forcing terms

A.1 Incident wave forcing, \mathbf{S}

For a linear monochromatic wave train in shallow water so that $C_g \sim C$, the radiation stress gradient is given by:

$$\bar{S}_i = \frac{g}{8(\bar{\eta} + h)} \frac{\partial}{\partial x_j} \left[a^2 \left(\delta_{ij} + \frac{k_i k_j}{|k^2|} \right) - \frac{a^2}{2} \delta_{ij} \right] \quad (\text{A.1})$$

where a^2 is a typical incident wave amplitude (half the significant wave height). The mean wave amplitude variation can be approximated by a breaking criterion, $a = \gamma(h^* + \eta)$ inside the surf zone and a shoaling law, $a = a_b h_b^{1/4} (h^* + \eta)^{-1/4}$ outside (where a_b and h_b are the wave amplitude and depth at the outer limit of the surf zone). While strictly in violation of the assumptions behind Equation A.1, for scaling purposes a spatially and temporally varying wave amplitude is allowed so that $a'_w = a[1 + f(\mathbf{x}, t)]$.

$$\bar{S}_i^{(ISZ)} \approx \frac{g\gamma^2}{8(h^* + \bar{\eta})} \frac{\partial}{\partial x_j} \left[(h^* + \bar{\eta})^2 [1 + f(\mathbf{x}, t)]^2 \left(\frac{\delta_{ij}}{2} + \frac{k_i k_j}{|k^2|} \right) \right] \quad (\text{A.2a})$$

$$\bar{S}_i^{(OSZ)} \approx \frac{g a_b^2 h_b^{1/2}}{8(h^* + \bar{\eta})} \frac{\partial}{\partial x_j} \left[(h^* + \bar{\eta})^{-1/2} [1 + f(\mathbf{x}, t)]^2 \left(\frac{\delta_{ij}}{2} + \frac{k_i k_j}{|k^2|} \right) \right] \quad (\text{A.2b})$$

where superscripts *ISZ* and *OSZ* indicate inside and outside the surf zone. To estimate the approximate size of these terms, it is assumed that the bottom slope gradient dominates over the spatial variation of $f(\mathbf{x}, t)$ or k_i . Applying a long time average and subtracting leaves the variable part:

$$S_i^{(ISZ)} \approx \frac{g\gamma^2}{2} \frac{\partial(h^* + \bar{\eta})}{\partial x_j} \left[f(\mathbf{x}, t) \left(\frac{\delta_{ij}}{2} + \frac{k_i k_j}{|k^2|} \right) \right] \quad (\text{A.3a})$$

$$S_i^{(OSZ)} \approx -\frac{ga_b^2 h_b^{1/2}}{8(h^* + \bar{\eta})^{5/2}} \frac{\partial(h^* + \bar{\eta})}{\partial x_j} \left[f(\mathbf{x}, t) \left(\frac{\delta_{ij}}{2} + \frac{k_i k_j}{|k^2|} \right) \right] \quad (\text{A.3b})$$

where $f(\mathbf{x}, t)^2$ has been neglected. For the purposes of scaling the incident wave forcing terms, two non-dimensional parameters are defined:

$$\vartheta^R = \sqrt{\int_T \Pi^R \left[f(\mathbf{x}, t) \left(\frac{\delta_{ij}}{2} + \frac{k_i k_j}{|k^2|} \right) \right]^2 dt} \quad (\text{A.4a})$$

$$\vartheta^D = \sqrt{\int_T \Pi^D \left[f(\mathbf{x}, t) \left(\frac{\delta_{ij}}{2} + \frac{k_i k_j}{|k^2|} \right) \right]^2 dt} \quad (\text{A.4b})$$

Physically, ϑ^R and ϑ^D quantify the amount of ‘‘curl’’ and ‘‘divergence’’ in the forcing due to the incident wave field. This is left in a fairly abstract form; an example of an analytic approximation is used by Schäffer (1994). To apply the above to a real sea state, a monochromatic wave with wavenumber \mathbf{k} and amplitude a'_w is assumed representative of the total effect of the random wave field. Finally, the second spatial derivative of the bottom slope is assumed small, $\frac{\partial^2 h^*}{\partial x_i \partial x_j} \ll 1$ and $\eta/h^* \sim \epsilon \ll 1$ to give typical magnitudes for the incident wave forcing terms

$$\mathbf{S}^{R(ISZ)} \sim \frac{g\gamma^2 s \vartheta^R}{2} \quad \mathbf{S}^{R(OSZ)} \sim -\frac{ga_b^2 h_b^{1/2} s \vartheta^R}{8(h^*)^{5/2}} \quad (\text{A.5a})$$

$$\mathbf{S}^{D(ISZ)} \sim \frac{g\gamma^2 s \vartheta^D}{2} \quad \mathbf{S}^{D(OSZ)} \sim -\frac{ga_b^2 h_b^{1/2} s \vartheta^D}{8(h^*)^{5/2}} \quad (\text{A.5b})$$

A.2 Lateral mixing, **L**

Typical values of Q_i^w and ν are parameterised following Svendsen and Putrevu (1994), $Q_i^w \approx 0.1\gamma h^* \sqrt{gh^*} k_i / |k|$ and $\nu_t \approx 0.01h^* \sqrt{gh^*}$ inside the surf zone and $\nu \approx [0.8(h^*/h_b)^{-4} 0.2] h_b \sqrt{gh_b}$ outside. Substituting these approximations into Equation 3.7 and simplifying where possible gives:

$$\bar{L}_i \sim \frac{1}{(h^* + \bar{\eta})} \frac{\partial}{\partial x_j} \left\{ (h^* + \bar{\eta}) \left[M_{jk} \frac{\partial \bar{U}_i}{\partial x_k} + M_{ik} \frac{\partial \bar{U}_j}{\partial x_k} \right] \right\} \quad (\text{A.6})$$

where:

$$M_{ij}^{(ISZ)} = g^{1/2} h^{3/2} \left(0.01 + \gamma^2 k_i k_j / |k|^2 \right) \quad (\text{A.7a})$$

$$M_{ij}^{(OSZ)} = g^{1/2} h_b^{3/2} \left(\left[0.008(h^*/h_b)^{-4} + 0.002 \right] + \frac{\gamma^2 (h^*/h_b)^3 k_j k_k / |k|^2}{[0.8(h^*/h_b)^{-4} + 0.2]} \right) \quad (\text{A.7b})$$

As shown by Svendsen and Putrevu (1994), and is clear from the relative sizes of terms in the brackets of M_{ij} ($\gamma^2 \sim 0.2 - 0.5$), the dispersive mixing usually dominate. The exception is when the incident waves approach perpendicular to the shore, where all dispersive terms except those involving $k_x k_x / |k|^2$ are zero (assuming the x -axis is perpendicular to the shoreline). This leads to the interesting situation where the lateral mixing of momentum is strongly anisotropic.

Simplifying under the assumption that the spatial derivatives of the velocity dominate in the expansion of terms, leaves:

$$\bar{L}_i = M_{jk} \frac{\partial \bar{U}_i}{\partial x_j \partial x_k} + M_{ik} \frac{\partial \bar{U}_j}{\partial x_j \partial x_k} \quad (\text{A.8})$$

In most cases, $M_{xx} \gg M_{xy} \gg M_{yy}$, so for the purposes of determining the magnitude of \mathbf{L} the dominant terms are,

$$\bar{\mathbf{L}} \sim \left[2M_{xx} \frac{\partial^2 \bar{U}}{\partial x^2}, M_{xx} \frac{\partial^2 \bar{V}}{\partial x^2} \right] \quad (\text{A.9})$$

This is not particularly convenient for explicit calculation under the projection operators, however, by again neglecting spatial variations of terms other than \mathbf{U} , the appropriate sizes of the terms for inside the surf zone will be:

$$\mathbf{L}^R \sim \frac{\gamma^2 g^{1/2} h^{*3/2} \mathcal{U}^R}{\mathcal{L}^2} \quad (\text{A.10a})$$

$$\mathbf{L}^D \sim \frac{\gamma^2 g^{1/2} h^{*3/2} \mathcal{U}^D}{\mathcal{L}^2} \quad (\text{A.10b})$$

A.3 Bottom friction, \mathbf{B}

The wave orbital speed, which can be estimated by $\tilde{u}^w = a\omega$, where ω is the peak spectral incident wave angular frequency. Using the estimates for wave amplitudes from Section A.1.

$$\bar{\mathbf{B}}^{(ISZ)} \approx -f_w \gamma \omega \bar{\mathbf{U}} \quad (\text{A.11a})$$

$$\bar{\mathbf{B}}^{(OSZ)} \approx -f_w \omega a_b h_b^{1/4} (h^* + \eta)^{-5/4} \bar{\mathbf{U}} \quad (\text{A.11b})$$

Following the same assumptions as for \mathbf{S} and \mathbf{L} , approximate equations for the variable bottom friction terms are

$$\mathbf{B}^{R(ISZ)} \approx f_w \gamma \omega \mathbf{u}^R \quad (\text{A.12a})$$

$$\mathbf{B}^{R(OSZ)} \approx f_w \omega a_b h_b^{1/4} (h^*)^{-5/4} \mathbf{u}^R \quad (\text{A.12b})$$

$$\mathbf{B}^{D(ISZ)} \approx f_w \gamma \omega \mathbf{u}^D \quad (\text{A.12c})$$

$$\mathbf{B}^{D(OSZ)} \approx f_w \omega a_b h_b^{1/4} (h^*)^{-5/4} \mathbf{u}^D \quad (\text{A.12d})$$

so the appropriate scaling is:

$$\mathbf{B}^{R(ISZ)} \sim f_w \gamma \omega \mathcal{U}^R \quad \mathbf{B}^{R(OSZ)} \sim f_w \omega a_b h_b^{1/4} (h^*)^{-5/4} \mathcal{U}^R \quad (\text{A.13a})$$

$$\mathbf{B}^{D(ISZ)} \sim f_w \gamma \omega \mathcal{U}^D \quad \mathbf{B}^{D(OSZ)} \sim f_w \omega a_b h_b^{1/4} (h^*)^{-5/4} \mathcal{U}^D \quad (\text{A.13b})$$

A.4 Reynolds type stress, \mathbf{T}

By analogy with an eddy viscosity argument, where the rotational variable current is exchanging momentum between different regions of the quasi-steady flow,

$$\mathbf{T} = \overbrace{(\mathbf{u} \cdot \nabla) \mathbf{u}} \sim \nabla \cdot \nu_u \nabla \mathbf{U}_o \quad (\text{A.14})$$

where ν_u is the effective eddy viscosity, with order of magnitude related to the rotational velocity and a mixing length, ℓ , by $\nu_u \sim \ell \mathcal{U}^R$. Strictly speaking, an eddy viscosity type argument is invalidated as field data implies that $\ell \sim \mathbf{L}$; this is discussed in Section 6.6). However, it is assumed that it is sufficient for an order of magnitude estimate to express \mathbf{T} in terms of an equivalent eddy viscosity. Under a similar assumption that was made for the lateral mixing term \mathbf{L} , that the spatial derivatives of the equivalent eddy viscosity and depth can be neglected in favour of derivatives of \mathbf{U}_o means that:

$$\mathbf{T}^R \sim \mathcal{U}^R \ell^o / \mathcal{L} \quad (\text{A.15a})$$

$$\mathbf{T}^D \sim 0 \quad (\text{A.15b})$$